UNIVERSITY OF CRETE

DEPARTMENT OF PHYSICS

PhD THESIS

Investigation of the High-Mass X-ray Binary populations in the Small Magellanic Cloud

Grigorios Maravelias

Advisor: *Prof.* Andreas Zezas - University of Crete

UNIVERSITY OF CRETE
DEPARTMENT OF PHYSICS

PhD THESIS
IN
- Astrophysics -

Defended by
Grigorios Maravelias

Investigation of the High-Mass X-ray Binary populations in the Small Magellanic Cloud

COMMITTEE

Prof. Zezas Andreas - University of Crete
Prof. Papadakis Iossif - University of Crete
Dr. Reig Pablo - Foundation for Research and Technology Hellas
Prof. Hatzidimitriou Despina - University of Athens
Prof. Kylafis Nikos - University of Crete
Prof. Pavlidou Vasiliki - University of Crete
Prof. Tassis Kostas - University of Crete

Date of defense:
18/09/2014

Περίληψη

Τα διπλά συστήματα εκπομπής ακτίνων X μεγάλης μάζας (ΔΣΕΧΜΜ) είναι μια φάση μόνο στη ζωή μερικών διπλών αστρικών συστημάτων, τα οποία αποτελούνται από ένα αστρικό υπόλειμμα (μαύρη τρύπα ή αστέρας νετρονίων) και ένα συνοδό μεγάλης μάζας (ένα νεαρό άστρο φασματικού τύπου OB). Το OB άστρο που κυριαρχεί στο οπτικό μέρος του φάσματος, χάνει ύλη είτε μέσω δυνατών ανέμων και/ή μέσω του λοβού Roche στα συστήματα με υπεργίγαντα άστρο-δότη ή μέσω ενός ισημερινού δίσκου εκροής σε συστήματα με άστρο-δότη τύπου Be (Be-ΔΣΕΧΜΜ). Η απελευθέρωση βαρυτικής ενέργειας κατά την πτώση της ύλης πάνω στο αστρικό υπόλειμμα παράγει τις ακτίνες X. Η μελέτη των ΔΣΕΧΜΜ μας προσφέρει πολύτιμες πληροφορίες σχετικά με την εξέλιξη των άστρων μεγάλης μάζας, τις τελικές τους καταστάσεις, και τη συμπεριφορά της ύλης υπό ακραίες συνθήκες.

Το Μικρό Νέφος του Μαγγελάνου (ΜΝΜ) είναι ένα εξαιρετικό εργαστήριο παραγωγής ΔΣΕΧΜΜ. Λόγω της εγγύτητάς του μπορούμε να παρατηρήσουμε μεμονωμένα άστρα στο ΜΝΜ και τα παρατηρητήρια ακτίνων X (*Chandra*, *XMM-Newton*) μπορούν συστηματικά να ανιχνεύσουν πηγές ακτίνων X με χαμηλή δραστηριότητα εκπομπής ακτίνων X, αποκαλύπτοντας ένα μεγάλο δείγμα του πληθυσμού τους (περίπου 100 συστήματα). Ωστόσο, κλειδί για την κατανόηση αυτών των πληθυσμών είναι ο χαρακτηρισμός του άστρου-δότη τους, και η ταυτοποίηση όσο περισσότερων πηγών είναι δυνατό, ειδικά εκείνων με χαμηλές λαμπρότητες στις ακτίνες X.

Για αυτό το λόγο πραγματοποιήσαμε μια φασματοσκοπική έρευνα για την απόκτηση οπτικών φασμάτων για ένα μεγάλο αριθμό ΔΣΕΧΜΜ στο ΜΝΜ, που είχαν ανιχνευτεί σε προηγούμενες έρευνες με τα παρατηρητήρια *Chandra* και *XMM-Newton*, χρησιμοποιώντας το φασματογράφο πολλαπλών ινών AAOmega/2dF στο Anglo-Australian Telescope. Βρήκαμε 5 νέα Be-ΔΣΕΧΜΜ (συμπεριλαμβανουμένου ενός αντικειμένου με κάποια αβεβαιότητα), ταυτοποιώντας το φασματικό τύπο των αντίστοιχων οπτικών πηγών τους, και επιβεβαιώσαμε την φασματική ταξινόμηση 15 γνωστών αντικειμένων. Συγκρίναμε τους φασματικούς τύπους, τις τροχιακές περιόδους, και τις εκκεντρότητες των πληθυσμών Be-ΔΣΕΧΜΜ στο ΜΝΜ και στο Γαλαξία μας και βρίσκουμε οριακά διαφορά μεταξύ των κατανομών για τους φασματικούς τύπους, αλλά όχι στατιστικά σημαντικές διαφορές για τις τροχιακές περιόδους και τις εκκεντρότητες τους. Επιπρόσθετα, η έρευνα μας ανέδειξε ότι ο γνωστός υπεργίγαντας B[e] LHA 115-S 18 (ή AzV 154) συνδέεται με την αμυδρή πηγή ακτίνων X CXOU J005409.57-724143.5. Αποδεικνύουμε ότι ο υπεργίγαντας

LHA 115-S 18 είναι η αντίστοιχη οπτική πηγή της πηγής ακτίνων X, και συζητάμε την προέλευση της χαμηλής λαμπρότητας σε ακτίνες X ($L_X \sim 4 \times 10^{33}\,\mathrm{erg\ s^{-1}}$) στα πλαίσια ενός ΔΣΕΧΜΜ με υπεργίγαντα δότη σε περιβάλλον με έντονη απορρόφηση των ακτίνων X.

Για να αποφύγουμε την υποκειμενικότητα στην φασματική ταξινόμηση των άστρων, που βασίζεται στην οπτική επισκόπηση των φασμάτων, αναπτύξαμε δύο μεθόδους στηριζόμενοι στην μέτρηση του ισοδύναμου πλάτους των σημαντικότερων διαγνωστικών φασματικών γραμμών, εστιάζοντας σε πρώτο επίπεδο στα νεαρά άστρα (OB). Αναπτύξαμε δύο διαφορετικές προσεγγίσεις: (α) η προσέγγιση Συνεχούς Προσαρμογής δίνει το φασματικό τύπο ενός άστρου από την λύση μια εξίσωσης που περιλαμβάνει τα ισοδύναμα πλάτη διαφορετικών φασματικών γραμμών, και (β) ο Απλός Μπευζιανός Ταξινομητής που δίνει την πιθανότητα ένα φάσμα να αντιστοιχεί σε ένα δεδομένο φασματικό τύπο, βάση της κατανομής των ισοδύναμων πλατών των διαγνωστικών γραμμών για άστρα διαφορετικών φασματικών τύπων. Η προσέγγιση Συνεχούς Προσαρμογής δίνει συμβατά αποτελέσματα (με σφάλμα 2 φασματικών υπο-τύπων) μεταξύ των δειγμάτων που χρησιμοποιήσαμε ($\sim 65\%$). Ο Απλός Μπευζιανός Ταξινομητής ταξινομεί σωστά την πλειονότητα ($\sim 70\%$) των νεαρών άστρων στα δείγματά μας, αλλά αποδίδει πιο φτωχά αποτελέσματα ($\sim 40\%$ επιτυχία) για δείγματα που περιέχουν άστρα με φασματικούς τύπους πέραν των νεαρών OB άστρων (αποτέλεσμα του περιορισμένου δείγματος εκπαίδευσης).

Για να επεκτείνουμε το δείγμα των Be-ΔΣΕΧΜΜ αναζητήσαμε πηγές με εκπομπή Hα αντίστοιχες των πηγών ακτίνων X που ανιχνεύτηκαν στην έρευνα του *XMM-Newton* στο ΜΝΜ (Sturm et al., 2013), χρησιμοποιώντας την κάμερα WFI στο τηλεσκόπιο MPG/ESO. Πραγματοποιήσαμε φωτομετρικές παρατηρήσεις στο φαρδύ φίλτρο R και στο στενό φίλτρο Hα για 6 πεδία στο ΜΝΜ με πρόσφατη αστρο-γέννεση. Προσδιορίσαμε 4747 πηγές με εκπομπή Hα μέχρι το φωτομετρικό όριο των 18.7 mag (που αντιστοιχεί σε άστρα τύπου ∼B8 της Κύριας Ακολουθίας). Αυτή είναι η βαθύτερη ευρεία έρευνα για άστρα με εκπομπή Hα στο ΜΝΜ. Βρίσκουμε ότι τα OBe άστρα αποτελούν το 13% του συνολικού πληθυσμού των νεαρών OB άστρων στο ΜΝΜ μέχρι το φωτομετρικό όριο των 18.7 mag. Διερευνώντας αυτό το ποσοστό συναρτήσει της λαμπρότητας των άστρων συμπεράνουμε ότι η εκπομπή Hα μεγιστοποιείται για φασματικούς τύπους O9-B2. Χρησιμοποιώντας τον αριθμό των επιβεβαιωμένων και υποψήφιων Be-ΔΣΕΧΜΜ, βάση του πιο πλήρη καταλόγου σημειακών πηγών ακτίνων X στο ΜΝΜ (Sturm et al., 2013), βρίσκουμε το ποσοστό τους σε σχέση με τον αριθμό των OBe άστρων μεταξύ των τιμών $\sim 0.5 - 1.4 \times 10^{-3}$ Be-ΔΣΕΧΜΜ/OBe, που αποτελεί μια απευθείας μέτρηση του ρυθμού σχηματισμού των Be-ΔΣΕΧΜΜ στο ΜΝΜ. Τέλος, δίνουμε τις αντίστοιχες οπτικές πηγές με εκπομπή Hα για 8 υποψήφια ΔΣΕΧΜΜ.

Abstract

High-Mass X-ray Binaries (HMXBs) are a phase in the life of some binary stellar systems that consist of a compact object (black hole or neutron star) and a massive companion (an early OB-type star). The OB star that dominates in the optical band, losses matter either through strong stellar winds and/or Roche-lobe overflow in the case of systems with a supergiant donor star or through an equatorial decretion disk in systems with a Be donor star (Be/X-ray Binaries;BeXRBs). The infall of this matter in the strong gravitational field of the compact object powers the observed X-ray emission. The study of HMXBs provides insights into the evolution of massive stars, their terminal states, and the behavior of matter in extreme conditions.

The Small Magellanic Cloud (SMC) is a powerhouse of HMXB production. Due to its proximity we can resolve its stellar population and the X-ray observatories (*Chandra*, *XMM-Newton*) can routinely detect X-ray sources down to luminosities of low-activity systems, providing a large sample of their population (almost 100 systems). However, key for understanding these populations is the characterization of their donor star, and the identification of as many sources as possible, specially in low X-ray luminosities.

For this reason we have performed a spectroscopic survey to obtain optical spectra for a large number of SMC HMXBs identified in previous *Chandra* and *XMM-Newton* surveys, using the AAOmega/2dF fiber-fed spectrograph at the Anglo-Australian Telescope. We find 5 new BeXRBs (including a tentative one), by identifying the spectral type of their optical counterparts, and we confirm the spectral classification of 15 known BeXRBs. We compared the spectral types, orbital periods, and eccentricities of the BeXRB populations in the SMC and the Milky Way and we find marginal evidence for difference between the spectral type distributions, but no statistically significant differences for the orbital periods and the eccentricities. Moreover, our search revealed that the well known supergiant B[e] star LHA 115-S 18 (or AzV 154) is associated with the weak X-ray source CXOU J005409.57-724143.5. We provide evidence that the supergiant star LHA 115-S 18 is the optical counterpart of the X-ray source, and we discuss the origin of its low X-ray luminosity (Lx $\sim 4 \times 10^{33}$ erg s^{-1}), in the context of an obscured supergiant X-ray binary.

In order to overcome the subjectivity in the spectral type classification of stars based on the visual inspection of their spectra, we developed two diagnostic schemes based on the measurement of the equivalent width of diagnostically important spectral lines, focusing at this point, on early-type stars. We developed two different approaches: (a) the Continuous Fit approach gives the spectral type of a star as the solution of an equation involving the equivalent widths of different spectral lines, and (b) a Naive Bayesian Classifier gives the probability that a spectrum corresponds to a given spectral type, based on the distribution of equivalent widths of diagnostic lines of stars of different spectral types. The Continuous Fit approach provides consistent results (within an error of 2 sub-spectral types) between the samples used ($\sim 65\%$). The Naive Bayesian Classifier correctly classifies the majority ($\sim 70\%$) of early-type stars in our samples, but it performs rather poorly ($\sim 40\%$ success rate) for samples with late-type stars (a result of the limited training sample).

In order to extend our sample of BeXRBs we searched for Hα emitting counterparts to X-ray sources detected in the *XMM-Newton* survey of the SMC (Sturm et al., 2013). For this, we performed a narrow-band Hα survey of the SMC using the WFI camera at the MPG/ESO telescope. We obtained broad-band R and narrow-band Hα photometry for 6 fields in the SMC with recent star formation, located on the Bar and Wing regions. We identified 4747 Hα emission sources down to a sensitivity limit of 18.7 mag (equivalent to ~B8 type Main Sequence stars). This is the deepest wide area search for emission-line stars in the SMC. We find that OBe stars are 13% of the total OB star population in the SMC down to 18.7 mag. By investigating this fraction as a function of the brightness of the stars we deduce that Hα excess peaks at spectral range O9-B2. Finally, using the number of confirmed and candidate BeXRBs, based on the most complete census of X-ray point sources in the SMC up to date (Sturm et al., 2013), we find their fraction with respect to the OBe stars to be in the range $\sim 0.5 - 1.4 \times 10^{-3}$ BeXRB/OBe, a direct measurement of the formation rate of HMXBs in the SMC. We also provide optical counterparts with Hα excess for 8 candidate HMXBs.

To my parents,
for their continuous encouragement

Acknowledgements

A PhD thesis is never a task to be completed solely by a person. There are always direct or indirect contributions. I will attempt to present a (non-exclusive) list.

I would like to to acknowledge the State Scholarships Foundation of Greece (IKY) which supported the work that led in this thesis in the form of a scholarship.

I am grateful to Nikos Kylafis, who did not discourage me from pursuing a PhD in Astrophysics and showed me where to look for the path.

Andreas Zezas did not just point to the path. Instead, he walked all the way with me, in sunny and rainy days. His guidance and support were always inspiring and, amazingly, endless. I thank him deeply for his time, energy and knowledge he offered me.

I am thankful to my PhD committee Iossif Papadakis and Pablo Reig, for their support during my PhD studies. I thank Pablo also for many discussions.

I cannot forget Vallia Antoniou, with who we spent days and nights working together either in person or through phone, mails, and every other possible way of communication. I thank my collaborators Despoina Hatzidimitriou for help and advice on stellar spectral classification, Eric Gaidos for offering me the opportunity to work on exoplanets, Chris Evans for providing the 2dF sample of spectra used for the development of the classifier, and Frank Haberl who provided access to the Hα imaging data.

Since I spent 4 years in Skinakas office (and many nights at the observatory) I cannot forget the people working there (yes...you are loud, but not for that!): Anna Steiakaki, George Paterakis, Tassos Kougentakis, Makis

Paleologou (I really enjoyed all the conversations!). I acknowledge also the support by the telescope operators Anton Strigachev and Evgeni Semkov.

I am more than just thankful to Thodoris Bitsakis, Paolo Bonfini, Antonis Manousakis, and Alexandros Maragoudakis. We spent hours and hours talking about everything almost everywhere. Many thanks also to: Tanio, Alexandros, Gina, Maria, Ioanna, Leonardos, Stergios, Giannis, Eleni.

I have to thank all my friends and relatives for their continuous support (even though they do not understand what I am doing!). Also, I am thankful to "KALLIRROON - Iron Palm Chinese Martial Arts School", who helped me to develop useful skills applicable to life and PhD theses. I appreciate the stimulative environment provided by (many) fellow amateur astronomers and the Hellenic Amateur Astronomy Association, which had played a significant role in the pursuit of a PhD in Astrophysics.

Last, I am grateful to my parents, Vagelis and Eudoxia, my sister Alexandra, and Elena, whose love is a continuous source of inspiration and motivation.

Contents

List of Figures

List of Tables

1
Introduction

1.1 Introducing X-ray binaries

It is almost 50 years ago that the first cosmic X-ray source was discovered. A rocket launch in 1962 identified a source at the direction of the constellation Scorpius, a binary stellar system named Scorpius X-1 (Giacconi et al., 1962). Since then, the advance of X-ray astronomy and the advent of new satellites (e.g. *Einstein, EXOSAT, RXTE, Chandra, XMM-Newton*) has increased dramatically the number of binaries discovered and, moreover, new kinds of systems have been identified.

X-ray binaries consist of a stellar source and a compact object (Lewin et al., 1997). Based on the nature of the compact object they can be divided into white-dwarf, neutron-star or black-hole systems (Figure 1.1; after Reig 2011). The strong gravitational potential of the compact object captures matter from the companion star and creates an accretion disk, i.e. a stream of matter that loses energy as it spirals inward towards the compact object (Carroll & Ostlie, 2006). Based on the nature of their companion, they can be divided (Charles & Coe, 2006) in low-mass binaries (LMXBs, with typical masses of $\lesssim 1$ $M_\odot$), and high-mass binaries (with typical masses of $\gtrsim 10$ $M_\odot$). A population of systems with masses in between these values, referred to as intermediate-mass binaries, is also expected. However, these systems are extremely short-lived ($\sim$1000 yr), and they do not correspond to a substantial percentage of the X-ray binary population in general (Tauris & van den Heuvel, 2006).

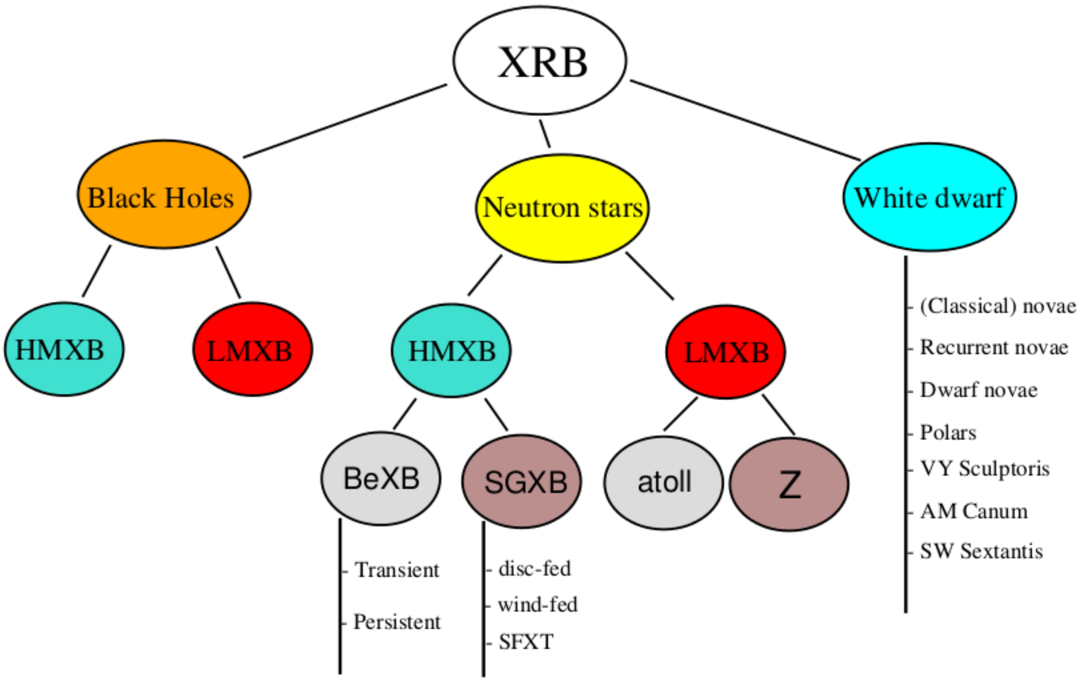

Figure 1.1: The classification scheme of X-ray binaries (after Reig 2011).

Binaries that consist of a white dwarf and low-mass evolved star are referred to as Cataclysmic Variables. Evolved low-mass companions with neutron stars or black holes form the Low-Mass X-ray Binaries (LMXBs) class. Young high-mass companions and neutron stars or black holes form the High-Mass X-ray Binaries (HMXBs) class. The companion star, usually referred to as donor or optical counterpart, provides the necessary material that accretes onto the compact object, and produces X-ray emission. Studying binaries is absolutely essential to determine their nature. The distinct classes of X-ray binaries exhibit different X-ray and optical properties due to the different components of which they consist of. Therefore, their study provides important insights of the physics of compact sources and accretion processes.

Moreover, X-ray binaries are fundamentally important to study stellar evolution. Not all binaries can become X-ray emitting sources unless certain conditions are satisfied (e.g. masses of the progenitors, orbital properties, supernova aftermath). Studying X-ray binaries helps to identify these conditions and obtain a more thorough understanding of how stellar evolutions works.

1.2 Formation and evolution of HMXBs and LMXBs

The HMXBs are actually a phase in the evolution of some massive binaries. In Figure 1.2 a schematic representation of the formation of a HMXB is demonstrated (after Tauris & van den Heuvel 2006).

Initially, the binary consists of stars that enter the main-sequence with masses over 8 $M_\odot$ (at Zero Age Main Sequence-ZAMS). The most massive one (primary) will evolve faster and within a few Myrs will fill its Roche-lobe, transfer most of its mass to its companion (secondary), and will explode as a supernova. If the explosion does not destroy the binary, then the remaining compact object (usually a neutron star) will remain gravitationally bound to the secondary in a wider and more eccentric orbit than the initial one. Depending on the nature of the secondary (which has now become the massive component of the system) the neutron star will accrete matter either through the stellar wind or an equatorial decretion disk. The accretion onto the neutron star leads to the production of X-rays and, thus, the system enters in the HMXB stage.

Gradually, angular-momentum loss decreases the orbital period, resulting in shorter orbits. When the orbit shrinks inside the envelope of the evolved star, the binary enters the common envelope phase. During this, short-lived ($\sim 10^3$ yr; Tauris & van den Heuvel 2006), stage the neutron star spirals in, and its orbital energy is deposited to the envelope. If the binary survives through this phase, i.e. there is enough energy to eject the envelope before the compact object merges with the stellar core, the helium core of the secondary evolves quickly to a second supernova explosion, leading to a double neutron star system.

It should be evident from the above that there are many parameters that determine the formation of HMXBs, making them a rather rare class of objects of high importance, due to the many physical processes involved.

The LMXB evolution is different to the HMXB channel (Figure 1.3). In the LMXBs the initial binary is composed by a massive primary and a low-mass secondary star. The primary evolves quickly (within a few Myr), passing from Roche-lobe overflow and common envelope phases, and ends again in a supernova explosion. The compact object left in this case needs time before it starts to accrete matter from the secondary. This time depends on the evolution time of the low-mass star, as a few Gyr are needed before the orbit of the system shrinks, the secondary fills its Roche-lobe, and their separation becomes smaller.

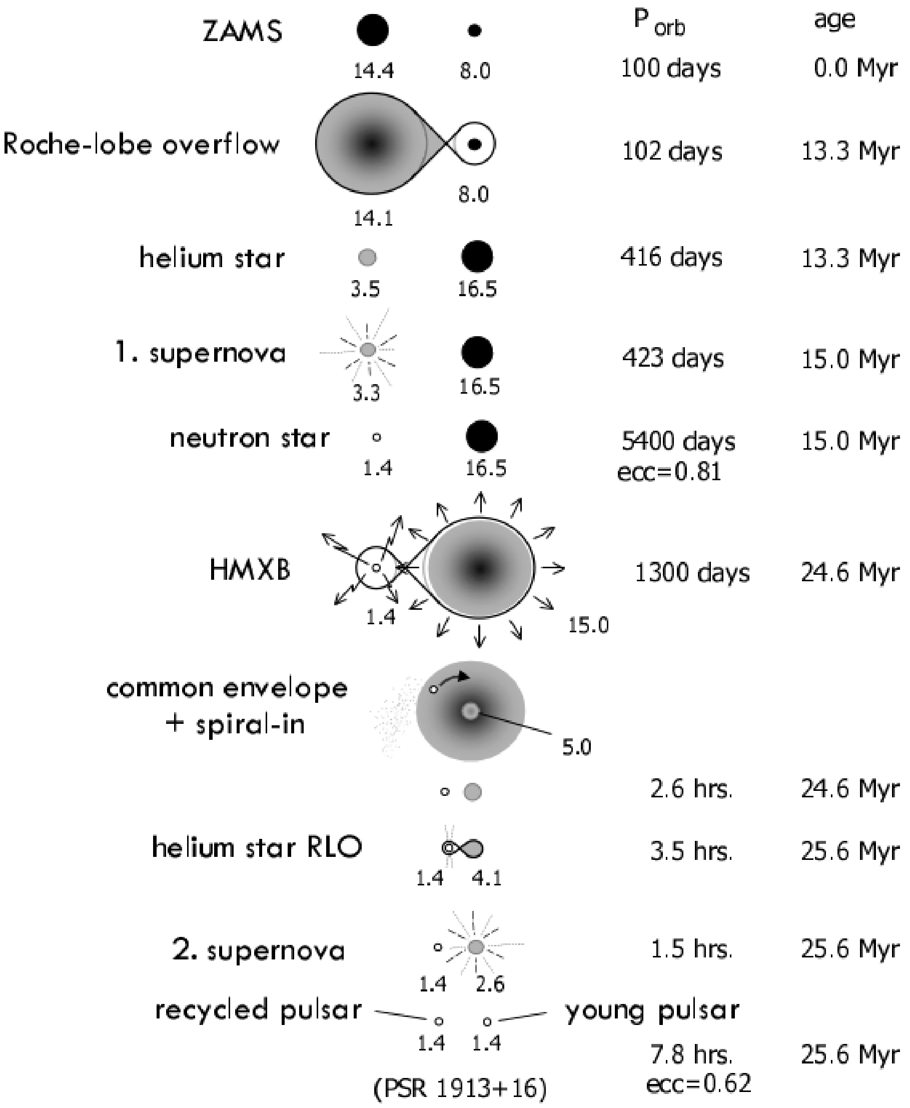

Figure 1.2: Schematic representation of the formation and evolution of a HMXB (from Tauris & van den Heuvel, 2006). The orbital period and the time evolution are also presented inline with the various evolution stages up to and after the HMXB phase (see Section 1.2 for details).

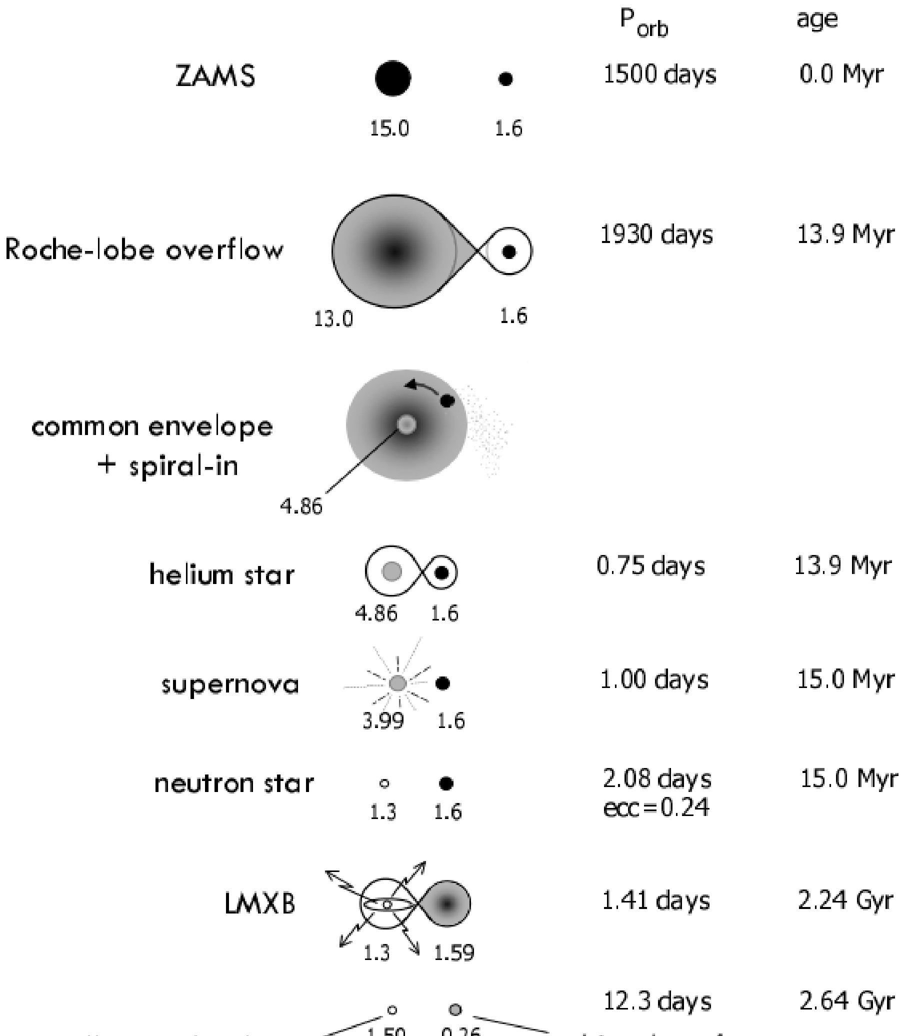

Figure 1.3: Schematic representation of the formation and evolution of a LMXB (from Tauris & van den Heuvel, 2006). The orbital period and age are also presented inline with the various evolution stages up to the LMXB phase (see Section 1.2 for details).

Thus, the LMXBs characterize a rather older stellar population, contrary to the HMXB population. In addition their more complex formation path results in an even less efficient formation than HMXBs.

1.3 The Galactic HMXB distribution

The disctinct differences beteen HMXBs and LMXBs are evident observationally. In Figure 1.4 the spatial distribution of the LMXB and HMXB populations in our Galaxy is presented (Grimm et al., 2002). The sample (86 LMXBs, 52 HMXBs) is derived from Rossi X-ray Timing Exlorer (*RXTE*) All-Sky Monitor data. The LMXBs (open circles/boxes) cluster around the Galactic center and they can also be found further away than this central region, representing the older stellar population found around the Galactic center and the globular clusters. On the other hand, the HMXBs (filled circles) are distributed along the Galactic plane and the spiral arms, indicating an association with star-forming regions and the younger stellar population.

This is depicted clearly in Figure 1.5, where the distribution of the HMXBs (49 *INTEGRAL* sources, shown as blue stars) and star-forming regions (464, black circles with sizes proportional to their star-formation activity) are plotted over a Galactic model (Bodaghee et al. 2007; 23 sources with unknown distances are presented as green pentagons at 8.5 kpc). As the time to form HMXBs is relatively short ($\sim 20\,\mathrm{Myr}$), the HMXBs do not have enough time to travel much from their forming areas, contrary to the LMXBs. Thus, they correlate well with star-forming regions, and as a result they can be used as indicators of star-forming activity (e.g. Antoniou et al. 2010).

1.4 The HMXB zoo

In HMXBs the massive companion (the donor or optical counterpart) dominates the light in the optical band, while the compact object dominates in the X-ray band. Depending on the luminosity class of the donor they are classified into two main categories: (a) the Be X-Ray Binaries (BeXRBs) in which the donor is a Be star of luminosity class V,IV, or III; and (b) the supergiant X-Ray Binaries (sgXRBs) in which the donor is a supergiant star of luminosity class I or II. This categorization reflects also the nature of accretion onto the compact object, either by a diffuse circumsterllar disk in the BeXRBs or through strong stellar wind and/or Roche-lobe overflow in the sgXRBs. Nevertheless, they share many common characteristics, and the next sections are dedicated in

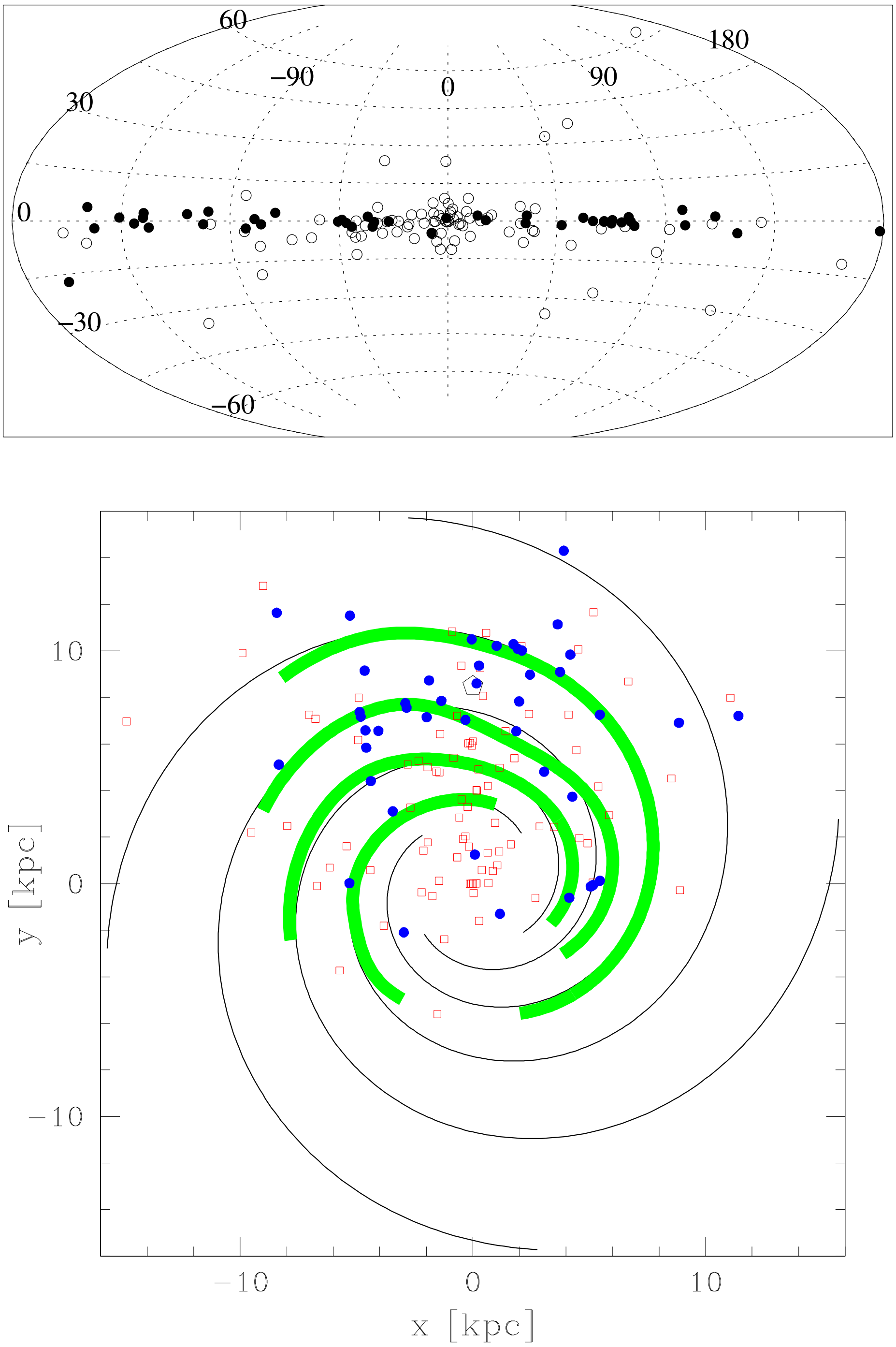

Figure 1.4: Top panel: The distribution of LMXBs (86, open circles) and HMXBs (52, filled circles) in the Galaxy, representing the older stellar population (around the Galactic center) and the younger stellar population (along the Galactic plane), respectively. Bottom panel: The same distributions (LMXBs represented as open squares, and HMXBs as filled circles) as seen from a face-on view of the Galaxy. The pentagon (located at x=0, y=8.5) is the position of the Sun. (Grimm et al. 2002; Sample derived from Rossi X-ray Timing Exlorer (*RXTE*) All-Sky Monitor data.)

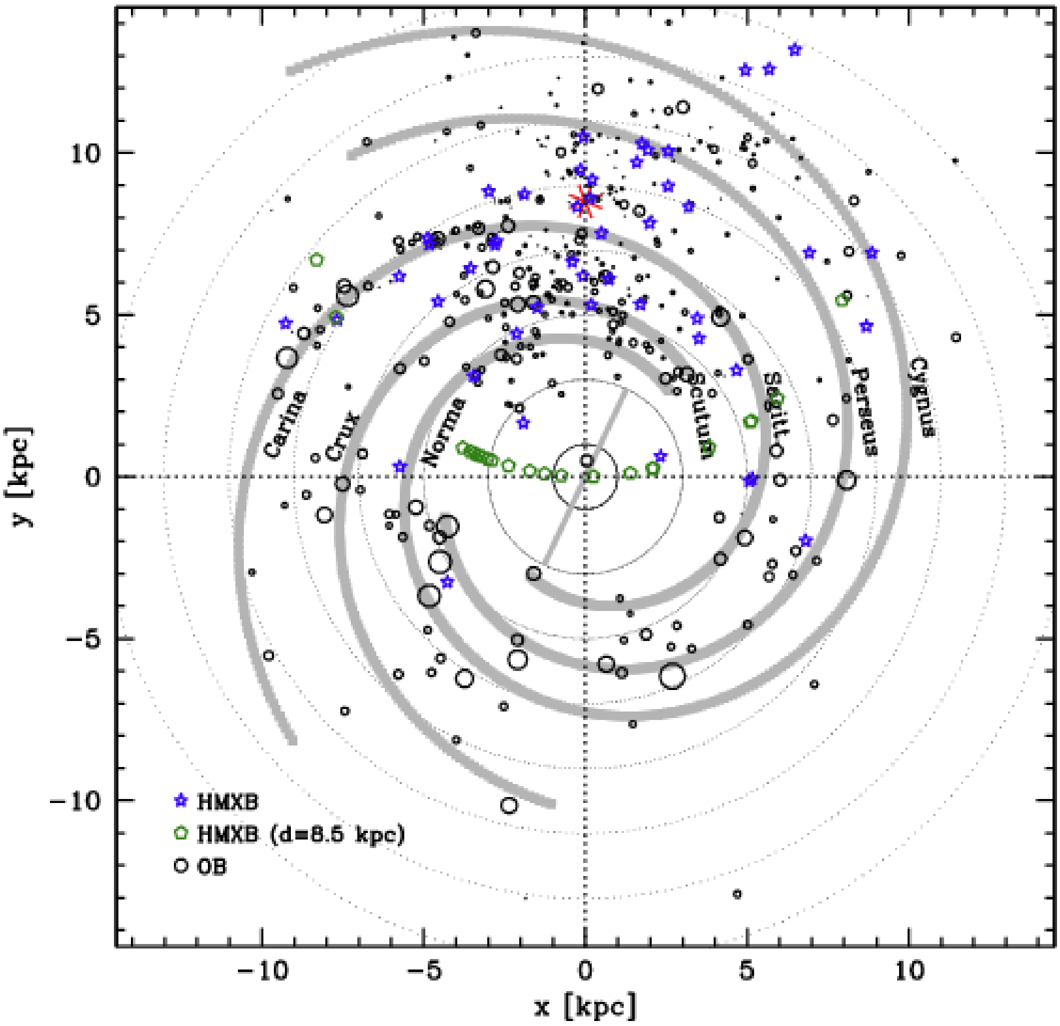

Figure 1.5: The distribution of Galactic HMXBs (blue stars) and star-forming regions (black circles, with sizes proportional to their star-forming rate) overplotted on a face-on model of the Galaxy. This figure shows the good correlation between the HMXBs and star formation. A number of sources (green pentagons) have unknown distances and they are presented at a distance of 8.5 kpc. The red star (located at x=0, y=8.5) is the position of the Sun. (Bodaghee et al. 2007; The HMXB sample is derived from *INTEGRAL* data.)

their presentation in reference to their different subclasses (see also Figure 1.1).

1.4.1 BeXRBs and X Per systems

In the BeXRBs the donor star (optical counterpart) is a Be star, i.e. *"a non-supergiant B star whose spectrum has, or had at some time, one or more Balmer lines in emission"*, which is indicated by the notation *"e"* following the spectral type (Collins 1987; for reviews see Porter & Rivinius 2003; Rivinius et al. 2013 and references therein). In the same context, this definition also includes late O-type stars of similar luminosity class that present emission lines.

This emission is due to a "decretion" disk[1], which forms as mass is lost from the stellar equator and accumulates in a geometrically thin, outward expanding disk (Rivinius et al. 2013, and references therein). The exact mechanism that leads to this mass loss is not known, but it is believed to result from the fast stellar rotation (Meynet & Maeder, 2000; Townsend et al., 2004) and/or non-radial pulsations (Rivinius et al., 2003).

The decretion Be disk serves as the main reservoir of matter that accretes onto the compact object. This is a neutron star than exhibits X-ray pulsations (X-ray pulsar) for all BeXRBs discovered so far (Coe et al. 2005; Reig 2011; Ziolkowski 2002; except for one case discussed at the end of this section). A schematic representation of a BeXRB system is given in Figure 1.6 (after Tauris & van den Heuvel 2006). When during its orbit the neutron star passes the periastron it attracts matter from the disk, creating an accretion disk. The gravitational energy release of the infalling matter powers up X-ray emission. As the neutron star travels farther in its orbit the X-ray emission decreases (depending on the available material and eccentricity of the orbit), and it may well become undetected. Thus, BeXRBs are transients, defined in Reig (2011) as sources with variability that exceeds at least two orders of magnitude the quiescent state, which often corresponds to a non-detection state.

After Reig (2011), the BeXRBs exhibit two types of outbursting activity:

- *Type I outbursts*: These are associated with the periastron passage of the neutron star, and as such they tend to be regular and (quasi-)periodic. Their duration is rather small ($\sim 0.2 - 0.3\, P_{\rm orb}$), and the increase in X-ray flux is typically one order of magnitude with respect to the previous (non-outbursting) state (outburst luminosities of $L_{\rm X} \leq 10^{37}$ erg s^{-1}).

---

[1] Opposite to the accretion disk in compact objects.

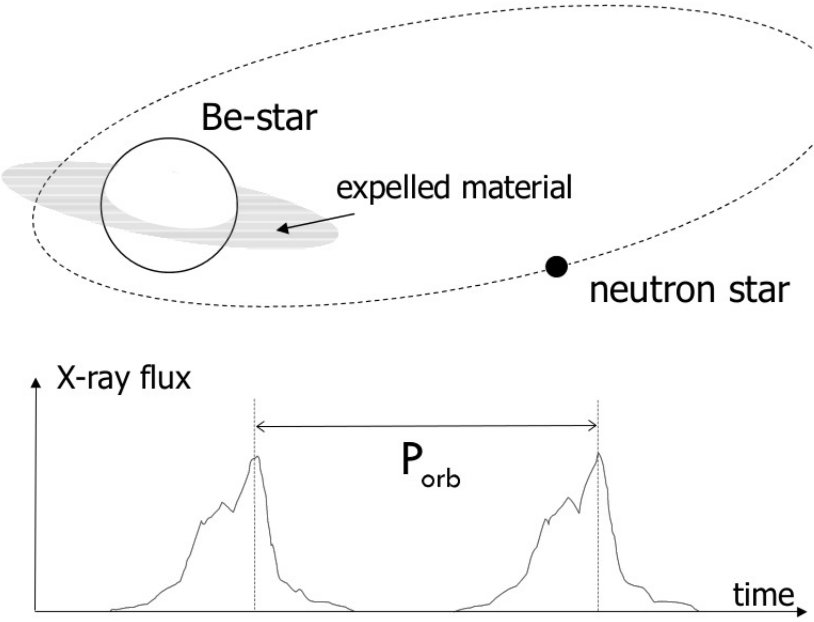

Figure 1.6: Schematic representation of a BeXRB (from Tauris & van den Heuvel, 2006). As the neutron star (compact object) passes close to the star, it accumulates material from the disk of the donor Be-star and enters an outburst event of Type I. The X-ray flux decreases (to a non-outbursting, often non-detectable phase) as the neutron star orbits away from the donor, and its flux raises again after one orbit when it approaches the periastron again.

- *Type II outbursts*: Contrary to Type I outbursts, these are aperiodic outbursts, that can last long (up to several orbital cycles), and can occur at any orbital phase. The flux increase is almost $10^3 - 10^4$ times the non-outbursting state, which makes these systems among the brightest X-ray sources in the sky. During these events an accretion disk may form, and the Be disk may be also affected severely (up to total disruption).

All BeXRBs also present short-term variability in the X-rays. Apart from aperiodic variations (e.g. due to irregular flaring, fluctuations) there are pulsations, indicative of the presence of a pulsar. The matter from the accretion disk is driven through the magnetic field lines onto the magnetic poles of the pulsar, leading to the formation of an accretion column and X-ray hot spots on the pulsars poles. The misalignment of the rotating and the magnetic axis in the neutron star, leads to a periodic movement of these hot spots and the accretion column with respect to the line-of-sight that produces periodic pulses. Typical spin periods for the pulsars identified in the BeXRBs are in the range of 1-1000s (Knigge et al., 2011).

It is found that the spin period of X-ray pulsars in the HMXBs correlates well with their orbital period (which has typical values of 11-412 days; e.g. Rajoelimanana, Charles, & Udalski 2011). This is evident in a spin-orbit period diagram, known also as Corbet diagram (Corbet 1984, 1986, see Figure 1.7, for an edited version of figure 6 from Drave et al. 2012, regarding Galactic HMXBs), where BeXRBs are presented as cyan open triangles. The correlation can be explained in terms of the equilibrium period, which is defined as the period at which the outer edge of magnetosphere rotates with the Keplerian velocity, and depends from the density of the surround medium, i.e. the mass flux of the infalling matter ($P_{eq} \propto \dot{M}^{-3/7}$; Ziolkowski 2002 and references therein). When the $P_{spin} > P_{eq}$ then the outer edge of the magnetosphere rotates with a small velocity that allows matter to accrete and add angular momentum to the neutron star (spinning it up), while when $P_{spin} < P_{eq}$ it rotates fast and matter is driven away from the neutron star (the propeller effect; Illarionov & Sunyaev 1975) which slows down the neutron star. Thus, accretion is allowed when the neutron star is close to the donor (e.g. close to periastron, when the density is high), while it is prohibited when the neutron star is away (e.g. at apoastron, when the density is low). The total effect of these mechanisms depends on the separation of the neutron star and the donor: wider systems (high eccentricities and orbital periods) result to a lower average density of the material surrounding the neutron star and lower spin periods, while narrower systems (lower eccentricities and orbital periods) result in higher mean density and allow higher spin periods (Corbet, 1984). We discuss the position of the sgXRBs in the next section.

Contrary to the X-ray band, which is dominated by the neutron star, the optical and infrared (IR) properties of a BeXRB system are dominated by the emission of its optical counterpart (the Be star). Its emission though is the sum of the intrinsic stellar luminosity and the emission from the decretion disk. As the disk is irradiated by the star, it is ionized and the recombination of the free electrons leads to the emission lines present in the optical spectrum (mainly Balmer lines, but others are possible also, e.g. Fe II; Hanuschik 1996). However, this is a dynamic process that results in variability of the structure of the disk that changes the appearance of the spectral lines (from emission to pure absorption lines, i.e. equivalent to a normal B spectrum, and everything in between). The most prominent emission line is the Hα line (at 6563 Å). Monitoring of the intensity and the profile of the Hα line provides information regarding the Be disk (e.g. size, shape, velocity, density; see Reig 2011 and references therein). For example "violet-to-red" (V/R) variations of the Hα line, i.e. the ratio of the blue and red peak for a double-peaked Hα line, reflect the movement of a denser region in the disk (Okazaki, 1991).

Observations in other wavelengths can probe different regions of the disk when present (e.g. Haubois et al., 2012). IR excess is a distinct characteristic of BeXRBs (continuum emission due to recombination of the electrons with the ionized atoms). It corresponds to regions closer to the star than those that are responsible for the Hα emission line (Carciofi, 2011).

Further information regarding the eccentricity and orbital period of a BeXRB can be obtained through optical variability. Systematic monitoring of these sources reveals periodic modulation in their optical light due to the regular interaction of the neutron star with the Be disk (duration of tens of days), or even due to the evolution of the Be disk itself (creation or loss of disk; duration of many hundreds of days; Rajoelimanana et al. 2011).

There is also a sub-class of BeXRBs that present persistent X-ray emission (e.g. Reig & Roche 1999; referred to also as X Per systems, after the prototype X Per). In contrast to the transient nature of all other BeXRBs, these sources are always visible in the X-rays, but with lower luminosities ($L_{\mathrm{X}} \sim 10^{34-35}$ erg s^{-1}), and their stochastic variability does not exceed a factor of 10 with respect to their normal state. They do not present any kind of outbursts, as in these systems the neutron-star orbit around the donor star has low eccentricity ($e \lesssim 0.2$). As a result, the neutron star does not pass close to the Be disk, and it accretes matter only from the outer regions of the Be envelope. They have large orbital periods ($P_{\mathrm{orb}} \gtrsim 200$ days) and their neutron stars

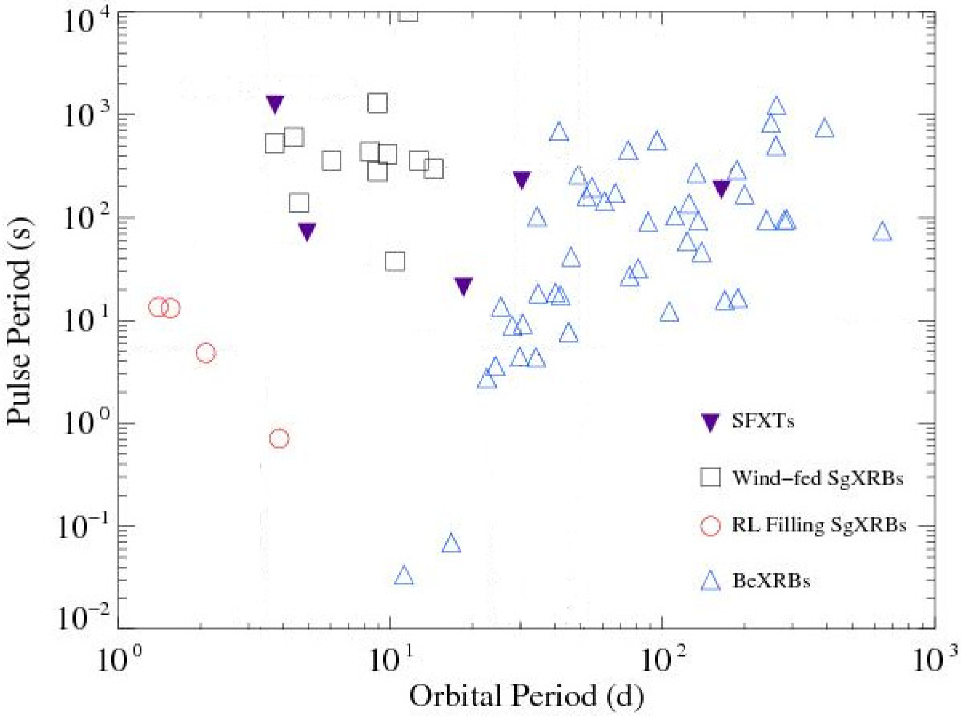

Figure 1.7: The spin (pulse) and orbital period diagram (Corbet diagram; Corbet 1986) for Galactic HMXBs (edited version of figure 6 from (Drave et al., 2012), which shows the different locations occupied by the HMXB subclasses. BeXRBs (cyan open triangles) display a good correlation between the two periods (see Section 1.4.1) at the right part of the diagram. The Roche-lobe overflow sgXRBs (red circles) occupy the lower left locus of small spin and orbital periods, while the wind-fed systems (green boxes) a rather flat region between the Roche-lobe systems and BeXRBs. The obscured sgXRBs (which are not shown explicitly in this plot) share the same region with wind-fed systems. The SFXTs (purple filled triangles) can be found within the location of both the wind-fed systems and the BeXRBs.

are slow rotators ($P_{\rm spin} \gtrsim 200$s), locating them in the upper right part of the Corbet diagram, in line though with the BeXRBs.

It is generally adopted that in all BeXRBs the compact object is a neutron star. However, there is no physical reason to exclude black holes. Belczynski & Ziolkowski (2009) estimated that, based on population synthesis modes and evolutionary scenarios, the ratio of BeXRBs with neutron stars to those with black holes is $\sim 30-50$, and if applied to the number of known Galactic BeXRBs results to $\sim 0-2$ systems with black holes. Therefore the non-detection of a population of black-hole BeXRBs is consistent with the observed number of ~ 60 BeXRBs with pulsars in our Galaxy (Liu et al., 2006).

Only very recently (Casares et al., 2014) presented strong evidence of such a system by identifying spectral features of the circumstellar environment (e.g. He II λ4686 in emission) and fitting their velocity curve in the optical spectra of a Be star (MWC 656) in a binary system. The identification of its X-ray counterpart, with X-ray properties consistent of a HMXB with black-hole compact object (Munar-Adrover et al., 2014), is in favor of a BeXRB system with black hole, but further investigation is needed.

1.4.2 Classical sgXRBs, obscured sources, and SFXTs

In the sgXRBs the compact objects are either neutron stars (X-ray pulsars) or black holes, while the donor is an evolved OB supergiant star (of luminosity class I or II). These stars have much stronger winds, with mass-loss rates $\dot{M} \sim 10^{-6} - 10^{-8}$ M$_\odot$ yr^{-1} at terminal velocities up to $v_\infty \sim 2000$ km s^{-1}, compared to their non-supergiant stars ($\dot{M} \lesssim 10^{-8}$ M$_\odot$ yr^{-1} and $v_\infty \sim 1000$ km s^{-1}; Mokiem et al. 2007). If the compact object lies close to the donor it can capture matter from the stellar wind and power X-ray emission (wind-fed sgXRBs). If the star fills its Roche lobe then more matter flows also via the inner Lagrangian point towards the compact object leading to the enhancement of the X-ray emission (Roche-lobe overflow sgXRBs). The compact objects in the sgXRBs are found generally in low eccentricity close orbits ($e \lesssim 0.3$ with $P_{\rm orb} \sim 3-40$ days; Townsend et al. 2011) which allows for continuous accretion of matter. Thus, sgXRBs are persistent sources with typical luminosities $L_{\rm X} \sim 10^{38}$ erg s^{-1} and $L_{\rm X} \sim 10^{35-36}$ erg s^{-1} for the Roche-lobe overflow and wind-fed systems, respectively (Liu et al., 2006).

Since sgXRBs are bright and persistent sources their population was quickly revealed and they were considered the *classical* (or *standard*) sources (as opposed to the BeXRBs). Nevertheless, with time and improvement of the survey sensitivity the new HMXBs discovered were primarily BeXRBs, mostly due to their transient nature. As of the turn of the millennium sgXRBs were only a mere 5% of the total number of Galactic HMXBs, while after the advance of the *INTEGRAL* mission their ratio increased to 30% Chaty et al. (2008). This abrupt increase in their percentage is due to the identification of new sgXRB classes: (a) the obscured (or highly-absorbed) sgXRBs, and (b) the Supergiant Fast X-ray Transients (SFXTs).

The obscured sgXRBs (Walter et al., 2006) share the same properties with the classical wind-fed systems, but they are much less luminous. Their X-ray emission is absorbed heavilly as it is observed through a high column density ($N_{\rm H} \sim 10^{24}\,{\rm cm}^{-2}$), which is almost two to three orders of magnitude larger than the column density measured for the classical systems. This is attributed to a dense absorbing environment (cool/warm gas and dust) in which the binary is deeply embedded (Chaty et al., 2008; Rahoui et al., 2008).

The supergiant Fast X-ray Transients (SFXTs; Negueruela et al. 2006) are systems with systematically low luminosity ($L_{\rm X} \sim 10^{32-34}$ erg s^{-1}; almost at the sensitivity limits of the telescopes used), which display regular, very short (from few minutes to several hours), flares with luminosity peaks of $L_{\rm X} \sim 10^{36}$ erg s^{-1}. They can be further classified into two groups, depending on the frequency and duration of their flares, and the variability ratio defined as the ratio of their max and min luminosity ($L_{\rm max}/L_{\rm min}$): (i) "classical" SFXTs, which are low-luminosity sources that exhibit variability ratios greater than 100 and flares of a few minutes, (ii) "intermediate" SFXTs, which are more luminous sources with smaller variability ratios and longer flares Chaty (2013). The flares are attributed to the accretion of either unique clumps in the stellar wind, or due to an asymmetric stellar wind composed by a polar spherically symmetric wind and a denser equatorial "disk" wind (Sidoli et al., 2008).

Even though there are black hole candidates within the class of sgXRBs (e.g. Cyg X-1), the majority of sgXRBs hosts a pulsar. If both spin and orbital periods are known then sgXRBs can be also placed in the Corbet diagram. In Figure 1.7 the Roche-lobe overflow sgXRBs (red circles) occupy the lower left locus of small spin and orbital periods, while the wind-fed systems (green boxes) a rather flat region between the Roche-lobe systems and BeXRBs. The obscured sgXRBs (which are not shown explicitly in this plot) share the same region with wind-fed systems. The SFXTs (purple filled triangles) can be found within the location of both the wind-fed systems and the BeXRBs. There is not a clear correlation between the spin and orbital periods for these sources, as the correlation observed for the BeXRBs.

1.5 HMXB populations in galaxies

1.5.1 In general

The observations of HMXBs in our Galaxy are hampered by extinction and distance uncertainties. Thus, the fraction of HMXBs identified so far is not representative of the actual population (due to extinction) and their luminosities are not accurately determined (due to distance). These two complications can be reduced if HMXBs are observed in nearby galaxies, when a common average extinction can be used and their distances are known. Moreover, this allows statistical studies of their populations.

Mineo et al. (2012) performed a detailed analysis of 29 nearby star-forming galaxies (distances$<$ 40 Mpc[1]) to identify HMXBs. They found approximately 700 sources that are possible HMXBs. However, their luminosities are at the high end ($L_{\rm X} \sim 10^{37-40}$ erg s^{-1}, which reflects the population of outbursting BeXRBs and sgXRBs, and more exotic sources like Ultra-Luminous X-ray sources. At these distances the detection limit is not low enough to identify sources over a broad range in luminosities. To make matters worse, information on the optical counterparts for these sources are hard or even impossible to obtain. In a more recent work, Williams et al. (2014) performed a spectroscopic survey for optical counterparts of HMXBs in the Andromeda galaxy, to obtain evidence for only 8 HMXBs (out of the 17 initial X-ray sources) at a luminosity range $L_{\rm X} \sim 10^{34-37}$ erg s^{-1}. Nevertheless, their optical counterparts correspond to the brightest stars (OB supergiants) for which spectroscopic observations can be obtained at this distance ($\sim$ 778 kpc).

Fortunately, there are galaxies close enough to our own Galaxy that allow us to resolve their stellar populations and detect faint X-ray sources: the Magellanic Clouds. The Large Magellanic Cloud (LMC) and the Small Magellanic Cloud (SMC) are located at distances of 50.0 kpc (Pietrzyński et al., 2013) and 60.6 kpc (Hilditch et al., 2005), respectively, and at a sky direction that suffers only lightly from obscuration by the Galactic interstellar medium. Accurate knowledge of their distances allows in precise calculation of luminosities.

At these distances Chandra and XMM-Newton can routinely detect sources down to a few $L_{\rm X} \sim 10^{33}$ erg s^{-1}, which are within the non-outbursting HMXB luminosity range. Moreover, photometric and spectroscopic observations of distinct stars can be obtained, which help to determine information regarding the optical counterparts of

---

[1] There is only one galaxy (Catrwheel) at a greater distance ($\sim$123 Mpc).

the HMXBs (e.g. construct color-magnitude diagrams to obtain ages, identify orbital periods, define the spectral type). In addition, studies regarding the star-formation history of the young stellar populations, can provide insights on the HMXB production efficiency.

1.5.2 The SMC: an excellent laboratory for HMXB studies

In contrast to the large angular extent of the LMC, the SMC (RA: 00h 52m 44.8s, Dec: $-72°49' 43''$) extends approximately 5.3 x 3 degrees in the sky. In Figure 1.8 we show an image of the SMC in visible wavelengths.

Rossi X-Ray Timing Explorer (RXTE) has been successful in discovering most HMXB pulsars in the SMC (Galache et al., 2008). The small size of the SMC allows for efficient coverage by the *Chandra* and *XMM-Newton* X-ray observatories during surveys (Antoniou et al., 2009b; Haberl & Pietsch, 2004; Liu et al., 2000, 2005). As of the writing of this thesis there are 94 (confirmed and candidate) HMXBs in the SMC (Sturm et al., 2013). Their distribution follows the SMC's "Bar"-shape, extending form North-East to South-West, and some are located also at the "Wing", a feature towards the LMC. The HMXB distribution correlates well with the young stellar population in the SMC (Zaritsky et al., 2000).

The large number of HMXBs in the SMC though is unexpected, since it is almost equal to the Galactic number (131; Reig 2011). Simply weighting by the number of HMXBs according to the mass of the host galaxy Majid et al. (2004) found that the SMC is over-abundant by a factor ~ 50[1] This would result in only 2-3 SMC HMXBs.

The difference in the metallicity between the two galaxies ($Z_{\mathrm{SMC}} = 0.2 Z_{\odot}$, where $Z_{\odot} = 0.02$ is the solar metallicity; Russell & Dopita 1992) could result in a difference in the HMXB production efficiency. Lower metallicity results in weaker (line-driven) winds for massive stars, that remove less mass and angular momentum from the stars. Ultimately, it leads to a larger population of binaries that pass through the HMXB phase. Still though, this enhancement would only be a factor of 3, in disagreement with the observed HMXB numbers (Dray, 2006).

Further evidence is available in the star-formation history (SFH) of the SMC. The proximity of the SMC provides the ability to resolve (e.g. Gardiner & Hatzidimitriou 1992; Hatzidimitriou & Hawkins 1989; Maragoudaki et al. 2001; Zaritsky et al. 2002) and study its stellar populations in detail. For example Meyssonnier & Azzopardi (1993) have cataloged a large number of Hα emission stars, while Murphy & Bessell

---

[1] Using the known numbers of HMXB with pulsars at the time (50 Galactic and 24 SMC sources).

Figure 1.8: The Small Magellanic Cloud (SMC) as observed in optical wavelengths. (North is up and East left; Image Credit and Copyright: Stéphane Guisard / Astronomy Picture Of the Day for October 1, 2007).

(2000) expanded this work to include more emission line sources (e.g. including planetary nebulae).

Harris & Zaritsky (2004) performed a systematic survey of the star-formation history of the SMC. A series of works (Antoniou et al., 2010, 2009b; Grimm et al., 2003; Majid et al., 2004; Shtykovskiy & Gilfanov, 2007) have shown a correlation between the young stellar population and the HMXBs. More specifically Antoniou et al. (2010) (see also Shtykovskiy & Gilfanov 2007) demonstrated that the population of HMXBs in the SMC is associated with stellar population ∼40 Myr old. The same timescale also represents the development of the Be phenomenon, peaking at ∼35 Myr (McSwain & Gies, 2005b).

In addition, the OGLE[1] and the MACHO[2] projects have been monitoring large areas of the SMC for periods of several years. They are invaluable resources for time-variability studies resulting in the recovery of orbital periods of several HMXBs (Bird et al., 2012; Coe et al., 2005; Schmidtke & Cowley, 2006; Schmidtke et al., 2004; Schurch et al., 2011). For example, Rajoelimanana et al. (2011) studied the OGLE light-curves to derive the orbital period for a large sample of SMC BeXRBs, and identify super-orbital periods that they associated with major Be-disk events (e.g. total disposal). Townsend et al. (2011) performed a comparison of the orbital parameters (eccentricity and orbital period) between the Galactic and SMC HMXBs to find no evidence of difference between the two populations.

In accordance with Townsend et al. (2011), a number of studies regarding the spectral-type distributions of the BeXRB populations in the Galaxy and the SMC reached to the same conclusion: the two populations display the same spectral range approximately between O8 to B3 (Antoniou et al., 2009a; Coe, 2005; McBride et al., 2008). Moreover, the measured space velocities for the Galactic BeXRBs (∼15 km s^{-1}; van den Heuvel et al. 2000a) are found to be comparable with the SMC BeXRBs (∼30 km s^{-1}; Coe et al. 2005, <15-20 km s^{-1}; Antoniou et al. 2010), which reflect the kick velocities imparted at the neutron stars during the supernova explosion. This similarity between the Galactic and SMC BeXRBs implies that there are no differences observed also during the formation of these systems.

In conclusion, the SMC is undoubtedly an excellent laboratory to study in detail the HMXB population, outside the Galactic environment.

---

[1] Optical Gravitational Lensing Experiment, `http://ogle.astrouw.edu.pl/`

[2] MAssive Compact Halo Objects, `http://wwwmacho.anu.edu.au/`

1.6 Tools used

In this section we summarize the strengths and the weaknesses of the optical spectroscopy and the Hα imaging, which are the main tools that have been used to identify HMXBs.

1.6.1 Hα imaging

Balmer emission lines are a characteristic property of BeXRBs (the majority of the HMXBs) when the disk is present. Of these lines the Hα line is the most prominent, and when strong enough, it can make these sources bright in Hα imaging. The identification of optical counterparts of HMXBs as Hα emission sources provides further evidence in favor of their HMXB nature. Moreover, Hα imaging can provide candidate sources as optical counterparts to HMXBs. However, care should taken when using Hα imaging to identify HMXBs, since there are other stellar populations that also display Hα emission (e.g. pre-main sequence Herbig Ae/Be stars, red giants, cataclysmic variables stars; Kogure & Leung 2007).

Due to the transient nature of the Hα emission in Be stars, Hα imaging can reveal only the "active" (with strong Hα emission) Be stars and BeXRBs at any specific observing epoch. This allows for the determination of the fraction of "active" sources with respect to their general population (which is an open question) and can provide insights in the efficiency of the HMXB production.

1.6.2 Optical spectroscopy

Spectroscopic observations of candidate HMXBs provide the best way to confirm their nature. If the spectral features of their optical counterparts are consistent with those for an early-type star then the system is considered as "confirmed HMXB". The spectral confirmation is important because candidate HMXBs based on photometric parameters maybe confused with other types of Hα excess sources (c.f. Section 1.6.1).

The assignment of a spectral type provides information regarding the physical parameters of the donor star (e.g. mass). For example, the typical spectral range of the optical counterparts is O8-B3 which corresponds approximately to 23-8 $M_\odot$ (for Main Sequence Galactic stars; Cox 2000).

As great as a tool optical spectroscopy can be, it is a time-consuming process and a rather small number of objects can be observed simultaneously. Moreover, obtaining quality spectra can be challenging for faint sources, such as the optical counterparts of HMXBs in the SMC.

1.7 Open questions and Outline

The scope of this work is to investigate the properties of the HMXBs in the SMC as a stellar population. In more detail we will address the following questions:

Q1 *What are the spectral types of the SMC HMXBs ?*

There is a large number of HMXBs in the SMC for which their spectral types are not known. Assigning spectral types, further confirms their HMXB nature and provides information regarding their physical parameters.

Q2 *Is there a way to perform an accurate optical spectral classification in an automated way ?*

Despite the power of the human eye as a pattern recognition classifier, a quantitative method does not exist for the early-type stars. Such a method would allow processing of large samples of stars and a quantitative way to assess the uncertainty in the spectral classification.

Q3 *How does the SMC HMXB population compare with the Galactic HMXB population ?*

In more detail, we would like to know how similar are these populations with respect to their observable parameters (e.g. spectral-type distributions, orbital periods), which reflect their evolution paths and can be used to constrain models for their formation.

Q4 *Are there any more new HMXBs ?*

Due to the transient nature of the BeXRBs we do not have a clear picture of their total population. Further search is needed to identify more BeXRBs, an constrain their duty cycles which will provide insights into their total population.

Q5 *What is the fraction of OBe stars and how HMXBs correlate with this?*

During each observing campaign, only a fraction of the OBe (early-type stars with Hα emission) can be recovered, due to their transient nature. We do not know what is this fraction and how it correlates with spectral type, stellar age, metallicity. Moreover, we would like to know what is the fraction of HMXBs with respect to the OBe population, which is important for the formation rate of BeXRBs.

To address these question in this thesis we present a systematic study of HMXBs, and a search for emission-line stars in the SMC, along with a new method to determine the spectral type of early type stars. In more detail:

In Chapter 2, we present our results from a dedicated spectroscopic campaign, where we extend their current spectral-type distribution (*Q1*) and under the light of this new sample, we perform a correlation between the two populations in the SMC and the Galaxy (*Q3*).

In Chapter 3, we present the development of an automated spectral-type classifier (*Q2*), employing two different methods, which are based on a physical and a statistical approach.

In Chapter 4, we present the results from a dedicated photometric campaign, in order to identify sources with Hα excess in the SMC. We compare these sources with candidate HMXBs to validate their nature (*Q4*), and investigate the fractions of "active" Be stars and HMXBs (*Q5*).

Finally, in Chapter 5 we summarize the conclusions of this thesis and we provide some future plans.

2

A spectroscopic survey for High-Mass X-ray Binary sources in the Small Magellanic Cloud

2.1 Introduction

High-Mass X-ray Binaries (HMXBs) are stellar systems consisting of a massive, early-type star (of O or B spectral type) and a compact object (neutron star or black hole). The material lost by the companion star (the donor) either through strong stellar winds or a circumstellar disk is accreted onto the compact object resulting in the formation of supergiant X-ray Binaries (sgXRBs) and Be/X-ray Binaries (BeXRBs) respectively. Predominantly the compact objects in these systems are pulsars with spin periods in the 1-1000 s range (e.g. Knigge et al. 2011). Depending on the available material and the geometry of the orbit of the systems, their X-ray emission can be either persistent or variable in timescales of days up to several months. Their typical luminosity ranges between $\sim 10^{34}$ (for low-activity systems) up to $10^{38}\,\mathrm{erg\ s^{-1}}$ (for outbursting systems).

In the BeXRBs, the most numerous subclass of HMXBs (Liu et al., 2005, 2006), the donor is a non-supergiant B star (luminosity class III-V) whose spectrum shows

---

[0] Published work: Maravelias G., Zezas A., Antoniou V., Hatzidimitriou D., *"Optical spectra of five new Be/X-ray binaries in the Small Magellanic Cloud and the link of the supergiant B[e] star LHA 115-S 18 with an X-ray source"*, MNRAS, **438**, 2005, (2014).

or, has at some time in the past shown, Balmer lines in emission (the so-called "Be phenomenon"; e.g. Porter & Rivinius 2003). This emission is produced by an equatorial disk of ionized material that has been expelled from the star due to its high (close to the critical limit) rotational velocity. Subsequently, part of this material is accreted on the compact object. Most BeXRBs are transient systems (e.g. Reig 2011) which can produce outbursts with luminosities in the range of $10^{36} - 10^{37}$ erg s^{-1} (type I outbursts, which occur at periastron and last a few days) or even stronger with luminosities $\gtrsim 10^{37}$ erg s^{-1} (type II outbursts, which are more rare and occur at irregular intervals). However, there are also persistent sources which display lower luminosity levels ($\sim 10^{34} - 10^{35}$ erg s^{-1}; for a review see Reig & Roche 1999).

In the case of sgXRBs (Charles & Coe 2006; Liu et al. 2006, and references therein), the donor is a supergiant O or B-type star (luminosity class I-II). Depending on the mass-transfer mechanism these systems are divided in Roche-lobe overflow (RLOF; e.g. Lamers et al. 1976) and wind-fed (e.g. Lutovinov et al. 2013). For systems in the first subclass, the steady mass-transfer rate through the Roche-lobe is high enough to lead to the formation of an accretion disk around the compact object, resulting in persistent systems with luminosities up to $\sim 10^{38}$ erg s^{-1}. In wind-fed systems, the donor star loses mass through a strong radial stellar wind (with mass-loss rates between $10^{-8} - 10^{-6}$ M$_{\odot}$ yr^{-1}). As the compact object lies in a close orbit around the donor, it becomes a persistent X-ray source with much lower luminosity (in the range $\sim 10^{35} - 10^{36}$ erg s^{-1}). These systems are referred as "classical". The advent of *INTEGRAL* has unveiled new populations of wind-fed systems: the supergiant Fast X-ray Transients (SFXTs; Negueruela et al. 2006) and the heavily obscured sgXRBs (Walter et al., 2006). The SFXTs display flaring activity which lasts from few minutes to several hours with a luminosity increase from $\sim 10^{33} - 10^{34}$ erg s^{-1} to $\sim 10^{36} - 10^{37}$ erg s^{-1}. On the other hand, the heavily obscured sgXRBs are actually similar to the "classical" wind-fed sgXRBs but the compact object is deeply embedded in a dense absorbing environment. Their H$_{\rm I}$ column density can be as high as $N_H \sim 10^{24}$ cm^{-2} thus suppressing significantly their observed X-ray luminosities. For comparison the measured absorbing column density for the "classical" systems is of the order of $\sim 10^{21} - 10^{22}$ cm^{-2} (for a review see Kaper et al. 2004; Chaty 2011).

The Small Magellanic Cloud (SMC) is an excellent laboratory to study the HMXBs, since it is nearby (D = 60 kpc; Hilditch et al. 2005) and well-covered by the *Chandra* and *XMM-Newton* X-ray observatories that can detect sources down to L$_{\rm X} \sim 10^{33}$ erg s^{-1} (i.e. reaching luminosities of non-outbursting sources). Moreover, it does not suffer from large extinction and distance uncertainties that often hamper studies of HMXBs in the Milky Way. It also has a relatively uniform metallicity among the young populations, and a well-determined star-formation history (Harris & Zaritsky, 2004). Most importantly it is host to a large number ($\sim$ 90) of HMXBs (Antoniou et al. 2009a, 2010, 2009b; Coe et al. 2005; Haberl & Pietsch 2004). Out of these systems only one is a sgXRB, source SMC X-1 (Webster et al., 1972), which is the only persistent accreting X-ray pulsar ($P_{spin} \sim 0.71$ s; Lucke et al. 1976) in the SMC fed through RLOF. This system has a B0 supergiant companion (Webster et al., 1972) with an orbital period of 3.89 days (Tuohy & Rapley, 1975) and an X-ray luminosity of $\sim 9.5 \times 10^{37}$ erg s^{-1} in the 0.2-12.0 keV energy band (e.g. XMMSL1; Saxton et al. 2008). In contrast, in the Milky Way the number of confirmed or suspected supergiant systems is much higher ($\sim$ 32% of the total number of HMXBs; Chaty 2011; Liu et al. 2006).

Although the number of known HMXBs in the SMC has increased dramatically in the last decade, only recently we started having a picture of the spectral classification of their donor stars (e.g. Antoniou et al., 2009a; McBride et al., 2008). This is important since it can yield valuable information on the evolution of massive binary stellar systems. Following our previous work (Antoniou et al., 2009a), we used the multiple-object mode of the AAOmega spectrograph, a fiber-fed optical spectrograph on the 3.9m Anglo-Australian Telescope (AAT), to obtain optical spectra of confirmed and candidate HMXBs, in order to identify BeXRBs and determine their spectral types.

In this work we present the results of this spectroscopic campaign, as following: In Section 2.2 we describe the sample of sources and in Section 2.3 we discuss the observations and the data reduction. In Section 2.4 we present the selection criteria of candidate BeXRBs. In Section 2.5 the spectral classification of the BeXRBs and the comparison of their spectral types with previous results are discussed. In Section 2.6 we discuss the properties of the overall population of BeXRBs in the SMC and we compare them with the BeXRB population in the Milky Way. We also discuss the nature of the X-ray source CXOU J005409.57-724143.5 that is associated with the supergiant B[e] star LHA 115-S 18 (hereafter S 18, Henize 1956; also known as AzV 154; Azzopardi et al. 1975). A summary of the main results of this study is given in Section 2.7.

2.2 Sample

The sample used in this work is derived from studies of X-ray sources detected with the *Chandra* and *XMM-Newton* X-ray observatories. As our basic sample we use the catalog of HMXB candidates detected in the *Chandra* shallow survey of the SMC (Antoniou et al., 2009b), which were identified based on the location of their optical counterparts in the (V, B-V) color-magnitude diagram (CMD). The chance-coincidence probability for a *Chandra* X-ray source to be associated with an OB star is estimated to be ∼20% (Antoniou et al., 2009b). This approach allowed us to identify candidate HMXBs even when we could not detect X-ray pulsations in the X-ray data, a tell-tale signature of BeXRB pulsars. It also allowed us to identify objects of lower X-ray luminosities than it would be impossible based on the detection of X-ray pulsations.

In this work we use the sample of Antoniou et al. (2009b), which includes the most likely optical counterpart of 158 *Chandra* sources with X-ray luminosities as low as $L_X \sim 4\times10^{33}$ erg s^{-1}, of uncertain or unknown spectral types. Moreover, this sample is supplemented by 211 additional sources detected in various *XMM-Newton* observations of the SMC reaching $L_X \sim 3.5\times10^{33}$ erg s^{-1} (Antoniou et al. 2010; Haberl & Pietsch 2004), which also have uncertain or unpublished spectral types. We were able to obtain spectra for 133 *Chandra* and 151 *XMM-Newton* sources in total.

2.3 Observations and data analysis

2.3.1 AAOmega spectroscopy

Although optical photometry for these sources has identified them as candidate HMXBs, and it is a powerful tool for identifying large samples of such objects, only optical spectroscopy can unambiguously confirm this classification, and provide additional information on the nature of these systems.

The optical spectra for this study were acquired during two nights of service time (on July 26 and September 19, 2008), using the multi-object mode of the AAOmega spectrograph (Sharp et al., 2006), a double-arm fiber-fed optical spectrograph (up to 400 fibers) on the 3.9m Anglo-Australian Telescope (AAT) fed by the 2 Degree Field (2dF) robotic fiber positioner. A summary of the observing runs is presented in Table 2.1. In addition, flat-field and arc (FeAr+CuAr+CuHe+CuNe) calibration exposures were taken each night for each setup.

The data reduction was performed with the 2dfdr[1] v4 package with default values. However, we did not perform the sky subtraction built in 2dfdr as we followed a different approach than the standard procedure. The steps taken during the 2dfdr process included: (i) bias subtraction and flat-fielding; (ii) wavelength calibration; (iii) combination of individual exposures for the same field. The extraction of the individual

---

[1] `http://www.aao.gov.au/2df/aaomega/aaomega_2dfdr.html`

spectra was performed with the *extract* command of the FIGARO v5.6-6 package of STARLINK (Shortridge et al., 2004).

After the extraction of all spectra from the AAOmega data, we performed the sky subtraction and initial characterization of the spectra. Flux calibration was not attempted since the wavelength-dependent throughput of each fiber is different and, ideally, a flux standard should be observed through each fiber. Nevertheless, our analysis is not affected because our classification criteria are based mainly on the presence or absence of spectral lines and not their absolute intensity. In addition, we can use the relative intensity of nearby lines, as the majority of the lines used in the classification are between 3900 Å and 4700 Å (with the exception of the Hα line), where the fiber response is fairly flat.

We considered for further analysis objects with S/N ratio above 20 (i.e. 400 counts) in the blue (4100 Å - 4300 Å) as well as the red (6410 Å - 6450 Å) parts of the spectrum. For the sky spectra, since the final sky spectrum resulted from the combination of several spectra, we set a limiting S/N ratio of 15 (i.e. 225 counts) in each of the two bands. After this selection, a total of 25 sky and 130 source spectra were kept from the September 19 observing run, while from the July 26 run we kept 5 sky and 53 spectra for further analysis.

The field of each sky fiber was examined visually (using the images from the OGLE-II project[1]; Udalski et al. 1998) in order to ensure that the spectra were not contaminated by any nearby source. After this process, 10 spectra were selected for further analysis from the south field (9 observed on September 19 and 1 on July 26) and 2 from the north field (observed on July 26). These sky spectra were combined into a median sky spectrum for each observation date and field.

All object and sky spectra were corrected for small residual wavelength offsets by measuring the positions of strong sky emission lines at 5577.3 Å and 6300.3 Å for the blue and the red band respectively. In order to account for throughput variations between the object and sky fibers, the fluxes for these sky emission lines were measured for each stellar spectrum and the corresponding sky spectrum was scaled in order to match the measured intensity of the lines. Then the rescaled sky spectrum was subtracted from the corresponding object spectrum.

Although this method is sufficient for the subtraction of sky emission from each spectrum, it is not sufficient for the removal of the contaminating interstellar emission in the stellar spectra. The selected fields in the SMC show strong and spatially variable diffuse emission from H$_{II}$ regions and supernova remnants. Among the interstellar

---

[1] `http://ogledb.astrouw.edu.pl/~ogle/photdb/`

emission lines, Hα is the strongest one but, at the same time, it is also a critical feature for the classification of BeXRBs. Ideally, sky subtraction would be performed with sky fibers placed within few arcsec from each source, in order to correct for the local interstellar contamination. However, due to hardware limitations we cannot place two fibers closer than $30''$[1], leaving us with the only option of measuring an average diffuse emission spectrum for each field.

By measuring a mean sky spectrum, we can remove a large part of the interstellar emission background but there may still be some residual contamination. This is indicated by the presence of typical interstellar emission lines (such as [OIII] λ5007 and [SII] $\lambda\lambda$6716,6731) in the sky subtracted spectra.

2.3.2 Optical and Infrared data for star S 18

Optical photometry for star S 18 (Henize 1956, or AzV 154 after Azzopardi et al. 1975) has been derived from the Optical Gravitational Lensing Experiment (OGLE) online database (see footnote 2; Szymanski 2005; Udalski et al. 1997). The retrieved data were obtained in the Bessell I-band. There are 327 observations between June 1997 and November 2000, with typical photometric errors of 0.003 mag. Although photometry for this star also exists in the MAssive Compact Halo Object (MACHO) database (Alcock et al., 1997, 1999), these data show unphysically large scale scatter of up to ∼1 mag compared to the OGLE data. We attribute this to confusion with a star of similar brightness located $\sim 4''$ from S 18 (for comparison the median seeing of the MACHO survey is $\sim 3''$; Alcock et al. 1997).

We used the catalog compiled by Bonanos et al. (2010) to retrieve the infrared photometric properties of star S 18 (discussed in Section 2.6.3.1): J=12.349±0.033 mag, H=11.931±0.038 mag, K_s=11.109±0.026 mag, [3.6μm]=9.177±0.042 mag, [8μm] = 6.966 ± 0.022 mag, [24μm]=4.786±0.007 mag.

---

[1] Although the minimum distance is $30''$, a typical distance is closer to 30-40$''$ (`http://www.aao.gov.au/AAO/2df/aaomega/aaomega_faq.html#fibsep`).

Table 2.1: Summary of the service-time observing runs with the AAOmega spectrograph.

Field ID	Field center		Observation	Exposure	Grating	λ Range	Dispersion	Resolution	Allocated objects*
	R.A. (J2000)	Dec.	date						
	(h m s)	(° ′ ″)		(s)		(Å)	(Å/pix)	Å	
26jul08_north	01 00 20	-72 25 25	26/7/2008	3x1800	580V	3733.0-5857.3	1.03	3.21	74(C),68(X),46(s)
					385R	5579.6-8808.9	1.57	5.70	
26jul08_south	00 43 10	-73 08 49	26/7/2008	4x1800	580V	3733.0-5857.3	1.03	3.21	59(C),78(X),25(s)
					385R	5579.6-8808.9	1.57	5.70	
19sep08_south	01 00 20	-72 25 25	19/9/2008	8x1200	580V	3682.6-5807.3	1.03	3.21	59(C),77(X),25(s)
					1000R	5907.5-7080.0	0.57	1.94	

* The allocated objects are *Chandra* sources (labeled as 'C'), *XMM-Newton* sources (labeled as 'X'), dedicated sky fibers (labeled as 's').

Unique observed objects in north field: 74 *Chandra* and 68 *XMM-Newton* sources.

Unique observed objects in south fields: 59 *Chandra* and 72 *XMM-Newton* sources. Additionally, there were 6 and 5 more *XMM-Newton* sources observed in 26jul08_south and 19sep08_south fields, respectively.

2.3.3 X-ray data for source CXOU J005409.57-724143.5

In the ∼9.4 ks long *Chandra* observation obtained in July 04, 2002, we detected this X-ray source with an absorption corrected X-ray luminosity of $\sim 3.5\times10^{33}$ erg s^{-1}, (0.5-7.0 keV; assuming a power-law spectrum with photon index $\Gamma = 1.7$ and an absorbing column density of $N_H = 6.23 \times 10^{20}\,cm^{-2}$, based on the average Galactic H_I column density along the line of sight of this field; Dickey & Lockman 1990) at an off-axis angle of $\sim 5'$ (Zezas, in prep.). The small number of net counts (9^{+3}_{-4}) did not allow us to derive and model the X-ray spectrum for this source.

Despite the low significance of its intensity (1.9σ above the background) this is a solid detection (see Kashyap et al. 2010 for a discussion of the detection and intensity significance). This source was also detected by *XMM-Newton* on Dec. 18, 2003 (ObsID 0157960201) and reported in the XMM Serendipitous Source Catalog (3XMM-DR4 Version[1]) as 3XMM J005408.9-724144. We reanalyzed these data with the *XMM-Newton* Science Analysis System (SAS v12.0.1). After processing the raw data with the *epchain* and *emchain* tasks, we filtered any bad columns/pixels and high background flares (excluding times when the total count rate deviated more than 3σ from the mean), resulting in 14.8 ks, 18.7 ks, and 17.2 ks net exposures for the European Photon Imaging Camera (EPIC) Metal Oxide Semi-conductor (MOS)1, MOS2, PN cameras, respectively. We only kept events of patterns 0-4 for the PN and 0-12 for the MOS detectors. Source detection was performed simultaneously in five energy bands (0.2-0.5 keV, 0.5-1.0 keV, 1.0-2.0 keV, 2.0-4.5 keV, and 4.5-12.0 keV) for each of the three EPIC detectors with the maximum likelihood method (threshold set to 7) of the *edetect_chain* task. At the position of CXOU J005409.57-724143.5 in the EPIC PN camera, there is source XMMU J005409.2-724143 with coordinates R.A.=00:54:09.16 (J2000.0), Dec.=-72:41:43.46 (J2000.0) and a positional error of $1.6''$ (at the 1σ level, including the relative as well as the absolute astrometric uncertainty). The *edetect_chain* task lists this source with 39 ± 9 counts (source-detection likelihood DET_ML = 24.6) at an off-axis angle of $4.89'$ in the 0.2-12.0 keV energy band[2]. The absorption corrected X-ray flux, assuming a spectral model of an absorbed power-law with a column density $N_H = 6.23 \times 10^{20}\,cm^{-2}$ and spectral slope $\Gamma = 1.7$, is then $(1.6 \pm 0.4) \times 10^{-14}\,erg\,cm^{-2}\,s^{-1}$. At the distance of the SMC, this corresponds to absorption corrected luminosity of $L_X^{abs.} = (7.1 \pm 1.7) \times 10^{33}\,erg\,s^{-1}$ (0.2-12.0 keV). We note that source XMMU J005409.2-724143 was not detected with ei-

---

[1] `http://xmmssc-www.star.le.ac.uk/Catalogue/3XMM-DR4/`

[2] Using the revised energy correction factors from `http://xmmssc-www.star.le.ac.uk/Catalogue/2XMMi-DR3/UserGuide_xmmcat.html#ProblECFs`.

ther of the EPIC MOS detectors, while the XMM Serendipitous Source Catalog lists it with slightly different coordinates and characteristics (DET_ML = 34.6 and mean $F_X \sim (1.0 \pm 0.4) \times 10^{-14}\,\mathrm{erg\,cm^{-2}\,s^{-1}}$), which are consistent with our measurements within the errors. Novara et al. (2011) who also analyzed these data do not report this source since they only focus on bright sources.

We then extracted the PN source spectrum from a 8.5″ radius aperture and a background spectrum from a 75" source-free region at the same distance from the readout as the source region. Unfortunately, the high background in combination with the small number of detected counts did not allow us to perform any spectral analysis.

The area around source CXOU J005409.57-724143.5 was also observed with *XMM-Newton* on November 01, 2006 (ObsID 0404680201). Following the same analysis procedure as above, we obtain a 30.5 ks net exposure for the EPIC PN camera. Despite the almost double exposure time compared to the 2003 observation, this time the source was undetected. We used the BEHR tool[1] (Park et al., 2006) and measured an intensity upper bound of 10.3 counts (at the 99% confidence level) at the location of the source. This corresponds to an observed X-ray luminosity of $L_X^{abs.} \sim 4.7 \times 10^{32}\,\mathrm{erg\ s^{-1}}$ (0.2-12 keV) assuming the same spectral parameters and distance as for the other *XMM-Newton* observation. This is a factor of 10 lower than the previously derived source intensity.

2.4 Selection of candidate BeXRBs

Here we use the spectra extracted as described in the previous section in order to identify the spectral types of the studied sources. However, since contamination by the interstellar emission can be significant, for our analysis we selected objects with minimum contamination based on the width of their Hα emission line and their [SII]/Hα ratio (c.f. Antoniou et al. 2009a). A minimum Full Width at Half-Maximum of the Hα emission line ($\mathrm{FWHM}_{\mathrm{H}_\alpha}$) is used to eliminate objects with too narrow emission, since BeXRBs have broader emission lines than the interstellar component (Coe et al., 2005). The selection of objects with [SII]/Hα ratio smaller than in the average "sky" spectrum also helps to eliminate objects with contamination from diffuse interstellar emission (mainly supernova remnants).

The minimum $\mathrm{FWHM}_{\mathrm{H}_\alpha}$ was based on the width of the Hα line measured in the sky spectra separately for each observation as the use of different gratings resulted in different spectral resolutions. For the July 26 data, there are only 3 sky spectra

---

[1] `http://hea-www.harvard.edu/AstroStat/BEHR/`

of suitable S/N (two from the north and one from the south field) which result in an average interstellar Hα width of $\langle \mathrm{FWHM}_{\mathrm{H}_\alpha} \rangle = 5.70 \pm 0.07$ Å. For the September 19 data, 9 good sky spectra were used resulting in an interstellar Hα width of $\langle \mathrm{FWHM}_{\mathrm{H}_\alpha} \rangle = 1.94 \pm 0.03$ Å. We selected for further analysis objects with a $\mathrm{FWHM}_{\mathrm{H}_\alpha}$ at least 3σ above the average width of the interstellar Hα emission. This means that only objects with $\mathrm{FWHM}_{\mathrm{H}_\alpha}$>5.91 Å for July 26, and $\mathrm{FWHM}_{\mathrm{H}_\alpha}$>2.03 Å for September 19, were considered for further examination.

In order to determine the average [SII]/Hα ratio for the interstellar emission we used again the sky spectra. We found [SII]/Hα=0.28±0.11 for the south field (September 19) and [SII]/Hα=0.38±0.02 for the north field (July 26). As no Hα emission was present in the only sky spectrum of the south field observed on July 26, we used the [SII]/Hα ratio measured in the September 19 run (since the flux of the lines is independent of the spectral resolution). These values are in agreement with the [SII]/Hα ratio ($\geq$0.4) expected in environments with supernova remnants, indicating that the ISM in these regions is to a large degree shock excited. Thus, all sources considered as BeXRB candidates should have a [SII]/Hα ratio smaller than the maximum values found for each field, in addition to the low limit on the $\mathrm{FWHM}_{\mathrm{H}_\alpha}$.

After applying these criteria, we are left with 21 sources out of the 272 initial targets that are BeXRB candidates and which are considered for spectral classification. These include 18 *Chandra* and 3 *XMM-Newton* sources.

The final spectra were normalized by subtracting the stellar continuum (after a spline fit), using the DIPSO v3.6-3 package of STARLINK (Howarth et al., 2004).

2.5 Spectral classification

2.5.1 Spectral classification criteria

As seen in the previous section, the selection of sources for further classification was based on their broad Hα lines, a key characteristic of BeXRBs. In Figs. 2.1, 2.2, and A.1, we present the spectra of the 21 sources selected for further analysis. As expected, by selection, they exhibit strong Hα emission. The left-hand panels in these figures show the blue part of the spectrum with the diagnostic lines for spectral-type classification marked, while the right-hand panels focus on the Hα line. Shaded areas indicate bad columns and/or sky subtraction residuals. We see that two sources (CH4-8, and CH4-2 in Fig. A.1) show asymmetric Hα profiles, while two more sources (CH3-7, and CH5-6 in Fig. 2.1), show double-peaked Hα emission. Although Herbig Ae/Be stars present

Table 2.2: Classification criteria for B-type stars in SMC from Antoniou et al. (2009a) and Evans et al. (2004).

Line identifications	Spectral Type
HeII λ4200,HeII λ4541,HeII λ4686 present	earlier than B0
HeII λ4541 and HeII λ4686 present, HeII λ4200 weak	B0
HeII λ4200 and HeII λ4541 absent, HeII λ4686 weak	B0.5
HeII λ4686 absent, SiIV $\lambda\lambda$4088,4116 present	B1
SiIV λ4116 absent, SiIII λ4553 appear	B1.5
OII+CIII λ4640-4650 blend decreases rapidly	later than B1.5
SiIV and SiII absent, MgII λ4481 $<$ SiIII λ4553	B2
MgII λ4481 $\sim$ SiIII λ4553	B2.5
MgII λ4481 $>$ SiIII λ4553	B3
OII+CIII λ4640-4650 blend disappears,	later than B3
OII λ4415-4417, NII λ4631 disappear	
clear presence of HeI λ4471 and absence of MgII λ4481	earlier than B5
SiIII λ4553 absent, SiII $\lambda 4128-4132 <$ HeI λ4121,	B5
HeI λ4121 $<$ SiII $\lambda 4128-4132 <$ HeI λ4144,	B8
MgII λ4481 $\leqslant$ HeI λ4471	
HeI λ4471 $<$ MgII λ4481,	B9
FeII λ4233 $<$ SiII λ4128-4132	

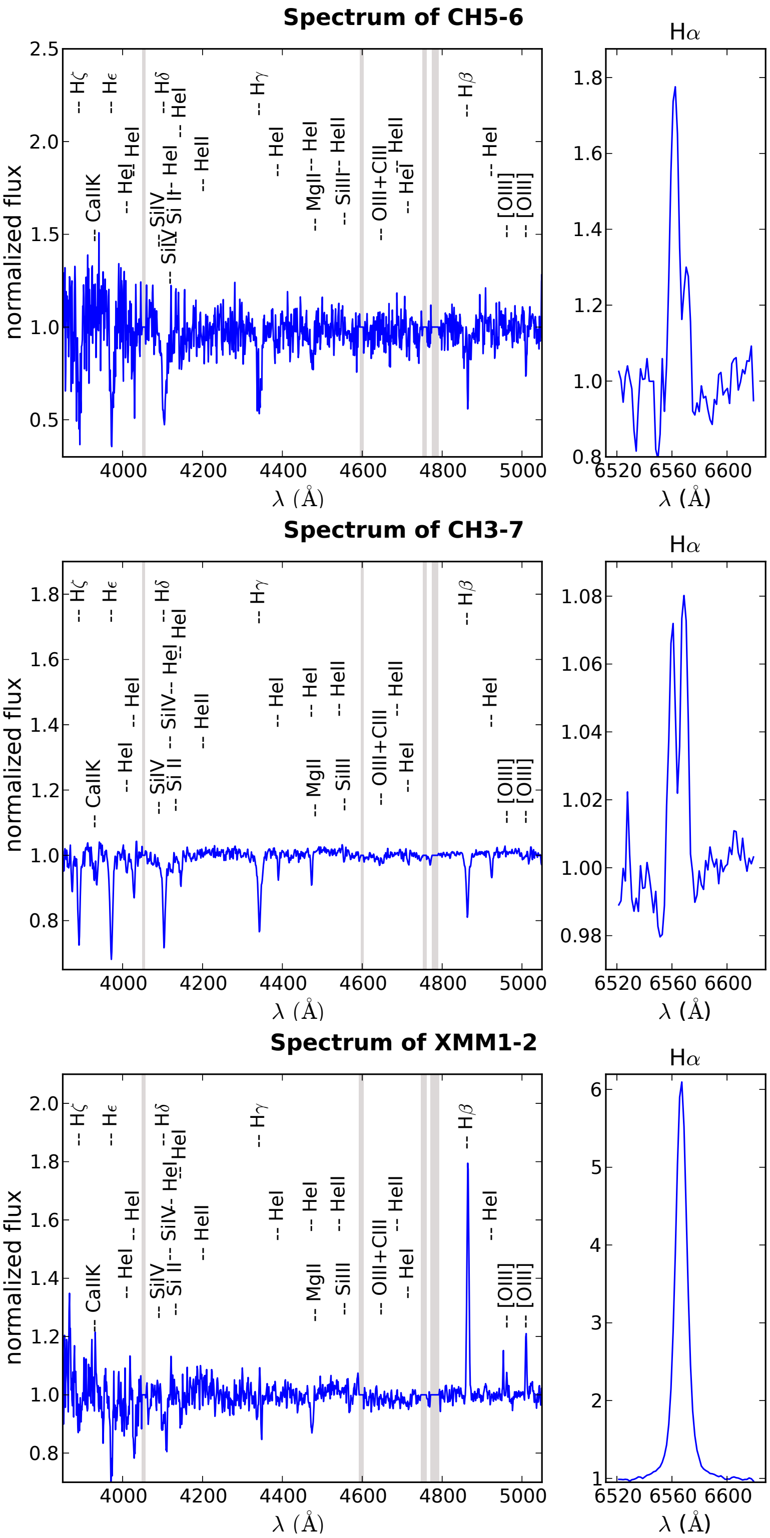

Figure 2.1: The spectra of the five new BeXRBs identified in this work (including the tentative BeXRB CH7-19). Shaded areas indicate wavelength ranges of bad columns and/or sky subtraction residuals.

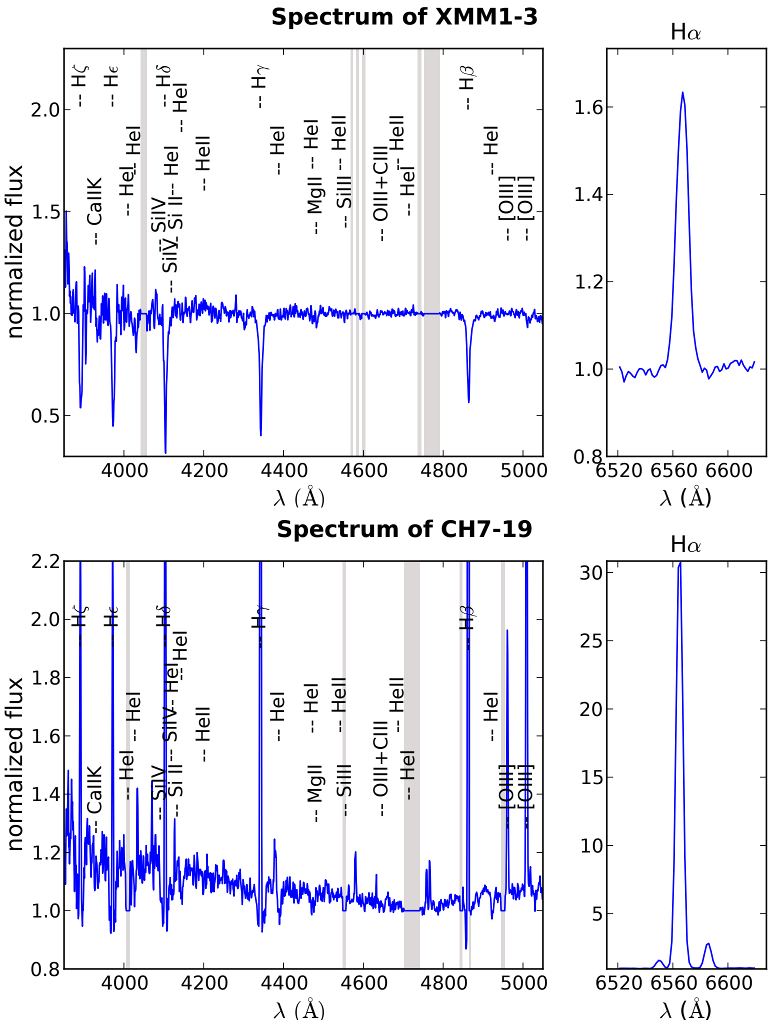

Figure 2.1: *continued*

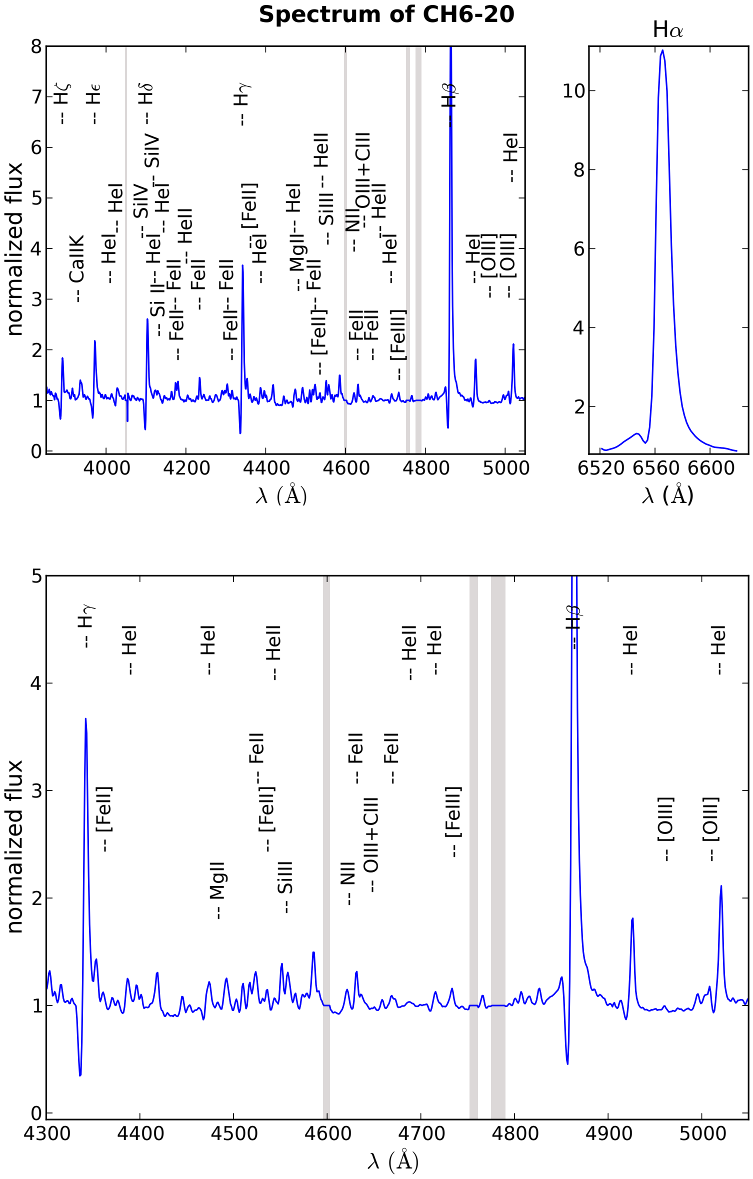

Figure 2.2: Spectrum of the optical counterpart to the *Chandra* source CXOU J005409.57-724143.5 (CH6-20) identified as a sgB0[e] star (Zickgraf et al., 1989), which is the known sgB[e] star LHA 115-S 18 (Henize, 1956). There is clear presence of emission lines of HeII, permitted and forbidden Fe lines, and Balmer lines with P Cygni profiles.

most of the time a double-peaked Hα profile (Vieira et al., 2003), we can safely rule out this possibility since the position of our objects in the *V, B-V* CMD (see fig. 3 of Antoniou et al. 2009b) ensures that they are not pre-main sequence objects. One more source (CH6-20) shows evidence for P-Cygni profiles (Fig. 2.2).

The spectral-type classification is based on the scheme of Evans et al. (2004), which was later applied to BeXRBs by McBride et al. (2008) and Antoniou et al. (2009a), supplemented by the atlas of Gray & Corbally (2009). In order to classify OB stars, the use of metal lines is normally preferred, but because of the low metallicity of the SMC they are much weaker and difficult to detect. Thus, we classify the spectra based on a combination of HeI, HeII, and metal lines. The spectral lines used for our classification are presented in Table 2.2.

In Table 2.3 we present the list of the HMXBs identified in our study, along with the classification derived from this and previous studies. In this table each source is identified with an ID of the type CH/XMM F-NN, where CH stands for *Chandra* and XMM for *XMM-Newton* sources, F is the field number, and NN is the source ID from the studies of Antoniou et al. (2009b), and Antoniou et al. (2010), respectively. We find 20 sources of B spectral type which in combination with their strong Hα lines and X-ray emission make them BeXRBs, and one X-ray emitting supergiant system with also strong emission in the Hα line and evidence for a strong wind, which makes it a possible HMXB. Next we discuss the new BeXRBs and the supergiant system identified in this work; sources that have been already classified as BeXRBs are discussed in detail in the Appendix.

For each source we measured the equivalent width (EW) of the Hα line as the ratio of the flux in the region of Hα (6553-6576 Å) over the continuum at the position of Hα as calculated by a linear fit to the flux of line-free regions adjacent to Hα (i.e. at 6530-6540.5 Å and 6630-6650 Å). These measurements are presented in Table 2.4.

2.5.2 Discussion of individual sources

- *CXOU J005409.57-724143.5 (source CH6-20) - classified as sgB0[e]*

  This is probably the most interesting object in our sample (see Fig. 2.2). Not only all the Balmer lines are in emission but we also observe HeII, as well as permitted and forbidden Fe lines in emission. Moreover, all the Balmer lines and some HeII lines present P Cygni profiles, typical of supergiant B[e] stars (Lamers et al., 1998; Shore et al., 1987; Zickgraf et al., 1989). However, due to the lack of characteristic lines (which are absent even in high resolution spectra, c.f. Graus et al. 2012), we cannot identify the spectral type of this source. Through a model atmosphere fit Zickgraf et al. (1989) concluded that the stellar temperature corresponds to a B0 spectral type. According to the classification criteria of Table 2.2 the spectrum should also show HeII λ4686 for this spectral type, which is however absent in our spectrum. Nevertheless, the variability in this line is known (Morris et al., 1996; Shore et al., 1987). To the best of our knowledge, there are no other classifications in the literature, thus we classify source CH6-20 as a sgB0[e]. This makes this source the second X-ray source associated with a supergiant in the SMC. We further discuss the nature of source CH6-20 in Section 2.6.3.

- *CXOU J005504.40-722230.4 (source CH5-6) - classified as B1-B5*

  The HeII $\lambda\lambda$4200, 4686 lines are absent so this spectrum is of B1 spectral type or later. As the HeI λ4471 line is present without any sign of the MgII λ4481 line, we can deduce that the source must be earlier than B5. No other line that would help us to further constrain the classification is visible, thus we only propose a B1-B5 spectral-type range for source CH5-6.

- *CXOU J005723.77-722357.0 (source CH3-7) - classified as B2*

  The HeI $\lambda\lambda$4144, 4387, 4471 absorption lines are clearly detected. Since no HeII $\lambda\lambda$4200, 4686 lines are visible the source has a spectral type of B1 or later. Moreover, the absence of the MgII λ4481 line and the presence of SiIII indicates that the star is earlier than B2.5, which is also supported by the presence of the OII λ4415-4417 lines and the OII+CIII λ4640-4650 blend. The SiIV $\lambda\lambda$4116, 4088 and SiII λ4128-4132 lines are not present, which means that all criteria for a B2 star are completely fulfilled for this previously unclassified source.

- *XMMU J010519.9-724943 (source XMM1-2) - classified as B3-B5*

  The absence of the HeII $\lambda\lambda$4200, 4686 lines supports a spectral type of B1 or later. We see no evidence for the OII+CIII λ4640-4650 blend, so the source must be later than B3, as this blend disappears after this class. Moreover, this source cannot be later than B5, since the HeI λ4471 line is present but without any sign of the MgII λ4481 line. We thus assign to the previously unclassified source XMM1-2 a spectral type of B3-B5. Noteworthy are the weak Hγ emission and the almost filled-in (by emission) Hδ line.

- *XMMU J010620.0-724049 (source XMM1-3) - classified as B9*

  The strong presence of the MgII λ4481 line is characteristic of a late B-type star. Moreover, the MgII λ4481 line is clearly stronger than the HeI λ4471 line, which immediately places this source in the spectral range later than B8. The CaII K λ3933 line is also present in later B types and it becomes a dominant metal line in A-type stars (being much stronger than MgII). In our case the CaII K λ3933 line is much stronger than the usual interstellar emission line seen in all other spectra, but it is weaker than the MgII λ4481 line, so we conclude that this, previously unclassified, star has a B9 spectral type.

- *CXOU J004941.43-724843.8 (source CH7-19) - classified as B1-B5*

  This source displays an Hα emission line with a $\mathrm{FWHM}_{\mathrm{H}_\alpha} = 5.21$ Å which is marginally lower than our limiting Hα FWHM ($\mathrm{FWHM}_{\mathrm{H}_\alpha} = 5.70 \pm 0.07$ Å for July 26; c.f. Section 2.4). Nevertheless, we decided to further examine this source. The most striking features of its spectrum are the emission in the Balmer lines series and the presence of the [OIII] $\lambda\lambda$4959, 5007 lines. As the sky subtraction is not perfect the [OIII] lines are residuals of the contribution from the surrounding environment. A previous classification for this source has been given by Murphy & Bessell (2000) as a potential Planetary Nebula (source 61 in their list). Their analysis showed that only 33% of the good candidates are real Planetary Nebulae, while source 61 is not characterized as a good candidate as its properties are closer to emission stars. Taking into account that their position accuracy was not better than 12" and that there is a star cluster in the same region (Bica & Schmitt, 1995), it is possible that this source was misclassified as a potential Planetary Nebula. In addition, the $\mathrm{FWHM}_{\mathrm{H}_\alpha} = 5.21$ Å translates to a rotational velocity of vsini ∼240 km s^{-1} which is within the normal range of rotational velocities for Be stars (Steele et al., 1999). Thus, the major contributor of the spectral lines is considered to be of stellar nature than interstellar. The absence of both HeII $\lambda\lambda$4200, 4686 lines suggests that the source is of spectral type B1 or later, but not later than B5 due to the absence of the MgII λ4481 line. Thus, we tentatively classify the previously unclassified source CH7-19 as B1-B5, although the Be nature is uncertain due to the marginal width of its Hα emission line.

2.6 Discussion

2.6.1 New Be/X-ray Binaries

In Table 2.3 we present the X-ray and optical properties of the BeXRBs studied in this work. From the 21 classified sources, 12 are in full agreement (within 0.5 spectral type) with the previous studies of McBride et al. (2008), and Antoniou et al. (2009a), while 3 have later spectral types (by 1 to 1.5 type) than previous results. Most importantly, we identify 4 new BeXRBs and 1 candidate sgXRB system (discussed in detail in Section 2.6.3). Although source CH7-19 is included in the table we exclude this source from further analysis, as its identification as an emission line star is tentative due to the possibly significant contamination of its spectrum by interstellar emission (see Sections 2.4 and 2.5.2). In the following discussion, we exclude from any comparisons with other samples source CH6-20 (the sgB[e]) since it does not belong to the same population as the luminosity class III-V BeXRBs. The remaining BeXRBs is hereafter referred to as the "sample".

The 4 new BeXRBs sources (hereafter referred to as "new") are: CXOU J005504.40-722230.4 (CH5-6), CXOU J005723.77-722357.0 (CH3-7), XMMU J010519.9-724943 (XMM1-2), and XMMU J010620.0-724049 (XMM1-3). The spectral types for sources CH3-7 and XMM1-3 (B2 and B9, respectively) are accurate to ± 0.5 subclass. XMM1-3 is the BeXRB with the latest spectral type (B9) known in the SMC. For the remaining new BeXRBs, we can provide only a range of spectral types: B1-B5 for the source CH5-6, and B3-B5 for the source XMM1-2.

All but source CH3-7 (V=14.71 mag), are faint objects with V-magnitudes in the range 16.4-17.9 mag (see Table 2.3) and have rather noisy spectra (see Fig. 2.1) which hampers their spectral classification. They are also faint X-ray sources with typical X-ray luminosities $\sim 10^{34}\,\mathrm{erg\,s^{-1}}$, outside the typical range of luminosities of outbursting BeXRBs. Overall our sample of BeXRBs spans 3 orders of magnitude in X-ray luminosity and it includes faint BeXRBs for which it is not possible to detect X-ray pulsations.

Table 2.3: Optical and X-ray properties of the studied sources.

X-ray source ID	Optical source ID	Optical Counterpart RA	Dec	Offset	V	B-V	X-ray Source ID	RA	Dec	$L_{X,unabs}$	Classification this work	previous
		(J2000)					CXOU=C, XMMU=X	(J2000)				
		(h m s)	(° ′ ″)	(″)	(mag)	(mag)		(h m s)	(° ′ ″)	(10^{33} erg s^{-1})		
(1)	(2)	(3)	(4)	(5)	(6)	(7)	(8)	(9)	(10)	(11)	(12)	(13)
CH4-8	O_4_171264	00 48 14.13	-73 10 03.5	0.63	15.74±0.04	0.00±0.05	C J004814.15-731004.1	00 48 14.15	-73 10 04.1	30.4	B1.5	B1.5 [A09]
CH7-1	O_5_65517	00 49 03.34	-72 50 52.1	0.45	16.94±0.06	0.09±0.10	C J004903.37-725052.5	00 49 03.37	-72 50 52.5	79.2	B1-B5	~B3 [M08]
CH4-2	O_5_111490	00 49 13.63	-73 11 37.4	0.47	16.52±0.02	0.10±0.04	C J004913.57-731137.8	00 49 13.57	-73 11 37.8	76.6	B3-B5	B1.5 [A09]
CH4-5	O_5_111500	00 49 29.81	-73 10 58.0	0.61	16.30±0.01	0.09±0.02	C J004929.74-731058.5	00 49 29.74	-73 10 58.5	37.6	B1-B5	B1 [A09]
CH7-19	O_5_146766	00 49 41.66	-72 48 42.9	1.36	17.16±0.55	0.27±0.60	C J004941.43-724843.8	00 49 41.43	-72 48 43.8	3.7	B1-B5*	unclassified
CH4-3	O_5_271074	00 50 57.12	-73 10 07.7	0.28	14.54±0.01	-0.06±0.01	C J005057.16-731007.9	00 50 57.16	-73 10 07.9	90.4	B1-B5	B0.5 [A09]
CH5-3	O_6_85614	00 51 53.11	-72 31 48.3	0.54	14.90±0.12	-0.27±0.13	C J005153.16-723148.8	00 51 53.16	-72 31 48.8	57.1	B0.5	O9.5-B0 [M08]
CH5-1	Z_2311496	00 52 05.69	-72 26 04.0	0.55	14.91±0.02	0.00±0.03	C J005205.61-722604.4	00 52 05.61	-72 26 04.4	1093.9	B3-B5	B1-1.5 [M08]
CH6-1	O_6_77228	00 52 08.95	-72 38 02.9	0.58	15.03±0.02	0.14±0.03	C J005208.95-723803.5	00 52 08.95	-72 38 03.5	2342.0	B1-B5	B1-3 [A09]
CH5-12	Z_2406014	00 52 45.10	-72 28 43.4	0.35	14.92±0.08	0.00±0.09	C J005245.04-722843.6	00 52 45.04	-72 28 43.6	7.2	B0	O9-B0 [A09]
XMM2-1	Z_2430066	00 52 55.27	-71 58 06.0	2.82	15.53±0.02	-0.05±0.04	X J005255.1-715809	00 52 55.10	-71 58 08.7	893.2	B1-B3	B0-B1 [M08]
CH5-16	Z_2573354	00 53 55.38	-72 26 45.3	0.83	14.72±0.03	-0.07±0.03	C J005355.25-722645.8	00 53 55.25	-72 26 45.8	4.4	B0	B0.5 [A09]
CH6-20	O_6_311169	00 54 09.53	-72 41 42.9	0.62	13.71±0.14	0.39±0.19	C J005409.57-724143.5	00 54 09.57	-72 41 43.5	3.5	sgB0[e]	sgB0[e] [Z89]
CH6-2	O_7_47103	00 54 55.87	-72 45 10.7	0.40	15.01±0.01	-0.02±0.01	C J005455.78-724510.7	00 54 55.78	-72 45 10.7	223.4	B1.5-B3	B1-1.5 [A09]
CH5-7	O_7_70829	00 54 56.17	-72 26 47.6	1.19	15.30±0.01	-0.04±0.02	C J005456.34-722648.4	00 54 56.34	-72 26 48.4	23.2	B0.5	B0 [A09]
CH5-6	Z_2748033	00 55 03.63	-72 22 31.2	3.60	17.86±0.03	-0.03±0.05	C J005504.40-722230.4	00 55 04.40	-72 22 30.4	38.3	B1-B5	unclassified
CH3-18	Z_2893439	00 56 05.56	-72 21 59.0	0.72	15.88±0.03	-0.04±0.03	C J005605.42-722159.3	00 56 05.42	-72 21 59.3	3.1	B2	B1 [M08]
CH3-7	Z_3075967	00 57 24.02	-72 23 56.4	1.30	14.71±0.03	-0.07±0.03	C J005723.77-722357.0	00 57 23.77	-72 23 57.0	14.9	B2	unclassified
CH3-3	O_8_49531	00 57 36.01	-72 19 33.8	0.14	16.01±0.02	-0.02±0.04	C J005736.00-721933.9	00 57 36.00	-72 19 33.9	53.7	B1-B5	B0-4 [A09]
XMM1-2	Z_4119599	01 05 20.72	-72 49 41.5	4.01	16.98±0.03	-0.09±0.04	X J010519.9-724943	01 05 19.90	-72 49 43.1	14.6	B3-B5	unclassified
XMM1-3	Z_4232476	01 06 21.02	-72 40 48.8	4.53	16.38±0.03	0.02±0.03	X J010620.0-724049	01 06 20.01	-72 40 49.1	35.9	B9	unclassified

Column description:

(1) Source ID - the name convention is CH/XMM F-NN, where CH stands for *Chandra* and XMM for *XMM-Newton* sources, F is the field number and NN is the source ID for this field (from Antoniou et al. 2009b and Antoniou et al. 2010, respectively).

(2) Optical counterpart ID given as O_F_NNNNNN from the OGLE-II catalog (Udalski et al., 1998), where F is the field number and NNNNNN is the optical source ID respectively, and Z_NNNNNN from the MCPS catalog (Zaritsky et al., 2002), where NNNNNN is the line number of the source in their table 1.

(3,4) Right Ascension and Declination (J2000) of the optical counterpart.

(5) Distance (in arcseconds) of the optical counterpart from the X-ray source.

(6,7) Apparent V magnitude and B-V color index, along with their errors, taken directly from the original catalogs without applying any reddening or zero-point correction.

(8) X-ray source names, *Chandra* sources (CXOU) labeled as C and *XMM-Newton* sources (XMMU) as X, followed by the designation.

(9,10) Right Ascension and Declination (J2000) of the X-ray source.

(11) Unabsorbed X-ray luminosity in the 0.5-7.0 keV band (assuming a power law with photon index $\Gamma = 1.7$ and $N_{\rm H} = 6 \times 10^{20}$ cm^{-2}, and 60 kpc distance; Hilditch et al. 2005) for *Chandra* sources (Zezas, in prep.; Antoniou et al. 2009b) and *XMM-Newton* sources (Antoniou et al., 2010).

(12) Spectral-type classification from this work.

(13) Classification published in other works: [A09]: Antoniou et al. (2009b); [M08]: McBride et al. (2008); [Z89]: Zickgraf et al. (1989).

$*$: the classification of source CH7-19 is tentative as its $\langle {\rm FWHM}_{{\rm H}_\alpha} \rangle$ is marginally lower than the limit set for BeXRBs.

2.6.2 Spectral-type distributions

By combining our results with these from previous studies of the BeXRBs in the SMC (e.g. Antoniou et al. 2009a; McBride et al. 2008) we can obtain a more complete sample of the properties of the BeXRB population in the SMC. In Fig. 2.3 we plot a histogram of the spectral-type distribution of our sample and new sources separately (as defined in Section 2.6.1), along with the samples of the previous studies by McBride et al. (2008) and Antoniou et al. (2009a). In order to account for the uncertainty in the spectral-type classification we split sources extending over more than one class equally between the encompassed class bins (e.g. a B0-B2 object will split into 1/3 in B0, B1, and B2 spectral class, respectively.) By inspecting this figure we see that there is a trend for our sample to extend to later spectral types than previous works. In order to assess the significance of this trend we compared the spectral-type distributions of these samples using a two-sample Kolmogorov-Smirnov test (KS test; Conover, 1999). We find that this trend is significant at more than 99% confidence level, which further indicates that the sources in our sample are skewed towards later types (see Fig. 2.4 for the cumulative distributions of the spectral types in these three samples).

In Fig. 2.5 we also present the unabsorbed X-ray luminosities of the sources identified in this study (new identifications are presented again separately) along with the maximum X-ray luminosity of known BeXRBs in the SMC, as given in table 1 of Rajoelimanana et al. (2011). As this list is not homogeneous we transformed these values to the 0.5-7 keV energy band that we used in our study, assuming a power law with photon index $\Gamma = 1.7$ and $N_H = 6 \times 10^{20}$ cm^{-2}. We obtained the maximum luminosities for our sources from table 1 of Rajoelimanana et al. (2011). For the sources that are not in this catalog we used the unabsorbed luminosities presented in Zezas (in prep.) and Antoniou et al. (2010, 2009b). We have also assumed that the X-ray luminosities given in Rajoelimanana et al. (2011) are unabsorbed. In any case, the difference between the unabsorbed and absorbed luminosities for the assumed model and energy band is not important for the purpose of the comparison presented here.

In Fig. 2.5 we see a weak trend for lower-luminosity sources to be associated with sources of wider spectral-type range, and extending to later types. A possible physical explanation for this trend may lie in the nature of the BeXRBs, especially if there is a correlation between the spectral type and the size of the equatorial disk. Although this is a very intriguing prospect, we should note that the observed trend could be the result of a selection bias: the list of Rajoelimanana et al. (2011) gives by construction the historically maximum detected X-ray luminosity for these sources, while our sample,

Table 2.4: Measured Hα equivalent widths (EW) for each source on July 26, 2008$^{(1)}$.

Source ID	$EW_{H\alpha}$ (Å)	$\pm\delta(EW_{H\alpha})$ (Å)
CH4-8	-6.45	0.07
CH7-1	-13.78	0.13
CH4-2	-24.22	0.52
CH4-5	-29.39	0.17
CH7-19	-187.68$^{(2)}$	0.36
CH4-3	-23.19	0.08
CH5-3	-2.90	0.04
CH5-1	-8.54	0.06
CH6-1	-7.65	0.10
CH5-12	-4.41	0.06
XMM2-1	-21.06	0.09
CH5-16	-12.31	0.04
CH6-20	-120.3	1.6
CH6-2	-42.68	0.14
CH5-7	-14.89	0.13
CH5-6	-12.31	0.04
CH3-18	-32.87	0.10
CH3-7	-1.01	0.05
CH3-3	-33.35	0.18
XMM1-2	-53.63	0.23
XMM1-3	-6.59	0.14

(1) For source CH4-2 the EW was measured on September 19, 2008.

(2) Part of the Hα emission line could be due to ISM contamination.

which mainly contributes to the lower luminosity, later spectral-type sources, includes sources for which the X-ray luminosity was measured from a single snapshot.

In Fig. 2.6 we compare the average orbital period ($Porb$) and eccentricity (e) as a function of spectral type of the BeXRB populations in the SMC and Milky Way (MW). Data for the orbital periods of BeXRBs in the SMC are taken from Rajoelimanana et al. (2011), and for the MW from Townsend et al. (2011). For the eccentricities we take all data (for both SMC and MW) from Townsend et al. (2011).

In Fig. 2.7 we present the cumulative distributions of the spectral types, orbital periods, and eccentricities for MW and SMC BeXRBs. For the SMC we used the spectral types of sources as derived from this work and the previous studies of McBride et al. (2008), and Antoniou et al. (2009a), while for the MW we take the data from the review paper of Reig (2011). We find marginal evidence for difference between the spectral type distributions of SMC and MW BeXRBs (∼99.9% confidence based on the KS test), in contrast to previous studies which found no evidence for difference between the BeXRB populations in these two galaxies (e.g. Antoniou et al. 2009a; McBride et al. 2008). We attribute this difference to the use of larger samples for both the SMC and the MW than previous studies, and the extension of the former to later spectral types. However, given the important implications of this difference for the evolution of BeXRBs in the SMC we consider it as only tentative at this point. On the other hand, we do not find any evidence for difference in the distribution of the orbital parameters ($Porb$, e) in SMC and MW BeXRBs, based on the KS test. This result provides an indication for the distribution of the kick velocities imparted on the pulsars during the supernova explosion. The vector of the kick and the mass of the secondary object (in the initial binary) will affect the orbit of the neutron star around it. Since the spectral types (which reflects the donor mass of the BeXRBs) are not dramatically different between the SMC and the MW, and the orbital-element distributions (period and eccentricity) are not different at a statistically significant level, we can deduce that there is an indication that the kicks imparted to the pulsars during the supernova explosions have similar strengths in the SMC and the MW. Further support comes from previous studies, where the measured kicks in the MW BeXRBs ($v \sim 15 \pm 6\,\mathrm{km\ s^{-1}}$; van den Heuvel et al. 2000b) are found to be comparable with these of the SMC BeXRBs ($v \sim 30$ km s^{-1}; Coe 2005, $v < 15 - 20$ km s^{-1}; Antoniou et al. 2010).

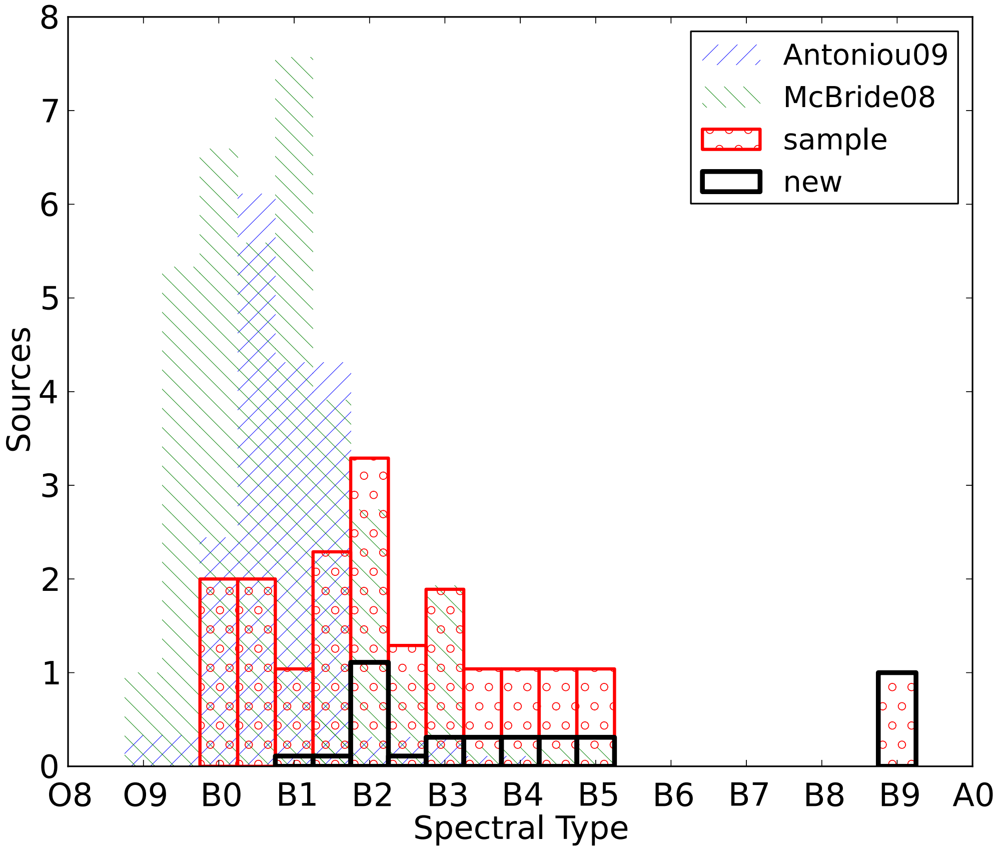

Figure 2.3: Comparison of spectral-type distributions of the different samples considered in this work: "Antoniou09" (blue, right diagonal line filled) and "McBride08" (green, left diagonal line filled) corresponds to the spectral-type distributions obtained from Antoniou et al. (2009a) and McBride et al. (2008), respectively; "sample" (red solid line, 'o' filled) and "new" (black solid line) correspond to the BeXRB sample studied in this work (excluding sources CH7-19 and CH6-20) and only the new sources (excluding source CH6-20) from this work respectively, as defined in Section 2.6.1. (For sources extending over more than one class their spectral type is split equally between the encompassed class bins, e.g. a B0-B2 object will split into 1/3 in B0, B1, and B2 spectral type, respectively.)

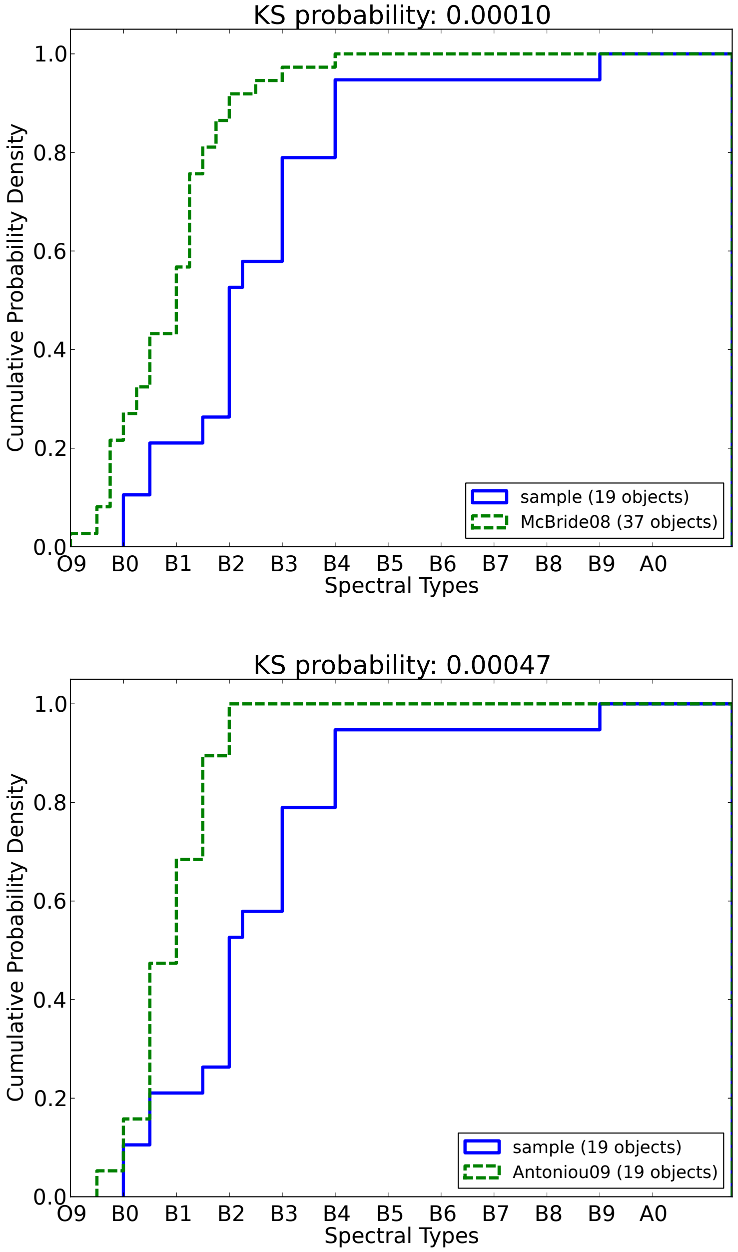

Figure 2.4: Cumulative distributions of the spectral types of BeXRBs populations in the SMC for our sample (solid blue, excluding source CH6-20) compared with the samples (dashed green) of Antoniou et al. (2009a) and McBride et al. (2008). By applying the Kolmogorov-Smirnov test we find that our sample is different from the previous ones, at more than 99% confidence level (the probability to reject the null hypothesis, that the two distributions come from the same parent distribution, is given above each plot). This indicates that our sample is skewed to later spectral types.

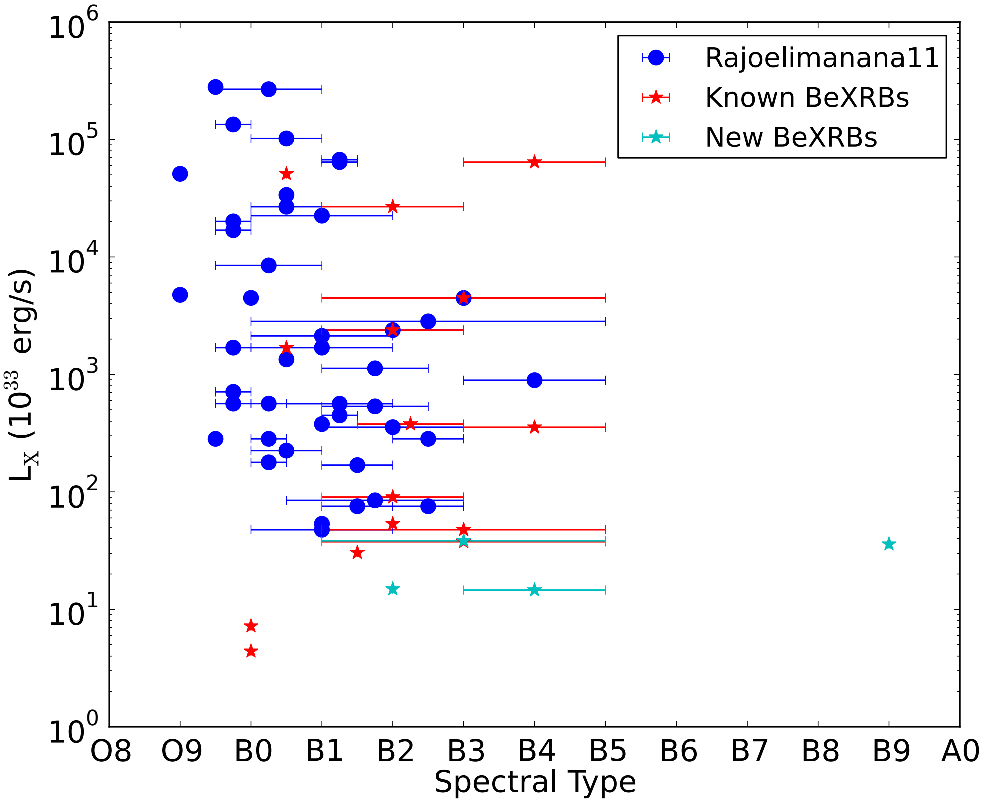

Figure 2.5: Unabsorbed X-ray luminosities (L_X) of SMC BeXRBs plotted against the spectral type of their optical counterparts. The blue circles represent the maximum observed L_X for sources obtained from table 1 of Rajoelimanana et al. (2011) and after transforming these values to the 0.5-7 keV energy band that we used in our study (assuming a power law with photon index $\Gamma = 1.7$ and $N_H \sim 6 \times 10^{20}$ cm^{-2}). The red asterisks ("Known BeXRBs") represent sources from our sample (see Table 2.3) with a previous classification and their maximum luminosities are derived either from table 1 of Rajoelimanana et al. (2011) or from Zezas (in prep., *Chandra* sources) and Antoniou et al. (2010, *XMM-Newton* sources). The cyan asterisks ("New BeXRBs") represent new sources identified in this work (see Section 2.6.1) with their luminosities taken from Zezas (in prep.), and Antoniou et al. (2010).

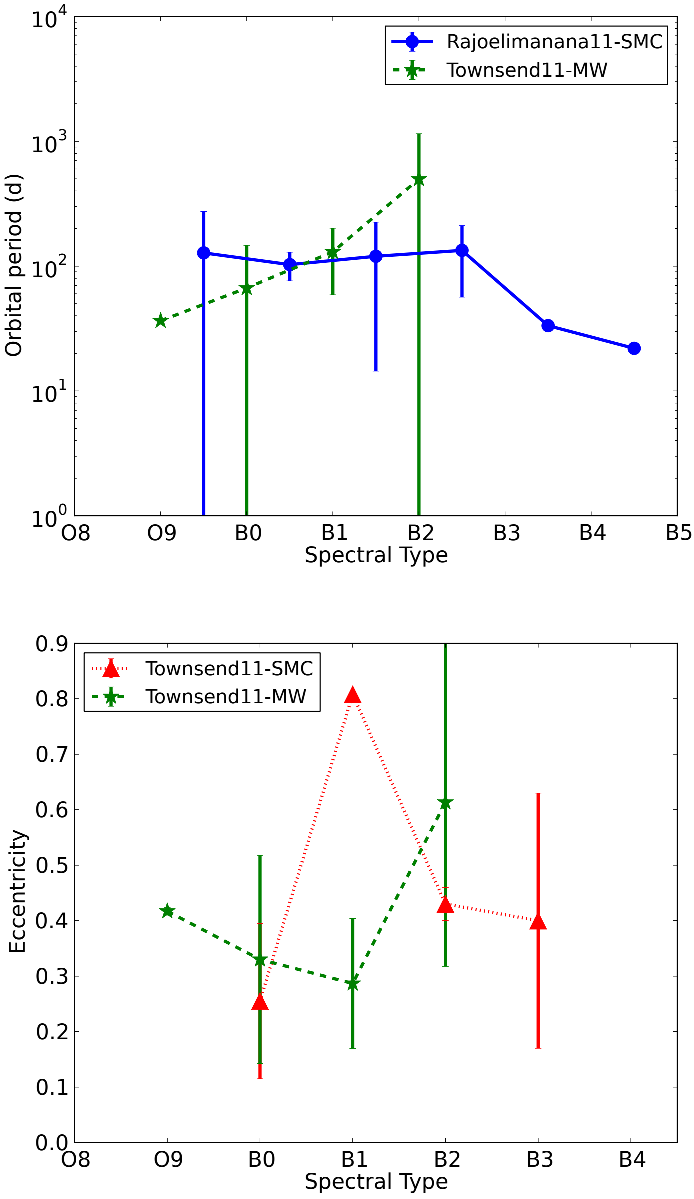

Figure 2.6: The orbital periods ($Porb$) and eccentricities (e) as a function of the spectral types of the optical counterparts of BeXRBs populations in the SMC and the Milky Way (binned to 1 spectral type). For the orbital periods the solid blue and the dashed green lines correspond to the samples of BeXRBs in the SMC (after Rajoelimanana et al. 2011) and in the Milky Way respectively (after Townsend et al. 2011). For the eccentricities we use data from Townsend et al. (2011) for BeXRBs in the SMC (dotted red) and Milky Way (dashed green). The error bars indicate the 1σ standard deviation for each of the two parameters within each spectral-type bin.

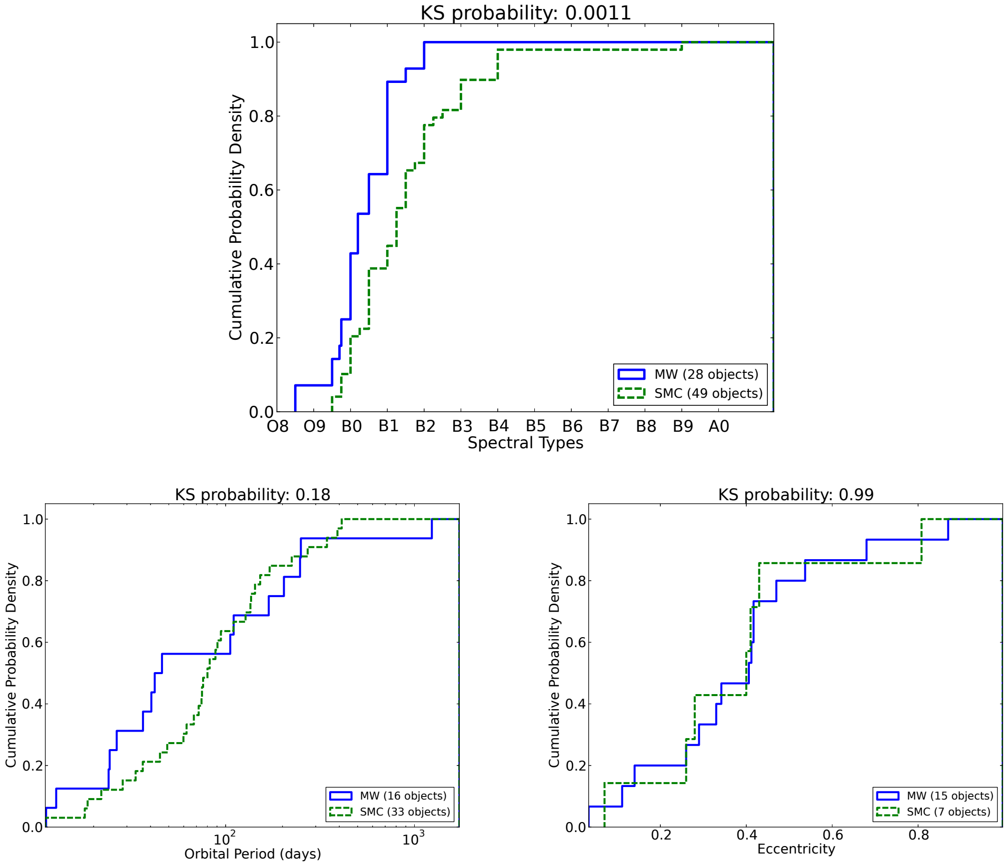

Figure 2.7: Cumulative distributions of the spectral types, orbital periods (P_{orb}), and eccentricities (e) for BeXRBs in the MW (solid blue) and the SMC (dashed green). For the spectral-type distributions the data come from this work, McBride et al. (2008), and Antoniou et al. (2009a), while for the MW we take the data from the review paper of Reig (2011). Data for the P_{orb} of BeXRBs in the SMC are taken from Rajoelimanana et al. (2011), and for the MW from Townsend et al. (2011). For the e we take all data (for both SMC and MW) from Townsend et al. (2011). The Kolmogorov-Smirnov test probabilities are given over each plot. We find marginal evidence for difference between the spectral type distributions of SMC and MW BeXRBs (at ∼99.9% confidence), while we do not find any evidence for difference in the distribution of the orbital parameters ($Porb$, e) in SMC and MW BeXRBs (see Section 2.6.2).

2.6.3 The case of the supergiant B[e] source CXOU J005409.57-724143.5

2.6.3.1 Optical and Infrared properties

The optical counterpart of source CXOU J005409.57-724143.5 (CH6-20) is classified in this work as a supergiant star. If the X-ray source is an accreting binary, it would be only the second to be found in the SMC after SMC X-1 (Webster et al., 1972). Its optical counterpart is star LHA 115-S 18 (Henize, 1956) also known as AzV 154 (Azzopardi et al., 1975), a well known bright emission-line star that has been studied systematically since 1956 (Massey & Duffy 2001; Morris et al. 1996; Shore et al. 1987; van Genderen & Sterken 2002; Zickgraf et al. 1989, and references therein), and more recently in Clark et al. (2013). In Fig. 2.8 we present a finding chart of the X-ray source and its corresponding optical counterpart.

According to the classification criteria for supergiant B[e] stars (Lamers et al., 1998), these objects exhibit strong Balmer emission lines (usually with P Cygni profiles indicating mass loss), low excitation permitted and forbidden lines (e.g. FeII), and strong near or mid-infrared excess (due to hot circumstellar dust). Moreover, they are rather stable photometrically (variation of the order of ∼0.1-0.2 mag) and spectroscopically, unlike the S Doradus / Luminous Blue Variable (LBV) stars which exhibit similar spectra (Zickgraf et al., 1986).

As discussed in Section 2.5.2, star S 18 presents the typical spectral characteristics of B[e] stars. In addition, it is very bright in the near-IR showing a very large color excess of J-[3.6μm]=3.17 ± 0.05 mag, compared to the main sequence and supergiant B stars (most Be stars show a color excess of J-[3.6μm]$\sim$ 0.8 mag; Bonanos et al. 2010).

In Fig. 2.9 we present the light curve of star S 18, using the OGLE-II data in the I filter (as discussed in Section 2.3.2), clearly indicating a highly variable source. In addition, S 18 exhibits spectroscopic variations (e.g. in the lines of HeII λ4686, CIV λ1550, NIV λ1487; Shore et al. 1987). This is in contrast with the photometric stability of typical sgB[e] stars, and it is more similar to the strong variability of LBV stars (e.g. Zickgraf et al. 1986). However, there is growing evidence that the sgB[e] and the LBV sources are not distinct classes (Clark et al., 2013; Morris et al., 1996; van Genderen & Sterken, 2002). In order to investigate if it is an accreting binary source we searched for modulation of its optical emission resulting from an orbital period. Due to the significant variability, we detrended the light curve following Schurch et al. (2011), by fitting a 2nd order polynomial to each year-long segment of the data. Then

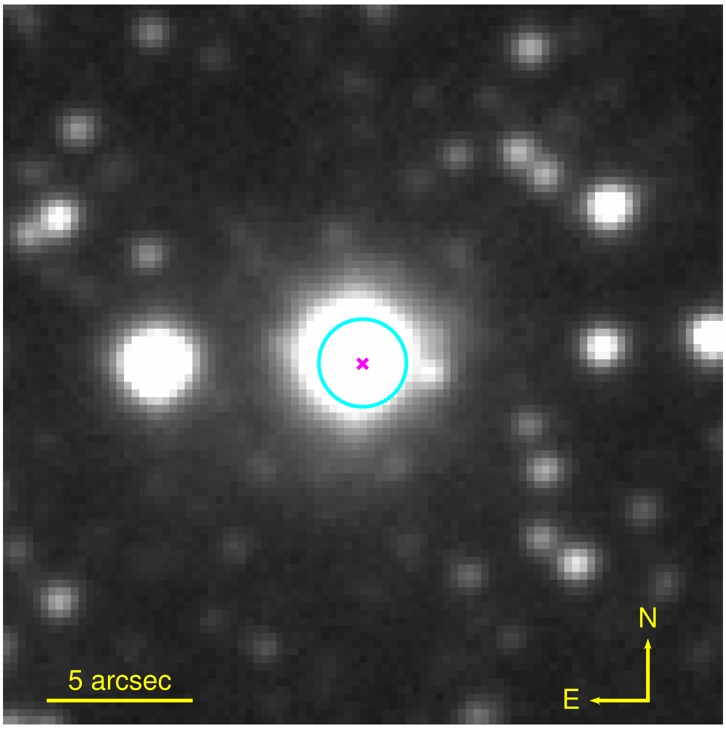

Figure 2.8: Finding chart of source CXOU J005409.57-724143.5 (or CH6-20 in Antoniou et al. 2009b) from an OGLE-III *I*-band image (Udalski et al., 2008). The dimensions of the field are 24.7"×24.7". The cyan circle indicates the positional error-circle of the *Chandra* source (1.5" radius, see Antoniou et al. 2009b for details) and the magenta x-symbol indicates the location of star number 7 from the OGLE-III SMC105.6 map, which is spatially coincident with star LHA 115-S 18 (Henize, 1956).

we obtained the Lomb-Scargle periodogram (Lomb, 1976; Scargle, 1982) for the entire detrended light curve. We did not find any periodicity at the 90% confidence level in agreement with the results of Clark et al. (2013). The significance level was estimated by simulating light curves based on the noise characteristics of the data and repeating the analysis for each simulated light curve.

2.6.3.2 X-ray properties

In order to explain the spectral variations of S 18, Shore et al. (1987) suggested the presence of a hot companion, possibly a helium star or a neutron star. But no further evidence of such an object existed as the X-ray observations at the time were not sensitive enough to observe any emission from accretion onto a putative compact object. Nowadays, *Chandra* and *XMM-Newton* are able to routinely detect sources with X-ray

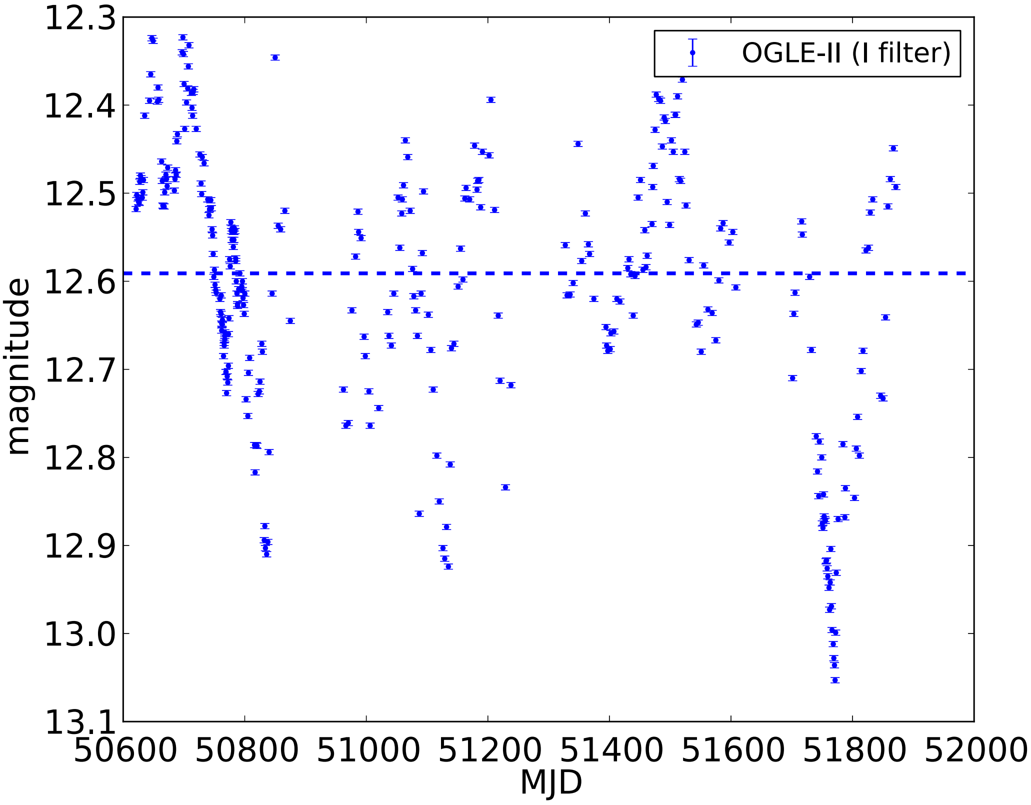

Figure 2.9: OGLE-II *I*-band light curve of the optical counterpart of source CH6-20 (*ROSAT* observations were obtained before the OGLE-II survey, while *Chandra* and *XMM-Newton* observations were obtained later). The horizontal line indicates the median value of ∼ 12.6 mag, and the errors on the photometric points are 0.003 mag. The observed aperiodic variability is larger than what expected for a normal supergiant B[e] star and it is more similar to the variability that Luminous Blue Variables display (see Section 2.6.3.1).

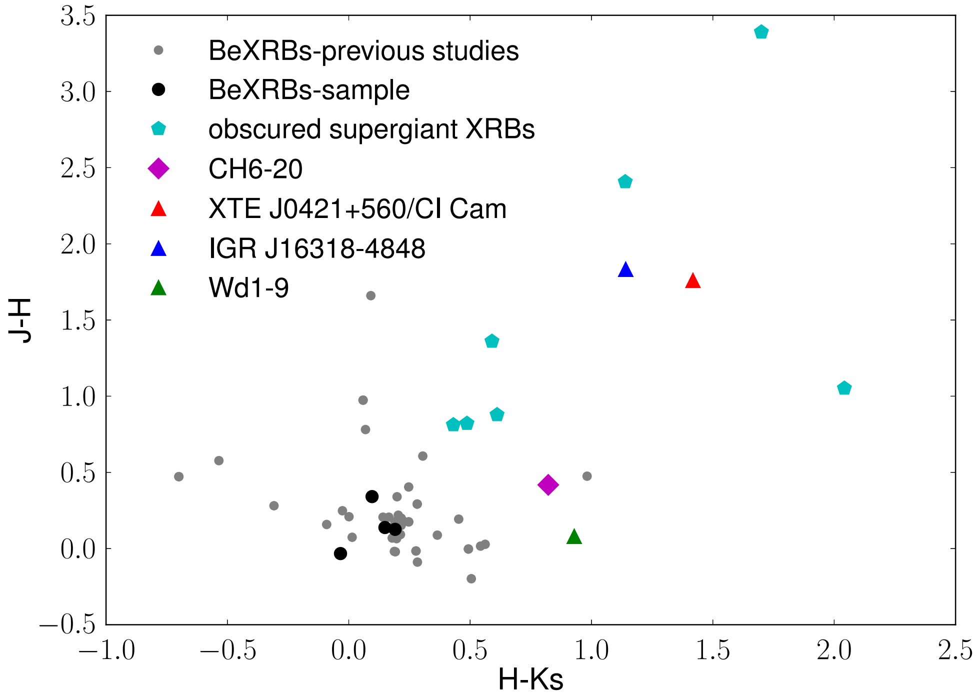

Figure 2.10: *J-H* vs. H-K_s color-color diagram of BeXRBs with available 2MASS data. Black dots show sources from our sample and gray dots show sources from the samples of McBride et al. (2008), and Antoniou et al. (2009a). We present also X-ray sources with a known sgB[e] companion (triangles) and the highly obscured sgXRBs identified so far by *INTEGRAL* (cyan polygons; Manousakis 2011). Our source CH6-20 is presented as a purple diamond.

luminosities down to $\sim 10^{33}\,\mathrm{erg\ s^{-1}}$ at the distance of the SMC (with 10-30 ks exposures) and have succeeded in detecting source CXOU J005409.57-724143.5 (CH6-20) which is spatially coincident with star S 18. In the study of Antoniou et al. (2009b) its proposed optical counterpart is star O_6_311169 (00:54:09.53, -72:41:42.9) from the OGLE-II catalog (Udalski et al., 1998), or Z_2611188 (00:54:09.57, -72:41:42.9) from the Magellanic Clouds Photometric Survey (MCPS) catalog (Zaritsky et al., 2002), which is coincident with star S 18. With this work we confirm that the optical counterpart of the source CXOU J005409.57-724143.5 (CH6-20) is the supergiant B[e] star S 18.

This source has only been detected in the X-ray band in only two epochs (see Section 2.3.3). The lack of previous detections with *ROSAT* or *Einstein* indicate that it is persistently at a low luminosity state ($\mathrm{L_x} < 10^{35}\,\mathrm{erg\ s^{-1}}$) since at higher luminosities it would have been detected already in one of the several pointings with these observatories. Although the intensity of CH6-20 is only $\sim 2\sigma$ above the background in the *Chandra* survey, the independent *XMM-Newton* detection with a source-detection likelihood of DET_ML=24.6 during the first *XMM-Newton* observation ensures that the source is not spurious.

Next we discuss the X-ray properties of this source in the context of typical supergiant wind-fed X-ray binaries. Assuming Bondi-Hoyle accretion from a stellar wind, the X-ray luminosity of the compact object is given by (e.g. Longair 2011):

$$\mathrm{L_X} \sim \eta \frac{\dot{M} c^2}{4} \left(\frac{2 G M_X}{\alpha} \right)^2 v_w^{-4}, \tag{2.1}$$

where η is the efficiency of the conversion of the rest mass energy of the accreted matter into radiation (~ 0.1), $\dot{M}$ is the mass-loss rate, c is the speed of light, G is the gravitational constant, M_X is the mass of the compact object, α is the separation between the compact object and the donor star, and v_w is the wind velocity. The distance α can be calculated at the periastron from Kepler's 3rd law:

$$\alpha = \left(\frac{G}{4\pi^2} \left(M_X + M_{OB} \right) P_{orb}^2 \right)^{\frac{1}{3}} \times (1 - e), \tag{2.2}$$

where M_{OB} is the mass of the donor OB star, P_{orb} is the orbital period of the system, and e is the eccentricity. For the donor star, Zickgraf et al. (1989) estimate a mass of $M_{OB} \sim 40\ \mathrm{M_\odot}$, a wind mass-loss rate of $\dot{M} \sim 3 \times 10^{-5}\ \mathrm{M_\odot\ yr^{-1}}$, and a velocity of $v_w \sim 750\ \mathrm{km\ s^{-1}}$. Since we have no information on the orbital parameters of the system we take the typical (median) values for the orbital period ($P_{orb} \sim 6.78\,\mathrm{d}$) and eccentricity ($e \sim 0.17$) for other known sgXRBs (from the data in table 7 of

Townsend et al. 2011, for SMC and Milky Way systems). This results in a peak X-ray luminosity at periastron of $L_X \sim 10^{37}$ erg s^{-1}. Keeping the same values for the orbital period and eccentricity, but using instead the typical wind parameters for supergiant stars in the SMC within the spectral range O9.5-B1 ($\dot{M} \sim 8.4 \times 10^{-7}$ $M_\odot$ yr^{-1} and $v_w \sim 1272$ km s^{-1}; Mokiem et al. 2007) we derive a luminosity of $L_X \sim 7 \times 10^{34}$ erg s^{-1}.

The estimated peak L_X at periastron from the values obtained from Zickgraf et al. (1989) is too high for this source to remain undetected for so long. On the other hand, when the values from Mokiem et al. (2007) are used, the estimated peak L_X is consistent with the measured luminosity and comparable to the detection limits of the *Chandra* and *XMM-Newton* observations. However, the above luminosities correspond to the peak L_X for this source when the neutron star is located at periastron, assuming a stable mass-loss rate. If the X-ray observations were obtained when the neutron star is away from the periastron and/or a lower mass-loss rate phase (as for example it would be expected from its significant optical variability) then the X-ray luminosity would be even lower than that estimated above.

Furthermore, a clumpy wind with a high mass-loss rate may provide an alternative interpretation for the nature of this source. In this case the high column density towards the neutron star due to the wind may obscure its X-ray emission. A column density of $N_H = 3 \times 10^{24}$ cm^{-2} (assuming a power-law spectrum with a photon index Γ=1.7 in the 0.5-7 kev energy band) would be enough to attenuate a source with intrinsic $L_X = 10^{37}$ erg s^{-1} (which is the upper range in its X-ray luminosity based on the parameters from Zickgraf et al. 1989) down to $L_X = 5.7 \times 10^{33}$ erg s^{-1}, while an $N_H = 1 \times 10^{24}$ cm^{-2} would be enough to attenuate a source with intrinsic $L_X = 7 \times 10^{34}$ erg s^{-1} (the luminosity expected from the parameters of Mokiem et al. 2007) down to $L_X = 1.6 \times 10^{33}$ erg s^{-1}. Both of these estimates are half the value we found with *Chandra*. However, we do have significant detection below 2 keV in both the *Chandra* and *XMM-Newton* observations (6^{+3}_{-2} and 39±11 counts respectively), and only upper limits or marginal detections above 4 keV, which do not allow us to set any useful constraints on the spectral parameters of this source.

There is an emerging subclass of highly obscured wind-fed sgXRBs, discovered in recent *INTEGRAL* observations (Walter et al., 2006). To date there are three known X-ray sources with B[e] companions: IGR J16318-4848 (Filliatre & Chaty, 2004; Walter et al., 2003), which is considered the prototype of highly obscured wind-fed sgXRBs, CI Cam/XTE J0421+560 (Boirin et al., 2002; Clark et al., 1999), the first HMXB with a sgB[e] companion, and Wd1-9 (Clark et al., 2008), a probable colliding-wind system. Recently, Bartlett et al. (2013) presented a detailed study of CI Cam observed in 2003 with *XMM-Newton*. This system has a B0-2[e] supergiant companion (Clark et al., 1999) and shows a heavily absorbed ($N_H \sim 4.4 \times 10^{23}$ cm^{-2}) power-law ($\Gamma \sim 1$) spectrum reaching $L_X \sim 4.1 \times 10^{33}$ erg s^{-1} (3-10 keV) in quiescence. In 1998 it showed an outburst reaching a flux of $\sim 4.8 \times 10^{-8}$ erg cm^{-2} s^{-1} (2 Crab) in the 2-10 keV energy band (Smith et al., 1998). Assuming a distance of 5 kpc, the outburst luminosity is $\sim 5.7 \times 10^{36}$ erg s^{-1}. The nature of the compact object in this system as well as in IGR J16318-4848 is unclear (Bartlett et al., 2013), although there is some indication that at least in the case of IGR J16318-4848 it might be a neutron star (Filliatre & Chaty, 2004).

The main difference of these systems from the "classical" sgXRBs is that they are much more absorbed in the X-ray band. The compact object is deeply embedded in the dense material of the wind and the absorbing column density changes during the orbit (it may increase up to ten times close to the eclipse; Manousakis & Walter 2011). Moreover, material away from the compact object (like the material around the sgB[e] star) may contribute to the absorption (e.g. as in IGR J16318-4848; Walter et al. 2006). In this case the source exhibits strong IR excess, attributed to free-free and bound-free emission from hydrogen in a circumstellar envelope (or disk; Wisniewski et al. 2007). At longer wavelengths such as those observed by *Spitzer*, the IR excess indicates the presence of warm dust in the circumstellar envelope or the disk. In Fig. 2.10 we present the location of source CH6-20 in a near infra-red (NIR) color-color diagram. This plot is an updated version of fig. 4 by Graus et al. (2012), where in addition to the BeXRBs we include all highly obscured sgXRBs identified so far by *INTEGRAL*. These sources show luminosities in the $10^{33} - 10^{34}$ erg s^{-1} range, they are highly variable and they have absorbing column densities in the $10^{23} - 10^{24}$ cm^{-2} range. We find that source CH6-20 shows redder NIR colors than the other BeXRBs which place it closer to the colors of the obscured supergiant HMXBs.

An alternative scenario for the nature of the CH6-20 is that it is a colliding-wind binary (e.g. Pollock 1987). These systems consist of two orbiting massive stars in orbit, and their low luminosity X-ray emission ($L_X \sim 10^{33} - 10^{34}$ erg s^{-1}) is produced by shocks at the collision front of the winds. Clark et al. (2013) point out that although S 18 (CH6-20) and the wind-fed sgXRB CI Cam exhibit many similarities, their long term photometric and spectroscopic behaviors are not quite the same, and argue for a colliding-wind nature for the former system instead of an accreting binary. This is supported by the location of source CH6-20 in the NIR color-color diagram (Fig. 2.10) which is also consistent with that of the colliding-wind system Wd1-9 (Clark et al., 2008) and their similar X-ray luminosity (unabsorbed $L_X \sim 4 \times 10^{33}$ erg s^{-1} for

Wd1-9, in the 0.5-8 keV band; Clark et al. 2008). The luminosities of both CH6-20 and Wd1-9 are well within the range of colliding-winds systems ($\sim 10^{32} - 10^{35}$erg s^{-1}, Gagné et al. 2012; Stevens et al. 1992). Although colliding-wind systems also have hard X-ray spectra, a possible discriminating feature from accreting pulsar binaries is that the spectra of the former have a cutoff at ∼10 keV, and they show effectively no photons with energies above 10 keV (Pollock, priv. comm.). Unfortunately the weak X-ray emission of this source does not allow us to detect any X-ray photons above 2 keV. This in combination with its highly variable optical light curve that does not allow us to measure its orbital parameters, hamper the distinction between these two scenarios. However, if the heavily obscured sgB[e] scenario proves to be correct then CXOU J005409.57-724143.5 (CH6-20) / S 18 will be the first extragalactic heavily obscured sgXRB, and the second sgXRB in the SMC.

2.7 Conclusions

In this paper we presented our results from optical spectroscopic observations of the optical counterparts of X-ray sources detected in the *Chandra* and *XMM-Newton* surveys of the SMC. We used the AAOmega spectrograph at the Anglo-Australian Telescope to observe sources identified in Zezas (in prep.) and Antoniou et al. (2010, 2009b), with the aim to identify new HMXBs and determine their spectral types. We identified 5 new BeXRBs and 1 known supergiant system which we associate with an X-ray source. We confirmed the previous classifications (within 0.5 spectral type) of 12 sources, while for 3 sources our revised classification, with higher resolution and S/N data, result in later (by 1-1.5 subclass) spectral types.

We were able to classify BeXRBs with X-ray luminosities over 3 orders of magnitude. The selection of the parent sample from *Chandra* and *XMM-Newton* observations of the SMC, allows us to extend our census of BeXRBs to almost quiescent luminosities. A comparison of the populations of BeXRBs in the SMC and the Milky Way with respect to their spectral types reveals a marginal evidence for difference. However, we find no statistically significant differences for their orbital parameters (periods and eccentricities). This result further supports other lines of evidence for similar supernova kick velocities between the low metallicity SMC and the Milky Way.

Finally, we discuss the X-ray, optical, and infrared properties of source CXOU J005409.57-724143.5. This intriguing source is associated with the well known supergiant star LHA 115-S 18. Its optical and X-ray properties do not allow us to distinguish between a colliding-wind system or a supergiant X-ray binary. If the second scenario proves to be correct, then this source would be the first extragalactic supergiant X-ray binary with a B[e] companion.

Acknowledgments

We would like to thank the referee, Phil Charles, whose comments and suggestions helped to improve the paper. We would like to thank the staff of the Anglo-Australian Observatory for obtaining the data used in this work. We thank A. Manousakis and R. Walter for useful discussions regarding the class of heavily obscured sgXRBs, and A. Pollock for advice regarding the class of colliding-wind binaries. GM acknowledges support by State Scholarships Foundation of Greece in the form of a scholarship. AZ acknowledges support by the *Chandra* grant GO3-14051X, the NASA grant NNX12AL39G, and the EU IRG grant 224878. Space Astrophysics at the University of Crete is supported by EU FP7-REGPOT grant 206469 (ASTROSPACE). VA acknowledges support by NASA grant NNX10AH47G issued through the Astrophysics Data Analysis Program, and *Chandra* grant GO3-14051X.

This research has made use of NASA's Astrophysics Data System, SIMBAD database (operated at CDS, Strasbourg, France), and data products from the Optical Gravitational Lensing Experiment and the Two Micron All Sky Survey, which is a joint project of the University of Massachusetts and the Infrared Processing and Analysis Center/California Institute of Technology, funded by the National Aeronautics and Space Administration and the National Science Foundation. Figures were generated using the matplotlib[1] library in the Python[2] programming language.

---

[1] `http://matplotlib.org/`

[2] `http://python.org/`

3

Towards an automated spectral classifier

3.1 Introduction

Be X-ray Binaries (BeXRBs) are a sub-class of High-Mass X-ray Binaries which consist of a compact object, typically a neutron star, and a massive companion of Be type (Rivinius et al., 2013). This companion is the donor of the material that is accreted by the compact object producing the X-ray emission (see the review by Reig 2011). Contrary to the X-ray band, where the emission is produced by the accretion flow on the compact object, it is the donor star that dominates the emission in the optical domain. Studies of BeXRBs in this wavelength range can reveal physical properties (e.g. masses of the two components, orbital period, eccentricity) that are fundamental for understanding their formation and evolution (Tauris & van den Heuvel, 2006).

Generally BeXRBs are first detected as X-ray sources and their nature is confirmed later from narrow-band imaging or even better spectroscopic observations. Therefore, dedicated spectroscopic observations of BeXRBs allow for the verification of the nature of the donor and the determination of its spectral type. Statistical studies of large samples of BeXRBs, with respect to their spectral-type/mass distributions, allow us to investigate differences between different populations (e.g. BeXRBs in our Galaxy and the Magellanic Clouds) and understand their evolution (Antoniou et al., 2009a;

Maravelias et al., 2014; McBride et al., 2008). Unfortunately, spectral classification in these studies (and in general spectral classification of stars) is qualitative, based on the presence or absence of diagnostic lines and suffers from subjectivity, despite the power of the human eye as a pattern recognition classifier. The best way to overcome this limitation is to use objective, preferably automated, methods based on quantitative measurements of spectral features.

Previously proposed algorithms in this direction, have been based either on the evaluation of specific criteria (e.g. spectral features) or on pattern recognition (see review by von Hippel et al. 1994b). The former approach resembles what a human classifier actually performs when visually examines a spectrum and assesses the presence of spectral lines. In the latter case the whole spectrum (or parts of it) is compared to a library of templates and then non-linear algorithms are used to identify the template that minimizes the distance from the observed spectrum, with prime example being the application of Artificial Neural Networks (Duan et al. 2009; Gulati et al. 1996; Navarro et al. 2012; von Hippel et al. 1994a). In addition, there is a number of techniques that combine measurements of spectral features with photometric properties (e.g. Allende Prieto et al. 2006).

The challenge for all these methods has been the automated classification over a wide range of spectral types (O- to M-type), where stars present a wide range of characteristic lines. The criteria-evaluation techniques have difficulty to account for all spectral features in a such wide range of spectral types. On the contrary, template-matching (cross-correlation) techniques are more flexible as they tend to identify how similar is an observed spectrum to a template spectrum. However, these techniques need template and test observed data of similar qualities (e.g. wavelength coverage, resolution, SNR), which is not typical for data from different observing facilities and/or strategies.

Even worse, in our case the Be-star donors in BeXRBs exhibit Balmer lines in emission[1] (e.g. Porter & Rivinius 2003; Rivinius et al. 2013). The emission is due to the ionization of the circumstellar disk, which is believed to result from the fast stellar rotation (Ekström et al., 2008; Meynet & Maeder, 2000; Townsend et al., 2004). The variable size of the circumstellar disk (in timescales of months) leads in variable Balmer lines Okazaki (1997). Therefore, Be stars (and BeXRBs) can be found in a state of pure absorption lines (absent circumstellar disk), to a state of no visible lines at all (when the emission is equally intense with the absorption), or even to strong emission lines (fully developed disk). This variability does not allow use of the key set of Balmer

---

[1] This is denoted in the spectral type by the index "e" (e.g. B2e).

lines for spectral type classification.

Our initiative is an attempt to develop an automated spectral classifier for the O- and B-type stars, based on the spectral classification criteria developed for these sources in our Galaxy (Walborn & Fitzpatrick, 1990) or in a low metallicity environment such as the Small Magellanic Cloud (SMC; Evans et al. 2004). We identified a set of diagnostic spectral lines to use as indicators of the different spectral subtypes. We use the equivalent widths of these lines in our diagnostic scheme, since they are a robust quantity for comparisons between spectra taken under varying circumstances (e.g. instruments used) and different formats (normalized or not). We developed two classification methods, established on totally different approaches: (a) a continuous approach based on the continuity of temperature as the physical quantity that drives the strength of the lines defining each spectral type (presented in Section 3.3), (b) a statistical approach of the data based on the application of the Naive Bayes Classifier on the distribution of the EW of the diagnostic lines (presented in Section 3.4.1). This method has been already applied in the classification of X-ray sources in the Carina region, combing information from optical and X-ray spectra, near- and mid-IR brightness, and the spacial distribution of sources (Broos et al., 2011).

3.2 Methodology

3.2.1 Samples

In this study we have used two sets of samples: the first to define the diagnostic scheme (training samples) and the second to test the methods (test samples).

3.2.1.1 Training samples

In order to develop classification diagnostics based on spectral lines we first define the template spectra to use (training samples). We are interested in features in the blue part of the optical regime ($\sim 3800 - 5000$ Å), since these are most useful in identifying spectral types (e.g. Walborn & Fitzpatrick 1990). In addition, we select spectra with resolution better than 5 Å, to resolve the HeI $\lambda 4471$ and MgII $\lambda 4481$ lines. Since the strength of the spectral lines depends on the metallicity we define two training samples: one based on Galactic stars, and one based on lower metallicity stars observed in the SMC (at 1/5 of the Gallactic metallicity).

Our Galactic training sample consists of spectra obtained from:

(a) the atlas of OB spectra by Walborn & Fitzpatrick (1990), which provides an observational catalog and detailed classification criteria for earlier than O9-type stars (which did not exist in the MK classification),

(b) the reference book of Gray & Corbally (2009), who discuss in detail the classification schemes for all types of stars, and

(c) data from the compilation of Jacoby, Hunter, & Christian (1984), obtained from the STSDAS/SYNPHOT package[1].

The SMC training sample was provided by C. Evans (2014; private commun.), as derived from the extensive spectroscopic survey of Evans et al. (2004) who focused on the accurate classification of a large sample of B- and A-type stars, along with a substantial number of O-type stars. However, the main sequence B-type stars are limited down to approximately mid-B types, since sources later than these are fainter and as such more difficult to obtain good quality spectra.

The selected spectra have a resolution of ~0.8-3 Å allowing an accurate measurement of the diagnostic lines. We used only sources of IV-V luminosity class, to better reflect the luminosity class of BeXRBs. The final sample includes 40 Galactic sources (of which 12 are from Walborn & Fitzpatrick 1990, 11 from Gray & Corbally 2009,and 17 from Jacoby et al. 1984) and 254 SMC sources (from Evans et al. 2004). In general, the spectral coverage of the training samples is between the O5-B9 types, but not adequately representative of the late B-type stars (there are 8 sources later than B4 in each of the Galactic and SMC samples, corresponding to 20% and a mere 3% of the total Galactic and SMC training sample, respectively).

3.2.1.2 BeXRB test samples

In order to test our classification methods we used samples of BeXRBs in our Galaxy and the SMC. The Galactic BeXRB sample consists of 5 sources, for 3 of which there are pairs of spectra, observed with different telescopes and different SNR (Reig 2014; private commun.). We consider these spectra as individual sources, and we treat the Galactic BeXRB sample as having 8 sources. The SMC sample consists of 19 sources, which have been previously visually classified (Maravelias et al., 2014).

---

[1] `http://www.stsci.edu/institute/software_hardware/stsdas/synphot`

3.2.2 Spectral line selection

The MK system of stellar spectral classification (e.g. Gray & Corbally 2009) is based on the presence and the relative intensity of characteristic spectral lines along the spectral type sequence. This sequence is actually a sequence of decreasing temperature, which is the basic physical parameter that determines the relative strength of the spectral lines. In the hottest, O-type stars, their spectra are dominated by the HeII lines, while as we move forward to B-type stars they disappear. The HeI lines peak close to B2-type stars and they disappear as we move further to A-type stars, where Balmer lines are dominant (peaking at A2). As we proceed from the hottest to coolest stars more metallic lines become apparent.

In our analysis, and particularly the application of the classification methods to BeXRBs, we cannot take advantage of the Balmer series, as they exhibit strong variability, due to the presence of the cirumstellar disk (Porter & Rivinius, 2003; Rivinius et al., 2013). The disk affects also the HeI lines but the effect is less significant compared to the Balmer series (Reig & Zezas, 2014).

We selected to use a set of 8 spectral lines: the HeII lines $\lambda\lambda$4200,4551, and 4686 lines (indicative of O-type stars), the HeI $\lambda\lambda$4144,4387, and 4471 lines (strongest around ~B2 spectral type), the MgII λ4481 line (indicative of late B-type stars), and the OII+CIII $\lambda\lambda$4640-4650 blend (present in the early B-type stars). These are the strongest and most clear lines facilitating their automated measurement. In contrast other lines are not sufficiently strong: e.g. the Si lines do help to distinguish between the different subtypes (e.g. Si III λ4553 is present from B1.5 to B4 subtypes) but it has been proved rather difficult to measure with precision, especially in low metallicity such as the SMC. This is further supported from our previous experience (Maravelias et al., 2014), which showed that indeed with visual spectral classification these lines are hard to identify.

3.2.3 Equivalent width measurements

In order to quantify the intensity of the spectral lines we measured their equivalent widths (EWs hereafter). The EWs provide a direct way to compare the strength of different spectral lines for several spectra regardless if they are in raw counts, flux, or rectified flux (i.e. normalized by a spline or polynomial to remove the curvature of the spectrum). It is defined as the width of the continuum region needed that contains the same flux as the spectral line examined. Hence:

$$EW = \int_{\lambda_1}^{\lambda_2} \frac{F_{cont}(\lambda) - F_{line}(\lambda)}{F_{cont}(\lambda)} \, \mathrm{d}\lambda = (\lambda_2 - \lambda_1) - \int_{\lambda_1}^{\lambda_2} \frac{F_{line}(\lambda)}{F_{cont}(\lambda)} \, \mathrm{d}\lambda, \tag{3.1}$$

Table 3.1: Classification criteria for B-type stars in the SMC from Maravelias *et al.* (2014) and Evans *et al.* (2004).

Line identifications	Spectral Type
HeII λ4200,HeII λ4541,HeII λ4686 present	earlier than B0
HeII λ4541 and HeII λ4686 present, HeII λ4200 weak	B0
HeII λ4200 and HeII λ4541 absent, HeII λ4686 weak	B0.5
HeII λ4686 absent, SiIV $\lambda\lambda$4088,4116 present	B1
SiIV λ4116 absent, SiIII λ4553 appear	B1.5
OII+CIII λ4640-4650 blend decreases rapidly	later than B1.5
SiIV and SiII absent, MgII $\lambda4481 <$ SiIII λ4553	B2
MgII $\lambda4481 \sim$ SiIII λ4553	B2.5
MgII $\lambda4481 >$ SiIII λ4553	B3
OII+CIII λ4640-4650 blend disappears, OII λ4415-4417, NII λ4631 disappear	later than B3
clear presence of HeI λ4471 and absence of MgII λ4481	earlier than B5
SiIII λ4553 absent, SiII $\lambda4128 - 4132 <$ HeI λ4121,	B5
HeI $\lambda4121 <$ SiII $\lambda4128 - 4132 <$ HeI λ4144, MgII $\lambda4481 \leqslant$ HeI λ4471	B8
HeI $\lambda4471 <$ MgII λ4481, FeII $\lambda4233 <$ SiII λ4128-4132	B9

where λ_1, λ_2 are the initial and final wavelength over which the line flux is calculated, and F_{cont}, F_{line} are the continuum and spectral-line flux density, respectively.

However, the spectral density is measured on individual pixels, which are quantized quantities and their relation with wavelength is given by the dispersion of the spectrum (d). Thus, we can transform the previous equation as:

$$EW = d \times N - \sum_{i=1}^{N} \frac{F_{line_i}}{F_{cont_i}} d = d \times N - d \times \frac{1}{C} \sum_{i=1}^{N} F_{line_i} \tag{3.2}$$

where the flux of the continuum is considered constant (C) over the wavelength range of N pixels of the line. The wavelength range of the spectral lines has been selected after visual inspection, in order to select the optimal initial and final wavelength values to use. This allows us to easily measure the total flux of the spectral line as the sum of the pixel values included within the $\lambda_1 - \lambda_2$ region. For the estimation of the continuum flux density we are using the value at the central wavelength of the line based on linear interpolation of the continuum intensity from regions at the blue and red sides of the line:

$$C = C_{blue} + \frac{C_{red} - C_{blue}}{\lambda_{red} - \lambda_{blue}} (\lambda_{line} - \lambda_{blue}) \tag{3.3}$$

where C_{blue} and C_{red} are the average values for the continuum flux density at the blue and red sides (in Å/px), and λ_{blue}, λ_{red}, and λ_{line} are the central wavelengths of the blue and red continuum, and the line regions respectively (see Figure 3.1). Although fitting an analytic function to the spectral line could give more accurate results this method allow us to measure very easily a large number of spectral lines.

After visual inspection we defined the appropriate wavelength ranges for the spectral lines and their continuum regions, making sure that they did not include other lines (even weak) or artifacts (e.g. sky lines). These ranges are presented in Table 3.2. We run the analysis for all lines but we select to keep the measurements only for the strongest and most characteristic lines: HeII $\lambda\lambda 4200, 4551, 4686$, HeI $\lambda\lambda 3133, 4387, 4471$, MgII $\lambda 4481$, and OII+CIII $\lambda\lambda 4640 - 4650$ lines (see Section 3.2.2). Even though the HeI $\lambda 4387$ line is not among the criteria presented in Table 3.2, we decided to use it as it generally follows the behavior of the other HeI lines. Moreover, it is easier to measure its intensity in comparison to other HeI lines which reside close to other lines or their corresponding continuum regions are further away from the line (e.g. the HeI $\lambda 4144$ line, see also figure 4.1 in Gray & Corbally 2009).

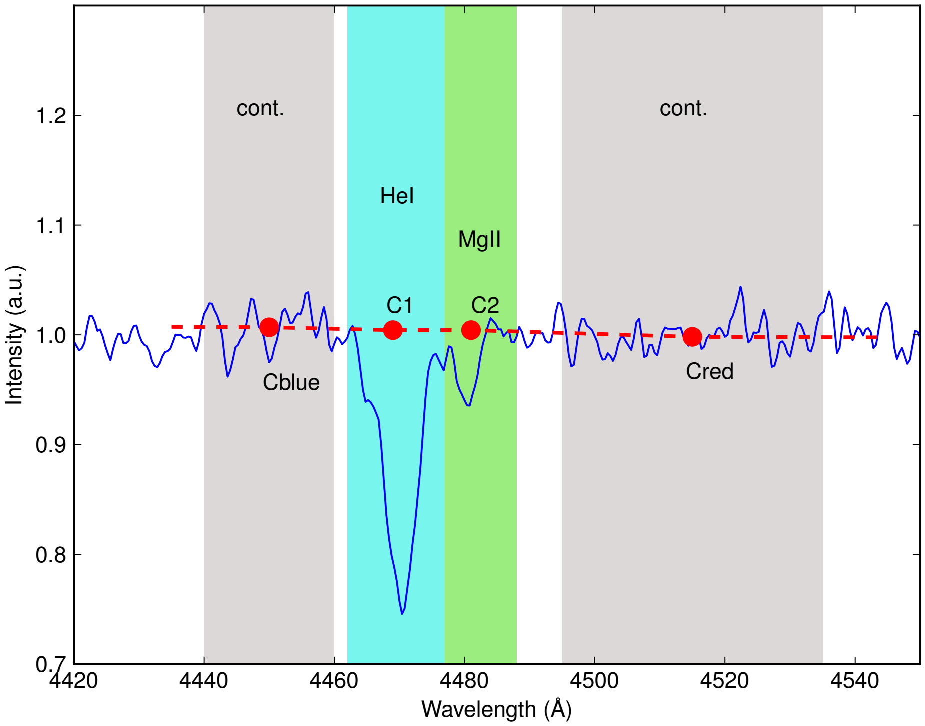

Figure 3.1: Example of the regions used to measure the EW for the lines HeI λ4471 (cyan) and MgII λ4481 (green) and their corresponding blue and red continuum (gray). First, we calculate the mean continuum intensity at the center of each continuum side (Cblue and Cred respectively), and then we perform a linear interpolation between the two points (red dashed line). Using this fit we calculate the continuum flux density at the center of each spectral line (C1,C2).

Table 3.2: Wavelength ranges for the spectral line measurements and their continuum regions. The spectral lines used in our analysis are highlighted.

Line ID/	Spectral line		Continuum blue		Continuum red	
λ_{central} (Å)	λ_{start} (Å)	λ_{end} (Å)	λ_{start} (Å)	λ_{end} (Å)	λ_{start} (Å)	λ_{end} (Å)
CaIIK/3928	3924	3932	3908	3922	3935	3955
HeI/4009	4004	4016	3935	3955	4035	4060
HeI/4026	4017	4035	3935	3955	4035	4060
SiIV/4088	4084	4091	4035	4060	4150	4190
SiIV/4116	4113	4118	4035	4060	4150	4190
HeI/4121	4118	4125	4035	4060	4150	4190
SiII/4130	4125	4135	4035	4060	4150	4190
HeI/4144	4140	4150	4035	4060	4150	4190
HeII/4200	4190	4207	4150	4190	4238	4260
FeII/4233	4229	4237	4150	4190	4238	4260
HeI/4387	4378	4395	4360	4380	4398	4411
OII/4416	4412	4421	4398	4411	4440	4460
HeI/4471	4462	4477	4440	4460	4495	4535
MgII/4481	4477	4488	4440	4460	4495	4535
HeII/4541	4537	4547	4495	4535	4580	4620
SiIII/4553	4548	4558	4495	4535	4580	4620
OII+CIII/4645	4635	4655	4600	4630	4660	4670
HeII/4686	4679	4692	4660	4670	4737	4747

3.3 The Continuous Fit approach

3.3.1 Framework

The stellar spectral classification is a sequence of decreasing temperature, the physical property which drives the presence and strength of spectral lines. Since there is a smooth temperature transition between spectral types, there is also a smooth transition in the intensities of spectral lines: for example Balmer lines are present from O- to M-type with peak intensity at A-type stars, the HeII lines are present only in O- with declining intensity towards later spectral types down to B-type stars.

Therefore, we investigate possible correlations between the EW of the different spectral lines and the spectral type, in order to derive diagnostics for spectral classification.

3.3.2 Description of the method

For different ranges of spectral types we can define combinations of spectral lines for which we plot the EW of one against the other. Objects of different spectral types or subtypes (hereafter referred generally as "spectral types") occupy different locations on this diagram (Figure 3.2). To determine the spectral type of a source one would simply need to identify the locus of the different spectral types in this diagram. However, the visual identification of the boundaries for the various spectral types is complicated because of the continuous variation of the line EW, intrinsic scatter and uncertainty measurements. We overcome this by fitting this correlation between the EW of each pair of diagnostic lines. In such a fit the spectral type in given by the location along the best-fit line. In Figure 3.2 we plot the EW of the HeII λ 4200 and the HeI λ 4471 lines for the Galactic training sample of Be stars. On the same plot we show the spectral types of sources as determined in the training sample. We clearly see a trend for earlier spectral types as we move from the top left to the bottom right corner of the diagram (highlighting areas occupied by indicative groups of spectral types). The same trend is seen in diagnostics involving other spectral types. Therefore, we could identify the spectral type of a sources based on its projected location on the best-fit correlation between the EW of the two spectral types. In order to measure this location we define an arbitrary point on the best-fit line, with respect to which we measure the distance along the line.

Since in our formulation we are treating the spectral types as a continuous quantity we convert them into numerical values by replacing the spectral type with "1" for O-

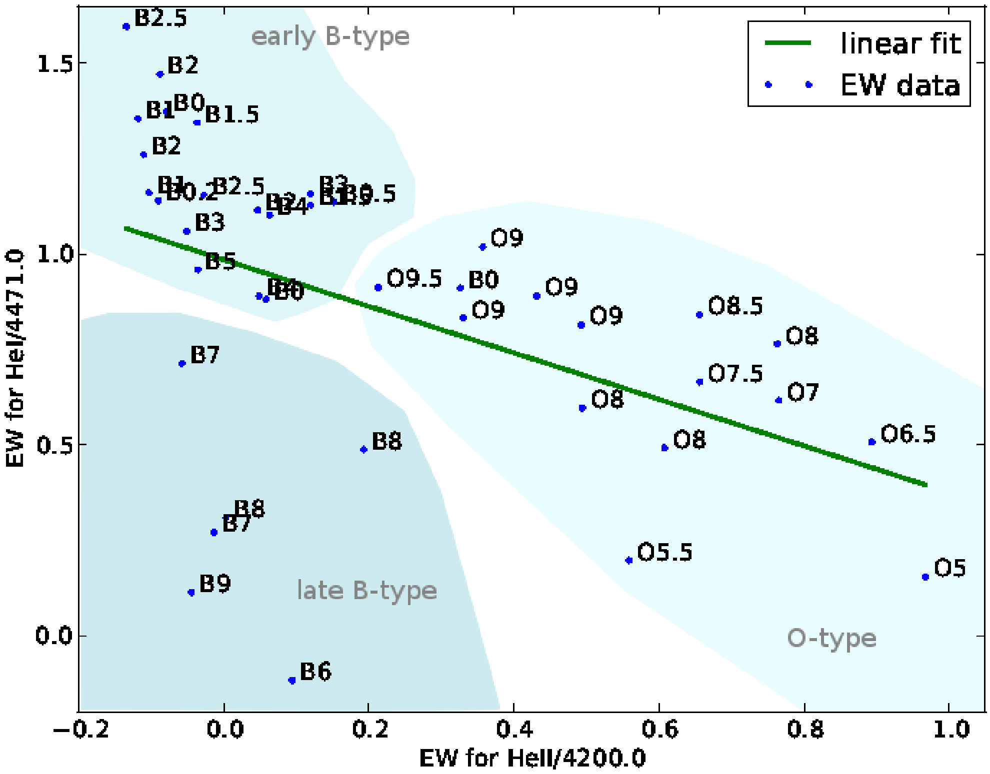

Figure 3.2: Example of a linear correlation between the EWs of the HeII $\lambda4200$ and the HeI $\lambda4471$ lines, for sources obtained from the Galactic training sample. We can identify the different-shaded loci for some groups of spectral types. The significant scatter is due to the intrinsic scatter of the data and measurement uncertainties (particularly at the spectral types with weakest lines)

type sources, and "2" for B-type sources, respectively, followed by their subtype (e.g. O8.5 corresponds to 18.5, B2 to 22.0).

The linear model fit (green line in Figures 3.2 and 3.3) is defined as:

$$y = ax + b, \tag{3.4}$$

where (x, y) are pairs of EW for each pair of diagnostic lines. Then if the reference point is (x_0, y_0) its Euclidean distance from any other point (x, y) is:

$$d_{pp}(x, y) = \sqrt{(x - x_0)^2 + (y - y_0)^2}, \tag{3.5}$$

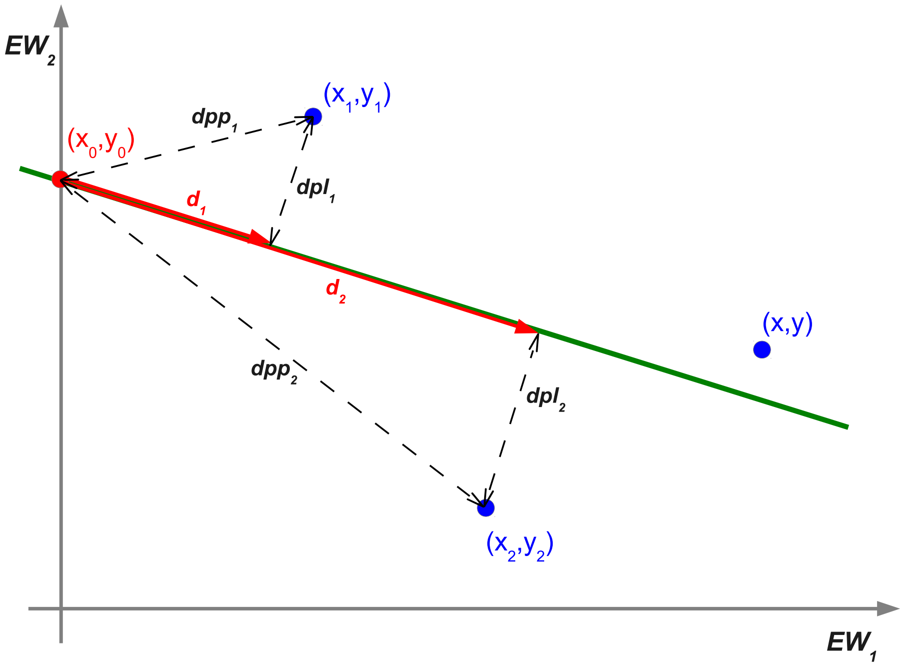

Figure 3.3: Determination of the distance d_i (red arrows) along the linear fit (green line) between the EW of the diagnostic lines (blue points) for data points (x_i, y_i) with respect to an arbitrary reference point (x_0, y_0). We also show the Euclidean distance dpp_i of each point (x_i, y_i) from the reference point (x_0, y_0), as well as their orthogonal distance dpl_i from the best-fit line. (See Section 3.3.2) for details.)

and the orthogonal distance between the same point and the fitted line[1] is:

$$d_{pl}(x, y) = \frac{|ax - y + b|}{\sqrt{a^2 + 1}}. \tag{3.6}$$

The "distance" d along the fitted line between the reference point (x_0, y_0) and the projection of point (x, y) on the best-fit line is found by combining the previous equations into:

$$d(x, y) = \sqrt{d_{pp}^2 - d_{pl}^2} = \sqrt{(x - x_0)^2 + (y - y_0)^2 - \frac{(ax - y + b)^2}{a^2 + 1}} \tag{3.7}$$

The point (x_0, y_0) is arbitrarily defined with the only requirement that it is located on the fitted line. For simplicity and to avoid complexities (e.g. negative distances) we selected this point to be the intercept of the line with the y-axis $(0, b)$ (red point in Figure 3.3), so we have:

$$d(x, y) = \sqrt{x^2 + (y - b)^2 - \frac{(ax - y + b)^2}{a^2 + 1}}. \tag{3.8}$$

If we now replace the variables x, y with the EWs (for the different spectral lines), we can determine a unique distance d for each pair of EWs:

$$d(EW_1, EW_2) = \sqrt{EW_1^2 + (EW_2 - b)^2 - \frac{(aEW_1 - EW_2 + b)^2}{a^2 + 1}}. \tag{3.9}$$

What we have accomplished is to transform the spectral type dependence of the EWs into a one-dimensional parameter that is a function of the spectral type. This becomes more clear if we plot the distance d along the best-fit line shown in Figure 3.2 against the spectral types of the training sample (Figure 3.4). We can see that we are able to distinguish the different spectral types based on their distance d along the fitted line for the EWs. Even though there is scatter in the data we are able to perform a second-order polynomial fit:

$$d(sp) = k_1 sp^2 + k_2 sp + k_3. \tag{3.10}$$

where sp corresponds to the continuous spectral type variable. Since we are able to define the distance d from Equation 3.9, we can easily transform the previous equation to:

$$k_1 sp^2 + k_2 sp + (k_3 - d(EW_1, EW_2)) = 0. \tag{3.11}$$

---

[1] The orthogonal distance of a point (x, y) from a line $C_1x + C_2y + b = 0$ is defined as:

$$d_{pl} = (|C_1x + C_2y + C3|)/\sqrt{{C_1}^2 + {C_2}^2}.$$

In our case (see Equation 3.4) $C_1 = a$, $C_2 = -1$, and $C_3 = b$.

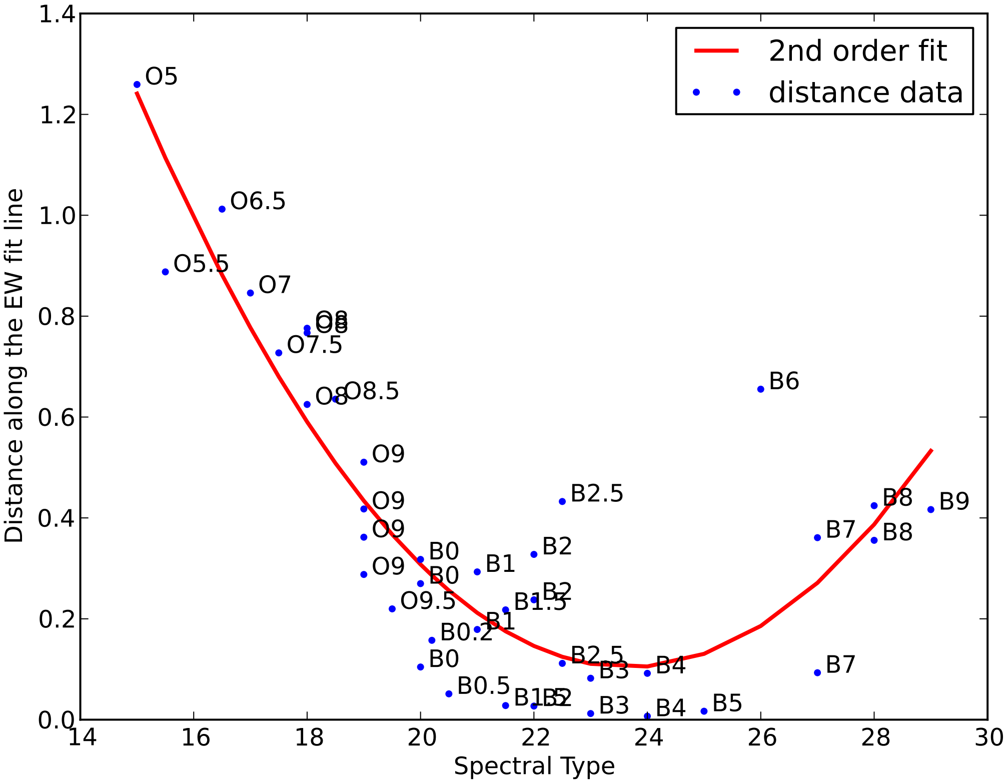

Figure 3.4: The distance d along the linear fit of the EWs for the HeII $\lambda4200$ and the HeI $\lambda4471$ lines, for the Galactic training sample, presented in Figure 3.2. We can easily see how well the distance represents the different spectral types. The red line is a 2nd order polynomial fit. (See Section 3.3.2 for details).

This is a quadratic equation, the roots of which represent two possible spectral types:

$$sp = -\frac{k_2 \pm \sqrt{k_2^2 - 4k_1(k_3 - d(EW_1, EW_2))}}{2k_1}. \tag{3.12}$$

By substituting d from Equation 3.9 we finally have:

$$sp = -\frac{k_2}{2k_1} \pm \frac{1}{2k_1}\sqrt{k_2^2 - 4k_1(k_3 - \sqrt{EW_1^2 + (EW_2 - b)^2 - \frac{(aEW_1 - EW_2 + b)^2}{a^2+1}})}. \tag{3.13}$$

The above equation gives us the capability to estimate the spectral type of a source by simply inserting the EW of the spectral lines of interest as measured directly from its spectrum, since the parameters in the equation (a, b for the EW linear fit, and k_1, k_2, k_3 for the 2nd-order fit of distance d) are defined already from fitting Equations 3.9 and 3.10 to the training samples.

3.3.3 Defining the spectral type

It is clear from Equation 3.13 that a pair of lines can give us two equally possible spectral types. Without any further constraint we are unable to discriminate between the two solutions.

However, we can overcome this limitation by including in our analysis additional spectral lines. In the scheme presented here we use 8 spectral lines (presented in Section 3.2.2 and highlighted in Table 3.2) in 4 combinations. The combinations have been selected in order to have the best discriminating power, since there are line combinations that give degenerate solutions. We present the corresponding fits of Equations 3.9 and 3.10 obtained for the SMC and the Galactic training samples in Figures 3.5-3.8 and 3.9-3.12, respectively. From these, we determined the best-fit parameters a, b, k_1, k_2, k_3 (c.f. Equation 3.13), which are presented in Table 3.3.

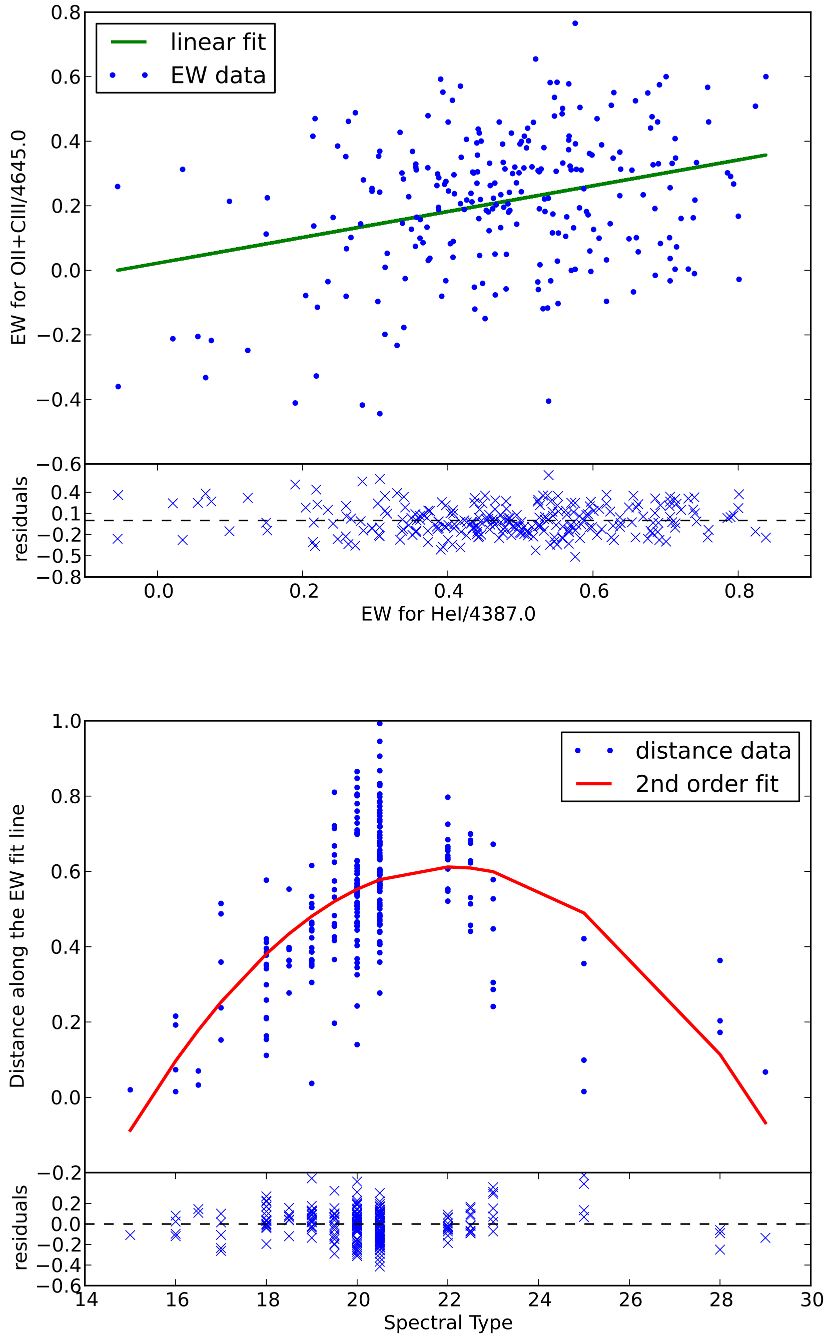

Figure 3.5: Calibration fits for the Continuous Fit method, for the SMC training sample (254 sources). Top panel: the linear fit between the EW data (in Å) for the HeI λ4387 and OII+CIII λ4640-4650 diagnostic lines. Bottom panel: the 2nd-order polynomial fit of the distance d (Equation 3.10) along the best-fit line in the top panel against the spectral type. The bottom panel in each figure shows the fit residuals.

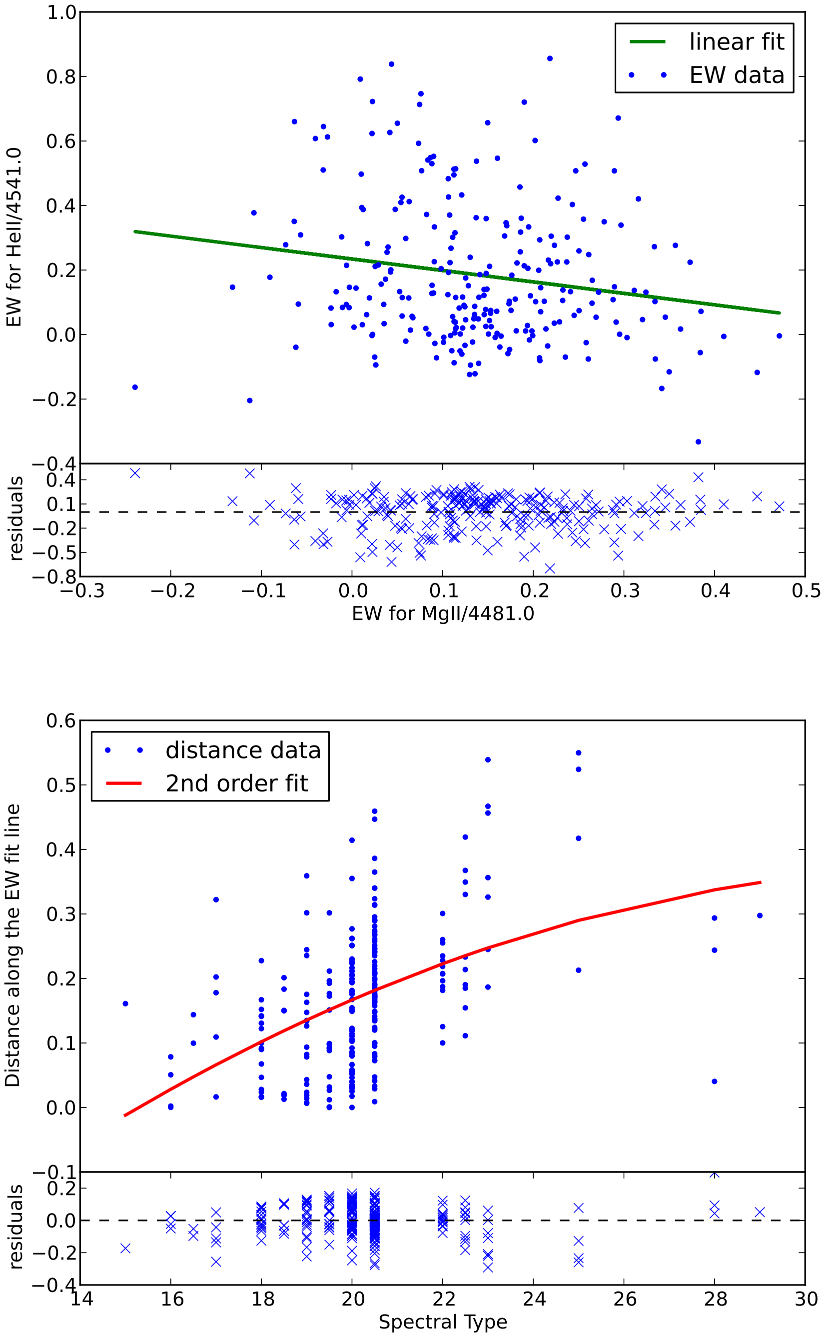

Figure 3.6: As in Figure 3.5, for the MgII $\lambda 4481$ and HeII $\lambda 4541$ diagnostic lines.

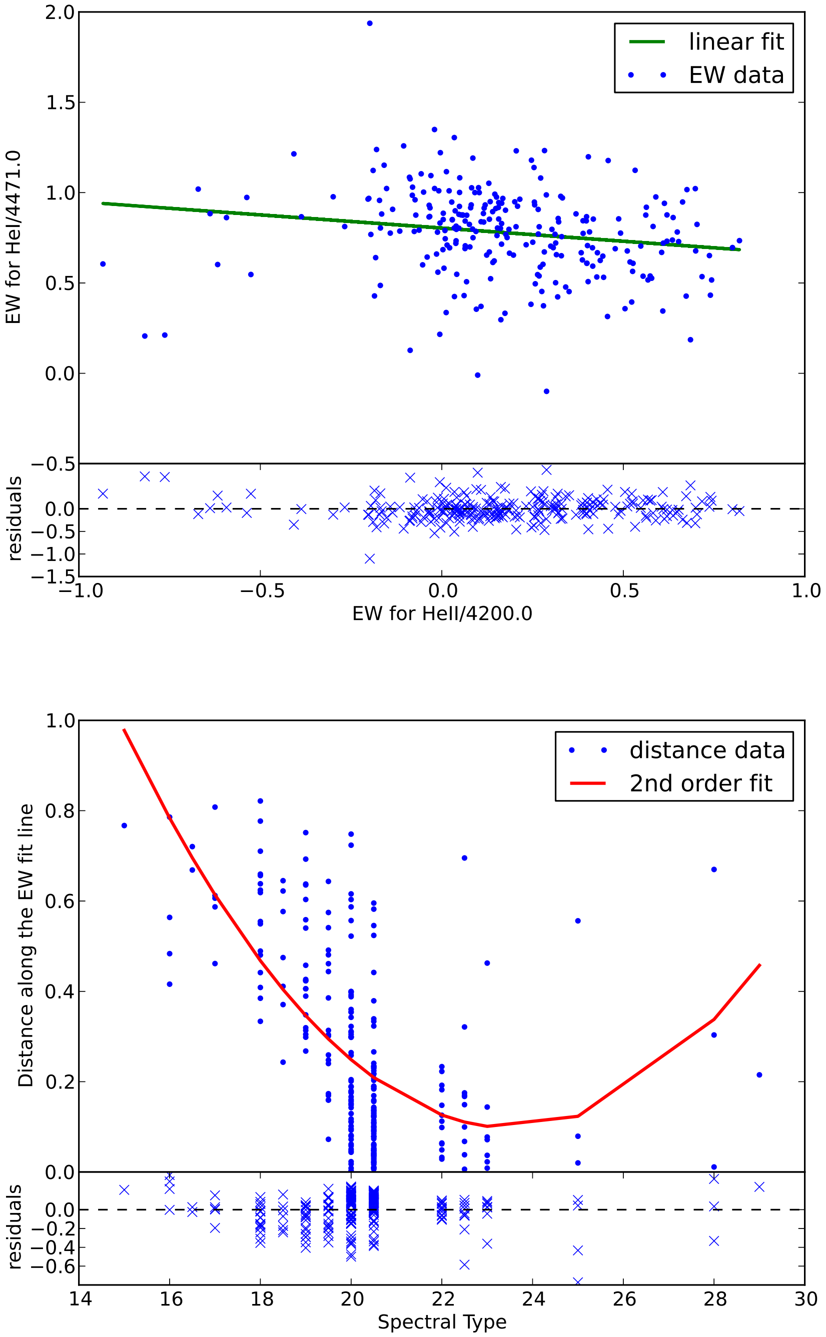

Figure 3.7: As in Figure 3.5, for the HeII $\lambda4200$ and HeI $\lambda4471$ diagnostic lines.

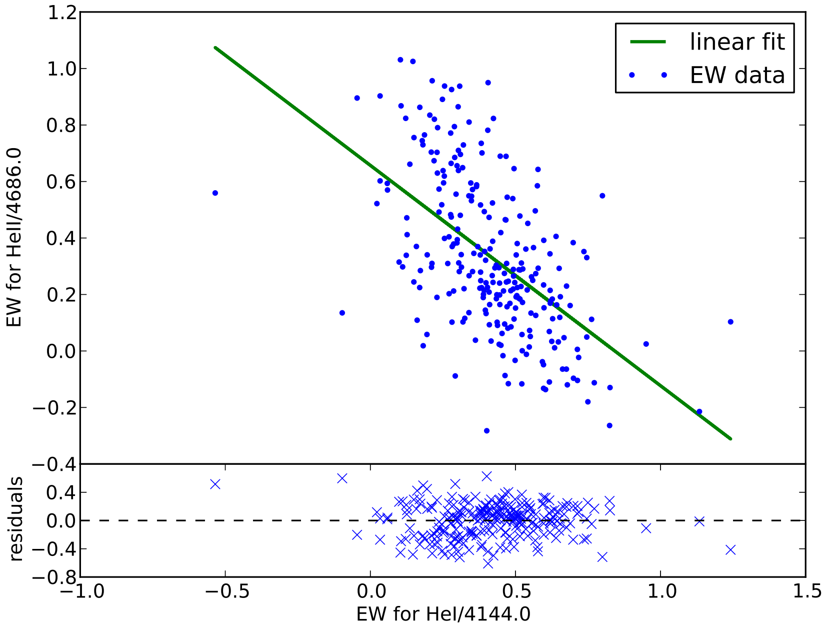

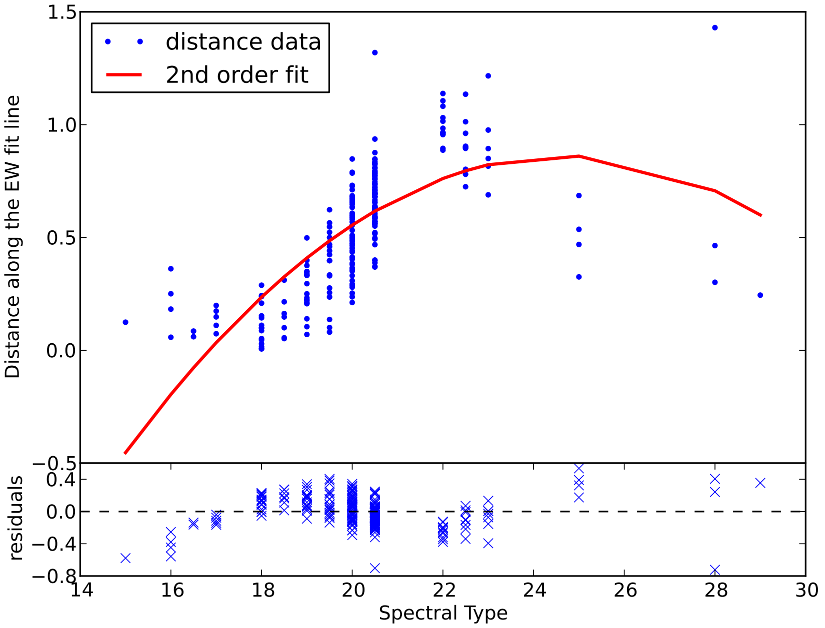

Figure 3.8: As in Figure 3.5, for the HeI $\lambda4144$ and HeII $\lambda4686$ diagnostic lines.

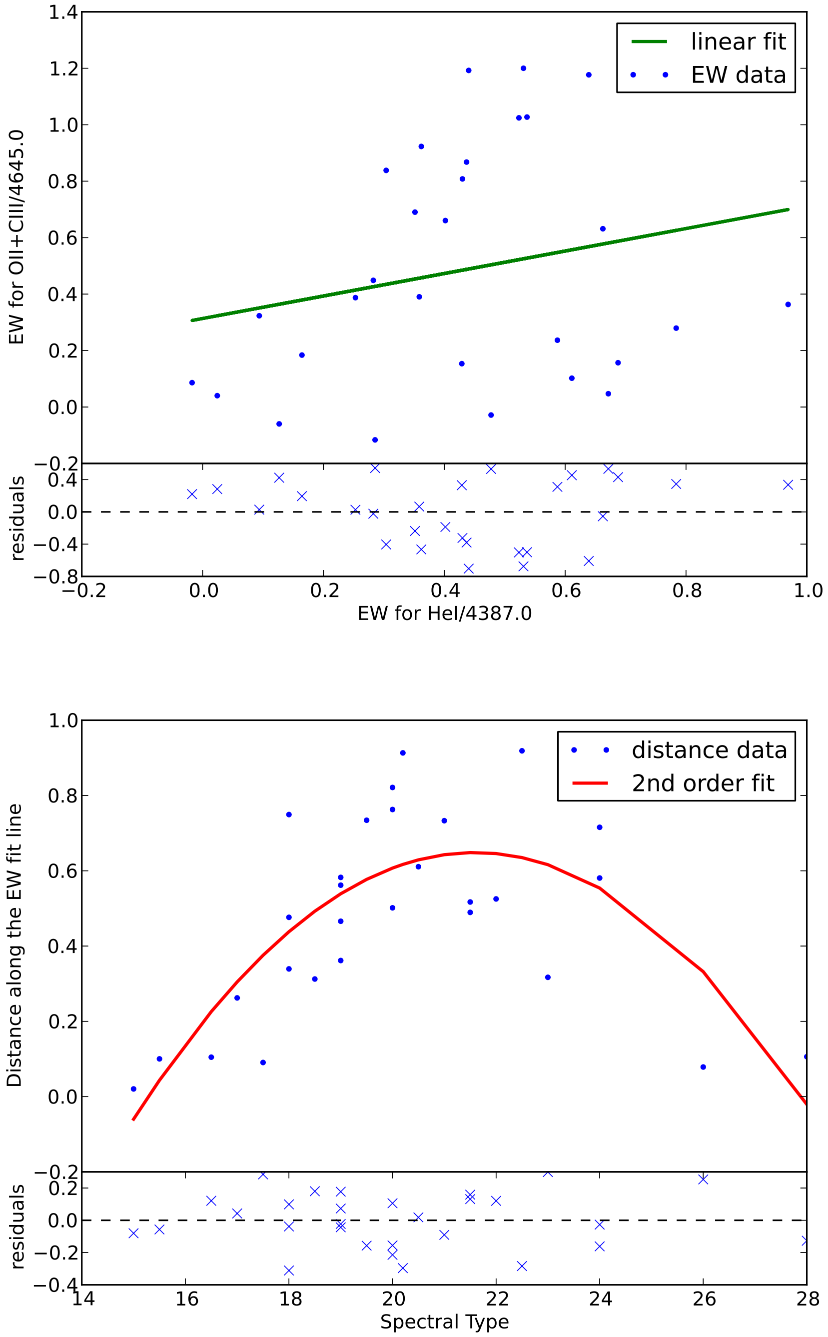

Figure 3.9: As in Figure 3.5, but for the Galactic training sample (40 sources). The comparison is between the HeI λ4387 and OII+CIII λ4640-4650 diagnostic lines.

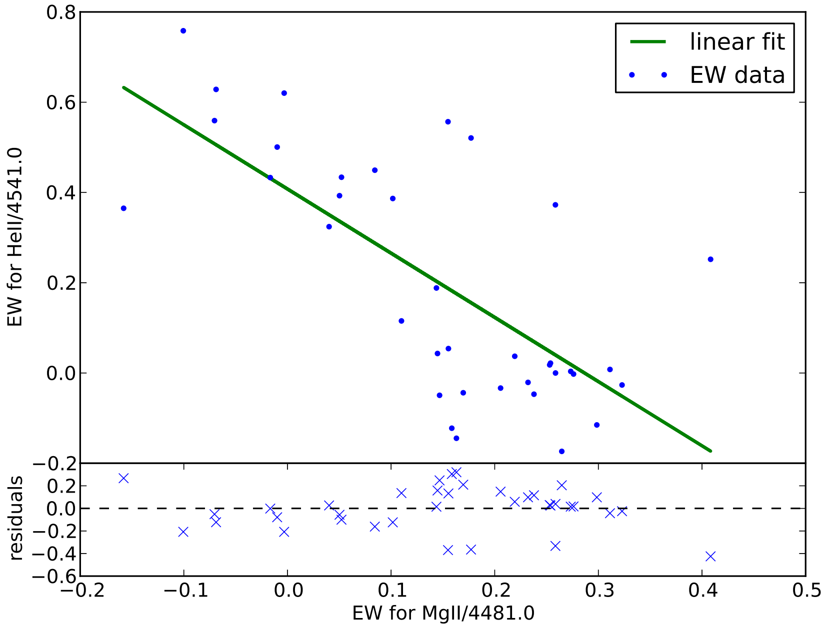

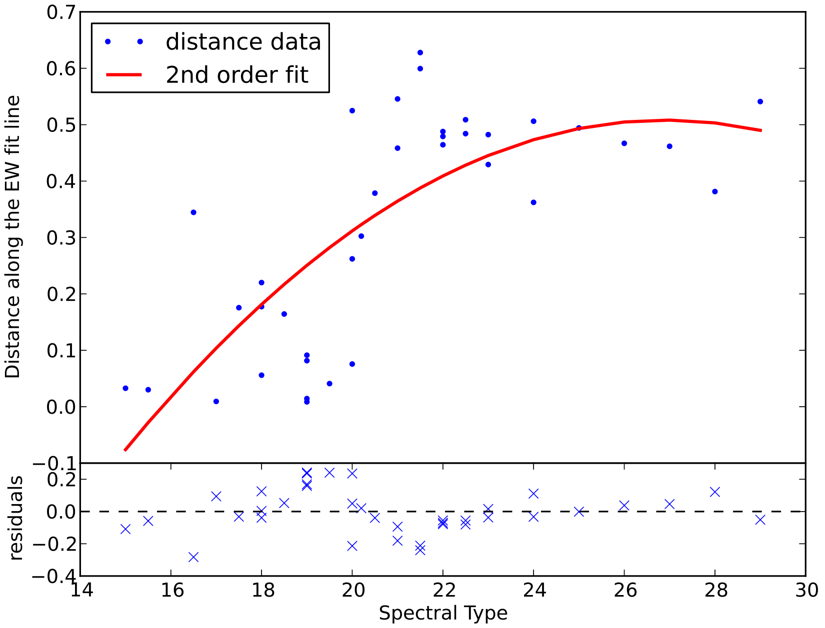

Figure 3.10: As in Figure 3.9, for the MgII $\lambda4481$ and HeII $\lambda4541$ diagnostic lines.

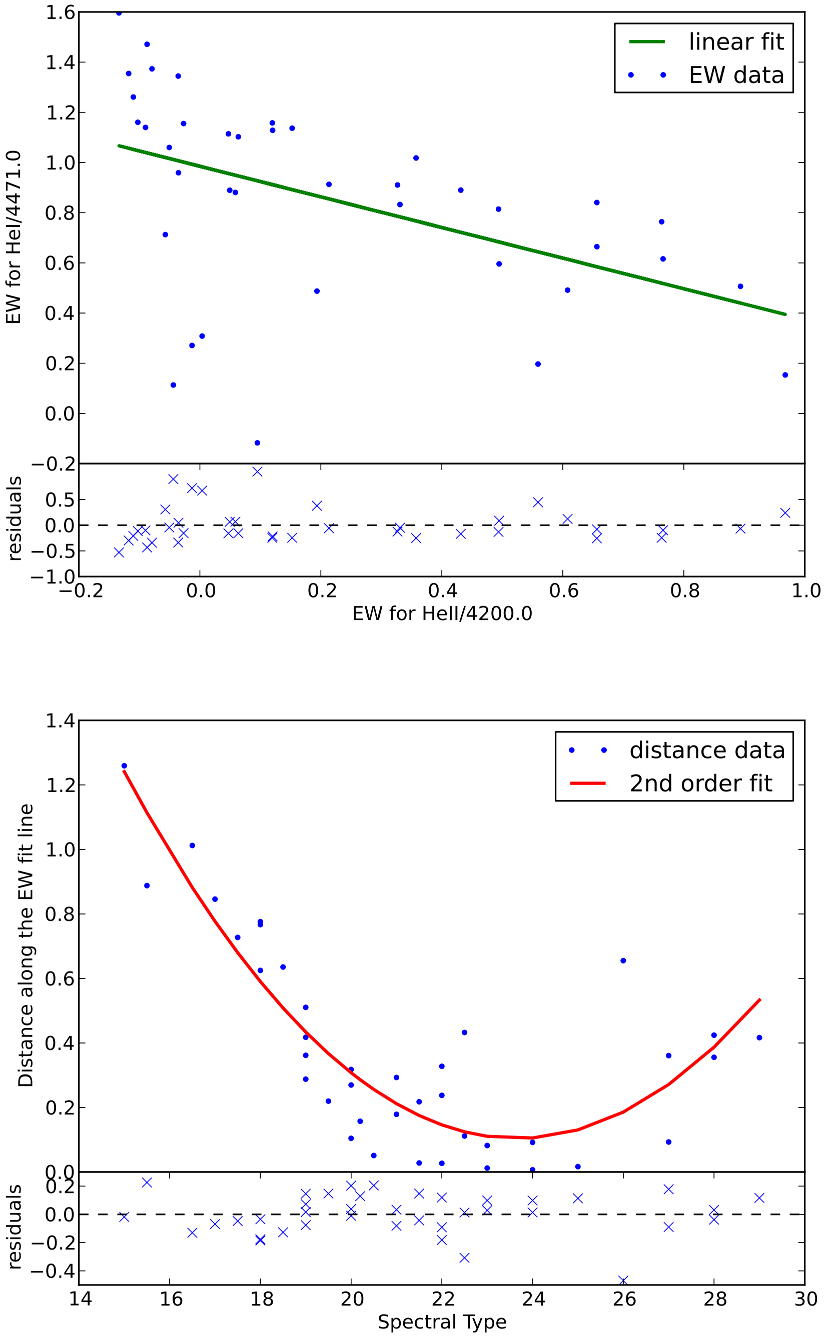

Figure 3.11: As in Figure 3.9, for the HeII $\lambda4200$ and HeI $\lambda4471$ diagnostic lines.

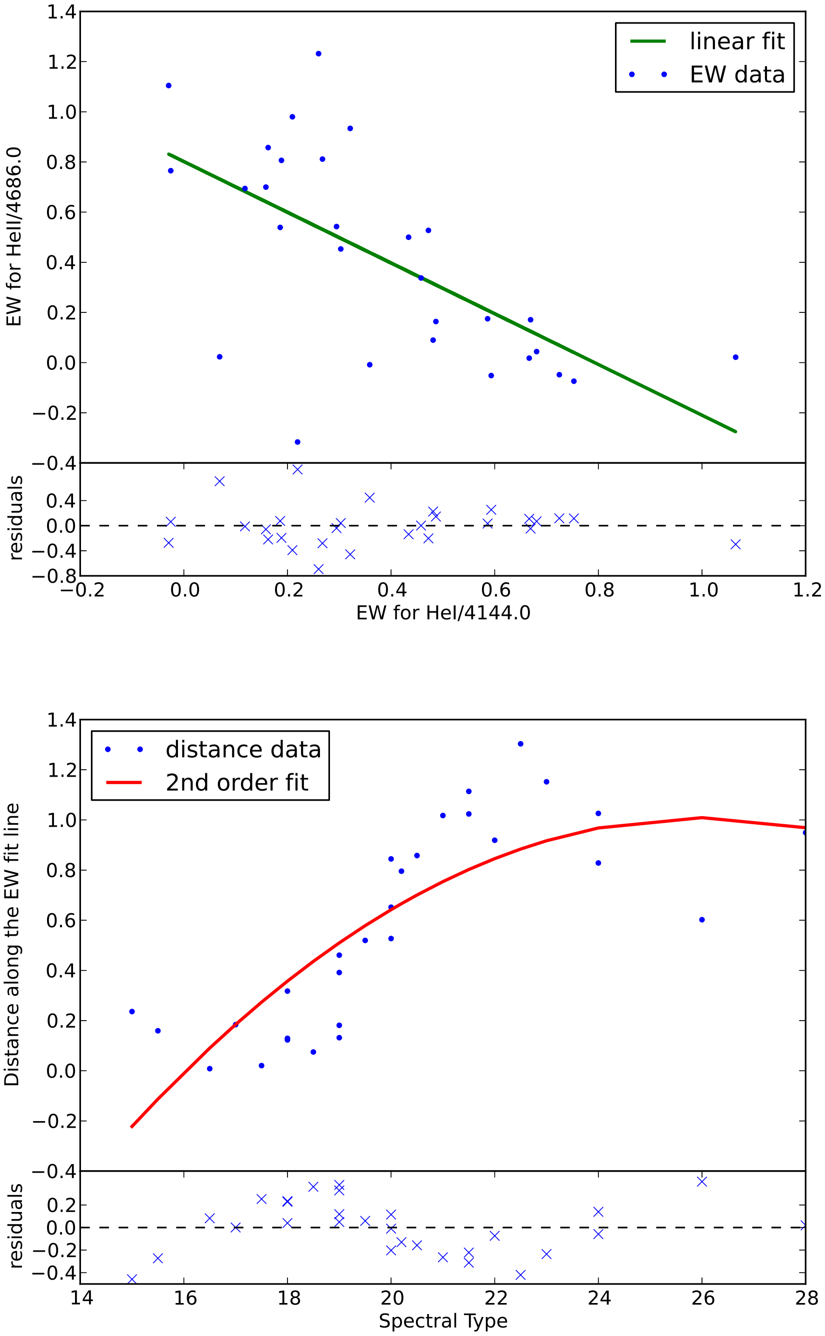

Figure 3.12: As in Figure 3.9, for the HeI $\lambda4144$ and HeII $\lambda4686$ diagnostic lines.

Table 3.3: Parameters for the Continuous Fit approach based on the SMC and the Galactic samples used.

Spectral lines (EW$_1$/EW$_2$)	Small Magellanic Cloud (a, b, k_1, k_2, k_3)	Galaxy
HeI λ4387/OII+CIII λ4645	(0.400, 0.022, -0.014, 0.621, -6.230)	(0.398, 0.314, -0.016, 0.704, -6.950)
MgII λ4481/HeII λ4541	(-0.355, 0.234, -0.001, 0.075, -0.881)	(-1.422, 0.408, -0.004, 0.222, -2.476)
HeII λ4200/HeI λ4471	(-0.146, 0.804, 0.0121, -0.568, 6.786)	(-0.610, 0.985, 0.0151, -0.716, 8.577)
HeI λ4144/HeII λ4686	(-0.780, 0.657, -0.014, 0.693, -7.691)	(-1.011, 0.802, -0.010, 0.528, -5.860)

Spectral type estimation (Equation 3.13): $sp = -\frac{k_2}{2k_1} \pm \frac{1}{2k_1}\sqrt{k_2^2 - 4k_1(k_3 - \sqrt{EW_1^2 + (EW_2 - b)^2 - \frac{(aEW_1 - EW_2 + b)^2}{a^2+1}}})$.

Application of this method to each of the 4 different pairs of diagnostic lines gives two solutions from which we have to select the most probable one. We first exclude solutions outside the region in which each diagnostic is defined. Then, we construct a list of all possible solutions[1] for each star. Since there is not a direct way to choose a single preferable value from the obtained solutions, it is reasonable to assume that the most likely spectral type will be that for which most diagnostics agree. To identify this solution and its uncertainty we follow this procedure: (i) we create all different combinations of solutions, since all different diagnostics are equivalent (ii) we calculate their numerical differences (that corresponds to spectral-type difference of the two solutions considered each time), (iii) we sort the solutions according to their difference, (iv) we select solutions with differences smaller than 4 (from the scatter of the datapoints in the training samples (e.g. see Figures 3.5 and 3.9) we deduce that the uncertainty is typically ∼2 spectral types; for some pairs of lines it could be larger, but it is counterbalanced by the other diagnostics), and if this is not possible we select the next closest solution, (v) we calculate the median value of the selected solutions. The last step gives us the final spectral type of the source, while the resulting range from step (iv) gives the uncertainty. A detailed example of the process is presented in Table 3.4.

3.3.4 Results

We tested this method by fitting separately the two training samples using the spectral-line combinations and their parameters given in Table 3.3, and selecting the most likely spectral type as described above. We plot the estimated spectral types for these sources against those determined from visual line identification methods ("real" spectral types) in Figure 3.13 (upper panel). Within the typical uncertainty of ∼2 spectral types we are able to correctly classify 72% (182 out of 254 sources) and 68% (26 out of 40 sources) of the SMC and the Galactic training samples, respectively.

It is interesting to point out that we obtain systematically similar success ratios for the two samples. The Galactic sample is almost one sixth of the SMC sample and it contains a significant number (10 sources, almost 25% of the sample) for which we do not have EWs for the OII+CIII $\lambda 4645$ and HeII $\lambda 4686$ lines, since these lines were not covered in the available spectra.

In the bottom panel of Figure 3.13 we present the classification results for the BeXRB samples in the Galaxy and SMC. The method performs almost equally well, classifying correctly within the two spectral uncertainty 58% (11 out of 19 sources) and

---

[1] Remember that the spectral types are converted to numerical values, see Section 3.3.2.

Table 3.4: An example of the solutions provided with the Continuous Fit approach for the source 2dF5044, classified as B0.5 IV by Evans *et al.* (2004).

List of all possible solutions	[23.9, 20.1, 46.9, 20.2, 28.4, 20.9]
Pair of solutions	Difference
(20.1, 20.2)	0.1
(20.2, 20.9)	0.7
(20.1, 20.9)	0.8
(23.9, 20.9)	3.0
(20.2, 23.9)	3.7
(20.1, 23.9)	3.8
(28.4, 23.9)	4.5
(20.9, 28.4)	7.5
(20.2, 28.4)	8.2
(20.1, 28.4)	8.3
(28.4, 46.9)	18.5
(23.9, 46.9)	23.0
(46.9, 20.9)	26.0
(20.2, 46.9)	26.7
(46.9, 20.1)	26.8
List of most probable solutions	[20.1, 20.2, 20.9, 23.9]
Median value ± error	20.6 ± 1.9
Spectral type	**B0.6**
Uncertainty range	**O8.7-B2.5**

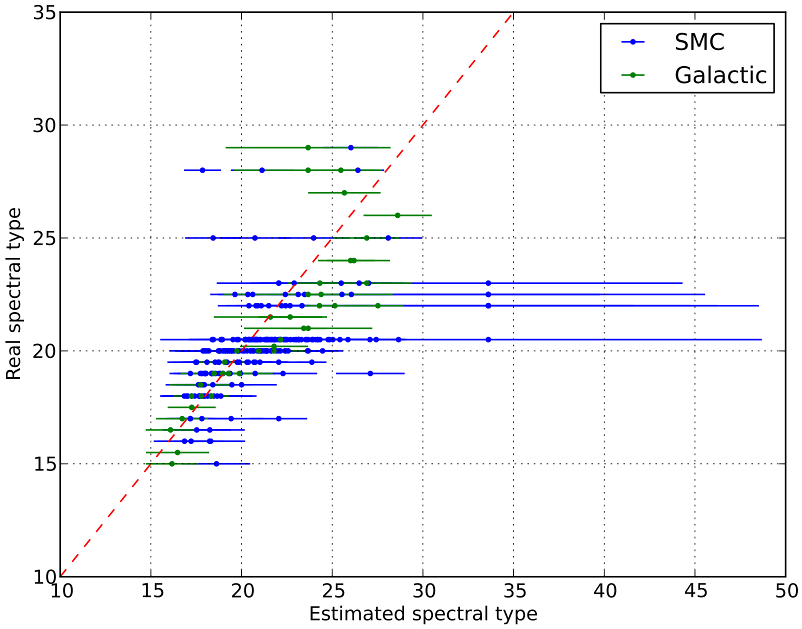

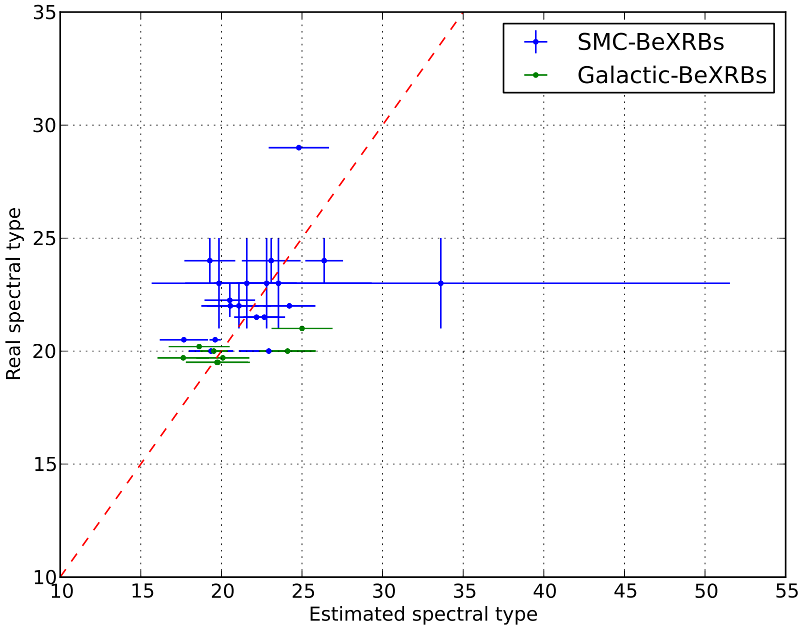

Figure 3.13: A plot of the "real" spectral types of stars in the SMC (blue) and the Galaxy (green) plotted against the spectral types determined from the Continuous Fit approach. The spectral types are represented by integers, with numbers between 10-19 corresponding to O stars and numbers between 20-29 corresponding to B stars (e.g. '18' corresponds to O8-type, while '22.5' corresponds to B2.5-type). The red-dashed line represents the 1-to-1 correlation. We see that the spectral types determined from the Continuous Fit approach agree well with the spectral types determined from detailed visual classification.

63% (5 out of 8 sources) of the SMC and the Galactic BeXRBs, respectively.

These results are consistent with the errors in spectral classification obtained with the Artificial Neural Networks applied by von Hippel et al. (1994a) (~2 spectral types) and Navarro et al. (2012) (~2-3 spectral types). However, we have to acknowledge that these works study a much wider range of spectral types.

3.4 The Naive Bayesian approach

3.4.1 Naive Bayes Classifier

In the previous sections we described a method to classify spectra based on a physical parameter (temperature) that drives the different spectral features used as diagnostics. However, the same features can be also treated statistically, and the different diagnostics can be derived from the statistical distributions of these features in the sample spectra. Moreover, in such a scheme data of diverse types may be combined to improve the diagnostics. For example, Broos et al. (2011) have applied the Naive Bayes Classifier to classify X-ray sources in the Carina region, combing information from optical and X-ray spectra, near- and mid-IR brightness, and the spacial distribution of sources. Next, we describe the Naive Bayes Classifier (Zhang, 2004) and its application to the spectral classification of stars.

Bayes' theorem (e.g. Wall & Jenkins 2012) provides us with a tool to quantify how the probability of an event B changes under the knowledge of data A. If our knowledge of the probability of an event before performing an experiment is $p(B)$ (the *prior probability*), and an experiment is designed so that the probability of obtaining data A given the event B is $p(A \mid B)$ (the *likelihood*), then the final probability of the event given the data $p(B \mid A)$ (the posterior probability) is:

$$p(B \mid A) = \frac{p(A \mid B)p(B)}{p(A)} \tag{3.14}$$

where $p(A)$ is the probability of the data (usually a normalization factor).

If the event B is a set of discrete classes B_j in which an object may belong to, then based on the data A from an experiment we can calculate the probability that this object belongs to a certain class if we know the probability distribution of the data for each class $p(A \mid B_j)$. If there are N features that can be used for this classification then these probabilities can be combined to provide the likelihood that the object belongs to each class B_j:

$$p(A_1, A_2, ..., A_N \mid \text{class} = B_j) \tag{3.15}$$

The Naive Bayes Classifier (Zhang, 2004) simplifies the estimation of the joint likelihood, as it assumes that all features are statistically independent, i.e. the presence or absence of any feature does not affect others. This is a valid assumption in our case since the diagnostic lines are well separated. In this case we can rewrite Equation 3.15 for each class B_j as:

$$\begin{aligned} &p(A_1, A_2, ..., A_N \mid \text{class} = B_j) \\ &\qquad = p(A_1 \mid \text{class} = B_j) p(A_2 \mid \text{class} = B_j) \cdots p(A_N \mid \text{class} = B_j) \\ &\qquad = \prod_{i=1}^{N} p(A_i \mid \text{class} = B_j). \end{aligned} \tag{3.16}$$

The meaning of this equation is that the likelihood of an object belonging to the class B_j is the product of the probability for each diagnostic feature A_i conditioned on the class B_j. This method can be applied in our case of spectral-type classification of stars.

In this case, the available data A_i are the EW measurements performed for the diagnostic spectral lines presented in Section 3.2.2 (also highlighted in Table 3.2), while the classes B_j in which our sources are classified are the spectral types O5-B9 (15 classes). The independence of these measurements is true for all of the diagnostic spectral lines used.[1]. Thus, the likelihood for a star of a given spectral type to have a set of EWs for a series of diagnostic spectral lines is found from Equation 3.16, and can be written as:

$$\begin{aligned} \mathcal{L} &= p(EW_1, EW_2, ..., EW_n \mid \text{spectral type}) \\ &= p(EW_1 \mid \text{spectral type}) p(EW_2 \mid \text{spectral type}) \cdots p(EW_n \mid \text{spectral type}) \\ &= \prod_{i=1}^{n} p(EW_i \mid \text{spectral type}). \end{aligned} \tag{3.17}$$

where n is an index that runs through the available spectral lines. If for any reason (e.g. insufficient wavelength coverage) a line is missing we can simply ignore that line from the calculation of the likelihood.

In order to estimate these likelihoods we need to define the probability distribution $p(EW_i \mid \text{spectral type})$ of EWs for a given line for a spectral type. Thus, based on the line measurements for the SMC training sample we produced histograms of the line EW measurements for different spectral types, which give us the likelihood to measure a

---

[1] Independence refers to the data/measurements. The presence of certain spectral lines is always associated with the presence or absence of others (e.g. the HeII λ4200 and HeII λ4686 for O-type stars are always present at the same time), which implies the underlying physical model we are looking for.

certain value of EW for each spectral type. The definition of these empirical likelihood functions is presented in Section 3.4.2.

According to Bayes' theorem (Equation 3.14) we have to assign a prior probability for each spectral type. As we do not have any initial preference for any spectral type we opted to assign the same prior probability to all spectral types ($p(\text{spectral type}) = 0.067$), i.e. to divide the probability equally to all 15 examined spectral types within the O5-B9 range.

Finally the posterior probability for each spectral type given the measurements of EW$_i$ for n spectral lines will be the product of the prior and the likelihood probability defined in Equation 3.17:

$$p(\text{spectral type} \mid EW) = \frac{\prod_{i=1}^{n} p(EW_i \mid \text{spectral type})}{\sum_{j=\text{O5}}^{\text{B9}} p(\text{spectral type}_j \mid EW)} p(\text{spectral type}) \tag{3.18}$$

where the denominator is the normalization factor, equal to the sum of all probabilities.

3.4.2 Likelihoods

Regarding the calculation of the likelihood of the measured EWs given a specific spectral type (see Equation 3.17), we first need to calculate the probability density function (PDF) of the EW for each diagnostic spectral line for a given spectral type or range of spectral types. For this, we build the normalized histograms of the EWs for each diagnostic spectral line (Figures 3.14 - 3.20), where the bin size is determined based on the number of available sources ($N_{\text{bins}} = \sqrt{n_{\text{sources}}}$, rounded to its integer part; Montgomery & Runger 2010, pg. 204). Then, the PDF for each line and each spectral type is:

$$p_{\text{bin}} = \frac{N_{\text{bin sources}}}{N_{\text{total sources}}} \tag{3.19}$$

where $N_{\text{bin sources}}$ is the number of sources with EWs within this bin, and $N_{\text{total sources}}$ is the total number of sources used in the histogram for each spectral line and each spectral type or range of spectral types.

In order to have sufficient number of sources to build the PDFs, when there were not enough sources within a spectral type, we grouped sources from adjacent spectral types[1]. When sufficiently large numbers of sources were available we split spectral types to 0.5 spectral type ranges (applicable to O8- to B3-type sources from the SMC sample).

---

[1] We use the following notation: a spectral type range Bx-By means that stars of spectral type Bx and any between Bx and By are included but not stars of type By (i.e. the range [Bx,By)).

Because of the much larger number of sources with available spectral classification for the SMC (Evans et al., 2004) we initially built the Naive Bayesian Classifier based on SMC stars. However, we note that due to the metallicity difference between the SMC and the Galaxy there might well be differences in the PDFs for stars in the SMC and the Galaxy.

We set a limit of EW>0.2 Å for the presence of a spectral line. Any spectral lines that have lower EW are considered too weak and they are not included in the calculation of the likelihood. This limitation could be alleviated by including measurement uncertainties in the considered EWs. However, since most of the training spectra used in the definition of the diagnostic are normalized we cannot calculate these uncertainties.

Unfortunately, this leads to loss of important information when the absence of a spectral line is a constraint of the spectral type itself (e.g. the absence of HeII lines is indicative of a later than B1 source). For these cases we can set the minimum EW for a diagnostically important line, below which we can rule out a range of spectral types based on the lack of that spectral line. This limiting EW is defined as the average EW from the PDF of the adjacent spectral type or spectral range for which the spectral line is clearly present.

Additionally, there were a number of cases that we had to treat separately, when defining the PDFs for the spectral line EW for each spectral type:

- HeI λ4471 for O8-O8.5 and B0-B0.5: Due to the binning scheme and the small number of sources there are EW bins with zero probability, in between bins with non-zero probabilities. As it is unnatural to think of a PDF that drops to zero for a bin and raises again in the next one, we split the probability of the non-zero bin equally between that and the zero probability bin (this is equivalent to smoothing slightly the PDF).

- HeI λ4471 for B8-B9, HeI λ4387 and MgII λ4481 for B5-B6: These spectral type ranges contain only a couple of sources, resulting in only one EW bin (with a probability value of 1). As this distribution is rather unnatural, we tapered it by including a bin with a probability of 10% in either side (and re-normalizing accordingly the central bin). An exception was made only for the HeI λ4471 line which was expanded only to higher values, since it is already close to our hard low-limit value of 0.2Å for a non-detection, as the tendency of this line is to disappear in late B-type stars.

- HeI λ4471 for B1-B2,B4-B5 and B6-B8, HeI λ4387 for B1-B2 and B4-B5, MgII λ4481 for B1-B2 and B4-6: Unfortunately, for none of the sources in the training sample for these spectral types was possible to measure the HeI λ4471 and λ4387, or the MgII λ4481 lines. To compensate for this we calculated the relevant probability distributions by interpolating from the available distributions for the adjacent spectral types, following these steps: (i) identify the lowest and the highest EW values of the PDFs of the same line for the adjacent spectral types, (ii) split this range into 3 or 4 bins, (iii) assign probability values to each bin by interpolating between the probabilities of the corresponding bins in the adjacent distributions.

- OII+CIII λ4640-4650 for B1-B3 and later than B3 types: The blend is present in late O-type stars and up to B1.5 but decreases rapidly after that. It was not possible to measure this line in any of the sources in our training sample with a spectral type later than B1. Since we know that there is a non-zero probability to observe this line within the B1-B3 (Evans et al., 2004; Walborn & Fitzpatrick, 1990) range we built this distribution as follows: (i) using the PDF of B0.5-B1 we determined the maximum EW value; the minimum EW coincides with our hard low-limit (0.2Å), (ii) we split the distribution to three bins with probability values the resemble the PDF of the B0.5-B1 distribution by adding 10% more for the smaller EW values (since the tendency for the spectral line is to disappear).

Since we have defined the probability distribution for the diagnostic lines for all spectral types we can now use Equation 3.17 to calculate the probability $p(EW_i \mid \text{spectral type}_j)$ for each spectral line. For any line with EW$<$ 0.2 Å the probability assigned is 0 (actually a very small number, 10^{-6}, to allow further computations), since this is our line "detection limit". If the EW examined is greater than our hard low-limit but not found within the range of the relevant PDF, then it is also assigned a probability of 10^{-6}. If the measured EW is within the range of the relevant PDF we obtain the corresponding probability. Since the width of the EW bins is different between different spectral types we divide the assigned probability by the width of the corresponding EW bin. This allows us to compare different spectral types in a consistent way. In any other case, the spectral line examined is excluded for the final calculation of the likelihood.

Having defined these likelihoods we can use the Naive Bayes Classifier (Equation 3.18) to calculate the posterior probability distribution of the spectral types for each source. An example of these calculations is presented in Table 3.5.

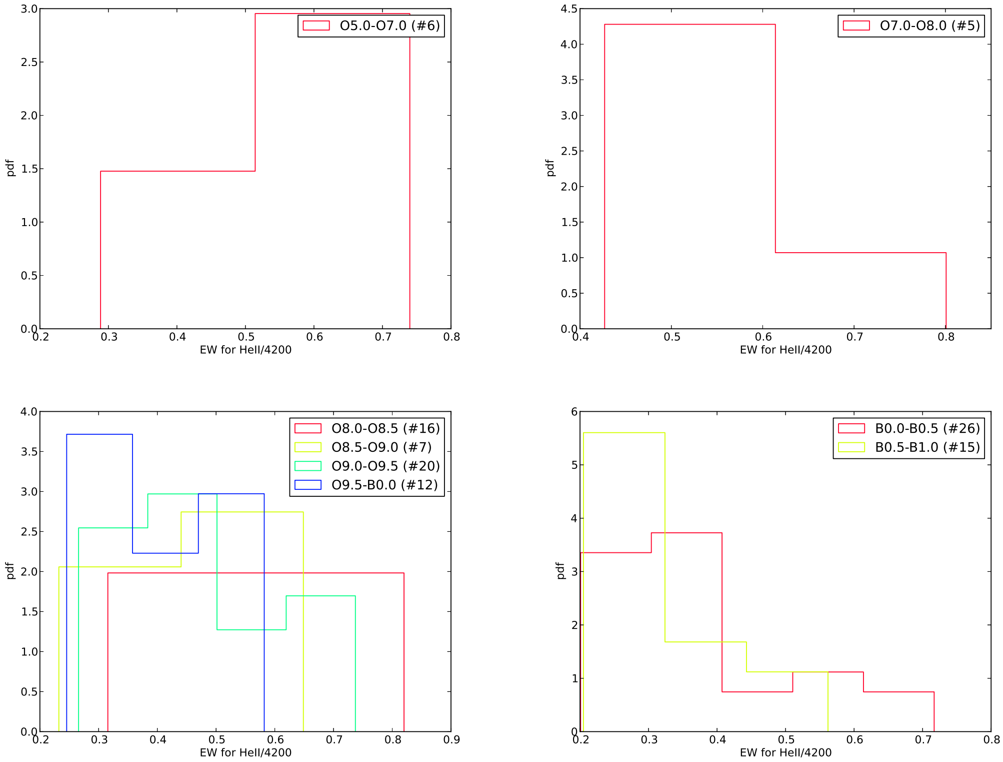

Figure 3.14: Histograms of the Probability Density Function (PDF) per spectral type bin. The spectral type(s) for each histogram are indicative in the label insert. The number in parentheses for each label gives the available number of sources for the particular spectral type/range. Data for the HeII λ4200 line.

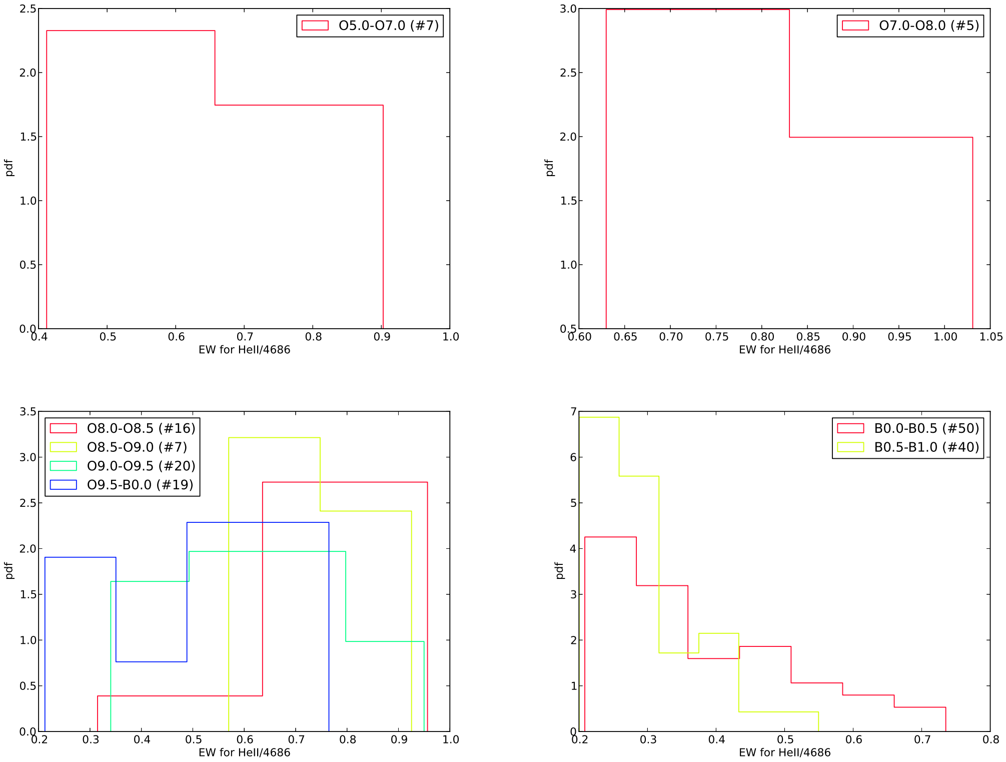

Figure 3.15: As in Figure 3.14, for HeII $\lambda4686$ line.

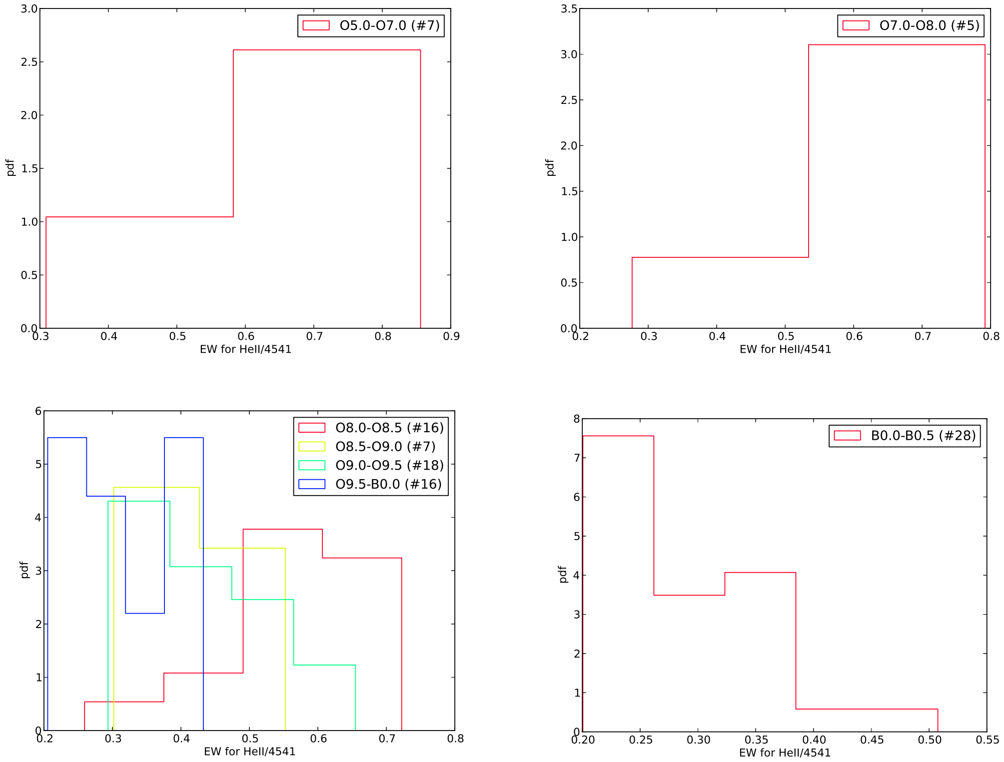

Figure 3.16: As in Figure 3.14, for HeII $\lambda4541$ line.

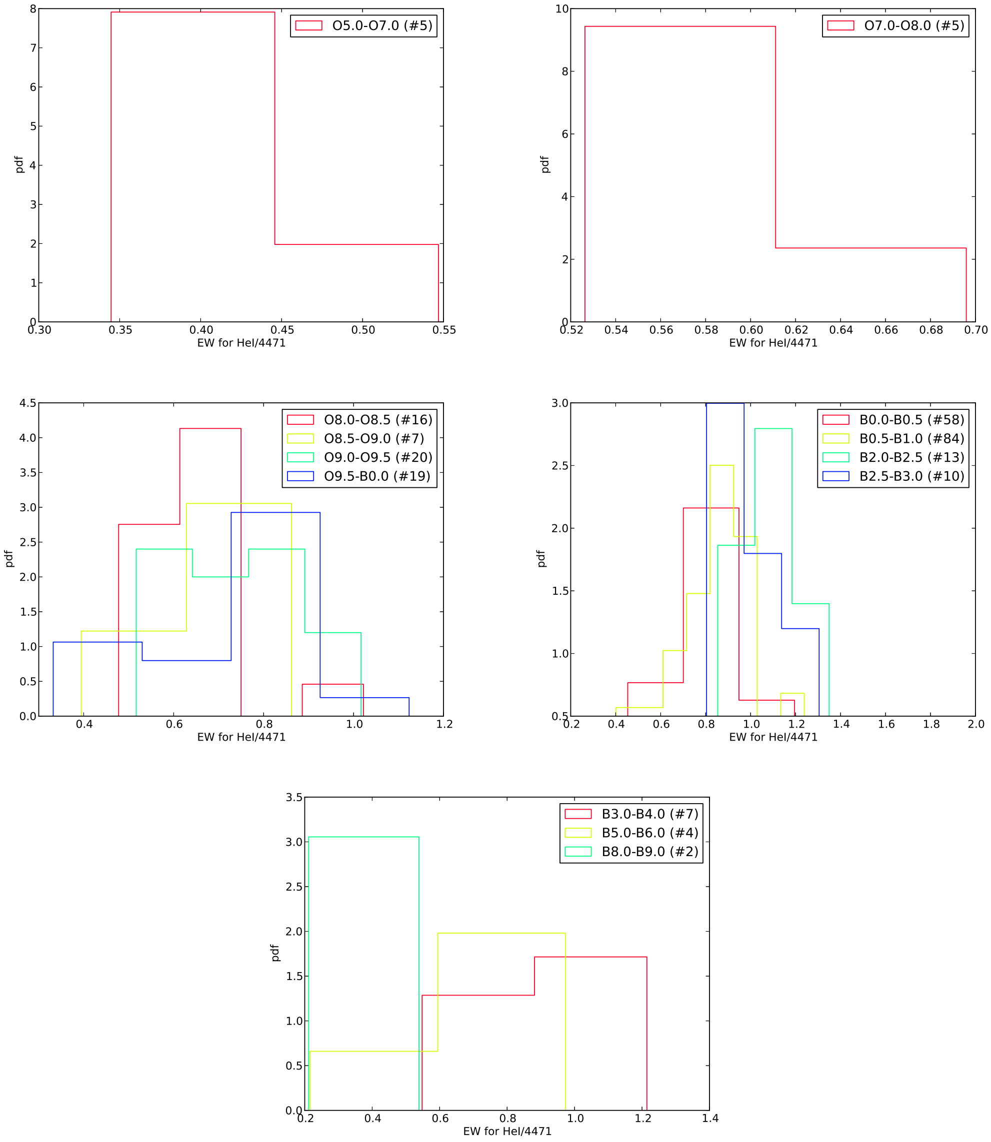

Figure 3.17: As in Figure 3.14, for HeI λ4471 line.

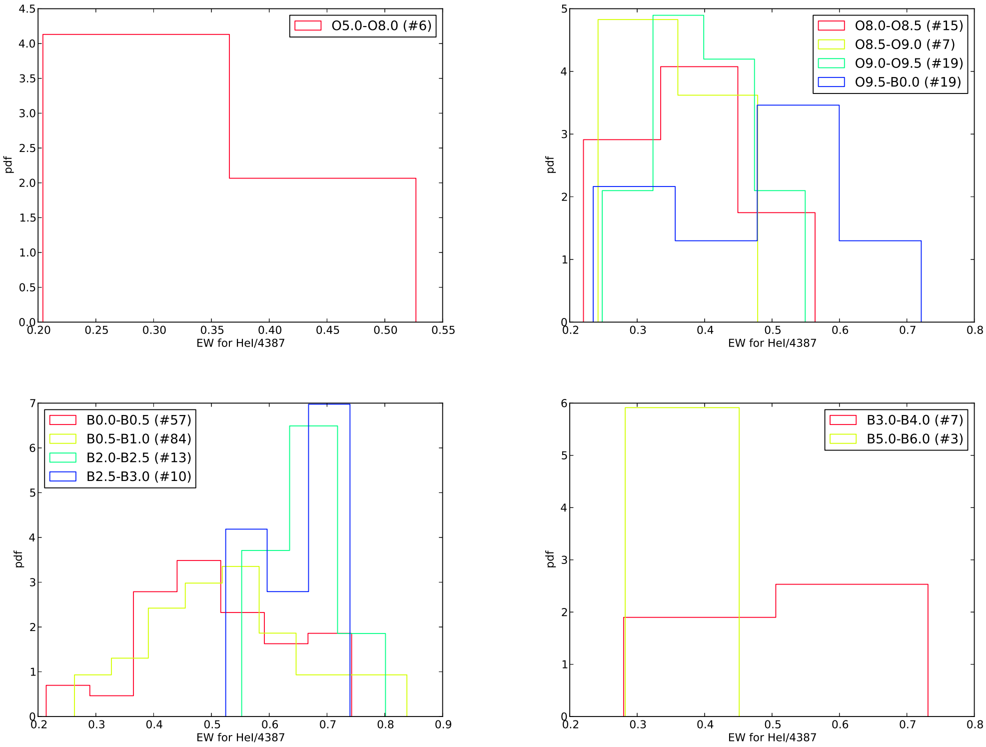

Figure 3.18: As in Figure 3.14, for HeI λ4387 line.

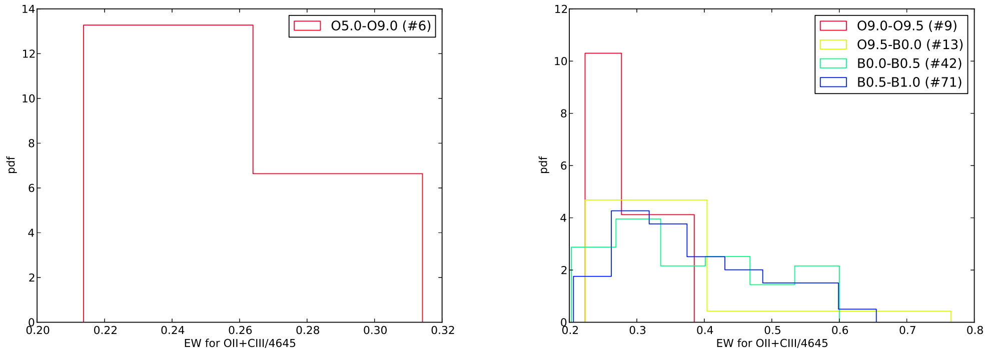

Figure 3.19: As in Figure 3.14, for OII+CIII λ4645 line.

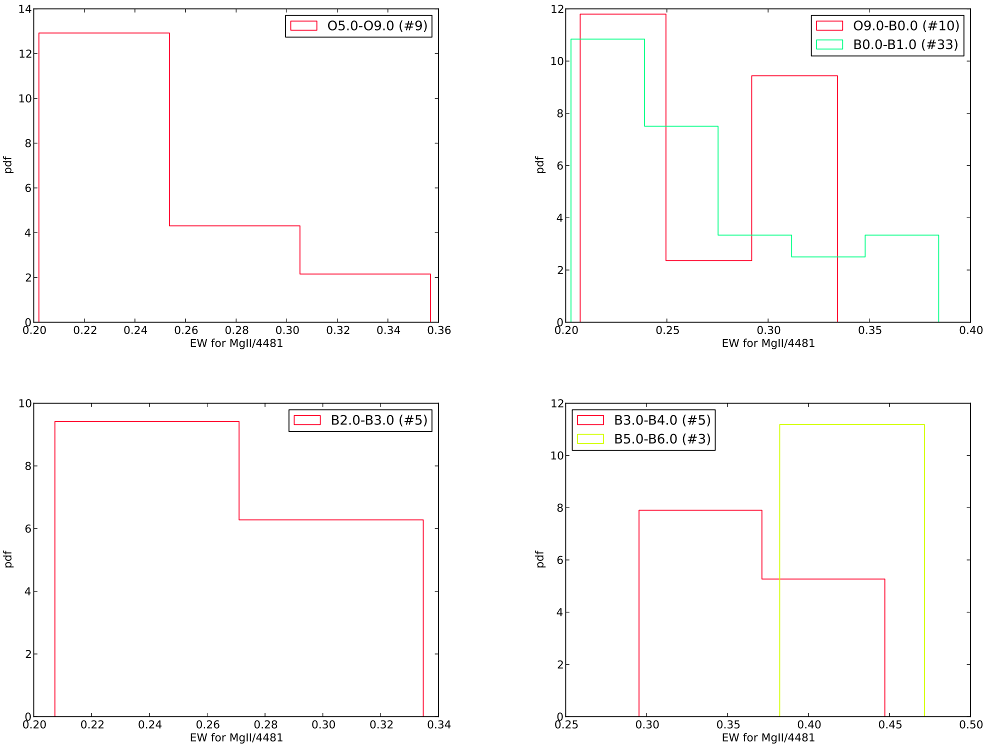

Figure 3.20: As in Figure 3.14, for MgII λ4481 line.

Table 3.5: An example of the calculated likelihoods for source HD 93028 classified as O9 V (Walborn & Fitzpatrick, 1990).

Classifier	Probability[1]							Likelihood	Posterior[2] probability
	HeI 4471	HeII 4686	HeII 4541	MgII 4481	OII+CIII 4640-50	HeI 4387	HeII 4200		
O5	10^{-6}	0.285	0.142	10^{-6}	10^{-6}	0.222	0.166	1.51×10^{-21}	2.60×10^{-07}
O6	10^{-6}	0.285	0.142	10^{-6}	10^{-6}	0.222	0.166	1.51×10^{-21}	2.60×10^{-07}
O7	10^{-6}	10^{-6}	0.2	10^{-6}	10^{-6}	0.222	10^{-6}	4.44×10^{-32}	7.65×10^{-18}
O8	0.857	0.062	0.276	10^{-6}	10^{-6}	0.447	0.339	2.25×10^{-15}	0.387
O9	0.439	0.307	0.277	10^{-6}	10^{-6}	0.263	0.358	3.54×10^{-15}	0.610
B0	0.398	0.052	0.035	10^{-6}	10^{-6}	0.059	0.292	1.29×10^{-17}	0.0022
B1	0.8	10^{-6}	10^{-6}	10^{-6}	10^{-6}	0.1	10^{-6}	8×10^{-32}	1.37×10^{-17}
B2	0.5	10^{-6}	10^{-6}	10^{-6}	10^{-6}	10^{-6}	10^{-6}	5×10^{-37}	8.60×10^{-23}
B3	0.428	10^{-6}	10^{-6}	10^{-6}	10^{-6}	0.428	10^{-6}	1.83×10^{-17}	3.16×10^{-17}
B4	1.0	10^{-6}	10^{-6}	10^{-6}	10^{-6}	10^{-6}	10^{-6}	1×10^{-36}	1.72×10^{-22}
B5	0.75	10^{-6}	10^{-6}	10^{-6}	10^{-6}	1.0	10^{-6}	7.5×10^{-31}	1.29×10^{-16}
B6	0.5	10^{-6}	10^{-6}	10^{-6}	10^{-6}	99.0	10^{-6}	4.95×10^{-29}	8.56×10^{-15}
B7	0.5	10^{-6}	10^{-6}	10^{-6}	10^{-6}	99.0	10^{-6}	4.95×10^{-29}	8.56×10^{-15}
B8	10^{-6}	10^{-6}	10^{-6}	10^{-6}	10^{-6}	99.0	10^{-6}	9.9×10^{-35}	1.71×10^{-20}
B9	10^{-6}	10^{-6}	10^{-6}	10^{-6}	10^{-6}	99.0	10^{-6}	9.9×10^{-35}	1.71×10^{-20}

[1] $[p(\text{spectral class} \mid EW)]$

[2] (Prior × likelihood) / Normalization , where:

Prior = 0.067 (see Section 3.4.1)

Normalization = $[\sum_{j=\mathrm{O5}}^{\mathrm{B9}} p(\text{spectral class}_j \mid EW)] = 3.872 \times 10^{-16}$

3.4.3 Results

In order to test the method we applied the Naive Bayes Classifier on the two training samples. The results are presented in Figure 3.22 (top panel), where we plot the estimated spectral types as obtained from the classifier against those from visual classification ("real" spectral types). The estimated spectral type is determined by the spectral type for which we have the highest probability density. Following Broos et al. (2011) we first sort all spectral types according to their probabilities and we accept only those for which their probability is less than 50% of the probability of the previous type. From the accepted spectral types we selected the minimum and maximum values (earliest and latest spectral types) to represent the range of accepted spectral types, and determine actually the uncertainty in the spectral-type estimation (see Figure 3.21).

We are able to correctly classify 85% (215 out of 254 sources) of the SMC training sample, while we recover 45% (18 out of 40 sources) of the Galactic training sample. The rather poor result obtained for the Galactic training sample is not totally unexpected, as it reflects the inability of the classifier to correctly classify the late B-type stars. The training of the classifier was based on the most numerous sample, which is the SMC training sample (254 sources). This sample is strongly biased towards early B-type stars, which results in poor determination of the $p(EW_i \mid \text{spectral type})$ for the diagnostic lines of later type stars. In the SMC training sample there are only 8 sources out to 254 ($\sim$ 3%) with spectral types later than B4, while in the Galactic training sample we have 8 sources out of 40 sources (20%). In addition, for the few SMC B8- and B9-types stars (3 sources) the measurements of the MgII line EW are not very accurate because of the noisy spectra.

By applying this method to our test samples of BeXRBs we obtained correct classifications for 32% (6 out of 19 sources) and 75% (6 out of 8 sources) of the SMC and the Galactic BeXRB samples, respectively. These classification results are presented in the bottom panel of Figure 3.22. We notice a striking difference between the success ratios obtained for the training and test samples. However, this can be attributed again to the presence of late-type sources. The Galactic BeXRB sample consists mainly by early (O9 to B1) type sources, while the SMC BeXRB sample is skewed to later type sources, coupled with rather large uncertainty errors (typically B1-B5 or B3-B5; Maravelias et al. 2014). Therefore, the classifier is able to classify correctly most of the Galactic but not all the SMC BeXRBs.

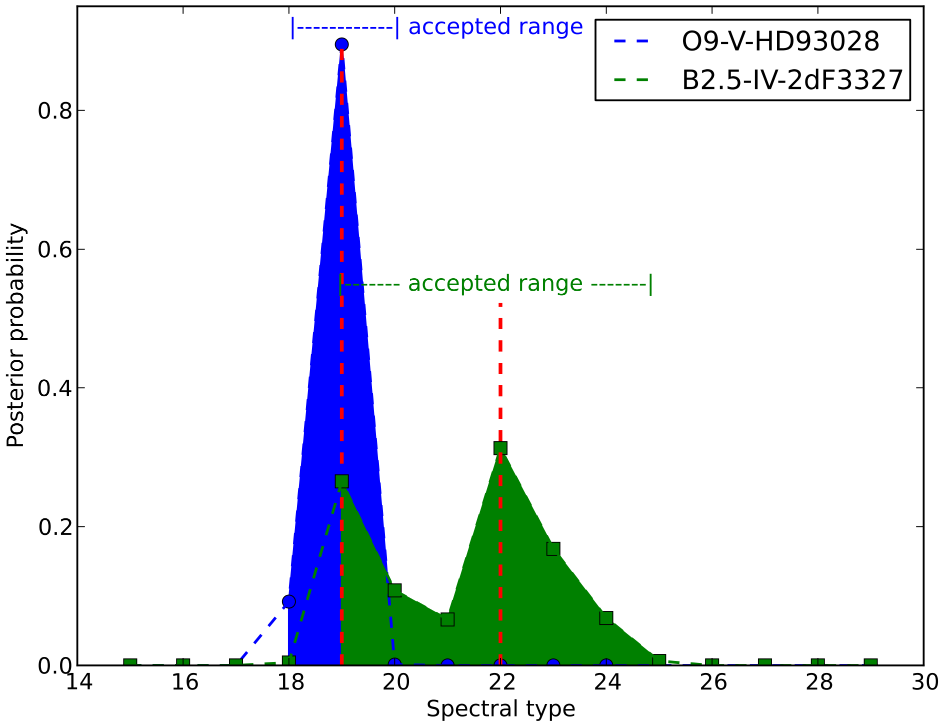

Figure 3.21: A plot of the posterior probability distributions with respect to the spectral types, for HD 93028 (blue) classified as O9 V (Walborn & Fitzpatrick, 1990) and 2dF 3327 (green) classified as B2.5 IV (Evans et al., 2004). The filled regions show the accepted spectral-type ranges, according to the decision procedure followed (see Section 3.4.3). The most probable values are shown as red dashed lines and the uncertainty ranges are given by the accepted spectral types indicated by the filled area for each source. The spectral types are represented by integers, with numbers between 10-19 correspond to O stars and numbers between 20-29 correspond to B stars (e.g. '18' corresponds to O8-type, while '22.5' corresponds to B2.5-type). So, our classification results, using the Naive Bayes Classifier, are O9.0±1 and B2.0±3 spectral types for HD 93028 and 2dF 3327, respectively.

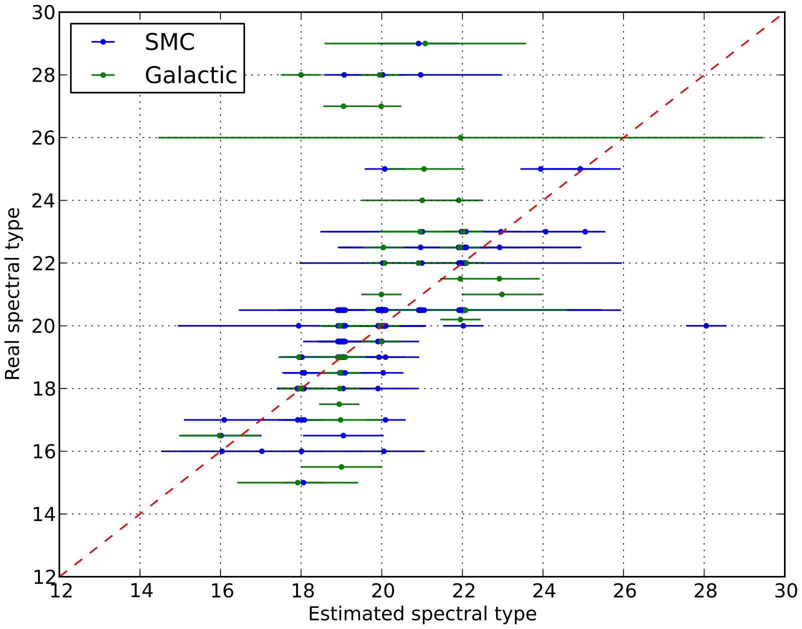

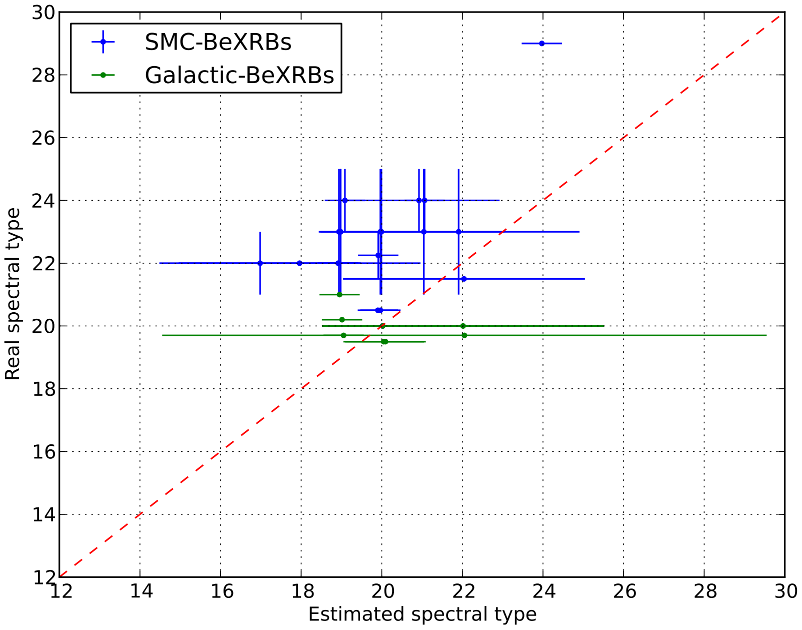

Figure 3.22: A plot of the real spectral types of stars in the SMC (blue) and the Galactic (green) plotted against the spectral types determined from the Naive Bayes Classifier. The spectral types are represented by integers, with numbers between 10-19 correspond to O stars and numbers between 20-29 correspond to B stars (e.g. '18' corresponds to O8-type, while '22.5' corresponds to B2.5-type). For presentation reasons we have added a small random offset in the estimated spectral types. The red-dashed line represents the 1-to-1 correlation.

3.5 Discussion and Conclusions

We have presented two quantitative methods for the classification of early-type (OB) stars, based on their EW of selected diagnostic spectral lines, using (a) a Continuous Fit approach and (b) a Naive Bayesian Classifier. Even though the two methods are based on different approaches they are both successful to correctly classify most sources. In this section we compare the two methods and discuss their efficiencies with respect to their success rate of recovering the true spectral types, and we discuss possible enhancements in both methods.

The Continuous Fit approach is based on the transformation of the quantized spectral types into a continuous function, reflecting the continuous nature of temperature which drives the different spectral types. With this method we are able to correctly classify, within the inherent uncertainty of two spectral types, 72% and 68% of the SMC and the Galactic training samples, respectively. Regarding the BeXRB test samples, which were not used to build the diagnostics, this method classifies correctly 58% and 63% of the SMC and Galactic BeXRBs, respectively.

The Naive Bayes Classifier is a purely statistical approach based on the collective properties of the data, and it is able to correctly classify 85% and 45% of the SMC and the Galactic training samples, respectively. Regarding the BeXRB test samples, which were not used to train the classifier, the method classifies correctly 32% and 75% of the SMC and Galactic BeXRBs.

By comparing the results from the two methods we can conclude that the Continuous Fit approach is more successful in recovering the classification obtained from visual examination of the spectra ("true" spectral types). The Naive Bayesian Classifier fails to classify mainly the late type sources, as a result of its training sample (due to the under-presentation of late type sources in this sample). The good success rate (85%) in classifying the SMC training sample shows that if a proper training sample was provided for the Galactic sources, we would expect a better success ratio. In addition, a Galactic sample would also reduce any differences imposed by the metallicity difference between the two galaxies (Galactic [Fe/H]=0.29, SMC [Fe/H]=-0.64; Russell & Dopita 1992).

Regarding the classification results obtained for the BeXRB test samples, we see that the Continuous Fit approach correctly classifies the majority of the sources, at almost the same efficiency with that for the training samples. This is not true for the Naive Bayesian Classifier, which correctly classifies 32% of the SMC BeXRBs.

However, it performs much better for the Galactic BeXRB sample, which consists of mainly early type sources (O9- to B1-type stars). The SMC BeXRBs are skewed to later types (Maravelias et al., 2014) which affects the classification with the Naive Bayesian Classifier. In addition, the weak spectral lines in a number of the SMC sources, which allow their visual spectral classification only within a range of spectral types (typically B1-B5 or B3-B5; Maravelias et al. 2014), does not allow their accurate measurement with the automated method adopted for the measurement of the line EWs. A physical reason could also lie within the diagnostics lines used. The HeI lines are affected by the presence of the circumstellar disk (Reig & Zezas, 2014), which may complicate the behavior of these lines in the BeXRB test sample compared to the B-type stars in our training samples.

Nevertheless, both methods give very promising results. There is significant potential for improvement in the following areas:

- Measure EW from spectral line fitting rather than integrated flux ratio in fixed bands. Although the latter has the advantage of easy application and speed, the former provides more accurate measurements, and allows the measurement of fainter lines and determination of the EW.
- Include measurement of uncertainties, which would provide improved constraints in the estimated spectral type uncertainties.
- Combine several different diagnostics in the Continuous Fit method.
- Increase the training sample, to better reflect the late B-type populations (and even the early O-type, as an extension).

The sample increase is not easy to perform for B-type stars in the SMC, due to its distance. However, we could take advantage of the Galactic sources which, simultaneously, acts also as a test study for any possible metallicity dependance.

4

A wide-field Hα imaging survey of the Small Magellanic Cloud

4.1 Introduction

The recent interaction history between the Small Magellanic Cloud (SMC) and our Galaxy has triggered the formation of a young stellar population (Harris & Zaritsky, 2004). Among this population we can find Be stars, i.e. main sequence B stars that have shown at least once in their lifetime Balmer lines in emission (e.g. Rivinius et al., 2013). Be stars are the massive donors of matter that fuels the X-ray emission from the Be X-ray Binaries (BeXRBs; e.g. Reig 2011), which compose virtually all High-Mass X-ray Binaries (HMXBs) in the SMC (Liu et al. 2005; except for SMC X-1; Webster et al. 1972, and the tentative source CH6-20/LHA 115-S 18; Clark et al. 2013; Maravelias et al. 2014, in which the donors are supergiant stars).

Several studies (e.g. Antoniou et al. 2009b; Grimm et al. 2003; Majid et al. 2004) have shown that there is a correlation between the young stellar population and the BeXRBs. Particularly Antoniou et al. (2010) and Shtykovskiy & Gilfanov (2007) demonstrated that the maximum of BeXRBs is expected from stellar population $\sim 40\,\mathrm{Myr}$ old. This timescale represents also the timescale of development of the

Be phenomenon, peaking at ∼35 Myr (McSwain & Gies, 2005b), therefore linking the BeXRB formation efficiency with star-formation rate (Antoniou et al., 2010). However, the formation rate is not currently well established, since the Be phenomenon is a transient event, and the observed population of Be stars, and consequently that of BeXRBs, in a singe epoch is always a lower limit of their actual number.

Similarly, the fraction of Be stars over the total population of B stars has been the target of many works, using spectroscopic and photometric techniques to identify sources with strong Hα emission. This is important in order to understand the conditions under which they develop this behavior, especially within then context of the general B-type stellar population. Studies in Galactic clusters have revealed fractions of $< 10\%$ (Mathew et al., 2008; McSwain & Gies, 2005a). In SMC open clusters this fraction varies from ∼8% (Martayan et al., 2010) up to $\sim 31\%$ (Iqbal & Keller, 2013), while in the field is found within the range of $\sim 5-11\%$ (Iqbal & Keller, 2013) and up to ∼26% (Martayan et al., 2007). Further investigation with respect to the metallicity difference between the Galaxy and the SMC identified that the population of SMC Be stars is larger by a factor of 2 to 5 (e.g. Maeder et al. 1999; Martayan et al. 2010; Wisniewski & Bjorkman 2006).

Within these fractions we can find the optical counterparts of BeXRBs. The detection of Hα emission from an optical counterpart of a candidate BeXRB is a strong evidence in favor of its Be nature. Sturm et al. (2013) compiled the most complete catalog of X-ray point sources in the SMC up to date ($\sim$ 3000 sources), identifying 94 BeXRBs (referred to as HMXBs in their catalog). A substantial number of these sources (45) are classified as candidate BeXRBs based on their broad-band optical photometry alone.

In order to further explore the nature of these sources we initiated an Hα imaging campaign, using the Wide Field Imager camera of the 2.2 m MPG/ESO telescope. We examined 6 selected regions of the SMC with recent star-formation to identify Hα emission sources. These sources are cross-correlated with the X-ray catalog by Sturm et al. (2013) to classify the X-ray sources with Hα emission counterpart. Moreover, we examine the fractions of OBe stars with respect to their total number of OB stars, and that of BeXRBs detected with respect to their total number of OB stars in order to address their formation rate.

In Section 4.2 and 4.3 we present the observations, and the data reduction, respectively. We discuss the source selection criteria in Section 4.4. The results are presented in Section 4.5, and they further discussed in Section 4.6. Section 4.7 summarizes this work presents the conclusions.

4.2 Observations

The observations were performed on November 16 and 17, 2011, using the Wide Field Imager (WFI) mosaic camera[1], at the 2.2-m MPG/ESO telescope at La Silla, Chile. This camera consists of 4×2 of 2k×4k CCDs providing a wide field of $34' \times 33'$ with a resolution of $0.238''$/pixel.

We obtained observations in the R_c and Hα filters for 7 fields in the SMC, shown in Figure 4.1. Each observation was split in 8 dithered exposures with offsets ranging between -12$''$ to 24$''$ and -72$''$ to 72$''$ for RA and Dec, respectively, with respect to the initial pointing in order to cover the area between the CCDs. The duration of each exposure was 390 s and 15 s, and after coadding the exposures for each filter the total exposure time for each field was 3120 s and 120 s for the Hα and Rc filters respectively. The details of the observations are given in Table 4.1.

Additionally, 5 spectrophotometric standards from the list of (Hamuy et al., 1992) have been observed throughout the night in order to flux calibrate the photometric results. Moreover, standard calibration images such as bias and dome-flat exposures were obtained as standard calibration images.

4.3 Data reduction

4.3.1 Mosaic construction

The data reduction was performed with THELI software (GUI v2.6.2) (Erben et al., 2005; Schirmer, 2013), which *"is a tool for automated reduction of astronomical images"*[2]. As it contains pre-configured settings for a large number of instruments (including the WFI camera), it provides an easy and convenient way to reduce multi-chip observations from the initial single dithered exposures to the final mosaic image. After the basic processing steps (bias subtraction, flat-fielding), THELI performs the astrometric calibration by: (i) creating a reference source catalog based on online databases, (ii) creating a source catalog obtained from running the SEXTRACTOR[3] (Bertin & Arnouts, 1996) source detection tool on each exposure, (iii) solving for the best astrometric solution.

---

[1] `https://www.eso.org/sci/facilities/lasilla/instruments/wfi.html`

[2] `http://www.astro.uni-bonn.de/~theli/`.

[3] `http://www.astromatic.net/software/sextractor`

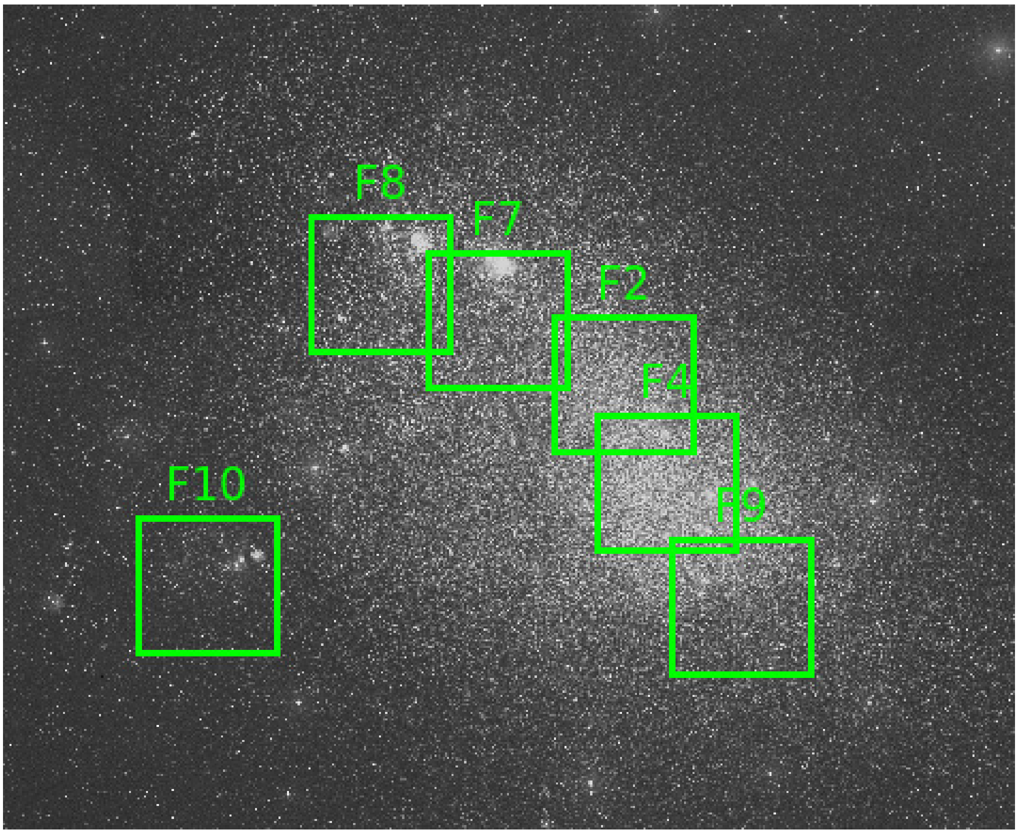

Figure 4.1: The Small Magellanic Cloud (SMC) and the observed fields with the WFI camera at the 2.2-m MPG/ESO. The dimensions of each field are 34′ × 33′. North is up and East left. (*Image Credit: Digitized Sky Survey - DSS.*)

Table 4.1: Observation log.

Field (1)	R.A. (J2000.0) (hh:mm:ss) (2)	Dec. (dd:mm:ss)	Date (3)	Filter (4)	Exposures (5)	Total time (s) (6)
F2	00:52:12.0	-72:39:11.6	16/Nov/2011	*Rc*	8	120
F2	00:52:12.0	-72:39:11.6	17/Nov/2011	Hα	8	3120
F4	00:49:47.6	-73:03:41.2	16/Nov/2011	*Rc*	8	120
F4	00:49:47.6	-73:03:41.2	16/Nov/2011	Hα	8	3120
F7	00:58:49.6	-72:22:47.0	17/Nov/2011	*Rc*	8	120
F7	00:58:49.6	-72:22:47.0	17/Nov/2011	Hα	8	3120
F8	01:04:59.7	-72:12:35.4	17/Nov/2011	*Rc*	8	120
F8	01:04:59.7	-72:12:35.4	17/Nov/2011	Hα	8	3120
F9	00:45:25.2	-73:33:53.8	16/Nov/2011	*Rc*	8	120
F9	00:45:25.2	-73:33:53.8	16/Nov/2011	Hα	8	3120
F10	01:16:13.4	-73:23:11.2	17/Nov/2011	*Rc*	8	120
F10	01:16:13.4	-73:23:11.2	17/Nov/2011	Hα	8	3120

Column description:

(1) Field ID of FX type, where X is the number of field.

(2) Sky coordinates for center of field.

(3) Date of observation.

(4) Filter used.

(5) Number of dithered exposures.

(6) Total exposure time.

Since our fields are crowded we wanted to use a reference catalog with the best astrometry. We opted for the PPMXL catalog[1], which combines deep optical data (up to 21 mag) from the USNO-B1 catalog with improved astrometry from 2MASS. The observed source list was generated by running SExtractor on each exposure using a rather high detection threshold (SNR = 30 and 40 for the *Rc* and Hα exposures, respectively) in order to limit the source list to the brighter sources, as fainter sources would result in higher chance coincidence probability when comparing to the reference catalog, which would deteriorate the astrometric solution. The astrometric solution is calculated by Scamp[2] (Bertin, 2006) for each exposure. Although the distortion matrix for focal plane of WFI is already defined in Theli, we noticed than it did not provide good results. Instead we had to create a new model for the focal plane based on our data, by deriving a common, median relative positioning of the individual CCDs within the focal plane[3]. Moreover, we had to allow for higher order polynomials in the distortion solution (degree 4 to 5) in order to properly model the the WFI focal plane[4]. Scamp produces a number of check plots which can be used to assess the quality of the astrometric solution before the final co-addition for the mosaic image. We reached an acceptable astrometric solution when we obtained a distortion map equivalent to a "ring"-like shape suitable for WFI, minimized the χ^2, and there were no trends in the fit residuals. The typical astrometric error of our catalog is $0.4''$.

The output of Scamp is WCS-compliant headers that can be used easily with SWarp[5] (Bertin et al., 2002) in order to create the final mosaic. Using the information in these headers SWarp re-samples all images into a combined output image through a weighted-average algorithm (using weight-maps that have been created already by Scamp). Although the individual exposures could be sky subtracted before coaddition we opted not to do so as the SMC fields present a highly variable background due to the extended HII regions. We also took care that for each field the output mosaic images for the two filters were centered exactly at the same coordinates and measured the same dimensions, in order to describe the sources with the same pixel values in each image (see Section 4.3.2 for details).

---

[1] See details at `http://www.astro.uni-bonn.de/~theli/gui/astromphotom.html#available-reference-catalogs` - accessed July 8, 2014.

[2] `http://www.astromatic.net/software/scamp`

[3] This translates in the parameters: `"Which focal plane?" = "Create new FP"`, and `"MOSAIC_TYPE" = "FIX_FOCALPLANE"`.

[4] See "Good distort examples" in `http://www.astro.uni-bonn.de/theli/gui/astromphotom.html#scamp` and related WFI image at `http://www.astro.uni-bonn.de/theli/gui/_images/d_g_4.png` - accessed July 8, 2014.

[5] `http://www.astromatic.net/software/swarp`

4.3.2 Source photometry

The next step in our analysis was source photometry. As the SMC in a nearby galaxy (60.6 kpc; Hilditch et al. 2005) we can resolve its stellar population even with ground telescopes (e.g. the OGLE project; Udalski et al. 1997; the Magellanic Clouds Photometric Survey; Zaritsky et al. 2002). Imaging of these regions results to images with a high concentration of sources and hence significant source confusion. Accurate photometry in crowded fields can be performed efficiently by PSF (Point-Spread Function) fitting. Due to the atmosphere and the aberrations along the optical path through the detection system (telescope-filter-detector) and the effect of diffraction, stars are not absolute point sources contained within a single pixel, but their light spreads over many pixels (the PSF). However, they all follow the same distribution which allows for modeling. By creating a good PSF model based on bright, but not saturated, stars we can rescale it to fit almost every star in the field. Moreover, PSF fitting enables the measurement of fainter stars that are hidden by the neighboring brighter ones, as these are revealed after subtracting the fitted brighter sources from the original image.

The presence of HII regions in the SMC complicates the photometry further, since the diffuse emission adds to the background. Performing source detection in the Hα image would result to many spurious sources. In order to avoid this and to make sure that we perform photometry to stellar sources only and not local enhancements of the diffuse emission, we ran the source detection in the *Rc* image first and we used this output list as an input for the photometry in the Hα. This is justified by the fact that the exposure time for the *R*-band is chosen to provide a sufficient SNR observations (~ 60) for stars down to $m_{Rc} = 18.7$ mag, corresponding to B8 spectral type stars at the distance of the SMC (Cox, 2000).

The PSF photometry was performed with the DAOPHOT package (Davis, 1993; Stetson, 1987) of IRAF[1] (v2.15), through the PYRAF[2] environment (v1.11). A typical analysis process we followed[3] consists of the following steps:

1. Run `daofind` on the *Rc*-band mosaic to create an initial source list.
2. Run `phot` on the output list of step 1 to create the initial photometry for the sources detected in step 1.

---

[1] IRAF is distributed by the National Optical Astronomy Observatories, which are operated by the Association of Universities for Research in Astronomy, Inc., under cooperative agreement with the National Science Foundation.

[2] PYRAF is a product of the Space Telescope Science Institute, which is operated by AURA for NASA.

[3] "A Reference Guide to the IRAF/DAOPHOT Package", Lindsey E. Davis, January 1994.

3. Run `pstselect` to select a predefined number of 120 of the brightest good sources (i.e. sources without bad pixels or pixel values well below the saturation limit) that will be used to build the PSF function of each mosaic image. Each candidate star was visually inspected and only stars with smooth profiles were selected for the PSF calculation.

4. Run `psf` to create the PSF model by fitting the PSF reference stars with an analytic model.

5. Run `allstar` on the initial image to fit simultaneously the PSF model to all sources measured in step 2. The same routine subtracts the fitted sources from the image and produces a final list of sources that have been successfully fitted and a subtracted image containing the residuals.

6. Re-run `daofind` on the subtracted image to create a second source list, identifying fainter and previously unidentified sources.

7. Re-run `phot` on the source list of step 6 to compute the photometric parameters of the new sources.

8. Merge the output `phot` list of step 7 (new sources) and the output `allstar` list of step 5 (old sources) to create a list of unique sources.

9. Re-run `allstar` on the initial image with the source list of step 8 in order to better determine their sky background and final photometry for all sources simultaneously.

10. Repeat steps 6-9 as many times as needed (after some passes the number of finally accepted sources will converge).

To achieve better and more accurate results, we had to carefully select the parameters of DAOPHOT, determined separately for each mosaic. Since these output mosaics for THELI are in units of counts per second, while the photometric analysis needs to be performed in counts, we multiplied the mosaic by the exposure time per field. In order to recover the number of counts for each source, and for proper error calculation, we used an effective gain and readaout noise which are suitable for the averaging method used to produce the mosaics. In this case, the effective gain is `epadu` $= N \times$ gain (in e^{-}/ADU) and the effective readout noise is `readnoise` $= \sqrt{N} \times$ readout noise, where

N is the number of exposure per mosaic, gain = 2 e^-/ADU and readout noise = 4.5 e^-/pixel are the values for the WFI camera[1].

We used `daoedit` to measure the `fwhm` (Full-Width at Half-Maximum) for a number (∼20-30) of bright, but not saturated, stars covering the whole field[2]. This is an approximation of the FWHM of the real PSF, which is used as a starting value for the algorithm that computes the PSF model.

We used `imexamine` to measure the sky background surface brightness and its standard deviation (parameter `sigma`) by picking randomly a large number (∼50) of regions, scattered again around the whole field. The minimum useful data (parameter `datamin`) are determined as `datamin` $= \text{sky} - 5 \times \sigma$, while for the maximum useful data (parameter `datamax`) we used approximately the 1/3 of the maximum value provided from the command `imstatistics` (to make sure that we are under the linearity limit).

Our detection threshold was set at 3σ above the background (parameter `threshold`). The effective exposure time was given through the parameter `itime`, and it was equal to the value with which the initial mosaic in count rate was multiplied with.

Regarding the PSF model we opted to use an empirical model based on approximately 100 stars per field, which was allowed to vary quadratically with position (`varorder`=2) to account for small differences due to the wide field-of-view. We did tested the parametrization of the PSF function, using the different available analytic models, to assess their effect in the final photometric results and the distribution of the residuals, but there was no evidence for any difference. So, we set the parameter `function` to "auto", to let the routine `psf` to automatically select the function that gives the least scatter in the fit of the PSF stars.

We slightly changed the parameter `psfrad`, which defines the source area over which the PSF model is fitted, to account better for the brighter stars in our fields (`psfrad` = 4.5 × `fwhm`). Since this value determines the radius that the light of the brighter stars blends with the background noise we set also the innermost radius of the region which is used for the sky estimation equal to the same value (`annulus` = 4.5 × `fwhm`). We left all the rest of the parameters (e.g. centering, photometric, and sky fitting algorithms) at their default values.

As described in Section 4.4 the source detection was performed first on the *Rc* image first (after 3 iterations). Since we are interested in the stellar sources only rather than diffuse features we used this source list as the initial list for `phot` (step 2) when we

---

[1] `https://www.eso.org/sci/facilities/lasilla/instruments/wfi/overview.html` - accessed July 10, 2014.

[2] Since we have included distortion corrections the fwhm does not change, significantly, along the field.

ran the analysis for the Hα image. We computed a PSF independently for the Hα observation as it is not necessarily true that the same selected stars from the *Rc* image could be used of the PSF (e.g. they may reside into HII regions). Then, the `allstar` routine needed to run only once (on the initial Hα image), since the source list contained already all the candidate sources. As we wanted to make sure that the photometry on the Hα filter would be performed on the same stars as in the *Rc*-band, initially we did not allow for re-centering of sources during the `allstar` run (parameter `recenter`; because of the significant source confusion allowing for recentering each source might shift its centroid and fit a neighboring source or diffuse feature on the Hα image). However, this resulted in poor fits and residuals, because of small differences in the source centroids between the two filters. To account for this, we allowed for re-centering within 1/2 of the Hα FWHM, to minimize any shifting of the fit to neighboring sources (`cbox`=`fwhm`/2). In Figure 4.2 we present an example of photometric results, *Rc* and Hα instrumental magnitudes, as obtained from DAOPHOT analysis for Field 2 (only a sample of 50000 sources is presented for better illustration purposes, while the actual number of detections in each filter is provided in the legend).

Regarding the standard star fields, we also applied PSF photometry with minor adjustments of the parameters, since we were actually interested in only one source. The sky standard deviation was estimated by a number of regions (∼10) close to the standard. The inner radius of the sky region was set to larger values (`annulus` and `sannulus` equal to 6×`fwhm`), while we used the default value for the `psfrad` (=4×`fwhm`). The detection threshold, useful to define only a list of the brighter stars to create the PSF, was set to a higher value (`threshold`=10). The PSF model was determined, with the same parameters as the field PSFs, from approximately 20-25 stars as close as possible to the standard, since their fields did not contain enough sources to allow for an astrometric solution with proper distortion corrections. Then we obtained the photometric parameters by fitting the PSF to each standard star with the `allstar` routine.

4.3.3 Flux calibration

Flux calibration is performed by observing photometric reference stars (standards stars). This is straightforward for the broad-band filter *Rc* but not for the narrow-band Hα filter. Because of its narrow width the transmitted flux depends strongly on the properties of the filter response function (i.e. the transmittance function composed by the contribution of telescope optics, filter and detector response). However, by convolving the calibrated spectrum of spectrophotometric standard stars with the response

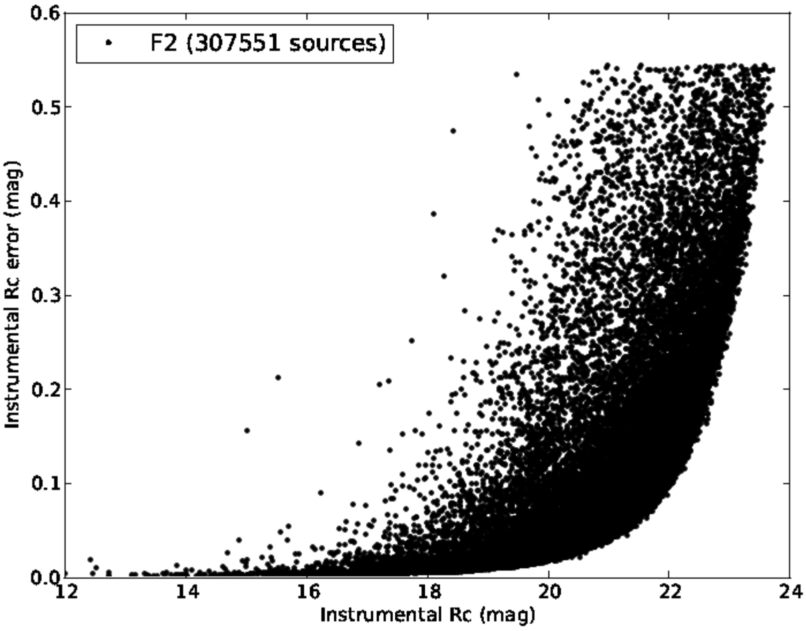

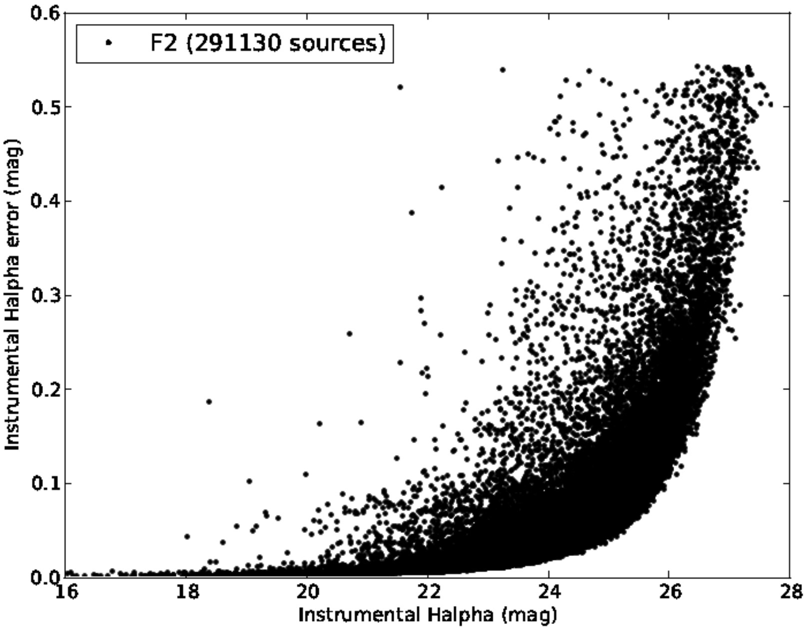

Figure 4.2: Photometric results for *Rc* and Hα mosaics as obtained from DAOPHOT analysis for Field 2. The total number of detections is presented in parentheses, as a sample of these sources (50000) has been used for the plot for better illustration purposes.

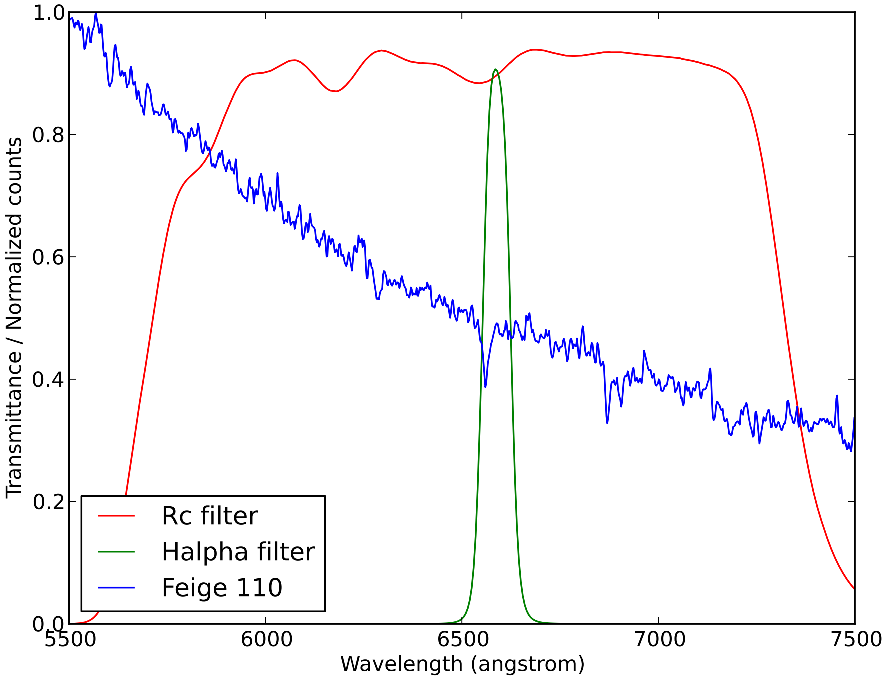

Figure 4.3: The response functions of the WFI/ESO filters *Rc* (red line; ESO# 844), and Hα (green line; ESO# 856). We also show a normalized spectrum for the standard star Feige 110 (blue line).

of the used narrow-band filter we can calculate the reference flux for each filter. The comparison of the measured flux from an observation of the spectrophotometric standard (instrumental magnitude) with that calculated from its reference spectrum can give us the flux calibration conversion factor.

For this reason a number of spectrophotometric stars from the list of (Hamuy et al., 1992) have been observed: LTT 1020, LTT 1788, LTT 2415, EG 21, Feige 110. For each one of them we measured their flux (in AB magnitudes) in the Hα filter from IRAF's library of standards[1]. The response function of the *Rc* (ESO# 844) and Hα (ESO# 856) filter used in our observations were obtained from the WFI/ESO site[2] and are shown in Figure 4.3, along with the spectrum of the standard star Feige 110.

By definition, AB magnitude refers to an object with constant flux per unit fre-

---

[1] Found at path_to_iraf/iraf/iraf/noao/lib/onedstds/.

[2] Retrieved from `https://www.eso.org/sci/facilities/lasilla/instruments/wfi/inst/filters.html` - accessed June 25, 2014.

quency interval:

$$m_{(\mathrm{AB})} = -2.5\log(f_\nu) - 48.590 \tag{4.1}$$

where f_ν is the flux measured in units of erg s^{-1} cm^{-2} Hz^{-1}, and the constant 48.590 mag is taken from Hamuy et al. (1992). Since we are working in the wavelength domain we need to convert these fluxes with respect to wavelengths:

$$f_\lambda = \frac{c}{\lambda^2} \times f\nu \tag{4.2}$$

where c is the speed of light (in Å/s), λ is the wavelength (in Å), and f_λ is given now in erg s^{-1} cm^{-2} $\mathrm{Å}^{-1}$. This gives:

$$m_{\mathrm{AB}} = -2.5\log f_\lambda) + [2.5\log\left(\frac{c}{\lambda^2}\right) + 48.590] \tag{4.3}$$

where the quantity inside the brackets is the zeropoint at the given wavelength.

In order to calculate the flux through the filter bandpass, we used the `sbands` routine[1]. We opted to perform the flux calculation for the broad-band filter Rc in addition to the Hα to obtain more accurate measurements with respect to filter's specific bandpass.

After determining the reference fluxes for each standard we converted them into AB magnitudes by using the following equations:

$$m_{H\alpha} = -2.5\log(f_{\lambda,H\alpha}) - 21.494 \tag{4.4}$$

$$m_{Rc} = -2.5\log(f_{\lambda,Rc}) - 21.463 \tag{4.5}$$

where the zeropoints have been determined by the conversion of the AB zeropoint to the corresponding central wavelength of each filter (6588 Å and 6517 Å for the Hα and Rc filters, respectively), using Equation 4.3.

Unfortunately, during the observations of the first night the standard stars were located on a CCD bad column. That did not allow always for optimal PSF fitting, resulting in unreliable photometry. We had to reject finally the use of LTT 2415 in both filters. This issue was corrected during the observations of the second night, and only one standard star observation (LTT 1020 in Rc filter) was rejected due to saturation.

Nevertheless, the number of standard stars observations was sufficient to perform a linear fit to their photometric data for each night per filter to obtain the photometric zeropoints and extinction coefficients. For this we have used:

$$m_{inst} = m_{ref} + ZP + K \times \chi \tag{4.6}$$

---

[1] Found under the `stsdas` package of IRAF. The `sbands` input must be a FITS file, so the flux data were converted from an ASCII to a FITS file through the `rspectext` command of the same package.

Table 4.2: Zeropoints and extinction coefficients, calculated from the standard star observations.

Night	Filter	Zeropoint (mag)	Extinction coefficient (mag)
16 Nov 2011	Rc	24.829	0.212
16 Nov 2011	Hα	22.136	0.603
17 Nov 2011	Rc	24.470	0.031
17 Nov 2011	Hα	21.105	0.065

where m_{inst} is the instrumental magnitude as calculated from the `allstar` routine, m_{ref} is the reference magnitude as calculated by the `sbands` package (see Equations 4.5), ZP is the zeropoint, K the extinction coefficient, and χ the airmass. However, there are no single observations available for the different standards stars, which does not allow the direct use of Equation 4.6. To account for this we re-write the equation as:

$$(m_{inst} - m_{ref}) = ZP + K \times \chi \tag{4.7}$$

where we can now use the magnitude difference between the instrumental and reference values and fit for the different standard stars. The results of these fits are presented in Table 4.2. The difference between the two nights is due to the non-pure photometric conditions.

These corrections have been finally applied to the data in order to flux calibrate the sources with respect to the standard stars used:

$$m_{cal} = m_{inst} - ZP - K \times \overline{\chi_{obs}} \tag{4.8}$$

where m_{cal} is the calibrated magnitude, m_{inst} the instrumental magnitude (as calculated by the `allstar` routine), ZP and K are the zeropoint and extinction correction according to the night of the observation and filter used, and $\overline{\chi_{obs}}$ is the mean airmass during the dithered exposures of the observed field.

4.4 Source selection

Since all stars are expected to be detected in the R-band image we first performed the source detection in those data. In order to remove spurious and non-stellar sources, we applied a selection process, based on the parameters provided by DAOPHOT. For each accepted source in the output list of `allstar` there are two parameters that define the goodness of the PSF fit: (a) χ^2, and (b) `sharpness`, defined as the difference between the observed width of the object (measured from a best-fit Gaussian profile for each source, during the `daofind` processing step) and the width of the PSF model. The optimal values for χ^2 are those close to unity, so we opted to select sources with χ^2 values smaller than 1.5. The sharpness is indicative of the nature of a source, as high values correspond to extended sources (e.g. galaxies), while (large) negative values are spurious detections (e.g. cosmic rays, hot pixels, etc.). Thus, we selected sources with $|\texttt{sharpness}| < 0.5$, which correspond to stellar sources.

Furthermore, since we are interested in early OB stars we selected sources with R-band magnitudes brighter than $Rc = 18.7$ mag, which corresponds to B8 spectral type at the distance of the SMC (c.f. Section 4.4). At the top panel of Figure 4.5 we present as an example the flux-calibrated Rc photometry for Field 2 (black dots), where we show the stellar sources detected, based on their χ^2 and `sharpness` (red stars), and the final selected sources (OB stars, blue dots) brighter than the limiting magnitude (18.7 mag; red dashed line). In order to validate our photometry, after having applied our selection criteria for the OB stars that we are interested in, we plot our flux-calibrated Rc magnitudes with R magnitudes from Massey (2002, photometric survey for massive stars in the Magellanic Clouds) in Figure 4.4 (for approximately 4600 common sources within $3''$ error radius for Field 2). Despite the small systematic offset (~ 0.2 mag; due to the different filters used) our photometry is in agreement with that of Massey (2002), and we start seeing incompleteness effects after $Rc \sim 15.5$ mag. This resulted in a clean only Rc source catalog after the χ^2 and `sharpness` cut of OB candidate stars.

Using TOPCAT[1] (Taylor, 2005) we performed first a cross-correlation within a search radius of 5 pixels of this clean catalog sources with the catalog obtained from the photometry on the Hα mosaic, to identify common sources. Then, we cross-correlated these sources with the MCPS point source catalog (Magellanic Clouds Photometric Survey; Zaritsky et al. 2002). The search radius was $3''$, based on the astrometric error of our catalog ($\sim 0.4''$) and the astrometric error of the MCPS catalog ($\sim 1.7''$; Zaritsky et al. 2002). This provided us with additional photometry parameters in the V and B bands for almost all ($\sim 97\%$) available sources from our analysis.

In order to select OB stars, we applied the criteria for the OB locus in the SMC

---

[1] `http://www.star.bris.ac.uk/~mbt/topcat/`

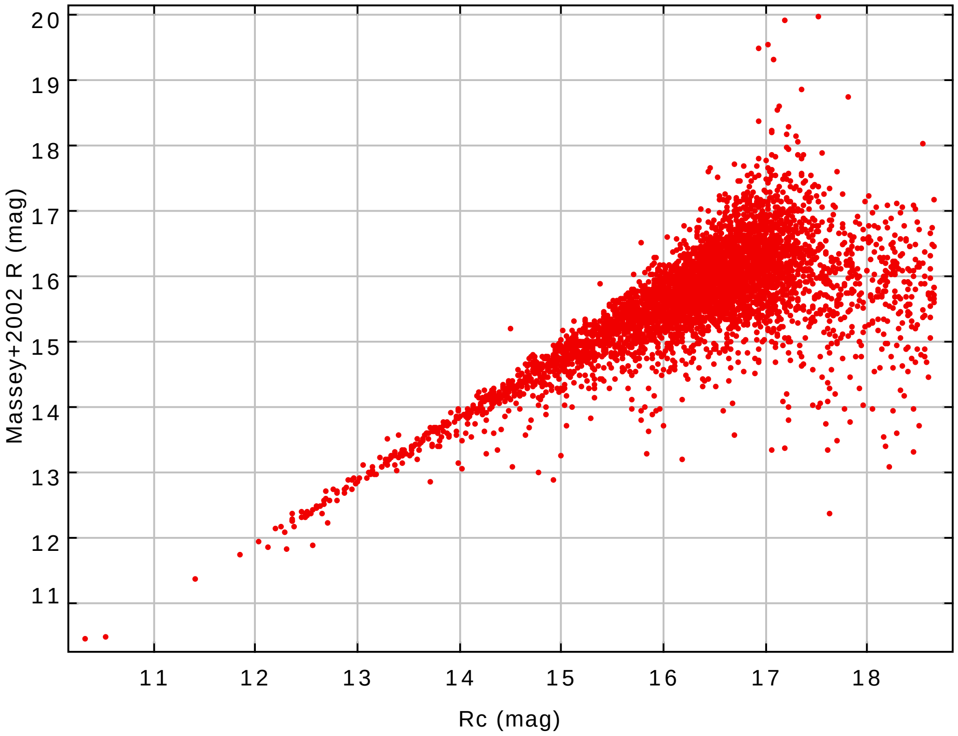

Figure 4.4: Comparison between our flux-calibrated *Rc* photometry and *R* photometry from Massey (2002). We see that the is a general agreement between the two lists. We notice a small offset (~ 0.2 mag) between the two catalogs, due to the different transmittance of the filters used. We are complete up to ~ 15.5 mag. The plot contains approximately 4600 sources common sources (within a $3''$ error radius) for Field 2.

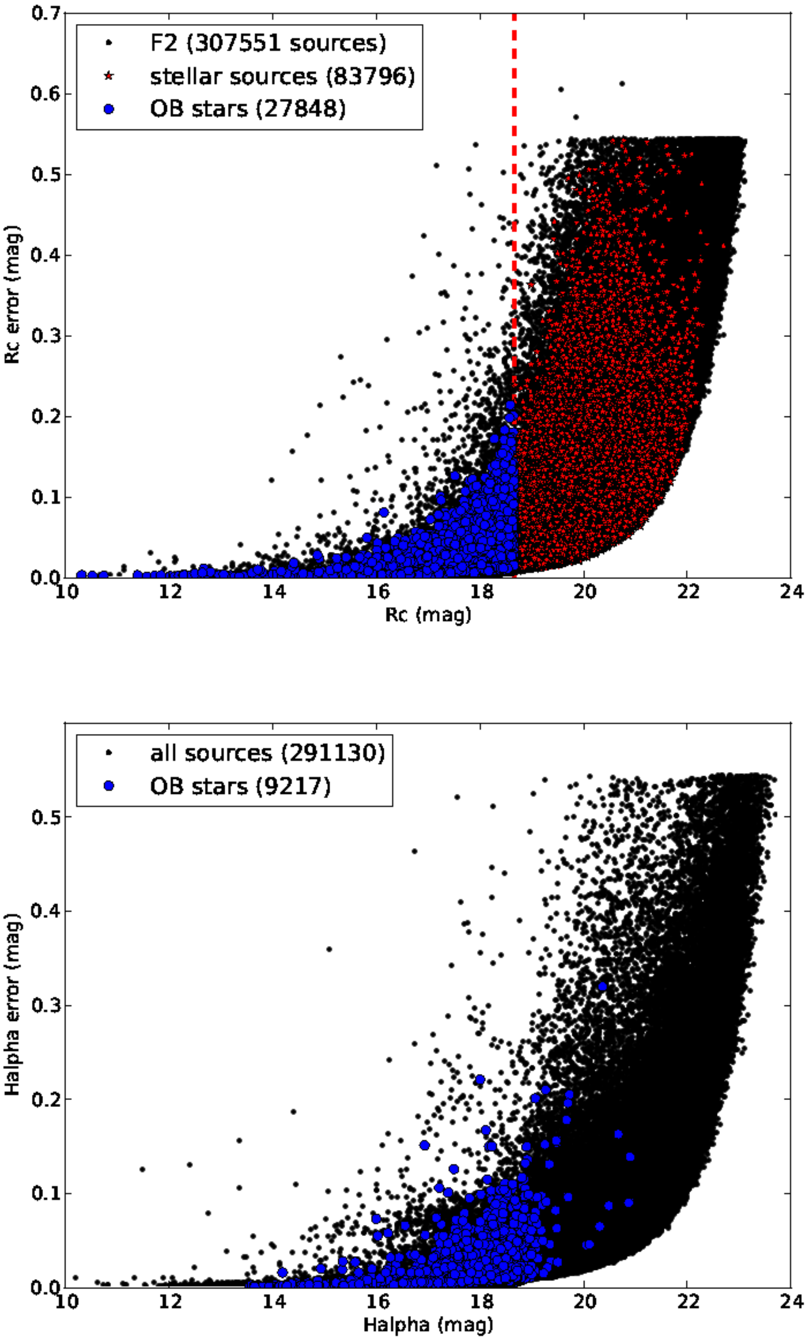

Figure 4.5: Top panel: flux-calibrated *Rc* photometry and its error for sources in Field 2 (black dots). We also present the most probable stellar sources with $\chi^2 < 1.5$ and $|\texttt{sharpness}| < 0.5$ (red stars), and the final selected sources with $Rc < 18.7$ mag (red dashed line) that correspond to OB stars (blue circles). Bottom panel: flux-calibrated Hα photometry and its error for source in Field 2 (black dots). We present the selected OB stars (blue circles) that have been selected after the cross-correlation of the Hα source list with the final clean *Rc* OB list. The total number of detections for each class of sources is presented in parentheses.

(Antoniou et al., 2009b):

$$\begin{aligned} 13.5 \leq V_o \leq 18.5 \\ -0.4 \leq (B-V)_o \leq 0.3 \end{aligned} \tag{4.9}$$

where V_o and $(B-V)_o$ are the reddening corrected parameters, assuming $E(B-V) = 0.09$ mag and $A_V = 0.29$ mag (Antoniou et al., 2009b). In the bottom panel of Figure 4.5 we show the flux-calibrated Hα magnitudes (black dots) for sources in Field 2, and the OB stars selected (blue circles), after the cross-correlation with the clean *Rc* list of OB stars.

For these sources we calculated their Hα index in mag (H$\alpha - Rc$), as the difference of their flux-calibrated magnitudes in the Hα and *Rc* filters. Its error is calculated by propagating the corresponding magnitude errors:

$$\Delta(H\alpha - Rc) = \sqrt{(\Delta H\alpha)^2 + (\Delta Rc)^2} \tag{4.10}$$

Following Zhao et al. (2005), the corresponding SNR is:

$$\mathrm{SNR} = G\frac{|H\alpha - Rc|}{\Delta|H\alpha - Rc|} \tag{4.11}$$

where $G = (2.5/ln10)[(1-10^{-0.4|H\alpha - Rc|})/|H\alpha - Rc|]$, and H$\alpha - Rc$ is the index in mag.

With the above methodology we are able to identify Hα emission sources, which display Hα emission line above the absorption line. The index H$\alpha - Rc$ corresponds to the equivalent width of the Hα emission line. However, the equivalent width depends on the spectral type of the source (c.f. figure 5 in Zhao et al. 2005), and the *R*-band magnitude. This effect is presented in the top panel of Figure 4.6, where we show the difference in the mean H$\alpha - Rc$ index between all detected sources (red line; including later than OB spectral types also) and only OB stars (blue line), in Field 4. In order to select Hα excess objects we need to define the minimum H$\alpha - Rc$ which corresponds to the optimally continuum subtracted Hα fluxes. Since the *Rc* filter includes the Hα filter (see Figure 4.3) the corresponding baseline for the Hα excess (i.e. stars without any excess) would be equal to H$\alpha - Rc = 0$ mag. However, because of the different width of the two filters and the range of spectral types considered, generally this value is not 0 for non-excess objects. Thus, we calculate this minimum H$\alpha - Rc$ as the average value that corresponds to the OB stars selected (since only a small fraction of stars show emission lines), and its error as the average H$\alpha - Rc$ error. We obtained these values individually for each field in order to account for any (small) photometric differences. The bottom panel of Figure 4.6 shows the histograms for the $H\alpha - Rc$ index for each field.

Finally, the best candidate Hα emission sources should display:

$$H\alpha - Rc < \langle H\alpha - Rc\rangle_{field} - 5 \times \langle\Delta(H\alpha - Rc)\rangle_{field} \tag{4.12}$$

if we wish to select sources at 5σ above the baseline excess. Finally, we considered only sources with SNR>5.

4.5 Results

In this Section we describe the results of our analysis:

1. For each field we have compiled a list of the identified Hα emission sources, as selected based on the criterion in Equation 4.12 and SNR>5. We present a sample list in Table 4.4, while the complete tables are presented in Appendix B. For each source in these tables we give sky coordinates, Hα and *Rc* magnitudes and their errors, H$\alpha - Rc$ index and its error, and SNR, from our analysis. In addition, we provide the V magnitude and $B - V$ color from the MCPS catalog (Zaritsky et al., 2002). In total we detected 5256 Hα emission sources in the locus of OB stars, in all fields. After accounting for the overlap between the fields the total number of Hα emitting OB stars is 4747.

2. The nature of Be stars is transient and only a fraction of the total population displays Hα emission during a single epoch observation. This means that their detected number is always a lower limit to their total population, and their true number could be 1.2 - 2.3 times larger (McSwain & Gies, 2005a). In Table 4.3 we present for each field the number of OB stars, as measured from the selection process presented in Section 4.4 applied to the MCPS catalog (Zaritsky et al., 2002), the number of identified Hα emission sources (which represents the OBe stars) and their corresponding ratio. We find this fraction to be $\sim 13\%$, and almost similar across all fields.

3. Since we are interested in the population of the BeXRBs (virtually all HMXBs in the SMC), we cross-correlated our list of Hα excess objects with the X-ray point source catalog from the XMM-Newton survey of the SMC Sturm et al. (2013), which includes 3053 sources. We identified 39 sources within a search radius of $3''$, which accounts for the astrometric error of our catalog and the $2.5''$ positional error reported by Sturm et al. 2013. Of those, based on the initial classification of Sturm et al. (2013), 25 are confirmed HMXBs, 8 are candidate HMXBs, 3 are

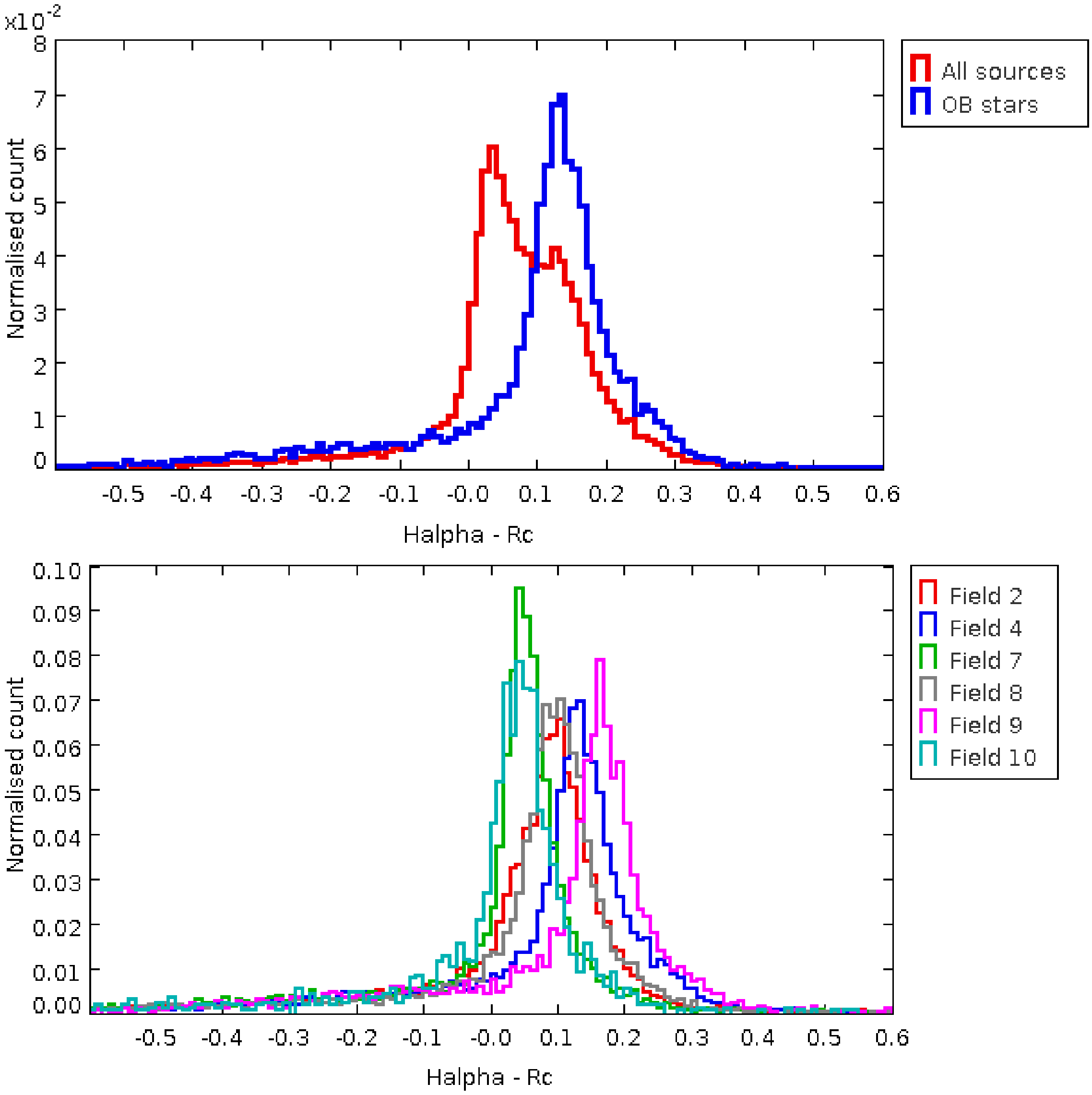

Figure 4.6: Top panel: Histograms for the Hα $-$ *Rc* index for all sources in Field 4 (dominated by later than B spectral types), and for OB sources only. Bottom panel: Comparison of histograms for the Hα $-$ *Rc* index for OB sources in each field.

Table 4.3: Fractions of OBe stars.

Field ID	OB stars	OBe stars	fraction
F2	9217	1180	0.128
F4	9799	1286	0.131
F7	8428	1199	0.142
F8	7305	864	0.118
F9	3672	484	0.132
F10	1687	243	0.144

candidate AGN sources, one star cluster, one candidate foreground star, and a source without any classification information. In Table 4.5 we present the detailed list of identifications of Hα emission sources with the X-ray sources of Sturm et al. (2013), using the corresponding ID number from Sturm et al. (2013) for the X-ray sources and the star ID from our source lists (see Appendix B).

Out of the 49 confirmed BeXRBs, 39 are located inside our fields and we are able to detect 25 Hα emission sources that coincide with these X-ray sources. This results to an identification ratio of 64.1% for the confirmed BeXRBs. Regarding the 31 candidate BeXRBs, in the catalog of Sturm et al. (2013), that are located inside our fields, we find that only 8 of them are associated with Hα emission sources, corresponding to an identification ratio of 25.8%. This significant difference (which is hard to explain as the result of variability of the Be stars) suggests that a number of these candidates are not HMXBs.

Table 4.4: A sample of Hα emitting sources identified in Field-10.

Source-ID (1)	RA (J2000.0) (2) (hh:mm:ss.s)	Dec (3) (dd:mm:ss.s)	Rc (4) (mag)	Hα (5) (mag)	V (6) (mag)	$B-V$ (7) (mag)	H$\alpha - Rc$ (8) (mag)	SNR (9)
F10-1	01:12:25.2	-73:18:04.5	17.445(0.005)	17.293(0.005)	17.317	-0.039	-0.152(0.007)	20.0
F10-2	01:12:34.0	-73:27:24.7	18.218(0.009)	18.04(0.024)	17.879	-0.210	-0.178(0.026)	6.4
F10-3	01:12:36.1	-73:24:40.8	17.983(0.007)	17.776(0.006)	17.812	0.018	-0.207(0.009)	20.4
F10-4	01:12:37.7	-73:35:19.0	17.506(0.005)	17.311(0.004)	17.356	-0.078	-0.195(0.006)	27.9
F10-5	01:12:38.6	-73:12:45.1	18.186(0.009)	18.083(0.009)	17.995	-0.068	-0.102(0.013)	7.7
F10-6	01:12:38.6	-73:38:13.2	17.351(0.006)	17.199(0.004)	17.046	-0.080	-0.152(0.007)	19.6
F10-7	01:12:40.3	-73:38:44.6	18.017(0.006)	17.915(0.008)	17.859	-0.016	-0.102(0.010)	9.8
F10-8	01:12:44.1	-73:26:58.1	17.095(0.004)	16.818(0.003)	16.927	-0.072	-0.276(0.005)	48.8
F10-9	01:12:45.3	-73:37:30.3	18.053(0.006)	17.927(0.007)	17.908	-0.005	-0.126(0.009)	13.0
F10-10	01:12:46.2	-73:25:56.4	18.213(0.006)	17.928(0.007)	18.064	-0.050	-0.285(0.009)	27.2
F10-11	01:12:47.5	-73:14:43.4	17.797(0.007)	17.686(0.008)	17.517	-0.313	-0.111(0.011)	10.0
F10-12	01:12:47.9	-73:14:43.7	18.64(0.019)	18.431(0.018)	17.757	-0.092	-0.209(0.026)	7.3
F10-13	01:12:48.4	-73:30:26.9	15.594(0.004)	15.33(0.002)	15.501	-0.041	-0.264(0.004)	52.3
F10-14	01:12:52.8	-73:17:56.9	17.398(0.007)	17.176(0.005)	17.199	0.041	-0.222(0.009)	23.4
F10-15	01:12:53.8	-73:30:26.1	14.794(0.005)	14.24(0.002)	14.74	-0.017	-0.555(0.005)	80.6

Column description:

(1) Source id in the form of FX-N, where FX corresponds to the field id as has been defined in Table 4.1 and N is the sequential number for the field (sorted by RA).

(2,3) Sky coordinates of the source, as derived from our analysis.

(4,5) Rc and Hα magnitudes and their errors in parentheses.

(6,7) V magnitude and $B-V$ color obtained from the MCPS catalog (Zaritsky et al., 2002).

(8) H$\alpha - Rc$ index and its error in parenthesis.

(9) SNR, as calculated by Equation 4.11.

Table 4.5: Identifications of Hα emission sources to X-ray sources from Sturm et al. (2013).

Sturm-ID	Classification	RA	Dec	Separation	Star-ID
		(J2000.0)			
(1)	(2)	(3)	(4)	(5)	(6)
		(hh:mm:ss.s)	(dd:mm:ss.s)	(")	
12	<HMXB>	01:19:38.94	-73:30:11.4	0.33	F10-238
49	HMXB	00:57:35.95	-72:19:34.1	0.26	F7-380
51	HMXB	01:01:20.68	-72:11:19.0	0.12	F7-1060
61	HMXB	00:55:35.39	-72:29:06.6	0.86	F7-39
63	HMXB	00:54:56.28	-72:26:47.3	0.65	F2-1019
68	HMXB	00:58:12.74	-72:30:48.4	0.82	F7-493
69	HMXB	00:56:05.72	-72:21:59.4	1.01	F7-120
92	HMXB	00:54:46.31	-72:25:23.1	0.52	F2-990
112	HMXB	00:47:23.30	-73:12:27.9	0.51	F4-119
115	HMXB	00:50:44.81	-73:16:05.1	0.50	F4-734
116	HMXB	00:50:57.29	-73:10:08.0	0.82	F4-785
119	HMXB	00:49:29.74	-73:10:58.9	0.59	F4-480
121	HMXB	00:48:34.09	-73:02:30.5	0.89	F4-296
133	<HMXB>	00:50:48.06	-73:18:17.6	0.42	F4-749
154	<HMXB>	01:00:30.26	-72:20:33.1	1.28	F7-975
227	HMXB	01:03:37.56	-72:01:32.9	0.42	F8-285
228	HMXB	01:05:55.41	-72:03:49.2	1.54	F8-627
247	<HMXB>	01:02:47.51	-72:04:50.9	1.99	F8-153
335	HMXB	00:54:55.94	-72:45:10.9	0.20	F2-1018
337	<HMXB>	00:56:14.65	-72:37:55.8	0.36	F7-152
344	<AGN>	00:54:22.09	-72:45:32.1	2.97	F2-897
535	Cl*	00:59:05.09	-72:10:33.2	2.50	F7-644
578	HMXB	00:49:03.33	-72:50:52.2	0.46	F2-21
581	HMXB	00:49:13.63	-73:11:37.7	0.17	F4-419
615	HMXB	00:49:30.62	-73:31:09.4	0.27	F9-481
654	HMXB	00:53:23.91	-72:27:15.3	0.23	F2-676
674	HMXB	00:59:28.87	-72:37:04.4	0.80	F7-778
742	<AGN>	00:55:35.65	-72:12:29.6	2.47	F7-43
816	HMXB	01:01:55.79	-72:32:36.6	0.09	F7-1123

Continued on next page

Table 4.5 – *Continued from previous page*

Sturm-ID	Classification	RA	Dec	Separation	Source-ID
935	HMXB	01:17:40.44	-73:30:50.7	1.43	F10-198
1400	<HMXB>	00:53:41.76	-72:53:10.1	2.01	F2-758
1481	<HMXB>	00:42:07.77	-73:45:03.4	1.09	F9-21
1562	<AGN>	00:58:22.18	-72:17:59.0	1.40	F7-517
1570	na	01:00:21.18	-72:18:37.3	2.45	F7-961
1702	<fg-star>	00:49:13.54	-73:26:00.0	0.33	F9-465
1802	HMXB	00:52:05.68	-72:26:05.0	0.75	F2-396
1828	HMXB	00:53:55.61	-72:26:44.4	1.68	F2-809
2300	<HMXB>	00:56:13.87	-72:29:59.7	1.38	F7-147
2710	HMXB	01:04:35.47	-72:21:47.2	1.36	F8-440

Column description:

(1) Source ID based on the catalog of Sturm et al. (2013).

(2) X-ray source classification by Sturm et al. (2013):
HMXB = confirmed HMXB in the SMC
<HMXB> = candidate HMXB in the SMC
<AGN> = candidate AGN
Cl* = star cluster
<fg-star> = candidate foreground star
na = no available classification

(3,4) Sky coordinates from the catalog of Sturm et al. 2013.

(5) Separation between the X-ray source (Sturm-ID) and $H\alpha$ emission source (Star-ID).

(6) Source ID in the form of FX-N, where FX corresponds to the field ID as has been defined in Table 4.1 and N is the sequential number for the field (sorted by RA).

4.6 Discussion

4.6.1 Hα emission sources

We have identified 4747 Hα emission sources, a major increase compared to the work by Meyssonnier & Azzopardi (1993) which has served as the main resource for Hα emission sources. Meyssonnier & Azzopardi (1993) had identified 1844 emission sources throughout the whole SMC, at a corresponding limiting magnitude $V \sim 16.5$ mag (estimated after cross-correlating their catalog with the MCPS catalog assuming $3''$ error; Zaritsky et al. 2002). In Figure 4.7 we present the detected sources in the two surveys: grey open circles are sources by Meyssonnier & Azzopardi (1993), blue circles are detections from our survey, and red crosses show common sources, i.e. sources which display Hα emission in both surveys. In Table 4.6 we give the number of detections from our survey per field, the number of sources from Meyssonnier & Azzopardi (1993) within that field, and the number of common sources. We see that we detect 2 to 4 times more sources in each field.

We have also included in Table 4.6 sources from the survey of Martayan et al. (2010), who performed slitless spectoscopic observations for a number of SMC open clusters (with a limiting V magnitude of $\sim 16.5 - 17$ mag). We identified $\sim 52\%$ and $\sim 44\%$ of the sources in Meyssonnier & Azzopardi (1993) and Martayan et al. (2010), respectively. Since our survey is deeper (at the limiting magnitude of $V = 18.5$ mag, corresponding to late B-type stars) than the previous works, the missing population can be attributed to the transient nature of Hα emission and our somewhat conservative criteria for identifying a source as Hα excess.

4.6.2 Fraction of OBe/OB stars

In order to estimate the OBe/OB fractions for each field, we are using the number of Hα emission sources detected (OBe) and the number of sources identified as OB stars based on their photometric parameters (as described in Section 4.4). The fractions of OBe/OB stars found from this work (presented in Table 4.3), have a mean value of $\sim 13\%$, and they are in general agreement with previous studies. For example, Martayan et al. (2007) have found a mean fraction $\sim 26\%$ for the field of the surrounding environment of the SMC cluster NGC 330, while Iqbal & Keller (2013) found fractions in the range $\sim 5 - 11\%$, also from fields close to open clusters. These fractions are larger when open clusters are included, since the clusters have a high density of young stellar population

Table 4.6: Comparison table for Hα emission sources identified in our survey, and those by Meyssonnier & Azzopardi (1993) [MA93] and Martayan et al. (2010) [M10].

Field-ID (1)	WFI (2)	[MA93] (3)	[MA93]+WFI (4)	[M10] (5)	[M10]+WFI (6)
F2	1180	281	166	50	21
F4	1286	291	165	70	26
F7	1199	293	164	82	52
F8	864	253	171	35	13
F9	484	255	38	33	6
F10	243	74	47	-	-

Column description:

(1) Field id, as defined in Table 4.1.

(2) Number of Hα emission sources for the corresponding field as detected in our survey.

(3) Number of sources from [MA93] that are located in field.

(4) Number of common sources (within 3″) between our survey and [MA93].

(3) Number of sources from [M10] that are located in field.

(4) Number of common sources (within 3″) between our survey and [M10].

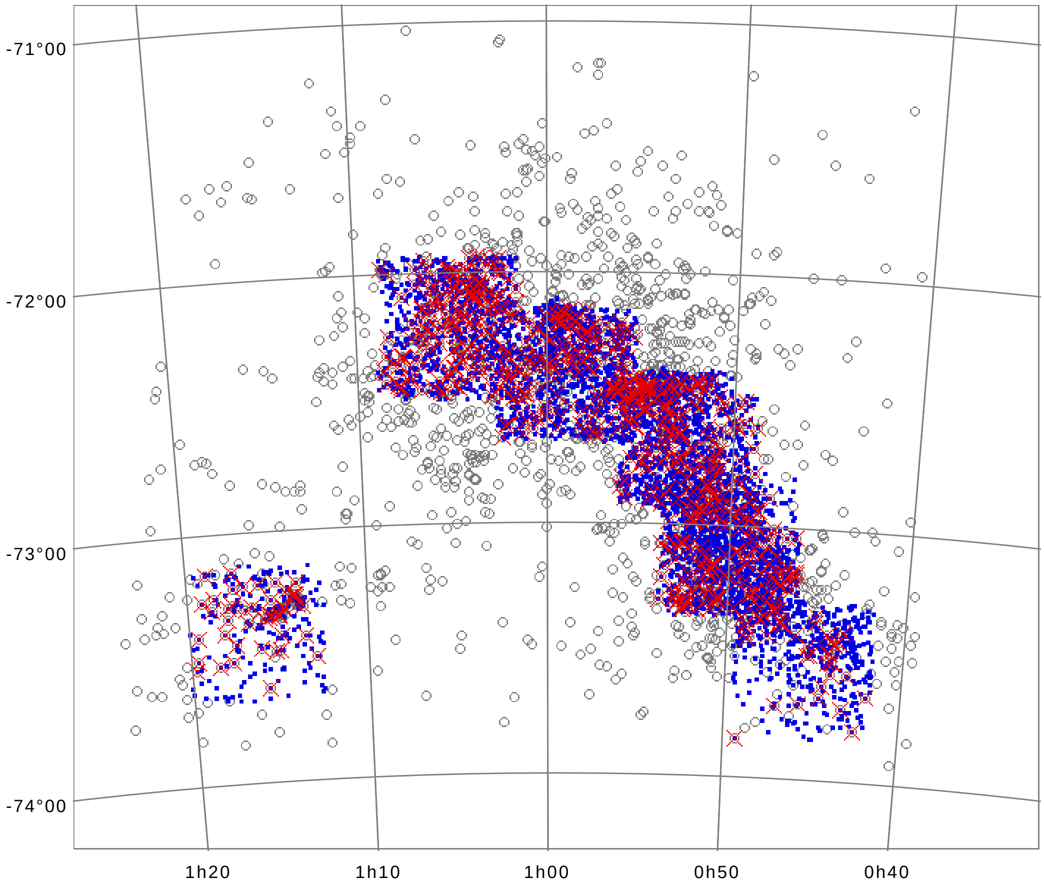

Figure 4.7: Illustrative comparison between Meyssonnier & Azzopardi (1993) and our survey for Hα emission sources in the SMC. The open gray circles correspond to 1844 sources identified in Meyssonnier & Azzopardi (1993), and the blue dots correspond to 4747 source identified in this work. The red crosses highlight the 701 common sources (within $3''$ error radius) between the two surveys.

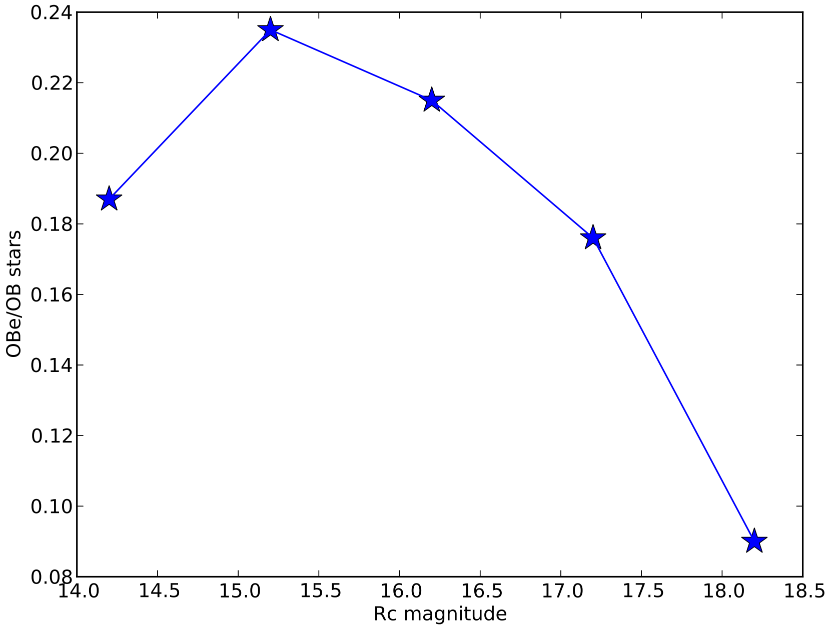

Figure 4.8: The fraction of OBe/OB stars as a function of *Rc* magnitude (corresponding roughly to the spectral type). We notice that the fraction peaks at ~15 mag, which corresponds to a spectral range O9-B2 at the distance of the SMC. The fraction drops with fainter sources (later spectral types).

(e.g. $\sim 12-40\%$; Wisniewski & Bjorkman 2006, $\sim 4-31\%$; Iqbal & Keller 2013).

We further investigate the fraction of OBe/OB stars with respect to their *Rc* magnitude, by dividing the *R*-band range into arbitrary bins which roughly correspond to a sequence of spectral types: brighter than 14.7 mag, 14.7 - 15.7 mag, 15.7 - 16.7 mag, 16.7 - 17.7 mag, fainter than 17.7 mag (up to our limit of 18.7 mag which corresponds to a B8 star). The 1 mag bin size roughly corresponds to 3 spectral types (c.f. Cox 2000). In Figure 4.8 we show the fraction of OBe/OB stars as a function of the *Rc* magnitude. We notice that the fraction peaks at $\sim$ 15 mag, which corresponds to the spectral range O9-B2 at the distance of the SMC, and drops fast with fainter sources (later spectral types). Martayan et al. (2010) have examined this correlation, using spectroscopy, and identified a similar trend (c.f. with their figure 12), but their sample was limited to $V \sim 16.5-17$ mag (corresponding to B2-B3 spectral types stars). Therefore, our analysis confirms this trend by extending the measurement of this fraction to spectral types later the B2.

4.6.3 Hα excess

In Figure 4.9 we plot the color-magnitude diagram (V,$B - V$) for sources from the MCPS catalog (grey; Zaritsky et al. 2002), OB stars (blue; identified based on their photometric parameters as described in Section 4.4), and Hα emission sources (OBe stars; red diamonds). We see that the Hα emission sources are placed to redder colors with respect to the main body of OB stars.

In order to investigate the Hα excess with respect to the star's brightness (or roughly its spectral type), we used the bins introduced in Section 4.6.2 to make histograms of their Hα excess (H$\alpha - Rc$) for different brightness ranges (Figure 4.10). We see that there is a decrease in Hα excess as we proceed from bright ($14.5 < Rc < 15.7$ mag) to fainter ($Rc > 17.7$ mag) sources, which is equivalent to late O- and early B-type stars to later B-type stars (down to ~B8). This effect indicates that the early type stars have larger equatorial decretion disks compared to the later type stars.

4.6.4 BeXRBs

As already presented in Section 4.5 we detected Hα emission sources for $\sim 64\%$ of the confirmed BeXRBs. The missing population can be attributed to the variability of Be stars (since the presence of the disk is a transient phenomenon; e.g. Rivinius et al. 2013) and to a number of sources below our sensitivity limit (i.e. sources with very weak Hα emission).

It is interesting to explore the fraction of BeXRBs with respect to the population of OBe stars, since this gives us a picture of their formation rate. In Table 4.7 we present the numbers of OBe stars, of confirmed and candidate BeXRBs (obtained from Sturm et al. 2013), and the fraction of the confirmed BeXRBs as well as the fraction of the total population of BeXRBs (confirmed and candidates) over the OBe population for each field. We find a ratio of $0.5 - 1.4 \times 10^{-3}$ and $1.6 - 2.1 \times 10^{-3}$ BeXRB/OBe for the confirmed and the total number of BeXRBs, respectively.

We also plot these fractions for each field in Figure 4.11. By comparing the trends of the confirmed BeXRBs (blue) and the total BeXRBs (red) we see good agreement in most cases. However, in Field 9 (F9) we notice a significant difference. The difference between the fraction of the total BeXRBs and of the confirmed BeXRBs is increasing, which is unexpected compared to the other fields. This can be only attributed to the fact that a number of candidate BeXRBs in this field are probably misclassified sources.

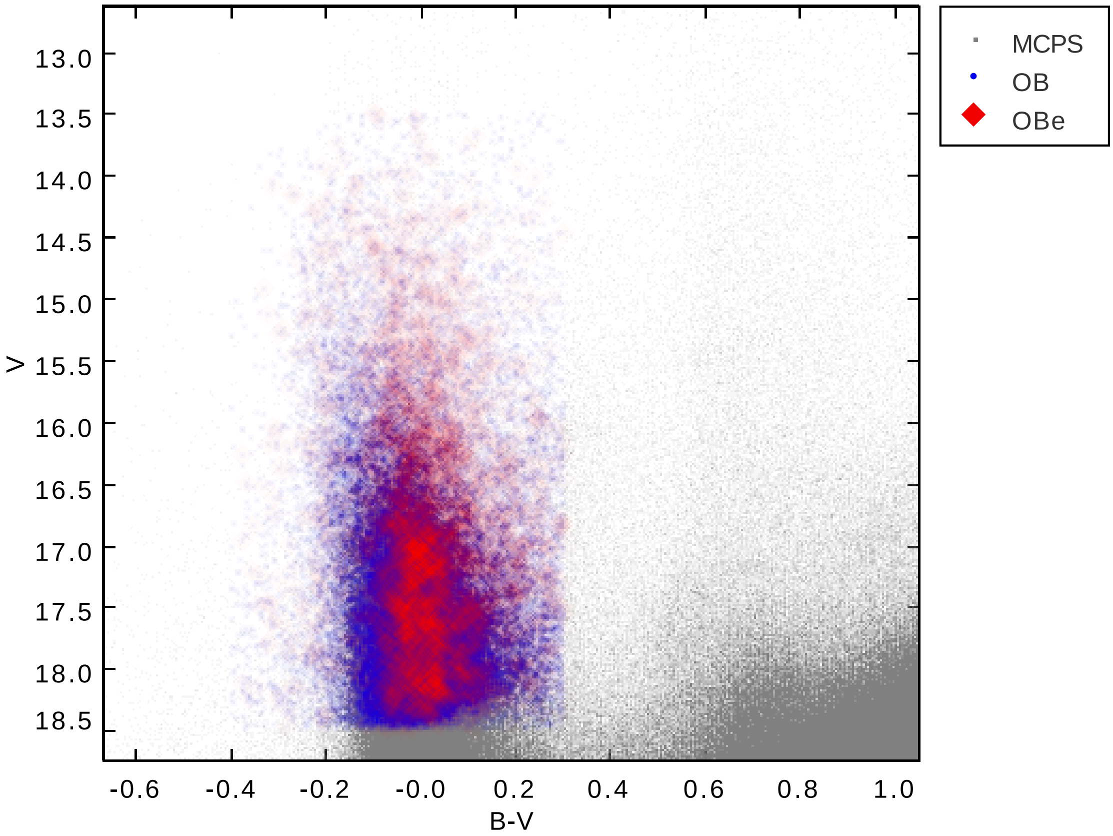

Figure 4.9: Color-magnitude diagram (V,$B-V$) of sources from the MCPS catalog (grey; Zaritsky et al. 2002), OB stars (blue), and Hα emission sources (OBe stars; red diamonds). We see the reddening of the Hα sources as they are located close but to the right of the main sequence.

Table 4.7: Fractions of BeXRBs stars.

Field ID	Confirmed BeXRBs	Candidate BeXRBs	OBe stars	Confirmed BeXRBs/OBe	Confirmed+Candidate BeXRBs/OBe
F2	11	6	9217	1.2×10^{-3}	1.8×10^{-3}
F4	12	6	9799	1.2×10^{-3}	1.8×10^{-3}
F7	12	9	8428	1.4×10^{-3}	2.5×10^{-3}
F8	6	6	7305	0.8×10^{-3}	1.6×10^{-3}
F9	2	6	3672	0.5×10^{-3}	2.1×10^{-3}
F10	2	1	1687	1.2×10^{-3}	1.8×10^{-3}

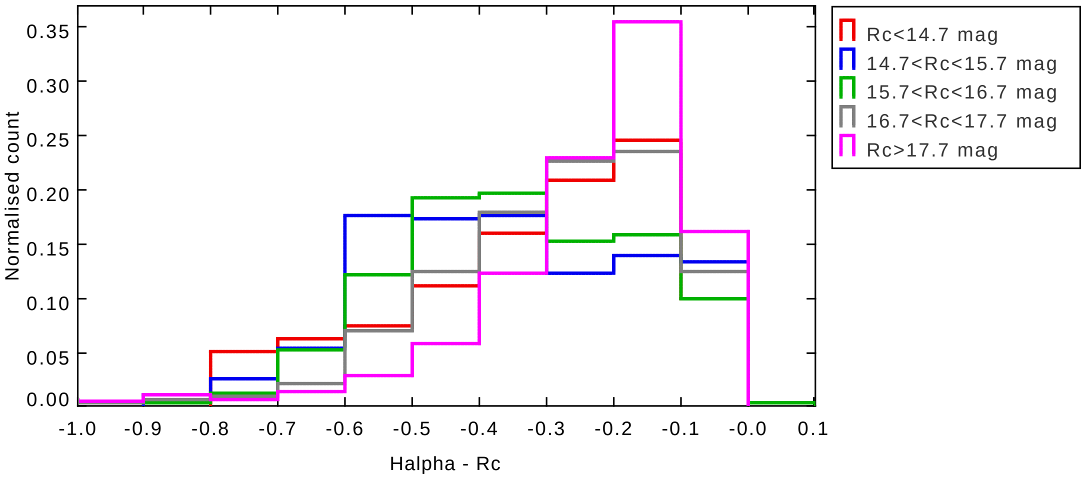

Figure 4.10: Histograms of the H$\alpha - Rc$ index for different R-band ranges. We see that there is a decrease in Hα excess as we proceed from bright (late O- and early B-type stars) to fainter sources (late B-type stars). This is indicative of the size of the equatorial decretion disk, which is larger in early-type B stars.

4.6.5 Candidate BeXRBs

Regarding the candidate BeXRBs, we identified only 25.8% of the candidate HMXBs in Sturm et al. (2013) as emission-line objects. The classification of these sources as candidate HMXBs by Sturm et al. (2013) has been determined by broad-band photometry, by selecting appropriate optical counterparts within the ranges: $13.5 < V < 17$ mag, $-0.5 < B - V < 0.5$ mag, $-1.5 < U - B < -0.2$ mag. The very low recovery rate of these objects as emission-line objects (particularly in comparison to the confirmed BeXRBs) indicates that many of them could be misclassified sources.

In any case we have identified 8 of these candidate BeXRBs as Ha emission OB stars (within $\lesssim 2''$ error radius; see Table 4.5), strongly supporting their BeXRB nature.

One interesting case demonstrating the power of Hα imaging in identifying the correct counterpart of X-ray sources is *XMM* J010247.5-720450. In Figure 4.12 we show the $15'' \times 12''$ region around source with ID 247 in the catalog of Sturm et al. (2013) which corresponds to the X-ray source *XMM* J010247.5-720450 (magenta cross) classified as candidate BeXRB, and located at RA = 01:02:47.5, Dec = -72:04:50.9 (J2000). Sturm et al. (2011) have identified as its optical counterpart the source that coincides with this position (at RA = 01:02:47.61, Dec = -72:04:51.2) with broad-band photometric parameters: U = 14.69 mag, B = 15.75 mag, V = 16.0 mag, I = 16.3 mag, J = 16.58 mag, H = 16.52, and Ks = 16.61 mag (green circle).

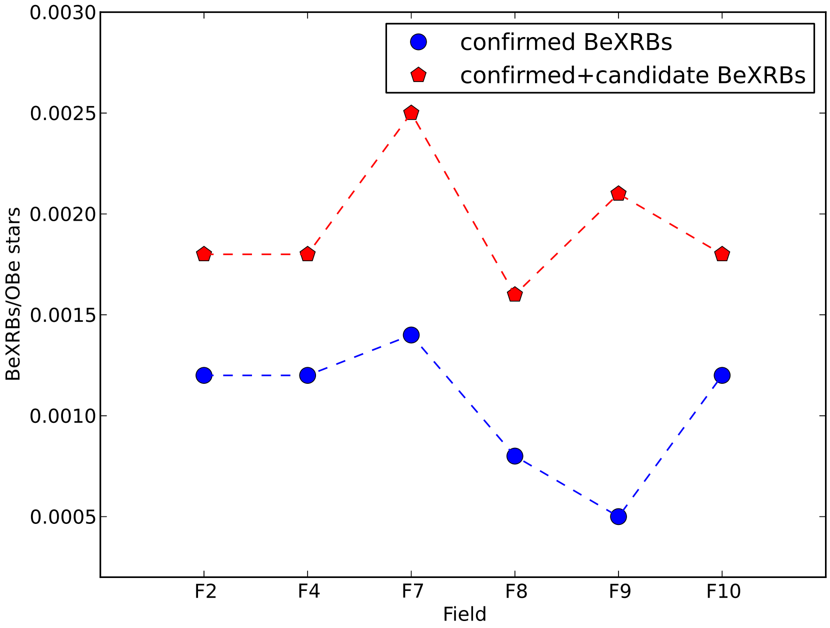

Figure 4.11: Fractions of confirmed BeXRBs (blue) and the total number of BeXRBs (confirmed and candidates) from the census of Sturm et al. (2013) over the number of OBe stars for each field. We notice that the trend of the total number follows that of confirmed except for Field 9 (F9), in which the number of candidate BeXRBs is probably overestimated.

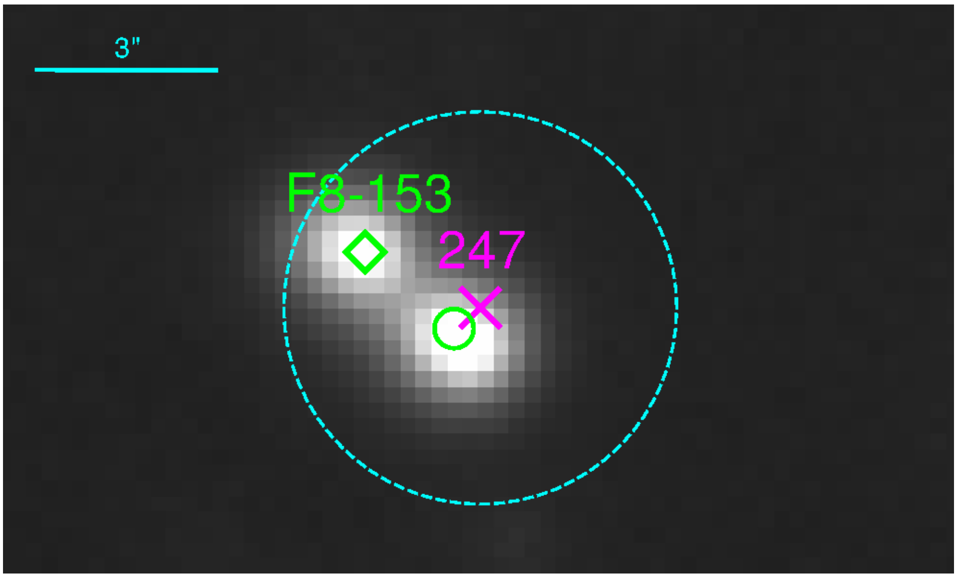

Figure 4.12: The region (15″ × 12″) around X-ray source *XMM* J010247.5-720450 (RA: 01:02:47.5, Dec: -72:04:50.9 (J2000)), classified as candidate BeXRB (magenta cross, source 247 in Sturm et al. 2013). The source at RA = 01:02:47.61, Dec = -72:04:51.2 (green circle; Sturm et al. 2011) has been identified as its optical counterpart. Within 2.01″ (RA: 01:02:47.9, Dec: -72:04:50.0 (J2000)) we find the Hα emission source F8-153 (green diamond), with H$\alpha - Rc = -0.238 \pm 0.033$ mag, and SNR$\sim$ 6.4. We propose this source as the optical counterpart of X-ray source, favoring its BeXRB nature. The search radius of 3″ around the X-ray source is also presented with a cyan circle.

In the same Figure we also show the position of the Hα emission source F8-153 (green diamond), and an error radius of 3″ (cyan circle). From our analysis we find that this source (located 2.01″ from the X-ray source) possess also properties of an OB star ($V = 16.051$ mag, $B - V = -0.2$ mag; Zaritsky et al. 2002). Thus, we propose that the optical counterpart of this X-ray source is source F8-153.

4.7 Summary

We have performed a wide-field Hα imaging survey in order to identify SMC BeXRBs with Hα excess, and obtain their fraction with respect to the general population of OBe stars. For this we used the WFI camera at the 2.2 m MPG/ESO telescope to observe 6 selected regions of the SMC with recent star-formation, in the broad-band Rc and the narrow-band Hα filters.

The dithered exposures were combined into mosaic images, independently for each filter, and the DAOPHOT/IRAF package was used to derive PSF photometry on the *R*-band mosaic. Flux calibration was performed using observations of standard stars and accounting for the filter responses. After cleaning the initial *Rc* sources list from non-stellar sources, we selected only those that are located within the locus of OB stars in the SMC (Antoniou et al., 2009b), and we cross-correlated this list with the photometry from the Hα mosaic.

We calculated the minimum H$\alpha - Rc$ index for the general population of OB stars (for each field separately), which corresponds to the index for non-Hα emitting stars. We selected sources at 5σ above that minimum. Our results from the Hα wide-area narrow-band imaging of the SMC can be summarized as:

- We detected 4747 Hα emission sources. We give the tables for these sources at the Appendix B. This is a major increase (2 to 4 times more in each field) compared to the previous work of (Meyssonnier & Azzopardi, 1993).
- We estimated the fraction of OBe/OB stars, and we find a mean value of ~13%. We further examined this fraction by looking into different *Rc* magnitude bins (corresponding aprroximately to 3 spectral types) to find that the fraction peaks at ~15 mag (corresponding to a spectral range O9-B2) and then decreases to fainter (later B-type stars). This is indicative of the size of the equatorial decretion disk, which is larger in early-type B stars.
- We cross-correlated our catalog with the X-ray catalog of Sturm et al. (2013), and identified 39 sources. Out of these sources 25 were already confirmed HMXBs, 8 were candidate HMXBs, and 5 other types of sources. We are recovering the ~64% and ~26% of the confirmed and candidate HMXBs. The missing population for the confirmed BeXRBs can be attributed to the variability of Be stars and to sources with very weak Hα emission. However, the fraction for the candidate HMXBs indicates possible misclassifications in the catalog of Sturm et al. (2013) (possibly due to chance coincidence).
- We provide strong support in favor of the BeXRB nature for 8 candidate HMXBs (Sturm et al., 2013) by identifying Hα emission from their optical counterparts.
- We studied the fraction of BeXRBs with respect to the OBe population in order to define their formation fraction. We find formation rates in the range of 0.5-1.4×10^{-3} BeXRB/OBe (for the different fields) when only the confirmed BeXRBs are used, and in the range of 1.6-2.1×10^{-3} BeXRB/OBe when the total number (confirmed and candidates) of BeXRBs is used.

5

Conclusions and Future perspectives

5.1 Conclusions

In this section we summarize the results obtained from our investigation of the High-Mass X-ray Binary (HMXB) population in the Small Magellanic Cloud (SMC), using two methods to obtain their observational parameters (spectral types, Hα excess), and the development of two techniques for automated and quantitative spectral classification.

5.1.1 Optical spectroscopy

Optical spectroscopy is the optimal tool to characterize optical counterparts of HMXBs. Signatures of early type stars (e.g. He II lines) and/or emission lines, provide the strongest evidence for a HMXB system. Only recently we have been able to obtain spectral classification for large samples of HMXBs (Antoniou et al., 2009a; McBride et al., 2008) in the SMC. Access to such a sample allows for comparison of the spectral-type distributions between the HMXB populations of our Galaxy and the SMC. This is of interest since these two populations reside in environments of different metallicities (SMC metallicity is 1/5 of that of our Galaxy). However so far there is no indication of any difference, although a significant fraction of the HMXBs have still unknown spectral types, and their majority have unknown orbital periods and eccentricities. In order to fully address this issue we need to work toward characterizing the remaining sample of HMXBs in the SMC.

For this reason we performed spectroscopic observations of the optical counterparts of X-ray sources detected in the *Chanda* and *XMM-Newton* surveys of the SMC, using the AAOmega multi-fiber spectrograph at the 3.9 m Anglo-Australian Telescope. Our aim was to observe sources identified in Antoniou et al. (2010, 2009b), in order to identify new HMXBs and determine their spectral types.

From this work we obtained the following results:

- ▷ Spectral-type classifications for 5 new BeXRBs and 1 known supergiant system. We confirmed the previous classifications (within 0.5 spectral type) of 12 sources, while for 3 sources our revised classification, with higher resolution and S/N data, result in later (by 1-1.5 subclass) spectral types.

- ▷ A comparison between the population of BeXRBs in the SMC and the Milky Way with respect to their spectral types reveals marginal evidence for difference. However, we find no statistically significant differences between their orbital parameters (periods and eccentricities). This result further supports other lines of evidence for similar supernova kick velocities between the low metallicity SMC and the Milky Way.

- ▷ We provide strong evidence for an association between the well known supergiant star LHA 115-S 18 and the X-ray source CXOU J005409.57-724143.5. However, its optical and X-ray properties do not allow us to distinguish between a colliding-wind system or a supergiant X-ray binary. If the second scenario proves to be correct, then this source would be the first extragalactic supergiant X-ray binary with a B[e] companion.

5.1.2 Development of automated spectral classifier

It is common to consider spectral classification as an art, because of the power of the human eye as a patter recognition classifier. Stellar spectral classification is based on the presence or absence of diagnostic lines, a process that often is subjective, and it gives only a rough estimate of the classification error. We can overcome these limitations using objective, and preferably, automated, methods based on quantitative measurements of spectral features.

We presented an automated spectral classifier for O- and B-type stars (although it can be used for any spectral type), based on the spectral classification criteria developed for stars in our Galaxy (Walborn & Fitzpatrick, 1990) or in a low metallicity environment such as the SMC (Evans et al., 2004).

We identified a set of diagnostic spectral lines to use as indicators of the different spectral types. We used their equivalent widths in our diagnostic scheme, since they are a robust quantity for comparisons between spectra taken under varying circumstances (e.g. instruments used) and different formats (normalized or not).

We developed two classification methods, established on totally different approaches:

- ▷ The Continuous Fit approach gives the spectral-type of a star as the solution of an equation involving the equivalent widths of different spectral lines. Within the typical uncertainty of this method (~ 2 spectral types) we are able to correctly classify the majority of the sources in our training and BeXRB test samples, for both galaxies ($58 - 72\%$ success rate).

- ▷ The Naive Bayesian Classifier gives the probability that a spectrum corresponds to a given spectral type, based on the distribution of equivalent widths of diagnostic lines of stars of different spectral types. The training of the classifier was done for the largest SMC training sample (which is however biased to early-type stars). Thus, we are able to correctly classify the majority of the early-type stars, found in the SMC training sample and the Galactic BeXRB test sample ($75 - 85\%$ success rate). The performance of the classifier is poorer for the Galactic training sample and the SMC BeXRBs ($32 - 45\%$ success rate), as it misclassifies the later-type stars of these samples.

- ▷ The results for both methods are very promising, and with some improvements their success rate can be improved further, allowing us to reliably and quantitatively classify automatically large samples of spectra.

5.1.3 Hα imaging

Strong Hα emission is a characteristic feature of BeXRBs, making them easily detectable in Hα imaging observations. For this reason we performed a wide-field Hα imaging campaign to identify Hα emission sources in the SMC. Using the WFI camera at the 2.2 m WFI/MPG telescope we observed 6 selected regions of the SMC with recent star-formation in the *Rc* and Hα filters. After the initial processing of the data, construction of mosaics, PSF photometry, and flux calibration in each band, we identified Hα emission sources at a 5σ level above the mean H$\alpha - Rc$ index for non Hα-excess stars (calculated individually for each field). We focused only on OB stars selected from their optical photometric properties following Antoniou et al. (2009b).

The results obtained from this analysis are:

▷ We detected 4747 Hα emission sources. This is a major increase (a factor of 2 to 4 for in each field) compared to the previous work of Meyssonnier & Azzopardi (1993).

▷ We estimated the fraction of OBe/OB stars, and we find a mean value of ∼13%. We further examined this fraction by looking into different *Rc* magnitude bins (corresponding approximately to 3 spectral types) to find that the fraction peaks at ∼15 mag (corresponding to a spectral range O9-B2) and then decreases to fainter (later B-type) stars. This is indicative of size of the equatorial decretion disk, which is larger in early type B stars.

▷ We cross-correlated our catalog with the X-ray catalog of from the XMM-Newton survey of the SMC (Sturm et al., 2013), and we identified 39 sources. Out of these sources, 25 were already confirmed HMXBs, 8 were candidate HMXBs, and 5 other types of sources. We are recovering the ∼64% and ∼26% of the confirmed and candidate HMXBs, respectively. The missing population for the confirmed BeXRBs can be attributed to the variability of Be stars and to sources with very weak Hα emission. However, the fraction for the candidate HMXBs indicates possible misclassifications in the catalog of Sturm et al. (2013) (possibly due to chance coincidence).

▷ We provide strong support in favor of the BeXRB nature for 8 candidate HMXBs (Sturm et al., 2013) by identifying Hα excess from their optical counterparts.

▷ We studied the fraction of BeXRBs with respect to the OBe population in order to define their formation fraction. We find rates in the range of 0.5-1.4$\times10^{-3}$ BeXRB/OBe (for the different fields) when only the confirmed BeXRBs are used, and in the range of 1.6-2.1$\times10^{-3}$ BeXRB/OBe when the total number (confirmed and candidates) of BeXRBs is used.

5.2 Future work

5.2.1 Automated spectral classifier

The results obtained from the automated spectral classifier developed for the classification of early-type stars are very promising. Measuring the equivalent width by fitting the spectral line rather than taking the ratio of integrated flux in fixed bands will allow for more accurate measurements of the line EW and the possibility to measure much fainter lines. Furthermore, the Continuous Fit method will be greatly improved by combining these more accurate measurements with a wider set of diagnostic spectral lines. This will also provide a better estimation of the spectral-type uncertainties.

The Naive Bayesian Classifier is efficient in spectral classification of early B-type sources, but really poor for late B-type sources. As it was shown this is due to the training of the classifier. A less biased training sample which would reflect better the late B-type sources would improve its efficiency.

With a sufficiently large Galactic training sample we could also test the effect of metallicity in the classification results, e.g. what would be the classification success ratio for a Galactic sample of stars when the classifier is trained with a sample of lower metallicity, like SMC (at 1/5 of the Galactic metallicity).

Although both methods were developed in order to classify the OB stars, there can be applied in other spectral types if an appropriate set of diagnostic lines exists and there is a sufficient sample of spectra to train the methods.

5.2.2 BeXRBs and Hα emission sources

We measured the fractions for OBe stars with respect to OB stars, and for BeXRBs with respect to OBe stars. These fractions are particularly important since they provide insights in their formation efficiency. Next steps in this investigation include:

(a) Comparison between the OBe stars in the field and in clusters. There are many studies for OBe fractions in SMC open clusters (e.g. Iqbal & Keller, 2013; Martayan et al., 2010) but a thorough investigation for the field has not been performed so far. This will allow us to investigate the effect of the environment.

(b) The fraction of OBe stars that are BeXRBs provide constrains in the formation rate of BeXRBs. Further investigation of this fraction as a function of the age of the stellar populations can provide information for the formation mechanisms of BeXRBs (e.g. Antoniou et al., 2010).

5.2.3 Optical spectroscopy of HMXBs

We have shown already that optical spectroscopy is the optimal tool to securely identify and classify HMXBs. However, a large fraction of candidate HMXBs in the SMC remains unconfirmed and unclassified, therefore this work needs to continue in order to: (i) confirm the HMXB nature of the candidate sources, (ii) find their spectral type (which reflects the mass of their donor star).

The knowledge of the spectral-type distributions allows the investigation for differences between the populations of HMXBs (and specially BeXRBs) between the SMC and the Galaxy. Studies so far (e.g Antoniou et al., 2009a; McBride et al., 2008; Townsend et al., 2011) did not show any sign of difference. However, we have identified a small (but significant at 99%) difference in the spectral-type distribution of our SMC BeXRBs sample with respect to the Galactic BeXRBs. Further investigation is needed in order to verify this result, which means that more and accurate spectral classifications of BeXRBs are required.

For this we have been granted already 2-nights at the VIMOS spectrograph at one of the 8.2 m ESO telescopes, to perform multi-slit spectroscopy on a large number of confirmed and candidate HMXBs. The observations are being performed while writing this thesis and the data will become available soon.

5.2.4 sgXRBs in the SMC

Our recent result on the association of the sgB[e] star LHA 115-S 18 with the X-ray source CXOU J005409.57-724143.5, opens the question regarding the population of sgXRBs in the SMC, as only one is known (SMC X-1; Webster et al. 1972) within its population of almost 100 HMXBs. We have discussed it in the context of obscured wind-fed sgXRBs (e.g. Walter et al., 2006), i.e. systems that are deeply embedded into a cocoon of dense matter. However, different approaches are possible, e.g. a colliding-wind binary (Clark et al., 2013).

Therefore, it is important to further explore the nature of this source and investigate for similar sources.

References

Alcock, C., Allsman, R. A., Alves, D., Axelrod, T. S., Becker, A. C., Bennett, D. P., Cook, K. H., Freeman, K. C., Griest, K., Guern, J., Lehner, M. J., Marshall, S. L., Peterson, B. A., Pratt, M. R., Quinn, P. J., Rodgers, A. W., Stubbs, C. W., Sutherland, W., & Welch, D. L. 1997, ApJ, 486, 697 28

Alcock, C., Allsman, R. A., Alves, D. R., Axelrod, T. S., Becker, A. C., Bennett, D. P., Cook, K. H., Drake, A. J., Freeman, K. C., Geha, M., Griest, K., Lehner, M. J., Marshall, S. L., Minniti, D., Peterson, B. A., Popowski, P., Pratt, M. R., Nelson, C. A., Quinn, P. J., Stubbs, C. W., Sutherland, W., Tomaney, A. B., Vandehei, T., Welch, D. L., & MACHO Collaboration. 1999, PASP, 111, 1539 28

Allende Prieto, C., Beers, T. C., Wilhelm, R., Newberg, H. J., Rockosi, C. M., Yanny, B., & Lee, Y. S. 2006, ApJ, 636, 804 62

Antoniou, V., Hatzidimitriou, D., Zezas, A., & Reig, P. 2009a, ApJ, 707, 1080 xxi, xxii, xxiii, 19, 25, 31, 37, 40, 43, 45, 46, 47, 50, 54, 61, 139, 144

Antoniou, V., Zezas, A., Hatzidimitriou, D., & Kalogera, V. 2010, ApJ, 716, L140 xxi, 6, 19, 25, 26, 37, 42, 43, 45, 48, 58, 105, 106, 140, 144

Antoniou, V., Zezas, A., Hatzidimitriou, D., & McDowell, J. C. 2009b, ApJ, 697, 1695 xxii, 17, 19, 25, 26, 37, 42, 43, 52, 55, 58, 105, 122, 138, 140, 142, 159, 165, 166

Azzopardi, M., Vigneau, J., & Macquet, M. 1975, A&AS, 22, 285 25, 28, 51

Bakos, G. Á., Hartman, J. D., Torres, G., Kovács, G., Noyes, R. W., Latham, D. W., Sasselov, D. D., & Béky, B. 2011, in European Physical Journal Web of Conferences, Vol. 11, European Physical Journal Web of Conferences, 1002 200

Baraffe, I., Chabrier, G., Barman, T. S., Selsis, F., Allard, F., & Hauschildt, P. H. 2005, A&A, 436, L47 201

Bartlett, E. S., Clark, J. S., Coe, M. J., Garcia, M. R., & Uttley, P. 2013, MNRAS, 429, 1213 56, 57

Belczynski, K. & Ziolkowski, J. 2009, ApJ, 707, 870 14

Berta, Z. K., Irwin, J., Charbonneau, D., Burke, C. J., & Falco, E. E. 2012, AJ, 144, 145 200

Bertin, E. 2006, in Astronomical Society of the Pacific Conference Series, Vol. 351, Astronomical Data Analysis Software and Systems XV, 112 110

Bertin, E. & Arnouts, S. 1996, A&AS, 117, 393 107

Bertin, E., Mellier, Y., Radovich, M., Missonnier, G., Didelon, P., & Morin, B. 2002, in Astronomical Society of the Pacific Conference Series, Vol. 281, Astronomical Data Analysis Software and Systems XI, 228 110

Bica, E. L. D. & Schmitt, H. R. 1995, ApJS, 101, 41 39

Bird, A. J., Coe, M. J., McBride, V. A., & Udalski, A. 2012, MNRAS, 423, 3663 19

Bodaghee, A., Courvoisier, T. J.-L., Rodriguez, J., Beckmann, V., Produit, N., Hannikainen, D., Kuulkers, E., Willis, D. R., & Wendt, G. 2007, A&A, 467, 585 xix, 6, 8

Boirin, L., Parmar, A. N., Oosterbroek, T., Lumb, D., Orlandini, M., & Schartel, N. 2002, A&A, 394, 205 56

Bonanos, A. Z., Lennon, D. J., Köhlinger, F., van Loon, J. T., Massa, D. L., Sewilo, M., Evans, C. J., Panagia, N., Babler, B. L., Block, M., Bracker, S., Engelbracht, C. W., Gordon, K. D., Hora, J. L., Indebetouw, R., Meade, M. R., Meixner, M., Misselt, K. A., Robitaille, T. P., Shiao, B., & Whitney, B. A. 2010, AJ, 140, 416 28, 51

Bonfils, X., Delfosse, X., Udry, S., Forveille, T., Mayor, M., Perrier, C., Bouchy, F., Gillon, M., Lovis, C., Pepe, F., Queloz, D., Santos, N. C., Ségransan, D., & Bertaux, J.-L. 2013, A&A, 549, A109 224

Bonfils, X., Gillon, M., Udry, S., Armstrong, D., Bouchy, F., Delfosse, X., Forveille, T., Fumel, A., Jehin, E., Lendl, M., Lovis, C., Mayor, M., McCormac, J., Neves, V., Pepe, F., Perrier, C., Pollaco, D., Queloz, D., & Santos, N. C. 2012, A&A, 546, A27 201

Borucki, W. J., Koch, D., Basri, G., Batalha, N., Brown, T., Caldwell, D., Caldwell, J., Christensen-Dalsgaard, J., Cochran, W. D., DeVore, E., Dunham, E. W., Dupree, A. K., Gautier, T. N., Geary, J. C., Gilliland, R., Gould, A., Howell, S. B., Jenkins, J. M., Kondo, Y., Latham, D. W., Marcy, G. W., Meibom, S., Kjeldsen, H., Lissauer, J. J., Monet, D. G., Morrison, D., Sasselov, D., Tarter, J., Boss, A., Brownlee, D., Owen, T., Buzasi, D., Charbonneau, D., Doyle, L., Fortney, J., Ford, E. B., Holman, M. J., Seager, S., Steffen, J. H., Welsh, W. F., Rowe, J., Anderson, H., Buchhave, L., Ciardi, D., Walkowicz, L., Sherry, W., Horch, E., Isaacson, H., Everett, M. E., Fischer, D., Torres, G., Johnson, J. A., Endl, M., MacQueen, P., Bryson, S. T., Dotson, J., Haas, M., Kolodziejczak, J., Van Cleve, J., Chandrasekaran, H., Twicken, J. D., Quintana, E. V., Clarke, B. D., Allen, C., Li, J., Wu, H., Tenenbaum, P., Verner, E., Bruhweiler, F., Barnes, J., & Prsa, A. 2010, Science, 327, 977 200

Boué, G., Figueira, P., Correia, A. C. M., & Santos, N. C. 2012, A&A, 537, L3 201

Boyajian, T. S., von Braun, K., van Belle, G., McAlister, H. A., ten Brummelaar, T. A., Kane, S. R., Muirhead, P. S., Jones, J., White, R., Schaefer, G., Ciardi, D., Henry, T., López-Morales, M., Ridgway, S., Gies, D., Jao, W.-C., Rojas-Ayala, B., Parks, J. R., Sturmann, L., Sturmann, J., Turner, N. H., Farrington, C., Goldfinger, P. J., & Berger, D. H. 2012, ApJ, 757, 112 202, 216

Broos, P. S., Getman, K. V., Povich, M. S., Townsley, L. K., Feigelson, E. D., & Garmire, G. P. 2011, ApJS, 194, 4 63, 88, 100

Brown, T. M., Latham, D. W., Everett, M. E., & Esquerdo, G. A. 2011, AJ, 142, 112 221

Brunini, A. & Cionco, R. G. 2005, Icarus, 177, 264 201

Carciofi, A. C. 2011, in IAU Symposium, Vol. 272, IAU Symposium, 325–336 12

Carone, L., Gandolfi, D., Cabrera, J., Hatzes, A. P., Deeg, H. J., Csizmadia, S., Pätzold, M., Weingrill, J., Aigrain, S., Alonso, R., Alapini, A., Almenara, J.-M., Auvergne, M., Baglin, A., Barge, P., Bonomo, A. S., Bordé, P., Bouchy, F., Bruntt, H., Carpano, S., Cochran, W. D., Deleuil, M., Díaz, R. F., Dreizler, S., Dvorak, R., Eislöffel, J., Eigmüller, P., Endl, M., Erikson, A., Ferraz-Mello, S., Fridlund, M., Gazzano, J.-C., Gibson, N., Gillon, M., Gondoin, P., Grziwa, S., Günther, E. W., Guillot, T., Hartmann, M., Havel, M., Hébrard, G., Jorda, L., Kabath, P., Léger, A., Llebaria, A., Lammer, H., Lovis, C., MacQueen, P. J., Mayor, M., Mazeh, T., Moutou, C., Nortmann, L., Ofir, A., Ollivier, M., Parviainen, H., Pepe, F., Pont, F., Queloz, D., Rabus, M., Rauer, H., Régulo, C., Renner, S., de La Reza, R., Rouan, D., Santerne, A., Samuel, B., Schneider, J., Shporer, A., Stecklum, B., Tal-Or, L., Tingley, B., Udry, S., & Wuchterl, G. 2012, A&A, 538, A112 200

Carroll, B. W. & Ostlie, D. A. 2006, An introduction to modern astrophysics and cosmology (Pearson Education Inc.) 1

Casares, J., Negueruela, I., Ribó, M., Ribas, I., Paredes, J. M., Herrero, A., & Simón-Díaz, S. 2014, Nature, 505, 378 14

Charbonneau, D., Berta, Z. K., Irwin, J., Burke, C. J., Nutzman, P., Buchhave, L. A., Lovis, C., Bonfils, X., Latham, D. W., Udry, S., Murray-Clay, R. A., Holman, M. J., Falco, E. E., Winn, J. N., Queloz, D., Pepe, F., Mayor, M., Delfosse, X., & Forveille, T. 2009, Nature, 462, 891 200

Charbonneau, D., Brown, T. M., Latham, D. W., & Mayor, M. 2000, ApJ, 529, L45 200

Charles, P. A. & Coe, M. J. 2006, Optical, ultraviolet and infrared observations of X-ray binaries, 215–265 1, 24

Chaty, S. 2011, in Astronomical Society of the Pacific Conference Series, Vol. 447, Evolution of Compact Binaries, 29 24, 25

Chaty, S. 2013, Advances in Space Research, 52, 2132 15

Chaty, S., Rahoui, F., Foellmi, C., Tomsick, J. A., Rodriguez, J., & Walter, R. 2008, A&A, 484, 783 15

Christian, D. J., Pollacco, D. L., Skillen, I., Street, R. A., Keenan, F. P., Clarkson, W. I., Collier Cameron, A., Kane, S. R., Lister, T. A., West, R. G., Enoch, B., Evans, A., Fitzsimmons, A., Haswell, C. A., Hellier, C., Hodgkin, S. T., Horne, K., Irwin, J., Norton, A. J., Osborne, J., Ryans, R., Wheatley, P. J., & Wilson, D. M. 2006, MNRAS, 372, 1117 202

Claret, A. 2000, A&A, 363, 1081 215

—. 2004, A&A, 428, 1001 215

Clark, J. S., Bartlett, E. S., Coe, M. J., Dorda, R., Haberl, F., Lamb, J. B., Negueruela, I., & Udalski, A. 2013, A&A, 560, A10 51, 52, 57, 105, 144

Clark, J. S., Muno, M. P., Negueruela, I., Dougherty, S. M., Crowther, P. A., Goodwin, S. P., & de Grijs, R. 2008, A&A, 477, 147 56, 57, 58

Clark, J. S., Steele, I. A., Fender, R. P., & Coe, M. J. 1999, A&A, 348, 888 56, 57

Coe, M. J. 2005, MNRAS, 358, 1379 19, 45

Coe, M. J., Edge, W. R. T., Galache, J. L., & McBride, V. A. 2005, MNRAS, 356, 502 9, 19, 25, 31

Collier Cameron, A., Pollacco, D., Street, R. A., Lister, T. A., West, R. G., Wilson, D. M., Pont, F., Christian, D. J., Clarkson, W. I., Enoch, B., Evans, A., Fitzsimmons, A., Haswell, C. A., Hellier, C., Hodgkin, S. T., Horne, K., Irwin, J., Kane, S. R., Keenan, F. P., Norton, A. J., Parley, N. R., Osborne, J., Ryans, R., Skillen, I., & Wheatley, P. J. 2006, MNRAS, 373, 799 203, 204, 205, 213

Collins, II, G. W. 1987, in IAU Colloq. 92: Physics of Be Stars, 3–19 9

Conover, W. J. 1999, Practical Nonparametric Statistics (John Wiley and Sons Ltd) 43

Corbet, R. H. D. 1984, A&A, 141, 91 11

—. 1986, MNRAS, 220, 1047 xx, 11, 13

Cox, A. N. 2000, Allen's astrophysical quantities (Springer-Verlag New York Inc.) 20, 111, 132, 202

Cumming, A., Butler, R. P., Marcy, G. W., Vogt, S. S., Wright, J. T., & Fischer, D. A. 2008, PASP, 120, 531 218

Davis, L. E. 1993, in Astronomical Society of the Pacific Conference Series, Vol. 52, Astronomical Data Analysis Software and Systems II, 420 111

Dickey, J. M. & Lockman, F. J. 1990, ARA&A, 28, 215 30

Dotter, A., Chaboyer, B., Jevremović, D., Kostov, V., Baron, E., & Ferguson, J. W. 2008, ApJS, 178, 89 221

Drave, S. P., Bird, A. J., Townsend, L. J., Hill, A. B., McBride, V. A., Sguera, V., Bazzano, A., & Clark, D. J. 2012, A&A, 539, A21 xx, 11, 13

Dray, L. M. 2006, MNRAS, 370, 2079 17

Duan, F.-Q., Liu, R., Guo, P., Zhou, M.-Q., & Wu, F.-C. 2009, Research in Astronomy and Astrophysics, 9, 341 62

Duncan, D. K., Vaughan, A. H., Wilson, O. C., Preston, G. W., Frazer, J., Lanning, H., Misch, A., Mueller, J., Soyumer, D., Woodard, L., Baliunas, S. L., Noyes, R. W., Hartmann, L. W., Porter, A., Zwaan, C., Middelkoop, F., Rutten, R. G. M., & Mihalas, D. 1991, ApJS, 76, 383 210

Ekström, S., Meynet, G., Maeder, A., & Barblan, F. 2008, A&A, 478, 467 62

Erben, T., Schirmer, M., Dietrich, J. P., Cordes, O., Haberzettl, L., Hetterscheidt, M., Hildebrandt, H., Schmithuesen, O., Schneider, P., Simon, P., Deul, E., Hook, R. N., Kaiser, N., Radovich, M., Benoist, C., Nonino, M., Olsen, L. F., Prandoni, I., Wichmann, R., Zaggia, S., Bomans, D., Dettmar, R. J., & Miralles, J. M. 2005, Astronomische Nachrichten, 326, 432 107

Evans, C. J., Howarth, I. D., Irwin, M. J., Burnley, A. W., & Harries, T. J. 2004, MNRAS, 353, 601 xxv, 37, 63, 64, 91, 92, 101, 141

Filliatre, P. & Chaty, S. 2004, ApJ, 616, 469 56, 57

Fressin, F., Torres, G., Charbonneau, D., Bryson, S. T., Christiansen, J., Dressing, C. D., Jenkins, J. M., Walkowicz, L. M., & Batalha, N. M. 2013, ApJ, 766, 81 219, 221

Fukugita, M., Ichikawa, T., Gunn, J. E., Doi, M., Shimasaku, K., & Schneider, D. P. 1996, AJ, 111, 1748 219

Gagné, M., Fehon, G., Savoy, M. R., Cartagena, C. A., Cohen, D. H., & Owocki, S. P. 2012, in Astronomical Society of the Pacific Conference Series, Vol. 465, Proceedings of a Scientific Meeting in Honor of Anthony F. J. Moffat, 301 58

Gaidos, E. 2013, ApJ, 770, 90 221

Gaidos, E., Fischer, D. A., Mann, A. W., & Howard, A. W. 2013, ApJ, 771, 18 217, 219, 221, 222

Gaidos, E. & Mann, A. W. 2013, ApJ, 762, 41 224

Galache, J. L., Corbet, R. H. D., Coe, M. J., Laycock, S., Schurch, M. P. E., Markwardt, C., Marshall, F. E., & Lochner, J. 2008, ApJS, 177, 189 17

Gardiner, L. T. & Hatzidimitriou, D. 1992, MNRAS, 257, 195 17

Giacconi, R., Gursky, H., Paolini, F. R., & Rossi, B. B. 1962, Physical Review Letters, 9, 439 1

Gillon, M., Pont, F., Demory, B.-O., Mallmann, F., Mayor, M., Mazeh, T., Queloz, D., Shporer, A., Udry, S., & Vuissoz, C. 2007, A&A, 472, L13 201, 210

Graus, A. S., Lamb, J. B., & Oey, M. S. 2012, ApJ, 759, 10 37, 57

Gray, R. O. & Corbally, J., C. 2009, Stellar Spectral Classification (Princeton University Press) 37, 64, 65, 67

Grimm, H.-J., Gilfanov, M., & Sunyaev, R. 2002, A&A, 391, 923 xix, 6, 7

—. 2003, MNRAS, 339, 793 19, 105

Gulati, R. K., Gupta, R., Gothoskar, P., & Khobragade, S. 1996, Bulletin of the Astronomical Society of India, 24, 21 62

Haberl, F. & Pietsch, W. 2004, A&A, 414, 667 17, 25, 26

Hamuy, M., Walker, A. R., Suntzeff, N. B., Gigoux, P., Heathcote, S. R., & Phillips, M. M. 1992, PASP, 104, 533 107, 116, 117

Hansen, B. M. S. & Murray, N. 2012, ApJ, 751, 158 201

Hanuschik, R. W. 1996, A&A, 308, 170 12

Harris, J. & Zaritsky, D. 2004, AJ, 127, 1531 19, 25, 105

Hartman, J. D., Bakos, G. Á., Kipping, D. M., Torres, G., Kovács, G., Noyes, R. W., Latham, D. W., Howard, A. W., Fischer, D. A., Johnson, J. A., Marcy, G. W., Isaacson, H., Quinn, S. N., Buchhave, L. A., Béky, B., Sasselov, D. D., Stefanik, R. P., Esquerdo, G. A., Everett, M., Perumpilly, G., Lázár, J., Papp, I., & Sári, P. 2011, ApJ, 728, 138 201

Hatzidimitriou, D. & Hawkins, M. R. S. 1989, MNRAS, 241, 667 17

Haubois, X., Carciofi, A. C., Rivinius, T., Okazaki, A. T., & Bjorkman, J. E. 2012, ApJ, 756, 156 12

Henize, K. G. 1956, ApJS, 2, 315 xx, xxii, 25, 28, 36, 51, 52

Henry, G. W., Marcy, G. W., Butler, R. P., & Vogt, S. S. 2000, ApJ, 529, L41 200

Hilditch, R. W., Howarth, I. D., & Harries, T. J. 2005, MNRAS, 357, 304 16, 24, 42, 111

Howard, A. W., Marcy, G. W., Bryson, S. T., Jenkins, J. M., Rowe, J. F., Batalha, N. M., Borucki, W. J., Koch, D. G., Dunham, E. W., Gautier, III, T. N., Van Cleve, J., Cochran, W. D., Latham, D. W., Lissauer, J. J., Torres, G., Brown, T. M., Gilliland, R. L., Buchhave, L. A., Caldwell, D. A., Christensen-Dalsgaard, J., Ciardi, D., Fressin, F., Haas, M. R., Howell, S. B., Kjeldsen, H., Seager, S., Rogers, L., Sasselov, D. D., Steffen, J. H., Basri, G. S., Charbonneau, D., Christiansen, J., Clarke, B., Dupree, A., Fabrycky, D. C., Fischer, D. A., Ford, E. B., Fortney, J. J., Tarter, J., Girouard, F. R., Holman, M. J., Johnson, J. A., Klaus, T. C., Machalek, P., Moorhead, A. V., Morehead, R. C., Ragozzine, D., Tenenbaum, P., Twicken, J. D., Quinn, S. N., Isaacson, H., Shporer, A., Lucas, P. W., Walkowicz, L. M., Welsh, W. F., Boss, A., Devore, E., Gould, A., Smith, J. C., Morris, R. L., Prsa, A., Morton, T. D., Still, M., Thompson, S. E., Mullally, F., Endl, M., & MacQueen, P. J. 2012, ApJS, 201, 15 218, 219, 224

Howard, A. W., Marcy, G. W., Johnson, J. A., Fischer, D. A., Wright, J. T., Isaacson, H., Valenti, J. A., Anderson, J., Lin, D. N. C., & Ida, S. 2010, Science, 330, 653 222

Howarth, I. D., Murray, J., Mills, D., & Berry, D. S. 2004, DIPSO – A friendly spectrum analysis program, Starlink User Note 50.24 32

Hünsch, M., Schmitt, J. H. M. M., Sterzik, M. F., & Voges, W. 1999, A&AS, 135, 319 210

Illarionov, A. F. & Sunyaev, R. A. 1975, A&A, 39, 185 11

Iqbal, S. & Keller, S. C. 2013, MNRAS, 435, 3103 106, 129, 132, 143

Isaacson, H. & Fischer, D. 2010, ApJ, 725, 875 210

Jacoby, G. H., Hunter, D. A., & Christian, C. A. 1984, ApJS, 56, 257 64

Kaper, L., van der Meer, A., & Tijani, A. H. 2004, in Revista Mexicana de Astronomia y Astrofisica Conference Series, Vol. 21, Revista Mexicana de Astronomia y Astrofisica Conference Series, 128–131 24

Kashyap, V. L., van Dyk, D. A., Connors, A., Freeman, P. E., Siemiginowska, A., Xu, J., & Zezas, A. 2010, ApJ, 719, 900 30

Knigge, C., Coe, M. J., & Podsiadlowski, P. 2011, Nature, 479, 372 11, 23

Kogure, T. & Leung, K. C. 2007, The Astrophysics of Emission-Line Stars (Springer Science+Business Media, LLC) 20

Kovács, G., Bakos, G., & Noyes, R. W. 2005, MNRAS, 356, 557 203

Kovács, G., Zucker, S., & Mazeh, T. 2002, A&A, 391, 369 203, 204

Kunitomo, M., Ikoma, M., Sato, B., Katsuta, Y., & Ida, S. 2011, ApJ, 737, 66 224

Lamers, H. J. G. L. M., van den Heuvel, E. P. J., & Petterson, J. A. 1976, A&A, 49, 327 24

Lamers, H. J. G. L. M., Zickgraf, F.-J., de Winter, D., Houziaux, L., & Zorec, J. 1998, A&A, 340, 117 37, 51

Laughlin, G., Bodenheimer, P., & Adams, F. C. 2004, ApJ, 612, L73 201

Lépine, S. & Gaidos, E. 2011, AJ, 142, 138 202

Lépine, S. & Shara, M. M. 2005, AJ, 129, 1483 202

Lewin, W. H. G., van Paradijs, J., & van den Heuvel, E. P. J. 1997, X-ray Binaries (Cambridge University Press) 1

Liu, Q. Z., van Paradijs, J., & van den Heuvel, E. P. J. 2000, A&AS, 147, 25 17

—. 2005, A&A, 442, 1135 17, 23, 105

—. 2006, A&A, 455, 1165 14, 23, 24, 25

Lomb, N. R. 1976, Ap&SS, 39, 447 52

Longair, M. 2011, High Energy Astrophysics (Cambridge University Press) 55

Lucke, R., Yentis, D., Friedman, H., Fritz, G., & Shulman, S. 1976, ApJ, 206, L25 25

Lutovinov, A. A., Revnivtsev, M. G., Tsygankov, S. S., & Krivonos, R. A. 2013, MNRAS, 431, 327 24

Maeder, A., Grebel, E. K., & Mermilliod, J.-C. 1999, A&A, 346, 459 106

Majid, W. A., Lamb, R. C., & Macomb, D. J. 2004, ApJ, 609, 133 17, 19, 105

Mann, A. W., Gaidos, E., & Aldering, G. 2011, PASP, 123, 1273 208

Mann, A. W., Gaidos, E., Kraus, A., & Hilton, E. J. 2013, ApJ, 770, 43 225

Mann, A. W., Gaidos, E., Lépine, S., & Hilton, E. J. 2012, ApJ, 753, 90 221

Manousakis, A. 2011, PhD thesis, Univ. of Genève xxiii, 54

Manousakis, A. & Walter, R. 2011, A&A, 526, A62 57

Maragoudaki, F., Kontizas, M., Morgan, D. H., Kontizas, E., Dapergolas, A., & Livanou, E. 2001, A&A, 379, 864 17

Maravelias, G., Zezas, A., Antoniou, V., & Hatzidimitriou, D. 2014, MNRAS, 438, 2005 62, 64, 65, 100, 104, 105

Markwardt, C. B. 2009, in Astronomical Society of the Pacific Conference Series, Vol. 411, Astronomical Data Analysis Software and Systems XVIII, 251 216

Martayan, C., Baade, D., & Fabregat, J. 2010, A&A, 509, A11 106, 129, 132, 143

Martayan, C., Floquet, M., Hubert, A. M., Gutiérrez-Soto, J., Fabregat, J., Neiner, C., & Mekkas, M. 2007, A&A, 472, 577 106, 129

Massey, P. 2002, ApJS, 141, 81 xxvi, 119, 120

Massey, P. & Duffy, A. S. 2001, ApJ, 550, 713 51

Mathew, B., Subramaniam, A., & Bhatt, B. C. 2008, MNRAS, 388, 1879 106

Mayor, M., Marmier, M., Lovis, C., Udry, S., Ségransan, D., Pepe, F., Benz, W., Bertaux, J. ., Bouchy, F., Dumusque, X., Lo Curto, G., Mordasini, C., Queloz, D., & Santos, N. C. 2011, ArXiv e-prints 224

McBride, V. A., Coe, M. J., Negueruela, I., Schurch, M. P. E., & McGowan, K. E. 2008, MNRAS, 388, 1198 xxi, xxii, xxiii, 19, 25, 37, 40, 42, 43, 45, 46, 47, 50, 54, 62, 139, 144, 159, 165, 166

McCook, G. P. & Sion, E. M. 1987, ApJS, 65, 603 209

McNeil, D. S. & Nelson, R. P. 2010, MNRAS, 401, 1691 201

McSwain, M. V. & Gies, D. R. 2005a, ApJ, 622, 1052 106, 123

—. 2005b, ApJS, 161, 118 19, 106

Meynet, G. & Maeder, A. 2000, A&A, 361, 101 9, 62

Meyssonnier, N. & Azzopardi, M. 1993, A&AS, 102, 451 xxvi, 17, 129, 131, 138, 142

Mineo, S., Gilfanov, M., & Sunyaev, R. 2012, MNRAS, 419, 2095 16

Mokiem, M. R., de Koter, A., Vink, J. S., Puls, J., Evans, C. J., Smartt, S. J., Crowther, P. A., Herrero, A., Langer, N., Lennon, D. J., Najarro, F., & Villamariz, M. R. 2007, A&A, 473, 603 14, 56

Montgomery, D. C. & Runger, G. C. 2010, Applied Statistics and Probability for Engineers (John Wiley and Sons Ltd) 90

Mordasini, C., Alibert, Y., & Benz, W. 2009, A&A, 501, 1139 201

Morris, P. W., Eenens, P. R. J., Hanson, M. M., Conti, P. S., & Blum, R. D. 1996, ApJ, 470, 597 38, 51

Munar-Adrover, P., Paredes, J. M., Ribó, M., Iwasawa, K., Zabalza, V., & Casares, J. 2014, ApJ, 786, L11 14

Murphy, M. T. & Bessell, M. S. 2000, MNRAS, 311, 741 17, 39

Navarro, S. G., Corradi, R. L. M., & Mampaso, A. 2012, A&A, 538, A76 62, 88

Negueruela, I., Smith, D. M., Reig, P., Chaty, S., & Torrejón, J. M. 2006, in ESA Special Publication, Vol. 604, The X-ray Universe 2005, ed. A. Wilson, 165 15, 24

Novara, G., La Palombara, N., Mereghetti, S., Haberl, F., Coe, M., Filipovic, M., Udalski, A., Paizis, A., Pietsch, W., Sturm, R., Gilfanov, M., Tiengo, A., Payne, J., Smits, D., & de Horta, A. 2011, A&A, 532, A153 31

Okazaki, A. T. 1991, PASJ, 43, 75 12

—. 1997, A&A, 318, 548 62

Park, T., Kashyap, V. L., Siemiginowska, A., van Dyk, D. A., Zezas, A., Heinke, C., & Wargelin, B. J. 2006, ApJ, 652, 610 31

Pietrzyński, G., Graczyk, D., Gieren, W., Thompson, I. B., Pilecki, B., Udalski, A., Soszyński, I., Kozłowski, S., Konorski, P., Suchomska, K., Bono, G., Moroni, P. G. P., Villanova, S., Nardetto, N., Bresolin, F., Kudritzki, R. P., Storm, J., Gallenne, A., Smolec, R., Minniti, D., Kubiak, M., Szymański, M. K., Poleski, R., Wyrzykowski, Ł., Ulaczyk, K., Pietrukowicz, P., Górski, M., & Karczmarek, P. 2013, Nature, 495, 76 16

Pollacco, D. L., Skillen, I., Collier Cameron, A., Christian, D. J., Hellier, C., Irwin, J., Lister, T. A., Street, R. A., West, R. G., Anderson, D. R., Clarkson, W. I., Deeg, H., Enoch, B., Evans, A., Fitzsimmons, A., Haswell, C. A., Hodgkin, S., Horne, K., Kane, S. R., Keenan, F. P., Maxted, P. F. L., Norton, A. J., Osborne, J., Parley, N. R., Ryans, R. S. I., Smalley, B., Wheatley, P. J., & Wilson, D. M. 2006, PASP, 118, 1407 200

Pollock, A. M. T. 1987, ApJ, 320, 283 57

Pont, F., Zucker, S., & Queloz, D. 2006, MNRAS, 373, 231 200, 213

Porter, J. M. & Rivinius, T. 2003, PASP, 115, 1153 9, 24, 62, 65

Rahoui, F., Chaty, S., Lagage, P.-O., & Pantin, E. 2008, A&A, 484, 801 15

Rajoelimanana, A. F., Charles, P. A., & Udalski, A. 2011, MNRAS, 413, 1600 xxi, xxii, 11, 12, 19, 43, 45, 48, 49, 50

Reid, I. N., Hawley, S. L., & Gizis, J. E. 1995, AJ, 110, 1838 209

Reig, P. 2011, Ap&SS, 332, 1 xix, xxii, 1, 2, 9, 12, 17, 24, 45, 50, 61, 105

Reig, P. & Roche, P. 1999, MNRAS, 306, 100 12, 24

Reig, P. & Zezas, A. 2014, A&A, 561, A137 65, 104

Rivinius, T., Baade, D., & Štefl, S. 2003, A&A, 411, 229 9

Rivinius, T., Carciofi, A. C., & Martayan, C. 2013, A&A Rev., 21, 69 9, 61, 62, 65, 105, 133

Rogers, L. A., Bodenheimer, P., Lissauer, J. J., & Seager, S. 2011, ApJ, 738, 59 201

Russell, S. C. & Dopita, M. A. 1992, ApJ, 384, 508 17, 103

Saxton, R. D., Read, A. M., Esquej, P., Freyberg, M. J., Altieri, B., & Bermejo, D. 2008, A&A, 480, 611 25

Scargle, J. D. 1982, ApJ, 263, 835 52

Schirmer, M. 2013, ApJS, 209, 21 107

Schmidtke, P. C. & Cowley, A. P. 2006, AJ, 132, 919 19

Schmidtke, P. C., Cowley, A. P., Levenson, L., & Sweet, K. 2004, AJ, 127, 3388 19

Schurch, M. P. E., Coe, M. J., McBride, V. A., Townsend, L. J., Udalski, A., Haberl, F., & Corbet, R. H. D. 2011, MNRAS, 412, 391 19, 51

Sharp, R., Saunders, W., Smith, G., Churilov, V., Correll, D., Dawson, J., Farrel, T., Frost, G., Haynes, R., Heald, R., Lankshear, A., Mayfield, D., Waller, L., & Whittard, D. 2006, in Society of Photo-Optical Instrumentation Engineers (SPIE) Conference Series, Vol. 6269, Society of Photo-Optical Instrumentation Engineers (SPIE) Conference Series 26

Shen, Y. & Turner, E. L. 2008, ApJ, 685, 553 222

Shore, S. N., Sanduleak, N., & Allen, D. A. 1987, A&A, 176, 59 37, 38, 51, 52

Shortridge, K., Meyerdierks, H., Currie, M., Clayton, M., Lockley, J., Charles, A., Davenhall, C., Taylor, M., Ash, T., Wilkins, T., Axon, D., Palmer, J., Holloway, A., & Graffagnino, V. 2004, FIGARO – A general data reduction system, Starlink User Note 86.21 27

Shtykovskiy, P. E. & Gilfanov, M. R. 2007, Astronomy Letters, 33, 437 19, 105

Sidoli, L., La Palombara, N., Oosterbroek, T., & Parmar, A. N. 2008, A&A, 488, 249 15

Skrutskie, M. F., Cutri, R. M., Stiening, R., Weinberg, M. D., Schneider, S., Carpenter, J. M., Beichman, C., Capps, R., Chester, T., Elias, J., Huchra, J., Liebert, J., Lonsdale, C., Monet, D. G., Price, S., Seitzer, P., Jarrett, T., Kirkpatrick, J. D., Gizis, J. E., Howard, E., Evans, T., Fowler, J., Fullmer, L., Hurt, R., Light, R., Kopan, E. L., Marsh, K. A., McCallon, H. L., Tam, R., Van Dyk, S., & Wheelock, S. 2006, AJ, 131, 1163 202

Smith, A. M. S., Collier Cameron, A., Christian, D. J., Clarkson, W. I., Enoch, B., Evans, A., Haswell, C. A., Hellier, C., Horne, K., Irwin, J., Kane,

S. R., Lister, T. A., Norton, A. J., Parley, N., Pollacco, D. L., Ryans, R., Skillen, I., Street, R. A., Triaud, A. H. M. J., West, R. G., Wheatley, P. J., & Wilsons, D. M. 2007, in Astronomical Society of the Pacific Conference Series, Vol. 366, Transiting Extrapolar Planets Workshop, 152 200, 213

Smith, D., Remillard, R., Swank, J., Takeshima, T., & Smith, E. 1998, IAU Circ., 6855, 1 57

Southworth, J., Hinse, T. C., Jørgensen, U. G., Dominik, M., Ricci, D., Burgdorf, M. J., Hornstrup, A., Wheatley, P. J., Anguita, T., Bozza, V., Novati, S. C., Harpsøe, K., Kjærgaard, P., Liebig, C., Mancini, L., Masi, G., Mathiasen, M., Rahvar, S., Scarpetta, G., Snodgrass, C., Surdej, J., Thöne, C. C., & Zub, M. 2009, MNRAS, 396, 1023 208

Steele, I. A., Negueruela, I., & Clark, J. S. 1999, A&AS, 137, 147 39

Stetson, P. B. 1987, PASP, 99, 191 111

Stevens, I. R., Blondin, J. M., & Pollock, A. M. T. 1992, ApJ, 386, 265 58

Sturm, R., Haberl, F., Pietsch, W., Ballet, J., Hatzidimitriou, D., Buckley, D. A. H., Coe, M., Ehle, M., Filipović, M. D., La Palombara, N., & Tiengo, A. 2013, A&A, 558, A3 vi, viii, xxvii, 17, 106, 123, 125, 128, 133, 135, 136, 137, 138, 142

Sturm, R., Haberl, F., Pietsch, W., & Udalski, A. 2011, The Astronomer's Telegram, 3761, 1 xxvii, 135, 137

Szymanski, M. K. 2005, Acta Astron., 55, 43 28

Tamuz, O., Mazeh, T., & Zucker, S. 2005, MNRAS, 356, 1466 203

Tauris, T. M. & van den Heuvel, E. P. J. 2006, Formation and evolution of compact stellar X-ray sources (Cambridge University Press), 623–665 xix, xx, 1, 3, 4, 5, 9, 10, 61

Taylor, M. B. 2005, in Astronomical Society of the Pacific Conference Series, Vol. 347, Astronomical Data Analysis Software and Systems XIV, 29 119

Townsend, L. J., Coe, M. J., Corbet, R. H. D., & Hill, A. B. 2011, MNRAS, 416, 1556 xxii, 14, 19, 45, 49, 50, 56, 144

Townsend, R. H. D., Owocki, S. P., & Howarth, I. D. 2004, MNRAS, 350, 189 9, 62

Tuohy, I. R. & Rapley, C. G. 1975, ApJ, 198, L69 25

Udalski, A., Kubiak, M., & Szymanski, M. 1997, Acta Astron., 47, 319 28, 111

Udalski, A., Soszyński, I., Szymański, M. K., Kubiak, M., Pietrzyński, G., Wyrzykowski, Ł., Szewczyk, O., Ulaczyk, K., & Poleski, R. 2008, Acta Astron., 58, 329 xxii, 52

Udalski, A., Szymanski, M., Kubiak, M., Pietrzynski, G., Wozniak, P., & Zebrun, K. 1998, Acta Astron., 48, 147 27, 42, 55

van den Heuvel, E. P. J., Portegies Zwart, S. F., Bhattacharya, D., & Kaper, L. 2000a, A&A, 364, 563 19

—. 2000b, A&A, 364, 563 45

van Genderen, A. M. & Sterken, C. 2002, A&A, 386, 926 51

Vieira, S. L. A., Corradi, W. J. B., Alencar, S. H. P., Mendes, L. T. S., Torres, C. A. O., Quast, G. R., Guimarães, M. M., & da Silva, L. 2003, AJ, 126, 2971 37

von Hippel, T., Storrie-Lombardi, L. J., Storrie-Lombardi, M. C., & Irwin, M. J. 1994a, MNRAS, 269, 97 62, 88

von Hippel, T., Storrie-Lombardi, L. J., Storrie-Lombardi, M. C., & Irwin, M. J. 1994b, in Astronomical Society of the Pacific Conference Series, Vol. 60, The MK Process at 50 Years: A Powerful Tool for Astrophysical Insight, 289 62

Walborn, N. R. & Fitzpatrick, E. L. 1990, PASP, 102, 379 xxv, 63, 64, 92, 101, 141

Wall, J. V. & Jenkins, C. R. 2012, Practical Statistics for Astronomers (Cambridge University Press) 88

Walter, R., Rodriguez, J., Foschini, L., de Plaa, J., Corbel, S., Courvoisier, T. J.-L., den Hartog, P. R., Lebrun, F., Parmar, A. N., Tomsick, J. A., & Ubertini, P. 2003, A&A, 411, L427 56

Walter, R., Zurita Heras, J., Bassani, L., Bazzano, A., Bodaghee, A., Dean, A., Dubath, P., Parmar, A. N., Renaud, M., & Ubertini, P. 2006, A&A, 453, 133 15, 24, 56, 57, 144

Webster, B. L., Martin, W. L., Feast, M. W., & Andrews, P. J. 1972, Nature Physical Science, 240, 183 25, 51, 105, 144

Wheatley, P. J., Pollacco, D. L., Queloz, D., Rauer, H., Watson, C. A., West, R. G., Chazelas, B., Louden, T. M., Walker, S., Bannister, N., Bento, J., Burleigh, M., Cabrera, J., Eigmüller, P., Erikson, A., Genolet, L., Goad, M., Grange, A., Jordán, A., Lawrie, K., McCormac, J., & Neveu, M. 2013, in European Physical Journal Web of Conferences, Vol. 47, European Physical Journal Web of Conferences, 13002 225

Williams, B. F., Hatzidimitriou, D., Green, J., Vasilopoulos, G., Covarrubias, R., Pietsch, W. N., Stiele, H., Haberl, F., & Bonfini, P. 2014, MNRAS, 443, 2499 16

Wisniewski, J. P. & Bjorkman, K. S. 2006, ApJ, 652, 458 106, 132

Wisniewski, J. P., Bjorkman, K. S., Bjorkman, J. E., & Clampin, M. 2007, ApJ, 670, 1331 57

Wright, J. T., Marcy, G. W., Howard, A. W., Johnson, J. A., Morton, T. D., & Fischer, D. A. 2012, ApJ, 753, 160 224

Yanagisawa, K., Shimizu, Y., Okita, K., Nagayama, S., Sato, Y., Koyano, H., Okada, T., Iwata, I., Uraguchi, F., Watanabe, E., Yoshida, M., Okumura, S.-i., Nakaya, H., & Yamamuro, T. 2006, in Society of Photo-Optical Instrumentation Engineers (SPIE) Conference Series, Vol. 6269, Society of Photo-Optical Instrumentation Engineers (SPIE) Conference Series

Young, A., Skumanich, A., Stauffer, J. R., Harlan, E., & Bopp, B. W. 1989, ApJ, 344, 427 210

Zaritsky, D., Harris, J., Grebel, E. K., & Thompson, I. B. 2000, ApJ, 534, L53 17

Zaritsky, D., Harris, J., Thompson, I. B., Grebel, E. K., & Massey, P. 2002, AJ, 123, 855 xxvi, 17, 42, 55, 111, 119, 123, 126, 129, 133, 134, 137, 167

Zhang, H. 2004, in Proc. 17th International Florida Artificial Intelligence Research Society Conference (FLAIRS 2004), AAAI Press 88, 89

Zhao, P., Grindlay, J. E., Hong, J. S., Laycock, S., Koenig, X. P., Schlegel, E. M., & van den Berg, M. 2005, ApJS, 161, 429 122

Zickgraf, F.-J., Wolf, B., Leitherer, C., Appenzeller, I., & Stahl, O. 1986, A&A, 163, 119 51

Zickgraf, F.-J., Wolf, B., Stahl, O., & Humphreys, R. M. 1989, A&A, 220, 206 xx, 36, 37, 38, 42, 51, 55, 56

Ziolkowski, J. 2002, Mem. Soc. Astron. Italiana, 73, 1038 9, 11

A

Spectra of SMC BeXRBs with previous classifications

In this section we review the spectral classification for the sources not discussed in Section 2.5.2 (15 in total). For sources that we confirm previous classifications we only give the spectral classification, while for sources with updated classifications we give a detailed account of the basis for these new classifications. We also present all spectra in Fig. A.1.

- *CXOU J004814.15-731004.1 (source CH4-8) - classified as B1.5*

  This source is classified as B1.5, in full agreement with Antoniou et al. (2009b).

- *CXOU J004903.37-725052.5 (source CH7-1) - classified as B1-B5*

  The absence of both HeII $\lambda\lambda$4200, 4686 lines and of the MgII λ4481 line combined with the presence of the HeI λ4471 line, constrain the spectral type in the B1-B5 range, in agreement with McBride et al. (2008) who classified this source as $\sim$B3.

- *CXOU J004913.57-731137.8 (source CH4-2) - classified as B3-B5*

  For this source we obtained spectra on both nights (July 26 and September 19, 2008). The spectral range B3-B5 is determined by the absence of the HeII $\lambda\lambda$4200, 4541, and 4686 lines, and the OII+CIII λ4640-4650 blend, as well as the stronger HeI λ4471 line compared to the MgII λ4481 line. The resulting spectral type is

A. Spectra of SMC BeXRBs with previous classifications

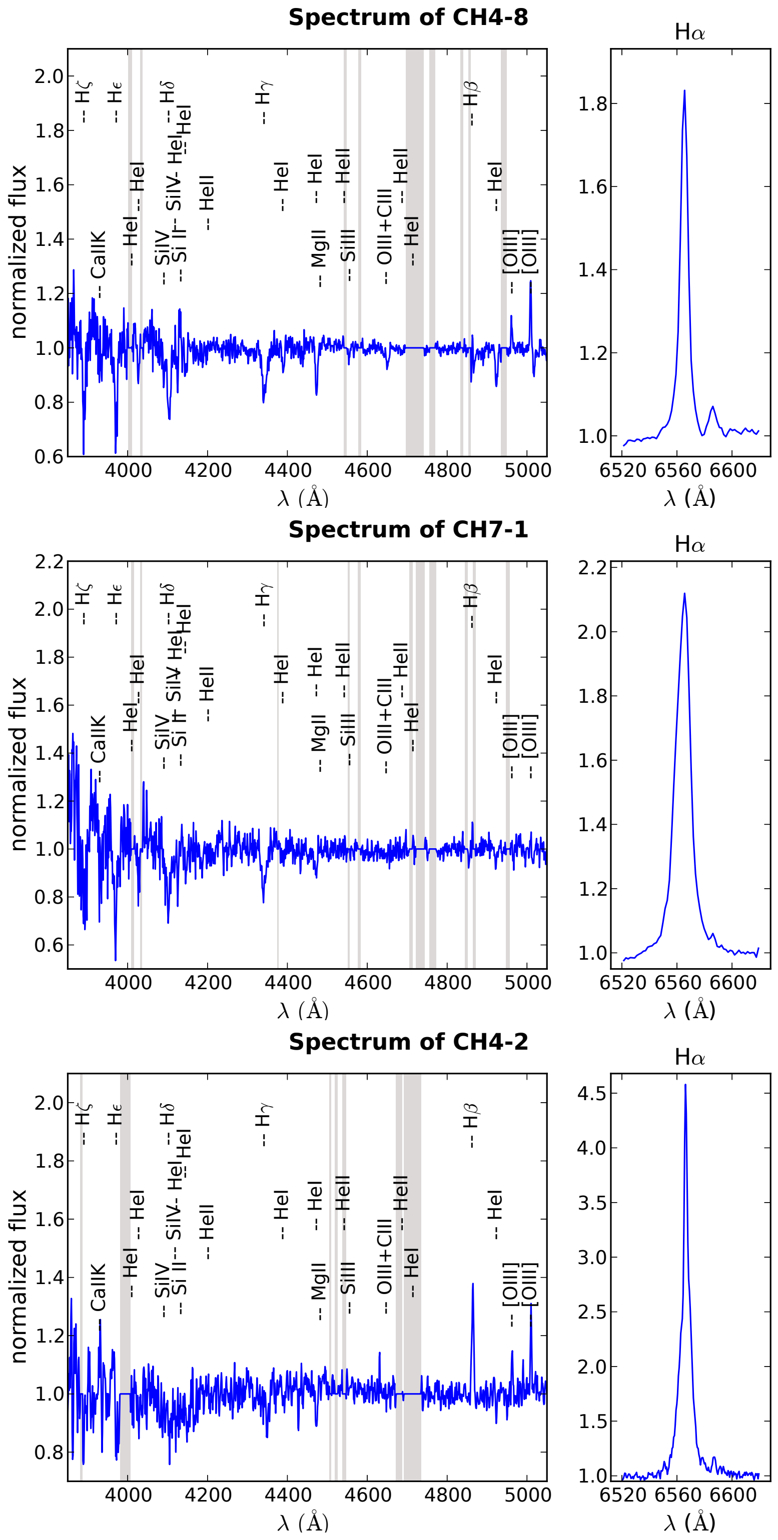

Figure A.1: The spectra of BeXRBs studied in this work with previously known classifications. Shaded areas indicate wavelength ranges for bad columns and/or sky subtraction residuals.

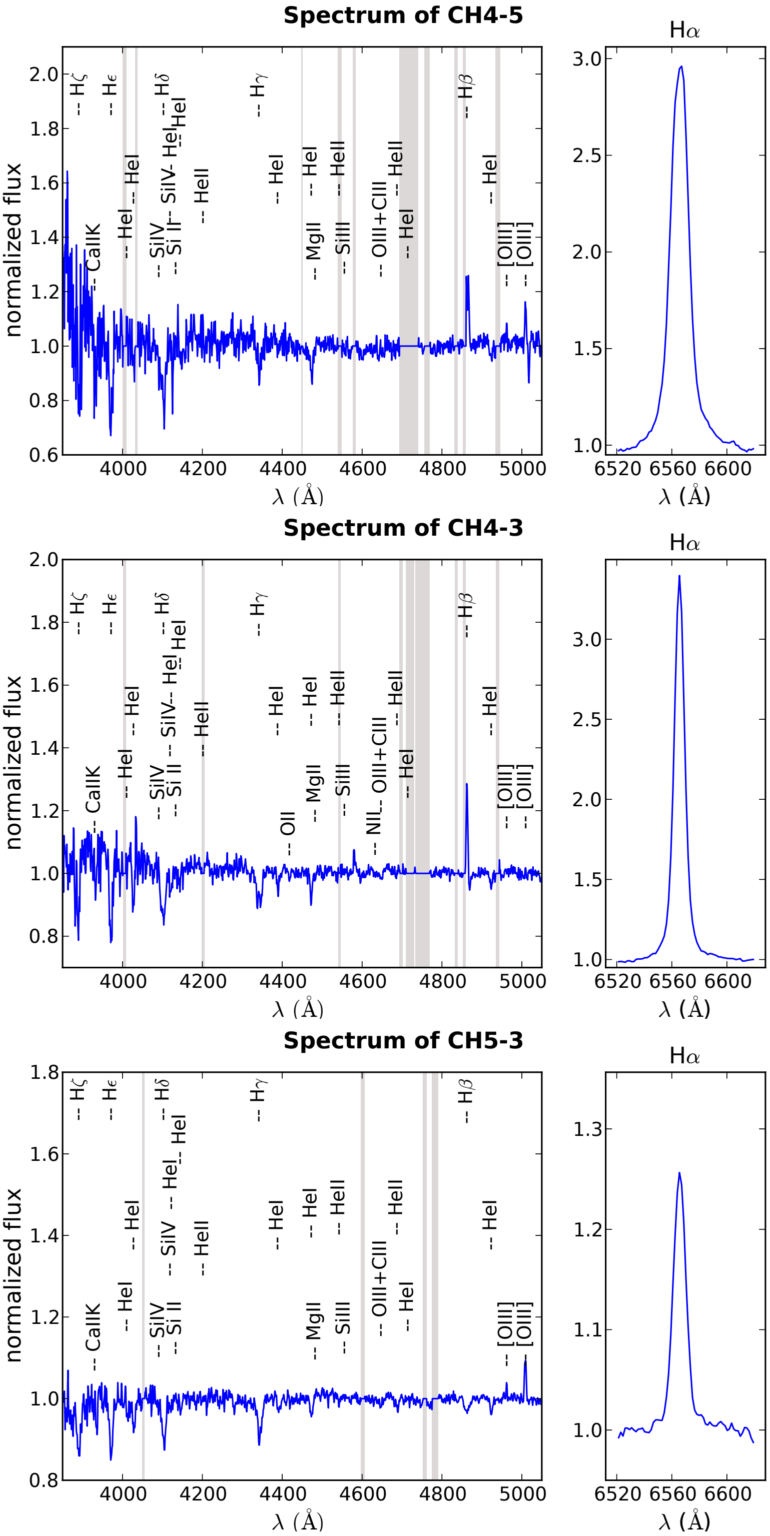

Figure A.1: continued

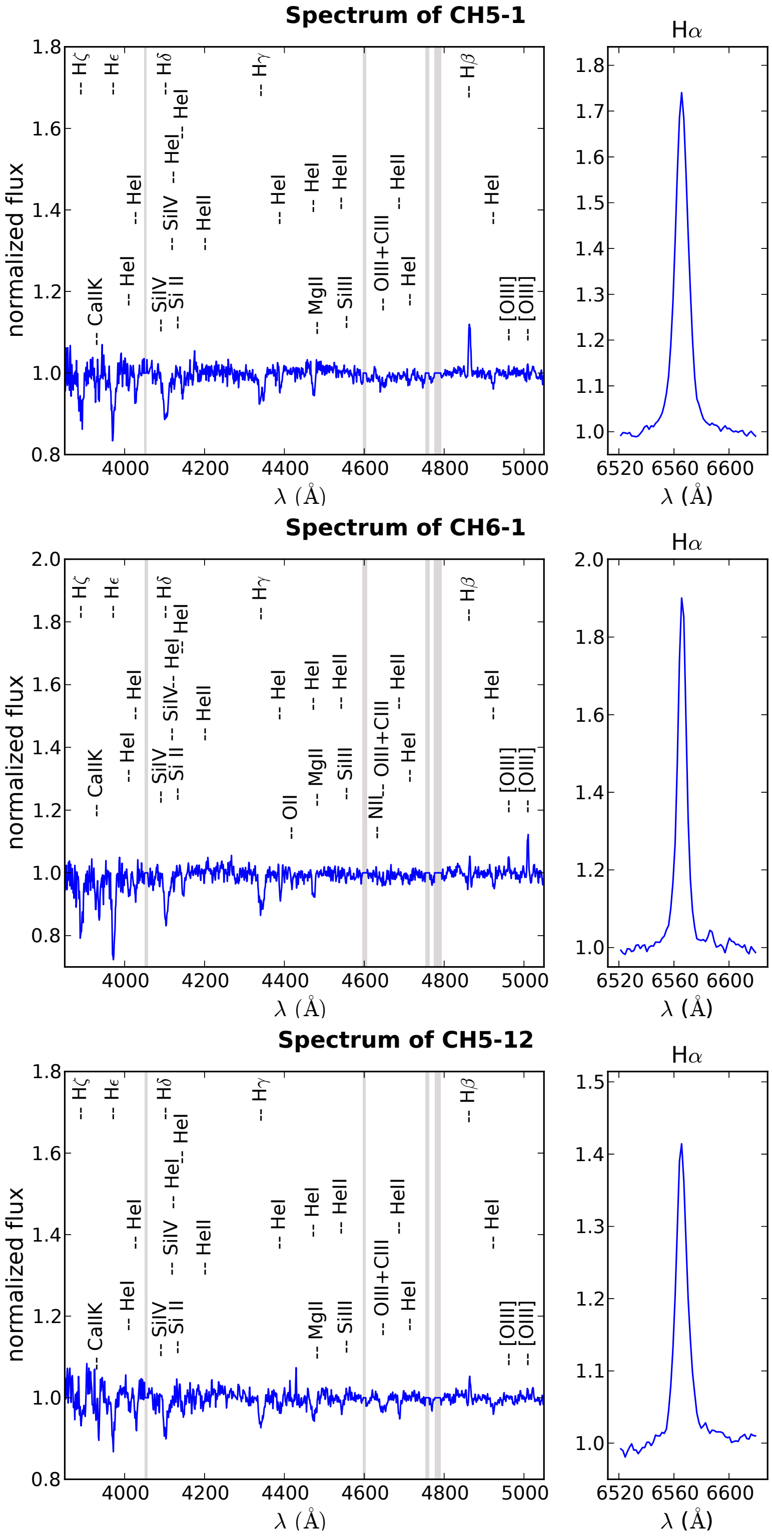

Figure A.1: continued

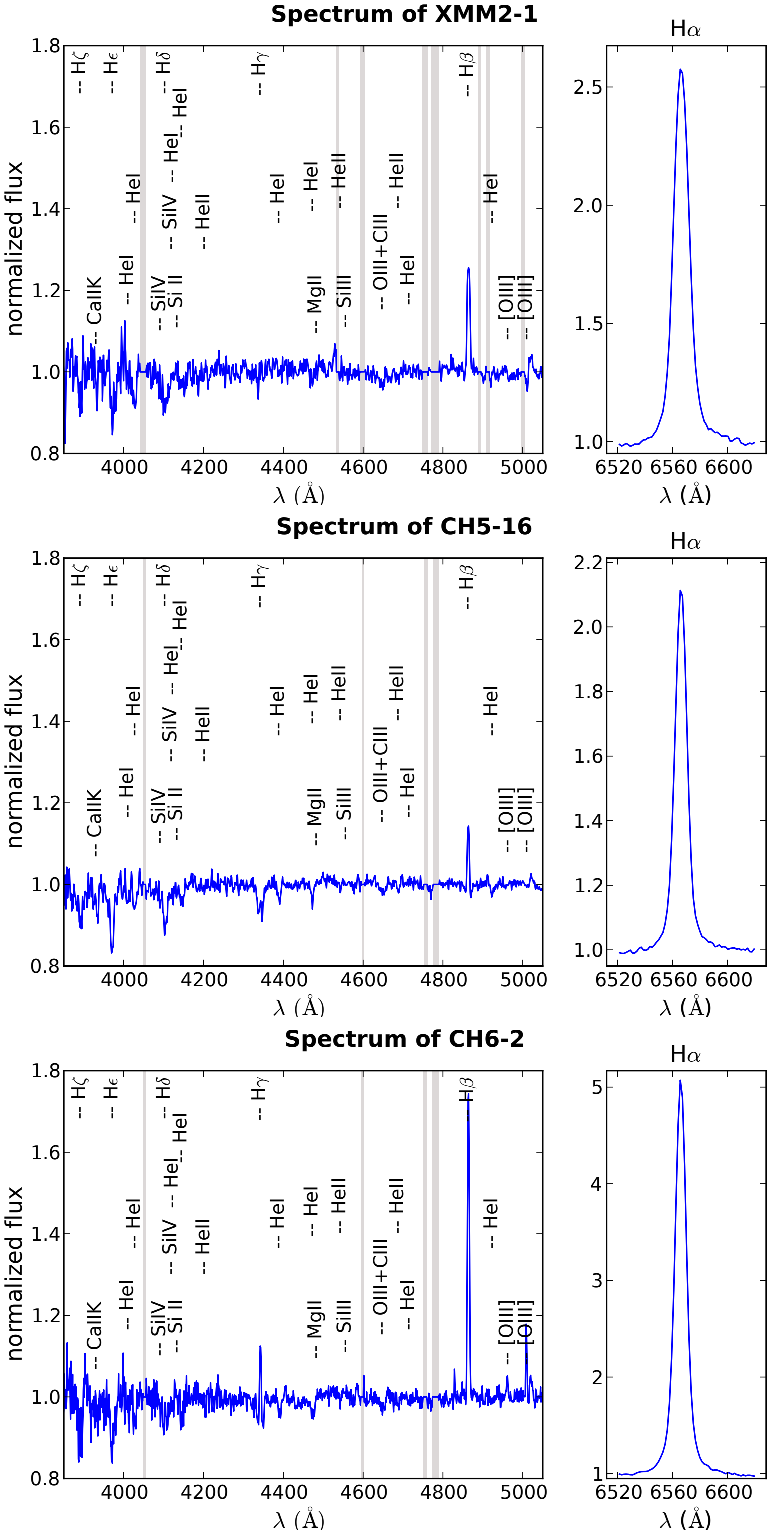

Figure A.1: continued

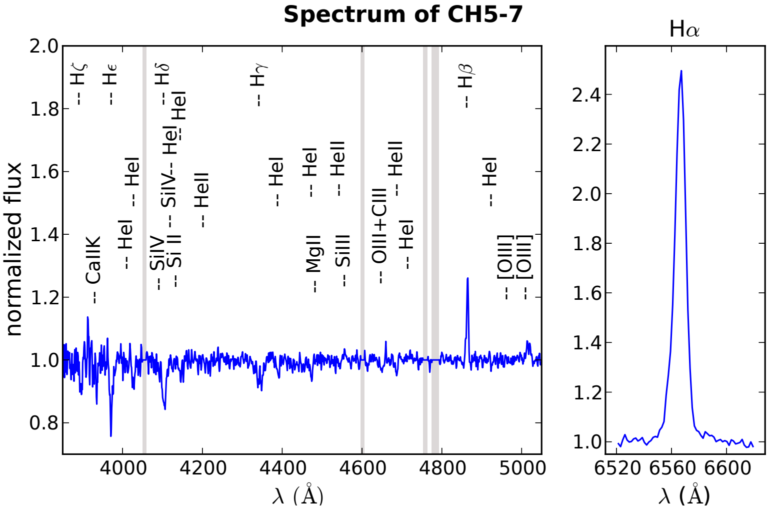

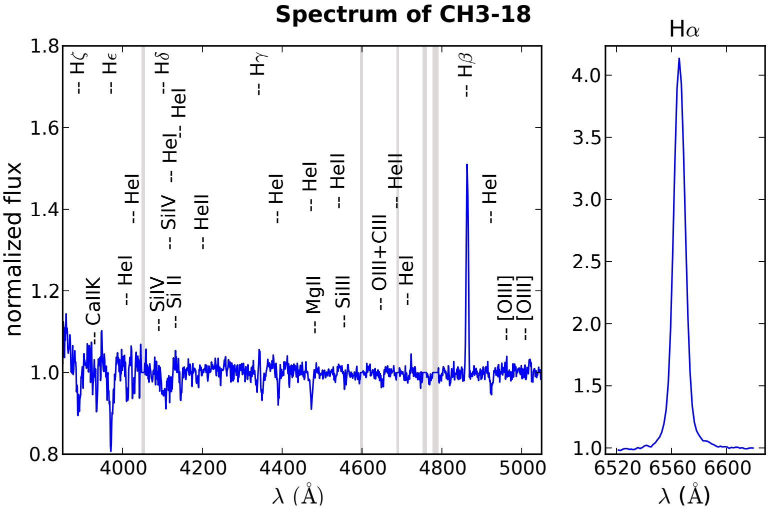

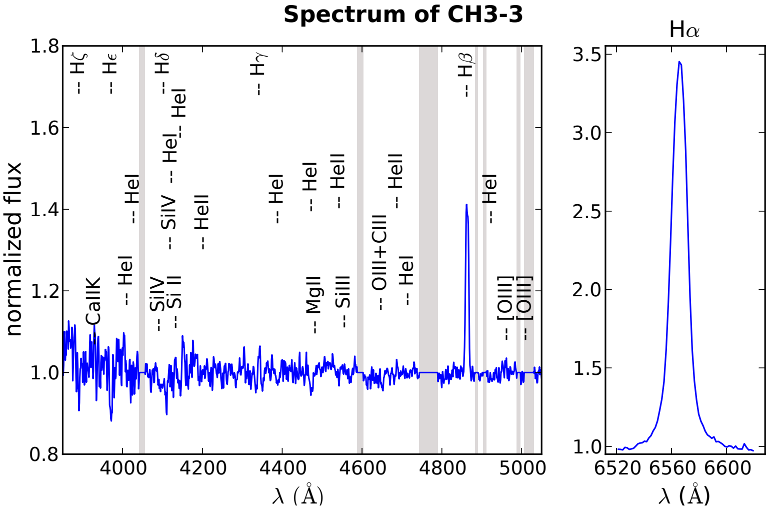

Figure A.1: continued

later than the previous classification of B1.5 in Antoniou et al. (2009b), where the OII+CIII λ4640-4650 blend and SiIV $\lambda\lambda$4088, 4116 lines were identified.

- *CXOU J004929.74-731058.5 (source CH4-5) - classified as B1-B5*

  The absence of the HeII $\lambda\lambda$4200, 4686 lines, and the combination with the clear presence of the HeI λ4471 line and the absence of MgII λ4481, indicates a spectral type in the B1-B5 range. Antoniou et al. (2009b) provided a spectral type of B1, based on the presence of the OII+CIII λ4640-4650 blend and SiIV $\lambda\lambda$ 4088, 4116 lines, which are not detected in our deeper, higher resolution spectra.

- *CXOU J005057.16-731007.9 (source CH4-3) - classified as B1-B3*

  Source CH4-3 was also observed both nights (July 26 and September 19, 2008). The absence of the HeII $\lambda\lambda$4200, 4686 lines and the presence of the OII λ4415-4417 and OII+CIII λ4640-4650 blend limit the spectral type in the B1-B3 range. This source has been classified previously as B0.5 by Antoniou et al. (2009b) due to the weak presence of the HeII λ4686 line, which is not detected in our spectra.

- *CXOU J005153.16-723148.8 (source CH5-3) - classified as B0.5*

  Given the weak HeII λ4686 line, and the absence of the HeII $\lambda\lambda$4200, 4541 lines, all the criteria for a B0.5 star are fulfilled, resulting in a little later type than the previous classification of O9.5-B0 by McBride et al. (2008), although in the latter work there are no details about the specific lines that led to this classification.

- *CXOU J005205.61-722604.4 (source CH5-1) - classified as B3-B5*

  The combination of the presence and relative strength of the HeI $\lambda\lambda$4009, 4026, and 4144 lines, and the absence of the MgII λ4481 line limits the spectral type to the B3-B5 range. This is later than the previous classification of B1-B1.5 by McBride et al. (2008), for which no details about the specific lines are presented.

- *CXOU J005208.95-723803.5 (source CH6-1) - classified as B1-B3*

  This source is classified as B1-B3, in full agreement with Antoniou et al. (2009b).

- *CXOU J005245.04-722843.6 (source CH5-12) - classified as B0*

  The clear presence of the HeII $\lambda\lambda$4541, 4686 lines combined with the fact that the HeII λ4200 is absent constrains the spectral type to B0, since for earlier types this line is of comparable strength to the HeII λ4541 line. Thus, all criteria for a B0 star are fulfilled, which improves the previous wider classification of O9-B0 by McBride et al. (2008).

- *XMMU J005255.1-715809 (source XMM2-1) - classified as B1-B3*

  The absence of the HeII $\lambda\lambda$4200, 4541, 4686 lines and the presence of the OII+CIII λ4640-4650 blend, allow us to classify source XMM2-1 as B1-B3, which is in marginal agreement with the previous classification of B0-B1 by McBride et al. (2008).

- *CXOU J005355.25-722645.8 (source CH5-16) - classified as B0*

  The HeII $\lambda\lambda$4541, 4686 lines are present, but not the HeII λ4200 line, indicating that this is a B0 star (earlier types display the HeII λ4200 line in at least comparable strength to the HeII λ4541 line). Antoniou et al. (2009b) have classified this source as B0.5 based on the absence of the HeII λ4541 line, in contrast to our deeper spectrum, where it is clearly seen.

- *CXOU J005455.78-724510.7 (source CH6-2) - classified as B1.5-B3*

  The presence of the HeII $\lambda\lambda$4200, 4686 lines and the absence of SiIV λ4116 limit the spectral range to an as early type as B1.5, while the presence of the OII+CIII λ4640-4650 blend limits the spectral type to no later than B3. This is marginally consistent with the previous classification of B1-B1.5 by Antoniou et al. (2009b), based on the presence of the SiIV $\lambda\lambda$ 4088, 4116 lines, which however are not detected in our deeper spectra.

- *CXOU J005456.34-722648.4 (source CH5-7) - classified as B0.5*

  The absence of the HeII λ4200 line and the presence of the HeII λ4686 line suggest a spectral type of B0.5. The slightly earlier classification of B0 by Antoniou et al. (2009b) was based on the presence of the HeII λ4200 line, which is not seen in our deeper spectrum.

- *CXOU J005605.42-722159.3 (source CH3-18) - classified as B2*

  The SiIII λ4553 line is clearly present but without any sign of the SiIV $\lambda\lambda$4088, 4116 lines. This combination is in agreement with the criteria set for B2 stars. This classification is later than the previous classification of B1 by McBride et al. (2008).

- *CXOU J005736.00-721933.9 (source CH3-3) - classified as B1-B5*

  The absence of the HeII $\lambda\lambda$4200, 4686 lines, in combination with a clearly present HeI λ4471 line and the absence of the MgII λ4481 line, suggest a spectral range of B1-B5. This classification result is in agreement with the also broad classification of B0-B4 by Antoniou et al. (2009b).

B

Catalog of Hα emission sources

B.1 Table description

We present Hα emission sources identified for each field in separate tables. Due to the large size of the detected sources we give the first 107 sources for each field in the printed form. The full lists can be accessed online at: `ftp://ftp.physics.uoc.gr/pub/tmp/gmaravel/WFI-Ha/`

For each source we give:

1. Source ID in the form of FX-N, where FX corresponds to the field ID as has been defined in Table 4.1 and N is the sequential number for the field (sorted by RA).
2. RA, in hh:mm:ss.s (J2000.0).
3. Dec, in dd:mm:ss.s (J2000.0).
4. Rc magnitude and its corresponding error in parenthesis.
5. Hα magnitude and its corresponding error in parenthesis.
6. V magnitude, retrieved from the MCPS catalog (Zaritsky et al., 2002).
7. $B-V$ color, retrieved from the MCPS catalog (Zaritsky et al., 2002).

8. H$\alpha - Rc$ index and its corresponding error in parenthesis.
9. SNR, as calculated by Equation 4.11.

Table B.1: Hα emission sources identified in Field-2.

Field-ID	RA	Dec	Rc	Hα	V	$B-V$	H$\alpha - Rc$	SNR
F2-1	00:48:33.7	-72:56:26.3	17.089(0.006)	16.9585(0.011)	16.988	-0.024	-0.130(0.013)	9.8
F2-2	00:48:37.1	-72:53:28.0	17.875(0.009)	17.7835(0.01)	17.826	0.023	-0.091(0.013)	6.5
F2-3	00:48:44.4	-72:53:31.2	16.969(0.005)	16.9235(0.006)	16.901	-0.010	-0.045(0.008)	5.7
F2-4	00:48:44.9	-72:36:12.7	17.016(0.014)	16.7435(0.007)	16.804	0.077	-0.272(0.016)	15.4
F2-5	00:48:45.0	-72:36:37.4	15.783(0.002)	15.3555(0.003)	15.835	0.032	-0.427(0.004)	97.9
F2-6	00:48:47.7	-72:40:00.2	18.381(0.011)	18.3085(0.008)	18.303	-0.062	-0.072(0.014)	5.1
F2-7	00:48:48.0	-72:47:19.2	16.562(0.005)	16.1335(0.005)	16.573	0.093	-0.428(0.007)	50.0
F2-8	00:48:49.3	-72:52:10.7	17.445(0.006)	17.1575(0.006)	17.699	0.198	-0.287(0.008)	29.7
F2-9	00:48:49.6	-72:45:51.1	17.923(0.007)	17.8315(0.006)	17.891	-0.048	-0.091(0.009)	9.5
F2-10	00:48:51.2	-72:49:42.0	17.612(0.006)	17.2835(0.006)	17.562	0.110	-0.328(0.008)	33.4
F2-11	00:48:51.2	-72:54:00.0	17.336(0.006)	17.1855(0.006)	17.306	0.040	-0.150(0.008)	16.5
F2-12	00:48:52.1	-72:52:06.1	18.016(0.012)	17.8545(0.008)	18.077	0.077	-0.161(0.014)	10.4
F2-13	00:48:52.4	-72:29:38.5	16.719(0.004)	16.4325(0.003)	16.744	0.011	-0.286(0.005)	50.3
F2-14	00:48:53.2	-72:38:27.5	17.625(0.012)	17.5545(0.006)	17.498	-0.053	-0.070(0.013)	5.1
F2-15	00:48:57.4	-72:53:51.3	16.886(0.012)	16.7425(0.007)	16.845	0.294	-0.143(0.014)	9.7
F2-16	00:48:58.3	-72:41:19.7	16.157(0.004)	15.5615(0.006)	16.142	-0.059	-0.595(0.007)	63.5
F2-17	00:48:59.3	-72:56:45.4	16.714(0.005)	16.6515(0.005)	16.704	0.094	-0.062(0.007)	8.5
F2-18	00:48:59.8	-72:41:31.8	17.839(0.006)	17.7095(0.005)	17.745	-0.050	-0.129(0.008)	15.6
F2-19	00:48:59.9	-72:31:01.1	17.814(0.007)	17.6215(0.005)	17.769	-0.168	-0.192(0.009)	20.5
F2-20	00:49:01.7	-72:53:54.7	16.126(0.003)	16.0765(0.009)	15.901	0.026	-0.049(0.009)	5.1
F2-21	00:49:03.3	-72:50:52.6	16.908(0.015)	16.7655(0.006)	16.778	0.081	-0.142(0.016)	8.2
F2-22	00:49:03.4	-72:53:06.7	17.606(0.007)	17.4505(0.007)	17.516	0.054	-0.155(0.010)	14.6

Continued on next page

Table B.1 – *Continued from previous page*

Field-ID	RA	Dec	Rc	Hα	V	$B-V$	H$\alpha - Rc$	SNR
F2-23	00:49:06.8	-72:29:30.9	16.981(0.006)	16.6835(0.003)	17.026	-0.053	-0.297(0.007)	38.7
F2-24	00:49:07.8	-72:49:15.8	18.314(0.008)	17.5215(0.004)	18.339	0.122	-0.792(0.009)	62.9
F2-25	00:49:09.6	-72:34:37.5	16.598(0.003)	16.4785(0.003)	16.567	-0.089	-0.119(0.004)	26.6
F2-26	00:49:10.9	-72:53:11.8	17.276(0.005)	17.1835(0.005)	17.237	0.030	-0.092(0.007)	12.5
F2-27	00:49:12.4	-72:36:13.0	17.885(0.007)	17.7975(0.008)	17.984	0.199	-0.087(0.011)	7.9
F2-28	00:49:13.2	-72:44:55.7	18.297(0.009)	18.0725(0.006)	18.198	-0.005	-0.224(0.011)	18.7
F2-29	00:49:13.7	-72:48:34.5	17.066(0.004)	16.6515(0.004)	17.158	0.163	-0.414(0.006)	60.9
F2-30	00:49:13.8	-72:46:37.0	17.588(0.006)	17.3795(0.005)	17.520	0.068	-0.208(0.008)	24.2
F2-31	00:49:14.9	-72:31:18.7	17.499(0.006)	17.4145(0.006)	17.505	-0.100	-0.084(0.008)	9.5
F2-32	00:49:16.8	-72:52:15.5	17.656(0.025)	17.3935(0.009)	17.406	0.118	-0.262(0.027)	8.8
F2-33	00:49:18.2	-72:45:29.8	16.393(0.003)	16.1435(0.004)	16.309	-0.091	-0.249(0.005)	44.5
F2-34	00:49:18.4	-72:41:27.9	17.353(0.006)	17.0015(0.006)	17.323	-0.009	-0.351(0.008)	35.4
F2-35	00:49:18.8	-72:55:02.4	17.164(0.005)	16.9565(0.007)	17.193	0.013	-0.207(0.009)	21.9
F2-36	00:49:18.8	-72:50:16.8	18.268(0.008)	18.1555(0.008)	18.245	0.046	-0.112(0.011)	9.4
F2-37	00:49:19.1	-72:53:10.9	17.934(0.013)	17.7355(0.007)	17.715	-0.071	-0.198(0.015)	12.3
F2-38	00:49:19.2	-72:48:01.4	16.936(0.005)	16.8965(0.004)	16.770	-0.105	-0.039(0.006)	6.0
F2-39	00:49:19.3	-72:42:36.3	18.398(0.012)	18.3015(0.008)	18.224	0.007	-0.096(0.014)	6.4
F2-40	00:49:19.4	-72:44:13.7	18.446(0.01)	18.3345(0.008)	18.312	0.014	-0.111(0.013)	8.2
F2-41	00:49:19.4	-72:43:22.4	18.245(0.008)	17.9765(0.006)	18.092	0.033	-0.268(0.010)	23.8
F2-42	00:49:19.8	-72:50:40.7	18.311(0.009)	18.1795(0.006)	18.195	0.031	-0.131(0.011)	11.4
F2-43	00:49:20.1	-72:52:48.2	17.861(0.008)	17.7405(0.006)	17.726	0.061	-0.120(0.010)	11.4
F2-44	00:49:20.5	-72:28:45.9	17.213(0.005)	17.1405(0.004)	17.217	-0.037	-0.072(0.006)	10.9

Continued on next page

Table B.1 – *Continued from previous page*

Field-ID	RA	Dec	Rc	Hα	V	$B-V$	H$\alpha - Rc$	SNR
F2-45	00:49:22.4	-72:37:39.9	16.817(0.013)	16.6495(0.004)	16.711	-0.045	-0.167(0.014)	11.4
F2-46	00:49:24.5	-72:43:45.4	17.932(0.011)	17.7565(0.006)	17.556	-0.204	-0.175(0.013)	12.9
F2-47	00:49:25.7	-72:35:27.0	18.163(0.01)	17.8295(0.03)	18.062	-0.025	-0.333(0.032)	9.1
F2-48	00:49:25.9	-72:32:20.4	17.287(0.005)	16.9155(0.004)	17.330	-0.009	-0.371(0.006)	49.1
F2-49	00:49:27.1	-72:55:22.6	17.062(0.005)	16.9465(0.004)	16.929	0.082	-0.115(0.006)	17.1
F2-50	00:49:27.3	-72:30:08.1	16.457(0.004)	16.3595(0.003)	16.314	-0.026	-0.097(0.005)	18.6
F2-51	00:49:28.6	-72:43:41.8	18.584(0.011)	18.2775(0.005)	18.468	-0.014	-0.306(0.012)	22.1
F2-52	00:49:29.2	-72:35:32.1	14.972(0.002)	14.4345(0.001)	15.055	0.025	-0.537(0.002)	189.5
F2-53	00:49:32.3	-72:41:43.1	17.534(0.005)	17.4015(0.004)	17.314	0.078	-0.132(0.006)	19.4
F2-54	00:49:33.5	-72:48:38.7	18.282(0.01)	18.1115(0.011)	18.074	0.011	-0.170(0.015)	10.6
F2-55	00:49:35.3	-72:40:47.0	17.124(0.005)	16.9835(0.004)	17.307	0.294	-0.140(0.006)	20.5
F2-56	00:49:35.4	-72:44:17.4	15.792(0.002)	15.4155(0.002)	15.716	-0.054	-0.376(0.003)	112.4
F2-57	00:49:35.5	-72:45:39.2	18.443(0.01)	18.2565(0.007)	18.223	0.084	-0.186(0.012)	14.0
F2-58	00:49:35.9	-72:38:58.5	17.85(0.007)	17.7705(0.006)	17.759	0.014	-0.079(0.009)	8.3
F2-59	00:49:36.4	-72:33:35.6	17.779(0.024)	17.4785(0.006)	17.686	-0.070	-0.300(0.025)	10.6
F2-60	00:49:36.8	-72:46:49.6	17.622(0.009)	17.3235(0.005)	17.524	-0.037	-0.298(0.010)	25.3
F2-61	00:49:38.0	-72:48:59.0	18.305(0.011)	18.1125(0.029)	17.768	0.129	-0.192(0.031)	5.7
F2-62	00:49:38.2	-72:49:52.2	16.051(0.002)	15.4775(0.003)	16.076	0.042	-0.573(0.004)	123.5
F2-63	00:49:39.2	-72:46:06.9	17.64(0.007)	17.4895(0.004)	17.521	0.041	-0.150(0.008)	17.4
F2-64	00:49:40.2	-72:41:02.6	18.463(0.01)	18.2855(0.007)	18.238	0.012	-0.177(0.012)	13.4
F2-65	00:49:41.1	-72:39:38.3	16.332(0.003)	16.2805(0.002)	16.640	0.070	-0.051(0.004)	13.8
F2-66	00:49:42.7	-72:39:50.1	18.41(0.01)	18.1655(0.007)	18.294	-0.052	-0.244(0.012)	17.9

Continued on next page

Table B.1 – *Continued from previous page*

Field-ID	RA	Dec	Rc	Hα	V	$B-V$	Hα − Rc	SNR
F2-67	00:49:44.6	-72:46:31.6	18.433(0.01)	18.1795(0.008)	18.285	-0.032	-0.253(0.013)	17.6
F2-68	00:49:45.0	-72:48:41.4	18.531(0.012)	18.3795(0.023)	18.380	0.016	-0.151(0.026)	5.4
F2-69	00:49:45.1	-72:52:01.4	16.941(0.021)	16.6125(0.006)	16.797	0.085	-0.328(0.022)	13.0
F2-70	00:49:45.1	-72:36:56.7	15.473(0.003)	14.9765(0.001)	15.491	-0.025	-0.496(0.003)	125.9
F2-71	00:49:48.2	-72:38:53.3	16.529(0.004)	16.2275(0.002)	16.529	-0.089	-0.301(0.004)	58.8
F2-72	00:49:49.2	-72:51:54.4	17.071(0.004)	16.9905(0.004)	17.364	0.193	-0.080(0.006)	13.7
F2-73	00:49:49.4	-72:42:57.8	17.903(0.01)	17.7935(0.006)	17.661	0.061	-0.109(0.012)	8.9
F2-74	00:49:49.5	-72:55:26.4	17.581(0.006)	17.5325(0.006)	17.533	0.124	-0.048(0.008)	5.5
F2-75	00:49:50.3	-72:51:19.1	18.162(0.01)	18.0665(0.008)	18.146	-0.013	-0.095(0.013)	7.1
F2-76	00:49:50.5	-72:53:49.0	17.311(0.005)	17.0875(0.006)	17.257	0.104	-0.223(0.008)	25.8
F2-77	00:49:51.1	-72:31:08.3	15.61(0.003)	15.2715(0.002)	15.675	-0.089	-0.338(0.004)	80.6
F2-78	00:49:51.5	-72:36:08.2	17.332(0.005)	17.2545(0.005)	17.194	-0.018	-0.077(0.007)	10.5
F2-79	00:49:51.9	-72:36:12.1	16.57(0.003)	16.2595(0.002)	16.221	0.068	-0.310(0.004)	74.8
F2-80	00:49:52.0	-72:29:54.0	17.948(0.008)	17.7815(0.007)	17.792	0.013	-0.166(0.011)	14.5
F2-81	00:49:52.4	-72:42:01.6	18.549(0.015)	18.3815(0.006)	18.131	0.143	-0.167(0.016)	9.6
F2-82	00:49:52.7	-72:55:55.5	18.156(0.013)	18.0255(0.011)	17.635	0.123	-0.130(0.017)	7.2
F2-83	00:49:55.0	-72:38:03.0	17.342(0.005)	17.2305(0.004)	17.151	0.036	-0.111(0.006)	16.5
F2-84	00:49:55.9	-72:36:57.7	18.501(0.013)	18.1935(0.008)	18.305	-0.016	-0.307(0.015)	17.5
F2-85	00:49:57.3	-72:45:01.3	16.924(0.004)	16.6385(0.003)	16.822	-0.019	-0.285(0.005)	50.1
F2-86	00:49:58.0	-72:37:07.0	17.956(0.014)	17.7615(0.006)	17.799	-0.020	-0.194(0.015)	11.7
F2-87	00:49:59.4	-72:35:38.2	17.901(0.007)	17.3045(0.004)	17.884	-0.043	-0.596(0.008)	56.9
F2-88	00:50:01.2	-72:32:33.1	16.233(0.003)	16.1035(0.003)	16.230	0.019	-0.129(0.004)	28.7

Continued on next page

Table B.1 – *Continued from previous page*

Field-ID	RA	Dec	Rc	Hα	V	$B-V$	H$\alpha - Rc$	SNR
F2-89	00:50:01.7	-72:46:31.9	16.489(0.007)	16.4335(0.003)	16.392	-0.008	-0.055(0.008)	7.1
F2-90	00:50:01.8	-72:47:56.8	18.637(0.011)	18.2745(0.011)	18.406	0.078	-0.362(0.016)	19.8
F2-91	00:50:02.0	-72:35:03.7	17.607(0.006)	17.5305(0.007)	17.576	-0.030	-0.076(0.009)	8.0
F2-92	00:50:02.1	-72:35:36.8	15.609(0.002)	15.1155(0.001)	15.594	-0.038	-0.493(0.002)	177.2
F2-93	00:50:02.2	-72:39:22.0	16.71(0.019)	16.2405(0.01)	16.181	-0.302	-0.469(0.021)	17.7
F2-94	00:50:02.8	-72:42:19.9	17.873(0.006)	17.5285(0.004)	17.748	-0.015	-0.344(0.007)	40.9
F2-95	00:50:05.2	-72:41:59.0	17.968(0.007)	17.9105(0.006)	17.741	-0.029	-0.057(0.009)	6.0
F2-96	00:50:07.6	-72:30:52.6	16.77(0.004)	16.6965(0.003)	16.651	-0.065	-0.073(0.005)	14.1
F2-97	00:50:07.8	-72:35:22.3	17.6(0.006)	17.4215(0.004)	17.427	0.033	-0.178(0.007)	22.8
F2-98	00:50:09.8	-72:42:54.6	18.009(0.013)	17.6705(0.005)	17.778	-0.101	-0.338(0.014)	20.9
F2-99	00:50:10.3	-72:49:29.8	17.785(0.026)	17.5175(0.004)	17.636	0.084	-0.267(0.026)	9.0
F2-100	00:50:11.0	-72:53:45.2	17.698(0.005)	17.5915(0.005)	17.624	-0.012	-0.106(0.007)	14.3
F2-101	00:50:11.5	-72:31:59.9	18.052(0.009)	17.4595(0.04)	17.966	-0.041	-0.592(0.041)	11.1
F2-102	00:50:11.6	-72:54:60.0	16.287(0.003)	15.7585(0.002)	16.035	0.066	-0.528(0.004)	116.0
F2-103	00:50:11.7	-72:28:03.9	18.049(0.093)	17.3685(0.028)	17.491	0.161	-0.680(0.097)	5.2
F2-104	00:50:11.8	-72:52:14.6	18.1(0.012)	17.8625(0.025)	18.095	0.024	-0.237(0.028)	7.7
F2-105	00:50:12.6	-72:53:34.7	18.476(0.01)	18.1545(0.027)	18.292	0.232	-0.321(0.029)	9.7
F2-106	00:50:13.2	-72:24:54.8	16.165(0.005)	15.8095(0.002)	16.140	-0.042	-0.355(0.005)	56.2
F2-107	00:50:13.3	-72:48:23.6	18.454(0.01)	18.3035(0.009)	18.491	-0.072	-0.150(0.013)	10.4

Table B.2: Hα emission sources identified in Field-4.

Field-ID	RA	Dec	Rc	Hα	V	$B - V$	Hα − Rc	SNR
F4-1	00:46:09.1	-73:17:19.5	18.227(0.01)	18.0363(0.006)	17.352	0.070	-0.191(0.012)	15.0
F4-2	00:46:09.2	-73:15:09.6	18.453(0.01)	18.2793(0.013)	18.367	0.226	-0.173(0.016)	9.8
F4-3	00:46:10.8	-73:03:37.5	18.355(0.012)	18.2223(0.009)	18.092	0.085	-0.133(0.015)	8.4
F4-4	00:46:13.0	-73:13:33.1	17.198(0.013)	17.0803(0.007)	16.756	0.201	-0.118(0.015)	7.6
F4-5	00:46:13.0	-73:16:03.1	17.308(0.004)	17.1883(0.004)	17.077	0.184	-0.120(0.006)	20.1
F4-6	00:46:14.1	-73:10:10.1	17.581(0.005)	17.1863(0.004)	17.042	0.274	-0.395(0.006)	51.7
F4-7	00:46:14.3	-73:05:39.5	17.442(0.005)	17.0313(0.007)	17.182	0.142	-0.411(0.009)	39.8
F4-8	00:46:17.0	-73:10:26.3	16.477(0.005)	16.0153(0.003)	16.309	0.290	-0.461(0.006)	64.4
F4-9	00:46:17.3	-73:12:35.4	14.931(0.002)	14.7543(0.002)	14.713	0.032	-0.177(0.003)	57.8
F4-10	00:46:17.6	-73:04:49.8	18.445(0.01)	18.3493(0.011)	18.196	0.041	-0.096(0.015)	6.2
F4-11	00:46:18.2	-73:11:14.4	16.956(0.004)	16.5133(0.003)	16.718	0.191	-0.442(0.005)	72.6
F4-12	00:46:22.8	-73:05:09.2	18.413(0.011)	18.3343(0.009)	18.246	0.166	-0.079(0.014)	5.4
F4-13	00:46:23.1	-73:01:10.6	17.677(0.006)	17.4983(0.005)	17.457	0.052	-0.179(0.008)	21.2
F4-14	00:46:23.8	-73:02:24.1	14.386(0.001)	14.0763(0.001)	14.355	-0.018	-0.310(0.001)	190.8
F4-15	00:46:27.7	-73:02:37.8	17.381(0.005)	17.1753(0.004)	17.085	0.024	-0.205(0.006)	29.2
F4-16	00:46:28.0	-73:14:43.4	18.189(0.01)	18.0763(0.008)	17.687	0.183	-0.112(0.013)	8.3
F4-17	00:46:28.2	-73:09:28.0	18.489(0.015)	18.3573(0.007)	18.140	0.093	-0.132(0.017)	7.5
F4-18	00:46:29.6	-73:14:43.5	15.248(0.002)	14.8063(0.001)	15.107	0.073	-0.442(0.002)	162.4
F4-19	00:46:29.9	-73:12:40.7	16.2(0.002)	15.8803(0.002)	16.055	0.075	-0.319(0.003)	97.8
F4-20	00:46:30.7	-73:17:10.6	17.32(0.005)	17.0893(0.004)	17.194	0.252	-0.230(0.006)	32.4
F4-21	00:46:31.1	-73:08:07.3	17.483(0.004)	17.3893(0.004)	17.267	0.191	-0.094(0.006)	16.0
F4-22	00:46:33.0	-72:57:32.1	17.657(0.007)	17.4543(0.006)	17.315	0.073	-0.203(0.009)	20.1

Continued on next page

Table B.2 – *Continued from previous page*

Field-ID	RA	Dec	Rc	Hα	V	$B-V$	H$\alpha - Rc$	SNR
F4-23	00:46:33.0	-73:19:19.8	16.962(0.004)	16.8443(0.003)	16.964	0.120	-0.117(0.005)	22.2
F4-24	00:46:33.2	-73:10:48.5	15.684(0.002)	15.1373(0.002)	15.541	0.134	-0.547(0.003)	152.0
F4-25	00:46:33.5	-73:13:03.3	17.061(0.004)	16.8643(0.005)	16.730	-0.044	-0.196(0.006)	28.0
F4-26	00:46:34.4	-73:11:25.6	16.152(0.002)	15.6273(0.002)	16.076	0.126	-0.525(0.003)	147.2
F4-27	00:46:35.0	-73:15:09.8	17.433(0.005)	17.2143(0.004)	17.038	0.032	-0.218(0.006)	30.9
F4-28	00:46:35.5	-72:58:13.5	17.636(0.006)	17.4153(0.004)	17.342	-0.015	-0.220(0.007)	27.6
F4-29	00:46:35.5	-73:13:07.0	17.934(0.01)	17.8103(0.007)	17.620	0.121	-0.124(0.012)	9.6
F4-30	00:46:36.1	-73:17:04.9	18.125(0.007)	17.9223(0.005)	17.916	0.070	-0.203(0.009)	21.5
F4-31	00:46:36.5	-73:21:36.8	17.52(0.008)	17.4443(0.012)	17.413	0.281	-0.075(0.014)	5.0
F4-32	00:46:37.6	-73:20:32.5	17.57(0.006)	17.4363(0.004)	17.414	0.221	-0.134(0.007)	17.5
F4-33	00:46:38.3	-73:11:09.6	16.724(0.003)	16.5443(0.003)	16.484	0.237	-0.179(0.004)	38.9
F4-34	00:46:38.3	-72:48:18.0	17.137(0.033)	16.9263(0.006)	16.789	0.217	-0.210(0.034)	5.7
F4-35	00:46:40.2	-72:51:02.8	16.479(0.003)	16.2963(0.003)	16.343	-0.013	-0.182(0.004)	39.5
F4-36	00:46:40.5	-73:01:07.8	18.384(0.01)	18.1263(0.009)	17.824	0.229	-0.257(0.013)	17.0
F4-37	00:46:41.8	-73:10:26.0	18.009(0.007)	17.8203(0.006)	17.686	0.250	-0.189(0.009)	18.8
F4-38	00:46:42.3	-73:11:09.4	17.887(0.007)	17.6793(0.005)	17.570	0.257	-0.208(0.009)	22.0
F4-39	00:46:44.0	-72:56:28.2	17.826(0.007)	17.5683(0.004)	17.659	0.014	-0.258(0.008)	28.5
F4-40	00:46:45.2	-73:14:42.3	17.895(0.008)	17.8353(0.006)	17.526	0.211	-0.059(0.010)	5.8
F4-41	00:46:45.6	-73:07:13.2	18.006(0.006)	17.9023(0.015)	17.762	0.153	-0.103(0.016)	6.1
F4-42	00:46:46.0	-73:11:36.5	17.977(0.006)	17.7663(0.004)	17.657	0.155	-0.211(0.007)	26.6
F4-43	00:46:46.8	-73:18:49.8	16.753(0.004)	16.5833(0.003)	16.522	0.179	-0.169(0.005)	31.3
F4-44	00:46:47.3	-73:14:16.7	18.285(0.008)	18.0993(0.006)	17.954	0.092	-0.185(0.010)	17.0

Continued on next page

Table B.2 – *Continued from previous page*

Field-ID	RA	Dec	*Rc*	Hα	*V*	$B-V$	Hα − *Rc*	SNR
F4-45	00:46:47.6	-72:53:25.9	17.819(0.007)	17.6023(0.006)	17.539	0.111	-0.216(0.009)	21.3
F4-46	00:46:47.6	-73:08:38.0	16.852(0.003)	16.3613(0.002)	16.715	0.258	-0.491(0.004)	109.6
F4-47	00:46:47.8	-73:05:17.3	17.169(0.004)	16.7443(0.003)	16.976	0.201	-0.425(0.005)	70.4
F4-48	00:46:49.2	-73:14:52.2	17.442(0.004)	17.2403(0.003)	17.237	-0.096	-0.201(0.005)	36.7
F4-49	00:46:49.3	-73:19:23.6	16.884(0.004)	16.6213(0.003)	16.799	0.246	-0.263(0.005)	46.7
F4-50	00:46:49.5	-73:14:34.0	17.759(0.01)	17.5173(0.005)	17.460	0.059	-0.241(0.011)	19.3
F4-51	00:46:50.1	-73:08:01.5	17.527(0.005)	17.2683(0.004)	17.221	0.255	-0.259(0.006)	36.0
F4-52	00:46:51.1	-73:02:15.7	16.381(0.002)	16.2863(0.003)	16.058	-0.315	-0.094(0.004)	25.0
F4-53	00:46:51.7	-73:05:31.1	17.73(0.006)	17.3273(0.005)	17.557	0.297	-0.402(0.008)	43.0
F4-54	00:46:51.8	-73:09:32.7	14.672(0.001)	14.5413(0.001)	14.390	-0.048	-0.131(0.001)	87.4
F4-55	00:46:52.0	-73:14:24.2	16.13(0.003)	15.9353(0.002)	15.807	0.231	-0.194(0.004)	49.3
F4-56	00:46:52.1	-73:12:29.6	17.595(0.005)	17.3603(0.005)	17.469	0.152	-0.234(0.007)	29.8
F4-57	00:46:53.6	-73:07:07.8	18.524(0.009)	18.4083(0.007)	18.108	0.033	-0.116(0.011)	9.7
F4-58	00:46:53.7	-73:14:46.4	17.489(0.004)	17.1883(0.003)	17.338	0.257	-0.301(0.005)	52.6
F4-59	00:46:54.5	-73:18:14.3	17.564(0.005)	17.3733(0.004)	17.364	0.263	-0.191(0.006)	27.4
F4-60	00:46:55.3	-73:12:08.1	16.451(0.004)	16.1713(0.002)	15.752	0.050	-0.279(0.004)	55.0
F4-61	00:46:55.6	-73:11:28.0	18.034(0.007)	17.9433(0.005)	17.792	0.049	-0.090(0.009)	10.1
F4-62	00:46:56.2	-73:10:54.7	14.55(0.002)	14.4483(0.001)	14.309	-0.093	-0.101(0.002)	43.2
F4-63	00:46:56.9	-73:14:34.2	18.474(0.01)	18.1493(0.006)	18.125	0.230	-0.324(0.012)	24.0
F4-64	00:46:58.6	-73:20:00.3	17.959(0.01)	17.8143(0.007)	17.673	0.054	-0.145(0.012)	11.1
F4-65	00:46:59.2	-73:18:36.1	17.57(0.005)	17.3943(0.004)	17.352	0.144	-0.176(0.006)	25.4
F4-66	00:47:00.1	-73:17:06.2	15.742(0.002)	15.3793(0.002)	15.632	0.219	-0.363(0.003)	109.1

Continued on next page

Table B.2 – *Continued from previous page*

Field-ID	RA	Dec	Rc	Hα	V	$B-V$	H$\alpha - Rc$	SNR
F4-67	00:47:00.1	-73:11:40.3	18.637(0.01)	18.4903(0.01)	18.373	0.135	-0.147(0.014)	9.7
F4-68	00:47:00.4	-73:04:44.4	17.675(0.007)	17.5483(0.007)	17.373	0.132	-0.127(0.010)	12.1
F4-69	00:47:00.7	-73:10:16.3	17.348(0.006)	17.1033(0.004)	17.005	0.019	-0.244(0.007)	30.3
F4-70	00:47:01.4	-72:59:54.7	17.43(0.008)	17.1003(0.004)	16.934	0.299	-0.329(0.009)	31.7
F4-71	00:47:03.3	-72:53:56.3	18.116(0.01)	18.0353(0.008)	17.911	0.091	-0.081(0.013)	6.1
F4-72	00:47:04.0	-73:19:17.6	16.514(0.003)	16.1263(0.002)	16.047	0.296	-0.387(0.004)	90.3
F4-73	00:47:04.0	-73:17:50.7	16.82(0.003)	16.4743(0.003)	16.593	0.087	-0.345(0.004)	69.7
F4-74	00:47:04.2	-73:09:33.5	18.509(0.008)	18.1153(0.005)	18.338	0.083	-0.394(0.009)	35.0
F4-75	00:47:04.3	-73:13:43.9	17.611(0.006)	17.5453(0.004)	17.127	0.207	-0.066(0.007)	8.9
F4-76	00:47:05.0	-73:06:11.9	17.688(0.006)	17.3563(0.005)	17.065	0.132	-0.331(0.008)	36.5
F4-77	00:47:06.4	-73:14:52.5	16.96(0.004)	16.8633(0.004)	16.698	0.031	-0.097(0.006)	16.4
F4-78	00:47:06.8	-73:13:39.7	16.512(0.003)	15.9333(0.002)	16.298	0.064	-0.578(0.004)	124.3
F4-79	00:47:06.8	-73:13:36.6	16.39(0.002)	15.9743(0.002)	16.221	0.040	-0.415(0.003)	122.0
F4-80	00:47:06.9	-73:16:48.0	18.61(0.018)	18.3873(0.009)	18.218	0.070	-0.222(0.020)	10.0
F4-81	00:47:07.1	-73:07:02.8	18.357(0.007)	18.1853(0.005)	18.007	0.099	-0.171(0.009)	18.4
F4-82	00:47:07.6	-73:16:02.0	15.857(0.005)	15.6093(0.002)	15.828	0.157	-0.248(0.005)	41.2
F4-83	00:47:08.4	-73:09:16.9	18.346(0.009)	18.1513(0.022)	18.090	0.105	-0.195(0.024)	7.5
F4-84	00:47:08.6	-73:17:11.6	16.633(0.003)	16.4353(0.003)	16.448	0.078	-0.197(0.004)	42.5
F4-85	00:47:08.9	-73:16:50.3	17.181(0.005)	17.0123(0.003)	16.874	-0.058	-0.169(0.006)	26.9
F4-86	00:47:09.1	-73:08:14.1	17.59(0.005)	17.4163(0.021)	17.182	0.044	-0.173(0.022)	7.4
F4-87	00:47:09.2	-73:13:03.4	16.98(0.003)	16.7473(0.003)	16.586	0.142	-0.233(0.004)	49.5
F4-88	00:47:09.3	-73:13:18.3	15.37(0.002)	15.2493(0.002)	15.170	0.055	-0.121(0.003)	40.5

Continued on next page

Table B.2 – *Continued from previous page*

Field-ID	RA	Dec	Rc	Hα	V	$B-V$	H$\alpha - Rc$	SNR
F4-89	00:47:09.4	-73:08:57.1	16.942(0.003)	16.5383(0.008)	16.654	0.054	-0.404(0.009)	39.5
F4-90	00:47:10.4	-73:13:06.5	17.802(0.052)	17.2503(0.006)	16.519	0.053	-0.552(0.052)	8.3
F4-91	00:47:11.5	-73:07:56.9	14.607(0.001)	14.5643(0.007)	14.261	-0.126	-0.043(0.007)	6.0
F4-92	00:47:11.6	-73:05:18.8	17.142(0.004)	16.7773(0.003)	16.982	0.069	-0.364(0.005)	61.9
F4-93	00:47:12.1	-73:07:31.9	17.311(0.005)	16.8063(0.002)	17.024	0.206	-0.504(0.005)	74.9
F4-94	00:47:12.1	-73:19:48.6	18.247(0.007)	18.1063(0.006)	18.030	0.060	-0.140(0.009)	14.3
F4-95	00:47:12.3	-73:15:55.4	18.503(0.011)	18.3283(0.007)	18.157	0.160	-0.174(0.013)	12.3
F4-96	00:47:13.1	-73:08:38.8	18.108(0.006)	17.7053(0.006)	17.891	0.268	-0.403(0.008)	39.7
F4-97	00:47:14.3	-73:17:17.8	16.319(0.005)	15.8313(0.004)	16.083	-0.252	-0.487(0.006)	61.3
F4-98	00:47:14.5	-73:13:50.3	14.889(0.002)	14.7643(0.001)	14.945	-0.108	-0.125(0.002)	52.9
F4-99	00:47:15.1	-73:14:09.3	16.828(0.011)	16.3103(0.003)	16.673	0.002	-0.517(0.011)	36.1
F4-100	00:47:16.1	-73:10:02.0	18.303(0.008)	18.1393(0.008)	18.120	0.217	-0.164(0.011)	13.5
F4-101	00:47:16.7	-72:54:02.6	17.206(0.005)	16.8893(0.003)	16.931	0.066	-0.317(0.006)	47.2
F4-102	00:47:16.8	-73:07:42.7	16.78(0.006)	16.6813(0.004)	16.380	0.142	-0.099(0.007)	13.1
F4-103	00:47:17.2	-73:08:58.1	17.383(0.004)	17.1853(0.005)	17.109	0.252	-0.197(0.006)	28.2
F4-104	00:47:17.9	-72:51:10.6	15.319(0.005)	15.2583(0.003)	15.110	0.074	-0.060(0.006)	10.0
F4-105	00:47:18.1	-73:19:08.0	17.872(0.007)	17.6593(0.004)	17.352	0.267	-0.212(0.008)	23.9
F4-106	00:47:18.3	-73:00:50.5	17.758(0.008)	17.4403(0.005)	17.508	0.129	-0.317(0.009)	29.2
F4-107	00:47:19.0	-73:11:33.6	18.366(0.008)	17.9803(0.007)	18.006	0.131	-0.385(0.011)	30.5

Table B.3: Hα emission sources identified in Field-7.

Field-ID	RA	Dec	Rc	Hα	V	$B-V$	H$\alpha - Rc$	SNR
F7-1	00:55:13.6	-72:29:14.0	15.744(0.014)	14.9746(0.008)	15.366	0.022	-0.770(0.016)	34.2
F7-2	00:55:15.5	-72:36:03.1	17.74(0.013)	17.5706(0.014)	16.966	0.183	-0.170(0.019)	8.2
F7-3	00:55:18.4	-72:34:31.4	18.499(0.011)	18.3036(0.01)	18.262	0.103	-0.196(0.015)	12.1
F7-4	00:55:19.2	-72:22:27.2	17.229(0.007)	16.9596(0.016)	17.002	-0.010	-0.270(0.017)	13.7
F7-5	00:55:19.6	-72:30:35.2	17.036(0.004)	16.5716(0.004)	16.753	0.152	-0.465(0.006)	66.8
F7-6	00:55:19.8	-72:39:10.6	16.447(0.003)	16.3176(0.003)	16.299	-0.001	-0.130(0.004)	28.8
F7-7	00:55:20.3	-72:37:10.4	14.827(0.002)	14.6786(0.001)	14.842	0.071	-0.149(0.002)	62.2
F7-8	00:55:21.0	-72:17:04.8	18.548(0.013)	18.2276(0.011)	18.368	0.024	-0.321(0.017)	16.3
F7-9	00:55:21.0	-72:33:42.9	15.264(0.005)	15.1916(0.002)	15.289	-0.091	-0.073(0.005)	13.1
F7-10	00:55:21.2	-72:12:03.2	18.139(0.012)	18.0456(0.009)	17.827	-0.079	-0.094(0.015)	6.0
F7-11	00:55:21.4	-72:35:26.2	18.464(0.013)	18.3706(0.008)	18.281	-0.031	-0.094(0.015)	5.9
F7-12	00:55:21.4	-72:32:15.3	17.235(0.005)	17.1146(0.006)	17.090	0.112	-0.121(0.008)	14.6
F7-13	00:55:21.8	-72:21:33.9	16.071(0.015)	15.8676(0.019)	15.914	0.001	-0.204(0.024)	7.7
F7-14	00:55:21.8	-72:31:23.6	18.161(0.006)	17.7176(0.005)	17.977	0.029	-0.444(0.008)	46.6
F7-15	00:55:22.2	-72:22:46.8	16.497(0.006)	16.3176(0.01)	16.247	-0.119	-0.180(0.012)	14.2
F7-16	00:55:22.7	-72:36:01.9	18.18(0.008)	18.0276(0.006)	17.979	0.065	-0.153(0.010)	14.3
F7-17	00:55:23.2	-72:29:05.5	18.474(0.008)	18.3186(0.009)	18.283	-0.010	-0.156(0.012)	12.1
F7-18	00:55:24.0	-72:35:46.9	18.495(0.009)	18.3616(0.009)	18.358	-0.008	-0.134(0.013)	9.9
F7-19	00:55:24.9	-72:15:30.8	16.147(0.003)	15.8136(0.003)	16.153	-0.028	-0.334(0.004)	67.7
F7-20	00:55:25.0	-72:29:34.5	15.757(0.002)	15.2596(0.002)	15.669	-0.058	-0.498(0.003)	141.2
F7-21	00:55:25.3	-72:29:57.0	16.244(0.002)	15.8486(0.002)	16.178	-0.023	-0.396(0.003)	117.3
F7-22	00:55:25.4	-72:35:43.4	15.799(0.002)	15.6116(0.003)	15.712	-0.102	-0.188(0.004)	47.8

Continued on next page

Table B.3 – *Continued from previous page*

Field-ID	RA	Dec	Rc	Hα	V	$B-V$	H$\alpha - Rc$	SNR
F7-23	00:55:27.0	-72:10:54.0	16.522(0.004)	16.4266(0.004)	16.338	-0.154	-0.096(0.006)	16.2
F7-24	00:55:27.1	-72:28:04.5	17.805(0.005)	17.6376(0.004)	17.605	-0.020	-0.168(0.006)	24.3
F7-25	00:55:28.2	-72:29:06.7	15.682(0.004)	15.2286(0.003)	15.472	0.007	-0.454(0.005)	74.2
F7-26	00:55:28.6	-72:33:39.2	16.795(0.013)	16.3126(0.007)	16.648	0.125	-0.483(0.015)	26.4
F7-27	00:55:28.7	-72:38:33.0	17.297(0.005)	17.1436(0.006)	17.250	0.030	-0.154(0.008)	18.4
F7-28	00:55:29.2	-72:31:23.4	18.237(0.007)	18.1746(0.007)	18.068	-0.024	-0.063(0.010)	6.2
F7-29	00:55:29.6	-72:40:04.6	18.017(0.011)	17.9216(0.014)	17.857	0.084	-0.096(0.018)	5.2
F7-30	00:55:29.7	-72:20:36.9	17.36(0.006)	17.0416(0.004)	17.258	0.012	-0.319(0.007)	38.3
F7-31	00:55:30.8	-72:25:20.5	15.563(0.002)	15.1786(0.001)	15.495	0.036	-0.385(0.002)	144.9
F7-32	00:55:30.9	-72:29:36.9	15.799(0.002)	15.3546(0.002)	15.758	0.024	-0.445(0.003)	129.0
F7-33	00:55:31.3	-72:19:57.5	17.608(0.006)	17.2446(0.006)	17.465	0.056	-0.364(0.008)	36.4
F7-34	00:55:31.8	-72:30:24.0	14.945(0.002)	14.7626(0.001)	15.056	-0.034	-0.183(0.002)	75.2
F7-35	00:55:32.2	-72:29:57.0	16.75(0.003)	16.4346(0.003)	16.700	-0.021	-0.316(0.004)	64.6
F7-36	00:55:33.6	-72:26:30.1	17.567(0.005)	17.3016(0.003)	17.490	-0.068	-0.266(0.006)	40.4
F7-37	00:55:33.9	-72:13:37.8	16.916(0.004)	16.5706(0.003)	16.931	-0.025	-0.346(0.005)	59.2
F7-38	00:55:34.7	-72:29:13.4	16.894(0.003)	16.4576(0.002)	16.608	-0.131	-0.437(0.004)	99.7
F7-39	00:55:35.2	-72:29:06.7	14.948(0.002)	14.7656(0.001)	14.686	-0.038	-0.183(0.002)	75.2
F7-40	00:55:35.3	-72:31:43.1	17.451(0.005)	16.9826(0.004)	17.411	-0.013	-0.469(0.006)	59.5
F7-41	00:55:35.3	-72:15:11.9	16.823(0.005)	16.5646(0.004)	16.676	0.008	-0.259(0.006)	36.0
F7-42	00:55:35.5	-72:32:00.7	16.04(0.003)	15.7886(0.002)	15.943	-0.022	-0.252(0.004)	62.3
F7-43	00:55:35.8	-72:12:27.2	17.607(0.019)	17.4726(0.013)	17.655	-0.112	-0.135(0.023)	5.5
F7-44	00:55:35.9	-72:36:27.5	17.533(0.005)	17.3426(0.008)	17.276	0.105	-0.191(0.009)	18.5

Continued on next page

Table B.3 – *Continued from previous page*

Field-ID	RA	Dec	Rc	Hα	V	$B-V$	H$\alpha-Rc$	SNR
F7-45	00:55:36.1	-72:29:15.1	18.194(0.007)	17.7926(0.006)	17.954	0.033	-0.402(0.009)	36.4
F7-46	00:55:37.9	-72:30:04.7	17.841(0.007)	17.4566(0.005)	17.736	-0.034	-0.385(0.009)	37.7
F7-47	00:55:38.1	-72:34:36.5	18.286(0.006)	18.1586(0.007)	18.239	-0.035	-0.128(0.009)	13.1
F7-48	00:55:38.2	-72:27:54.8	17.146(0.005)	16.7066(0.005)	17.168	-0.076	-0.440(0.007)	51.1
F7-49	00:55:40.1	-72:29:45.0	16.329(0.003)	15.8606(0.002)	16.077	-0.005	-0.469(0.004)	105.6
F7-50	00:55:40.1	-72:26:41.9	16.493(0.004)	16.0126(0.002)	16.338	0.110	-0.481(0.004)	86.9
F7-51	00:55:41.2	-72:33:11.6	17.435(0.004)	17.2986(0.004)	17.383	-0.039	-0.137(0.006)	22.7
F7-52	00:55:42.4	-72:35:37.2	16.923(0.004)	16.7506(0.003)	16.754	0.060	-0.173(0.005)	32.0
F7-53	00:55:42.6	-72:23:58.4	16.004(0.003)	15.8486(0.003)	15.842	0.037	-0.156(0.004)	34.2
F7-54	00:55:43.0	-72:15:37.7	18.043(0.007)	17.7116(0.006)	17.939	-0.020	-0.332(0.009)	31.0
F7-55	00:55:43.2	-72:30:49.3	16.083(0.003)	15.5416(0.002)	16.092	-0.011	-0.542(0.004)	118.3
F7-56	00:55:43.5	-72:31:33.0	16.262(0.004)	15.7946(0.002)	16.083	0.004	-0.468(0.004)	85.0
F7-57	00:55:43.8	-72:18:23.6	17.987(0.008)	17.8856(0.007)	17.774	0.004	-0.102(0.011)	9.1
F7-58	00:55:44.0	-72:14:15.5	15.625(0.003)	14.8476(0.001)	15.731	-0.060	-0.778(0.003)	175.6
F7-59	00:55:44.2	-72:28:07.6	17.875(0.006)	17.4396(0.005)	17.575	0.136	-0.436(0.008)	46.0
F7-60	00:55:44.3	-72:34:37.2	17.429(0.004)	17.1476(0.004)	17.279	-0.006	-0.282(0.006)	43.9
F7-61	00:55:44.5	-72:18:16.4	16.438(0.007)	16.3666(0.006)	15.718	-0.128	-0.072(0.009)	7.5
F7-62	00:55:44.5	-72:20:38.4	16.205(0.003)	15.7216(0.002)	16.177	0.025	-0.484(0.004)	108.3
F7-63	00:55:44.5	-72:25:44.1	16.941(0.004)	16.6106(0.003)	16.849	-0.026	-0.331(0.005)	57.0
F7-64	00:55:44.7	-72:35:50.3	17.571(0.005)	17.5016(0.004)	17.438	-0.052	-0.070(0.006)	10.6
F7-65	00:55:44.7	-72:16:07.7	17.221(0.015)	16.9226(0.021)	17.004	-0.112	-0.299(0.026)	10.1
F7-66	00:55:45.0	-72:09:15.2	18.261(0.009)	18.1636(0.008)	18.167	-0.049	-0.098(0.012)	7.8

Continued on next page

Table B.3 – *Continued from previous page*

Field-ID	RA	Dec	Rc	Hα	V	$B-V$	H$\alpha - Rc$	SNR
F7-67	00:55:45.2	-72:19:35.0	17.421(0.006)	17.1596(0.005)	17.323	-0.041	-0.262(0.008)	29.8
F7-68	00:55:45.6	-72:36:33.4	18.219(0.008)	18.0256(0.006)	18.060	0.007	-0.194(0.010)	17.7
F7-69	00:55:45.8	-72:14:03.5	18.16(0.01)	18.0306(0.009)	18.071	-0.181	-0.130(0.013)	9.1
F7-70	00:55:45.9	-72:33:13.5	16.062(0.006)	15.8546(0.002)	15.868	-0.077	-0.208(0.006)	29.9
F7-71	00:55:46.7	-72:15:44.2	18.383(0.009)	18.2806(0.007)	18.144	0.029	-0.103(0.011)	8.6
F7-72	00:55:47.2	-72:20:23.3	16.988(0.009)	16.4646(0.004)	16.964	0.020	-0.524(0.010)	42.2
F7-73	00:55:47.3	-72:27:46.8	18.29(0.008)	18.2246(0.005)	18.050	-0.062	-0.066(0.009)	6.8
F7-74	00:55:47.4	-72:39:08.4	16.286(0.006)	16.1306(0.005)	16.263	-0.232	-0.156(0.008)	18.6
F7-75	00:55:47.6	-72:37:20.8	17.217(0.004)	16.7936(0.003)	17.042	0.075	-0.424(0.005)	70.2
F7-76	00:55:48.1	-72:28:14.1	17.749(0.005)	17.4576(0.004)	17.632	-0.028	-0.292(0.006)	40.0
F7-77	00:55:48.8	-72:27:12.9	17.399(0.005)	17.1866(0.004)	17.296	-0.060	-0.213(0.006)	30.2
F7-78	00:55:48.9	-72:14:23.9	18.112(0.008)	17.8236(0.005)	17.970	-0.001	-0.289(0.009)	26.9
F7-79	00:55:49.0	-72:30:39.3	18.219(0.028)	17.9016(0.008)	18.030	-0.022	-0.318(0.029)	9.5
F7-80	00:55:49.6	-72:25:27.5	14.564(0.002)	14.0436(0.002)	14.565	0.197	-0.521(0.003)	146.3
F7-81	00:55:49.7	-72:37:52.4	18.079(0.006)	17.9696(0.007)	17.875	0.080	-0.110(0.009)	11.3
F7-82	00:55:49.9	-72:18:42.6	17.595(0.007)	16.9916(0.004)	17.556	0.004	-0.604(0.008)	57.4
F7-83	00:55:50.5	-72:15:40.2	16.937(0.004)	16.5766(0.003)	16.939	-0.023	-0.361(0.005)	61.4
F7-84	00:55:50.8	-72:28:49.5	18.319(0.018)	18.0676(0.011)	17.937	0.224	-0.252(0.021)	10.7
F7-85	00:55:51.2	-72:39:17.3	18.54(0.012)	18.3236(0.013)	18.174	0.107	-0.217(0.018)	11.1
F7-86	00:55:51.9	-72:25:51.0	17.096(0.003)	16.9826(0.003)	16.901	-0.086	-0.114(0.004)	25.5
F7-87	00:55:52.3	-72:26:04.0	17.172(0.004)	16.7956(0.003)	17.072	0.002	-0.377(0.005)	63.7
F7-88	00:55:52.6	-72:20:24.0	18.435(0.011)	18.1486(0.009)	18.236	0.078	-0.287(0.014)	17.7

Continued on next page

Table B.3 – *Continued from previous page*

Field-ID	RA	Dec	Rc	Hα	V	$B-V$	H$\alpha - Rc$	SNR
F7-89	00:55:52.8	-72:27:33.8	18.238(0.009)	18.0676(0.006)	18.070	0.130	-0.171(0.011)	14.6
F7-90	00:55:53.7	-72:15:57.4	18.243(0.014)	18.0486(0.007)	18.109	-0.056	-0.195(0.016)	11.4
F7-91	00:55:53.9	-72:09:54.5	16.093(0.003)	15.9896(0.002)	16.287	-0.180	-0.104(0.004)	27.5
F7-92	00:55:54.0	-72:36:47.5	18.061(0.005)	17.9296(0.005)	17.739	0.020	-0.132(0.007)	17.6
F7-93	00:55:54.4	-72:34:12.8	18.361(0.008)	18.0376(0.006)	18.269	0.022	-0.324(0.010)	28.0
F7-94	00:55:55.0	-72:25:38.7	17.642(0.005)	17.4056(0.003)	17.510	-0.012	-0.237(0.006)	36.5
F7-95	00:55:55.4	-72:37:40.7	17.129(0.005)	17.0506(0.003)	16.946	-0.046	-0.079(0.006)	13.0
F7-96	00:55:55.5	-72:26:58.5	17.598(0.005)	17.2876(0.004)	17.321	-0.013	-0.311(0.006)	42.2
F7-97	00:55:56.3	-72:23:33.6	16.546(0.003)	16.0386(0.002)	16.486	-0.023	-0.508(0.004)	112.5
F7-98	00:55:56.5	-72:33:51.2	17.899(0.006)	17.5806(0.004)	17.764	0.054	-0.319(0.007)	38.3
F7-99	00:55:57.4	-72:14:00.4	16.04(0.003)	15.7486(0.002)	16.025	-0.083	-0.292(0.004)	71.0
F7-100	00:55:57.5	-72:27:18.0	17.748(0.004)	17.5376(0.006)	17.647	-0.093	-0.211(0.007)	26.6
F7-101	00:55:57.5	-72:29:17.5	17.219(0.003)	16.8856(0.003)	17.063	-0.043	-0.334(0.004)	67.7
F7-102	00:55:58.0	-72:23:49.5	18.293(0.01)	18.1696(0.009)	18.099	-0.042	-0.124(0.013)	8.7
F7-103	00:55:58.1	-72:36:03.7	17.511(0.005)	17.3986(0.004)	17.312	0.037	-0.113(0.006)	16.7
F7-104	00:55:58.7	-72:31:43.7	18.088(0.018)	17.8186(0.015)	17.734	0.088	-0.270(0.023)	10.2
F7-105	00:55:59.3	-72:20:53.8	18.539(0.012)	18.3306(0.015)	18.229	0.037	-0.209(0.019)	9.9
F7-106	00:55:59.4	-72:30:34.6	15.884(0.002)	15.4446(0.003)	15.762	-0.062	-0.440(0.004)	100.3
F7-107	00:55:59.5	-72:24:55.8	17.937(0.008)	17.8206(0.006)	17.747	0.008	-0.117(0.010)	11.1

Table B.4: Hα emission sources identified in Field-8.

Field-ID	RA	Dec	Rc	Hα	V	$B-V$	H$\alpha - Rc$	SNR
F8-1	01:01:29.5	-72:14:58.8	18.059(0.009)	17.9164(0.01)	18.019	-0.137	-0.142(0.013)	9.9
F8-2	01:01:29.5	-72:23:20.2	13.922(0.007)	13.7014(0.002)	13.851	-0.001	-0.220(0.007)	27.4
F8-3	01:01:33.1	-72:18:50.7	16.925(0.004)	16.6504(0.004)	16.754	0.020	-0.274(0.006)	42.9
F8-4	01:01:34.2	-72:21:05.3	17.919(0.007)	17.6764(0.007)	17.634	-0.003	-0.242(0.010)	21.9
F8-5	01:01:34.8	-72:07:09.7	15.45(0.006)	15.0244(0.003)	15.573	-0.156	-0.425(0.007)	52.5
F8-6	01:01:34.8	-72:24:59.2	17.189(0.004)	16.9374(0.004)	17.034	0.026	-0.251(0.006)	39.7
F8-7	01:01:35.4	-72:15:15.2	17.684(0.005)	17.6384(0.005)	17.569	-0.124	-0.045(0.007)	6.3
F8-8	01:01:36.0	-72:03:36.4	17.951(0.008)	17.8684(0.009)	17.874	-0.112	-0.082(0.012)	6.6
F8-9	01:01:36.1	-72:09:54.4	16.881(0.004)	16.4624(0.003)	16.941	-0.096	-0.418(0.005)	69.4
F8-10	01:01:36.9	-72:04:15.1	16.186(0.004)	15.8484(0.003)	16.266	-0.163	-0.337(0.005)	58.0
F8-11	01:01:37.3	-71:56:50.9	15.943(0.014)	14.9284(0.006)	14.876	-0.187	-1.014(0.015)	43.3
F8-12	01:01:37.4	-71:59:41.0	16.713(0.021)	16.5494(0.005)	16.704	-0.136	-0.163(0.022)	7.0
F8-13	01:01:37.9	-72:24:21.3	18.195(0.01)	18.0734(0.008)	17.630	-0.290	-0.121(0.013)	9.0
F8-14	01:01:39.8	-72:19:06.4	18.192(0.006)	18.0734(0.007)	18.035	0.029	-0.118(0.009)	12.2
F8-15	01:01:41.3	-72:22:59.4	17.241(0.006)	17.0414(0.003)	17.146	0.115	-0.199(0.007)	27.2
F8-16	01:01:42.4	-72:10:26.9	16.413(0.003)	16.0804(0.002)	16.384	-0.048	-0.332(0.004)	79.4
F8-17	01:01:42.5	-72:19:19.7	17.75(0.005)	17.6084(0.004)	17.614	0.004	-0.141(0.006)	20.7
F8-18	01:01:43.5	-72:07:52.1	16.838(0.004)	16.5294(0.003)	16.869	-0.047	-0.308(0.005)	53.7
F8-19	01:01:43.8	-72:12:46.9	17.716(0.006)	17.6574(0.006)	17.575	-0.004	-0.058(0.008)	6.7
F8-20	01:01:44.7	-72:22:16.4	17.542(0.004)	17.3654(0.005)	17.434	0.014	-0.176(0.006)	25.4
F8-21	01:01:46.8	-72:22:02.9	17.733(0.005)	17.6474(0.005)	17.655	0.008	-0.085(0.007)	11.6
F8-22	01:01:47.5	-72:26:45.1	18.554(0.017)	18.3374(0.012)	18.310	0.032	-0.216(0.021)	9.4

Continued on next page

Table B.4 – *Continued from previous page*

Field-ID	RA	Dec	Rc	Hα	V	$B-V$	H$\alpha-Rc$	SNR
F8-23	01:01:47.7	-71:57:39.6	18.189(0.017)	17.7444(0.009)	17.564	-0.124	-0.444(0.019)	19.0
F8-24	01:01:48.2	-71:58:40.8	18.464(0.013)	18.3744(0.01)	18.228	-0.076	-0.089(0.016)	5.2
F8-25	01:01:49.7	-72:24:54.5	16.316(0.002)	16.0924(0.003)	16.224	0.049	-0.223(0.004)	56.0
F8-26	01:01:49.9	-72:13:14.9	15.352(0.009)	15.0054(0.002)	14.759	-0.245	-0.346(0.009)	32.2
F8-27	01:01:50.5	-71:58:51.4	17.813(0.008)	17.7014(0.009)	17.795	-0.091	-0.111(0.012)	8.8
F8-28	01:01:50.9	-72:26:39.9	16.775(0.015)	16.3914(0.003)	16.649	-0.039	-0.383(0.015)	21.1
F8-29	01:01:51.6	-72:12:59.5	17.961(0.007)	17.8584(0.005)	17.806	-0.024	-0.102(0.009)	11.4
F8-30	01:01:52.3	-71:57:25.1	17.548(0.01)	17.4184(0.009)	17.299	-0.137	-0.129(0.013)	9.1
F8-31	01:01:52.4	-72:19:31.9	16.821(0.013)	16.2614(0.004)	16.682	-0.028	-0.559(0.014)	32.1
F8-32	01:01:52.8	-71:56:30.3	17.288(0.038)	16.1254(0.005)	16.106	-0.181	-1.162(0.038)	18.6
F8-33	01:01:54.0	-72:26:16.7	17.613(0.005)	17.4484(0.004)	17.483	-0.005	-0.164(0.006)	23.8
F8-34	01:01:54.1	-72:15:31.2	16.013(0.002)	15.5964(0.002)	15.895	-0.012	-0.416(0.003)	122.3
F8-35	01:01:54.1	-72:18:55.0	16.704(0.003)	16.4104(0.003)	16.860	-0.070	-0.293(0.004)	60.6
F8-36	01:01:54.2	-72:19:54.3	17.42(0.005)	17.1104(0.003)	17.223	0.028	-0.309(0.006)	46.2
F8-37	01:01:54.3	-72:00:29.3	16.638(0.009)	16.4244(0.007)	16.396	0.173	-0.213(0.011)	17.0
F8-38	01:01:54.5	-72:08:39.0	17.427(0.009)	17.1584(0.01)	17.283	-0.038	-0.268(0.013)	17.7
F8-39	01:01:56.1	-72:07:43.0	17.488(0.006)	17.1054(0.004)	17.457	-0.095	-0.382(0.007)	44.7
F8-40	01:01:56.4	-72:11:18.7	16.451(0.028)	15.3194(0.001)	15.867	-0.119	-1.131(0.028)	25.1
F8-41	01:01:56.6	-72:15:26.7	16.465(0.003)	16.3634(0.002)	16.260	0.088	-0.101(0.004)	26.9
F8-42	01:01:57.0	-72:24:38.5	17.601(0.005)	17.4884(0.004)	17.495	0.010	-0.112(0.006)	16.7
F8-43	01:01:58.0	-72:02:39.2	18.317(0.011)	17.9504(0.007)	18.092	-0.099	-0.366(0.013)	23.9
F8-44	01:01:58.3	-72:24:27.6	16.489(0.013)	16.0264(0.003)	16.414	0.012	-0.462(0.013)	28.2

Continued on next page

Table B.4 – *Continued from previous page*

Field-ID	RA	Dec	*Rc*	Hα	*V*	$B-V$	Hα − *Rc*	SNR
F8-45	01:01:58.4	-71:57:43.8	18.475(0.016)	18.2804(0.014)	18.312	-0.031	-0.194(0.021)	8.4
F8-46	01:01:59.4	-72:14:15.0	17.841(0.047)	17.0134(0.028)	16.171	-0.001	-0.827(0.055)	10.6
F8-47	01:01:59.5	-72:01:46.9	15.762(0.002)	15.4194(0.002)	15.364	0.104	-0.342(0.003)	103.8
F8-48	01:01:59.6	-72:06:41.9	17.097(0.004)	16.7434(0.003)	17.076	-0.054	-0.353(0.005)	60.3
F8-49	01:01:59.8	-72:14:36.9	18.349(0.007)	18.2364(0.007)	18.183	-0.041	-0.112(0.010)	10.8
F8-50	01:01:59.9	-71:57:22.2	17.847(0.052)	17.3674(0.008)	17.338	-0.070	-0.479(0.053)	7.4
F8-51	01:02:00.0	-72:16:47.1	17.751(0.004)	17.6464(0.005)	17.612	0.009	-0.104(0.006)	15.5
F8-52	01:02:00.5	-72:06:25.2	16.951(0.005)	16.6214(0.003)	16.874	-0.042	-0.329(0.006)	48.7
F8-53	01:02:00.6	-72:28:09.4	17.641(0.006)	17.5294(0.005)	17.508	-0.086	-0.111(0.008)	13.6
F8-54	01:02:00.9	-72:10:49.6	15.731(0.002)	15.1214(0.002)	15.671	-0.035	-0.609(0.003)	164.9
F8-55	01:02:01.2	-72:18:53.6	17.903(0.006)	17.8434(0.005)	17.665	-0.050	-0.059(0.008)	7.4
F8-56	01:02:01.5	-72:10:51.6	18.394(0.011)	18.2024(0.009)	18.326	-0.112	-0.191(0.014)	12.3
F8-57	01:02:01.6	-72:25:06.0	16.054(0.002)	15.6634(0.002)	16.041	0.011	-0.390(0.003)	115.9
F8-58	01:02:01.9	-72:15:12.4	17.997(0.012)	17.6574(0.009)	17.813	-0.323	-0.339(0.015)	19.4
F8-59	01:02:02.1	-72:14:01.0	17.151(0.004)	16.8084(0.003)	17.010	-0.011	-0.342(0.005)	58.7
F8-60	01:02:03.0	-72:04:08.7	18.317(0.01)	18.1514(0.009)	18.260	-0.076	-0.165(0.013)	11.4
F8-61	01:02:03.2	-72:26:12.1	15.568(0.002)	15.1934(0.002)	15.457	0.062	-0.374(0.003)	112.0
F8-62	01:02:04.7	-72:19:52.4	16.182(0.01)	15.7914(0.002)	16.006	-0.032	-0.390(0.010)	32.2
F8-63	01:02:05.4	-72:08:13.5	17.039(0.009)	16.6644(0.006)	16.822	0.021	-0.374(0.011)	29.3
F8-64	01:02:05.8	-72:19:21.0	15.645(0.006)	15.2744(0.001)	15.563	-0.030	-0.370(0.006)	51.6
F8-65	01:02:07.6	-72:30:13.4	18.315(0.01)	18.2344(0.01)	18.166	-0.002	-0.080(0.014)	5.5
F8-66	01:02:08.4	-72:19:27.6	18.612(0.009)	18.4174(0.008)	18.401	0.011	-0.194(0.012)	14.8

Continued on next page

Table B.4 – *Continued from previous page*

Field-ID	RA	Dec	Rc	Hα	V	$B-V$	H$\alpha - Rc$	SNR
F8-67	01:02:08.9	-72:29:14.0	15.803(0.004)	15.4324(0.003)	15.835	0.019	-0.370(0.005)	62.8
F8-68	01:02:09.0	-72:23:44.8	18.395(0.016)	18.2864(0.013)	18.182	-0.054	-0.108(0.021)	5.0
F8-69	01:02:09.0	-72:20:16.4	16.218(0.006)	15.6974(0.002)	16.107	0.065	-0.520(0.006)	65.4
F8-70	01:02:10.1	-72:23:55.6	15.336(0.003)	14.8314(0.002)	15.394	-0.055	-0.504(0.004)	111.9
F8-71	01:02:10.4	-72:01:26.8	16.87(0.004)	16.8134(0.002)	16.827	-0.076	-0.056(0.004)	12.3
F8-72	01:02:10.5	-72:18:53.6	17.772(0.005)	17.4964(0.004)	17.476	0.031	-0.275(0.006)	38.0
F8-73	01:02:10.7	-72:07:21.6	16.854(0.004)	16.5904(0.003)	16.805	-0.077	-0.263(0.005)	46.8
F8-74	01:02:10.8	-71:56:40.4	16.87(0.034)	16.2184(0.005)	16.102	-0.118	-0.651(0.034)	14.3
F8-75	01:02:11.5	-72:27:26.9	15.978(0.01)	15.6714(0.002)	15.413	-0.146	-0.306(0.010)	26.2
F8-76	01:02:11.6	-72:08:54.3	16.548(0.003)	16.1104(0.002)	16.582	-0.065	-0.437(0.004)	99.9
F8-77	01:02:12.2	-72:15:49.1	17.529(0.004)	17.4874(0.004)	17.358	0.000	-0.041(0.006)	7.2
F8-78	01:02:13.0	-72:18:31.0	16.696(0.003)	16.2084(0.002)	16.663	-0.098	-0.487(0.004)	108.9
F8-79	01:02:13.6	-72:08:32.7	16.627(0.004)	16.1464(0.002)	16.575	0.042	-0.480(0.004)	86.8
F8-80	01:02:13.8	-72:22:13.4	14.377(0.002)	14.0374(0.001)	14.312	0.092	-0.339(0.002)	130.4
F8-81	01:02:14.4	-72:11:16.1	15.249(0.019)	14.8344(0.003)	14.568	-0.220	-0.414(0.019)	17.9
F8-82	01:02:15.3	-71:59:50.1	16.754(0.004)	16.6164(0.003)	16.751	-0.079	-0.137(0.005)	25.8
F8-83	01:02:15.8	-72:18:41.3	15.901(0.012)	15.8204(0.004)	15.391	-0.078	-0.080(0.013)	6.1
F8-84	01:02:15.9	-72:15:01.9	17.48(0.004)	17.4004(0.004)	17.309	-0.026	-0.079(0.006)	13.5
F8-85	01:02:16.0	-72:25:16.0	16.443(0.015)	16.0694(0.002)	16.070	-0.049	-0.373(0.015)	20.9
F8-86	01:02:16.4	-72:13:47.1	18.013(0.008)	17.9094(0.006)	17.805	-0.068	-0.103(0.010)	9.9
F8-87	01:02:17.2	-71:58:23.9	17.66(0.055)	17.1124(0.008)	16.967	-0.122	-0.547(0.056)	7.7
F8-88	01:02:17.9	-72:12:41.3	17.919(0.007)	17.8054(0.005)	17.772	-0.063	-0.113(0.009)	12.5

Continued on next page

Table B.4 – *Continued from previous page*

Field-ID	RA	Dec	Rc	Hα	V	$B-V$	Hα $-$ Rc	SNR
F8-89	01:02:18.6	-72:23:12.5	18.211(0.008)	17.7994(0.012)	18.028	-0.145	-0.411(0.014)	23.7
F8-90	01:02:18.7	-72:04:39.5	17.25(0.005)	16.6894(0.002)	17.211	-0.179	-0.560(0.005)	81.3
F8-91	01:02:18.9	-72:17:40.5	15.381(0.006)	15.1464(0.001)	15.225	0.036	-0.234(0.006)	34.7
F8-92	01:02:19.2	-72:21:21.3	17.763(0.006)	17.5854(0.004)	17.598	-0.029	-0.177(0.007)	22.7
F8-93	01:02:19.8	-72:00:48.3	18.585(0.012)	18.4824(0.01)	18.469	-0.076	-0.102(0.016)	6.3
F8-94	01:02:20.0	-72:19:24.6	17.772(0.005)	17.6394(0.004)	17.608	-0.149	-0.132(0.006)	19.5
F8-95	01:02:20.2	-72:12:47.4	17.362(0.009)	16.9854(0.007)	17.002	0.145	-0.376(0.011)	27.9
F8-96	01:02:22.1	-72:01:06.3	18.35(0.011)	18.0194(0.008)	18.162	0.104	-0.330(0.014)	20.9
F8-97	01:02:22.6	-72:07:46.5	17.256(0.004)	17.0394(0.004)	17.042	-0.014	-0.216(0.006)	34.7
F8-98	01:02:22.9	-72:05:53.9	17.472(0.005)	17.4114(0.004)	17.434	-0.079	-0.060(0.006)	9.2
F8-99	01:02:22.9	-72:00:29.6	18.407(0.01)	18.2824(0.013)	18.283	-0.139	-0.124(0.016)	7.2
F8-100	01:02:23.4	-72:00:06.1	14.881(0.003)	14.6414(0.003)	14.873	-0.177	-0.239(0.004)	50.6
F8-101	01:02:24.0	-72:23:21.6	17.966(0.006)	17.8974(0.006)	17.735	-0.004	-0.068(0.008)	7.8
F8-102	01:02:24.0	-72:12:55.3	18.621(0.012)	18.3924(0.01)	18.415	0.027	-0.228(0.016)	13.2
F8-103	01:02:24.0	-72:21:09.0	17.138(0.01)	16.6524(0.002)	16.941	0.012	-0.485(0.010)	38.4
F8-104	01:02:24.4	-72:00:30.6	18.39(0.008)	18.3144(0.01)	18.160	-0.120	-0.075(0.013)	5.7
F8-105	01:02:24.9	-72:08:45.0	15.531(0.003)	15.0444(0.003)	15.035	0.225	-0.486(0.004)	92.4
F8-106	01:02:25.9	-72:02:38.3	17.445(0.005)	17.3034(0.013)	17.184	-0.120	-0.141(0.014)	9.5
F8-107	01:02:26.6	-72:00:20.5	17.883(0.007)	17.7134(0.006)	17.748	-0.016	-0.169(0.009)	17.0

Table B.5: Hα emission sources identified in Field-9.

Field-ID	RA	Dec	Rc	Hα	V	$B-V$	H$\alpha-Rc$	SNR
F9-1	00:41:44.4	-73:37:52.9	18.409(0.008)	18.0323(0.006)	18.078	-0.011	-0.376(0.010)	31.8
F9-2	00:41:44.5	-73:30:45.5	16.779(0.004)	16.7073(0.004)	16.517	0.074	-0.071(0.006)	12.2
F9-3	00:41:45.6	-73:36:14.7	17.825(0.005)	17.5963(0.005)	17.573	0.048	-0.228(0.007)	29.1
F9-4	00:41:46.4	-73:34:06.7	16.941(0.007)	16.7753(0.006)	16.693	0.021	-0.165(0.009)	16.6
F9-5	00:41:48.6	-73:19:28.9	18.634(0.079)	18.0893(0.021)	17.713	-0.033	-0.544(0.082)	5.2
F9-6	00:41:48.9	-73:34:09.8	18.141(0.007)	18.0633(0.007)	17.875	-0.029	-0.077(0.010)	7.5
F9-7	00:41:49.2	-73:28:10.6	17.713(0.006)	17.6653(0.006)	17.317	-0.010	-0.047(0.008)	5.5
F9-8	00:41:50.5	-73:33:05.4	18.03(0.008)	17.9093(0.006)	17.642	0.059	-0.120(0.010)	11.4
F9-9	00:41:50.6	-73:34:40.0	18.341(0.008)	18.1243(0.006)	18.087	-0.040	-0.216(0.010)	19.6
F9-10	00:41:51.7	-73:27:03.7	17.609(0.009)	17.5423(0.006)	17.251	0.072	-0.066(0.011)	5.9
F9-11	00:41:55.2	-73:28:51.4	17.114(0.004)	16.9973(0.004)	16.864	0.010	-0.116(0.006)	19.5
F9-12	00:41:57.1	-73:39:32.2	16.408(0.003)	15.9083(0.002)	16.236	-0.050	-0.499(0.004)	111.0
F9-13	00:41:58.0	-73:28:43.8	16.15(0.009)	15.7593(0.002)	15.652	0.031	-0.390(0.009)	35.6
F9-14	00:41:58.6	-73:34:17.2	18.506(0.008)	18.4213(0.008)	18.146	0.012	-0.084(0.011)	7.2
F9-15	00:42:01.1	-73:23:46.6	17.208(0.004)	17.0413(0.003)	16.972	0.052	-0.166(0.005)	30.8
F9-16	00:42:01.4	-73:46:40.3	18.019(0.006)	17.8433(0.004)	17.724	0.018	-0.175(0.007)	22.4
F9-17	00:42:01.9	-73:25:56.6	18.136(0.007)	17.9563(0.005)	17.844	0.095	-0.179(0.009)	19.2
F9-18	00:42:03.5	-73:35:41.9	17.705(0.005)	17.5353(0.005)	17.472	0.002	-0.169(0.007)	22.2
F9-19	00:42:04.6	-73:21:09.7	14.713(0.009)	14.3343(0.002)	14.243	0.259	-0.378(0.009)	34.6
F9-20	00:42:06.4	-73:21:17.8	18.12(0.011)	17.5073(0.004)	17.157	0.100	-0.612(0.012)	40.0
F9-21	00:42:07.9	-73:45:02.5	17.163(0.003)	16.7923(0.003)	16.776	-0.099	-0.370(0.004)	74.0
F9-22	00:42:08.1	-73:20:11.9	17.496(0.029)	17.0423(0.014)	17.196	-0.030	-0.453(0.032)	11.5

Continued on next page

Table B.5 – *Continued from previous page*

Field-ID	RA	Dec	Rc	Hα	V	$B-V$	H$\alpha - Rc$	SNR
F9-23	00:42:08.6	-73:35:01.7	18.56(0.008)	18.3803(0.007)	18.126	0.039	-0.179(0.011)	15.5
F9-24	00:42:08.7	-73:18:51.7	18.182(0.04)	17.3403(0.006)	17.349	0.061	-0.841(0.040)	14.5
F9-25	00:42:10.8	-73:43:48.2	17.272(0.004)	17.1363(0.002)	16.995	0.047	-0.135(0.004)	28.4
F9-26	00:42:14.7	-73:22:26.6	18.194(0.02)	18.0433(0.006)	17.914	0.045	-0.150(0.021)	6.7
F9-27	00:42:15.1	-73:38:31.8	17.578(0.005)	17.4343(0.003)	17.366	0.035	-0.143(0.006)	23.0
F9-28	00:42:17.9	-73:26:41.3	17.357(0.004)	17.1673(0.006)	17.132	-0.018	-0.189(0.007)	24.1
F9-29	00:42:18.0	-73:30:48.2	17.959(0.006)	17.6643(0.005)	17.669	0.057	-0.294(0.008)	33.0
F9-30	00:42:18.2	-73:31:37.4	17.867(0.006)	17.5933(0.006)	17.614	-0.020	-0.273(0.008)	28.5
F9-31	00:42:18.9	-73:31:03.1	17.559(0.005)	17.4603(0.004)	17.184	0.017	-0.098(0.006)	14.7
F9-32	00:42:19.8	-73:22:09.3	17.763(0.008)	17.6593(0.006)	17.515	-0.011	-0.103(0.010)	9.9
F9-33	00:42:21.1	-73:35:52.1	16.505(0.004)	16.3533(0.003)	16.478	0.152	-0.151(0.005)	28.2
F9-34	00:42:21.2	-73:44:06.5	17.636(0.007)	17.4283(0.024)	17.050	0.093	-0.207(0.025)	7.5
F9-35	00:42:21.6	-73:44:13.5	17.666(0.006)	17.4213(0.011)	17.307	0.061	-0.244(0.013)	17.5
F9-36	00:42:26.5	-73:40:32.7	16.767(0.006)	16.6433(0.003)	16.808	-0.021	-0.123(0.007)	17.4
F9-37	00:42:28.3	-73:23:47.9	17.231(0.005)	17.0413(0.004)	16.971	0.036	-0.189(0.006)	27.1
F9-38	00:42:28.7	-73:42:17.9	17.578(0.004)	17.4523(0.003)	17.296	0.014	-0.125(0.005)	23.7
F9-39	00:42:28.9	-73:20:19.1	17.259(0.03)	17.0643(0.004)	16.431	0.137	-0.194(0.030)	5.9
F9-40	00:42:30.0	-73:30:45.1	15.616(0.021)	14.8773(0.001)	14.488	0.299	-0.738(0.021)	25.5
F9-41	00:42:31.2	-73:19:42.0	18.608(0.016)	18.0823(0.007)	17.643	-0.039	-0.525(0.017)	23.8
F9-42	00:42:33.5	-73:32:08.6	15.963(0.002)	15.7453(0.002)	15.867	0.020	-0.217(0.003)	69.6
F9-43	00:42:34.2	-73:27:09.0	17.969(0.005)	17.8683(0.007)	17.634	0.035	-0.100(0.009)	11.1
F9-44	00:42:35.0	-73:39:21.0	18.16(0.005)	18.0433(0.004)	17.790	0.013	-0.116(0.006)	17.2

Continued on next page

Table B.5 – *Continued from previous page*

Field-ID	RA	Dec	Rc	Hα	V	$B-V$	H$\alpha - Rc$	SNR
F9-45	00:42:36.0	-73:47:54.4	14.737(0.002)	14.3933(0.001)	14.593	-0.105	-0.343(0.002)	131.6
F9-46	00:42:36.5	-73:32:16.8	16.199(0.003)	16.1283(0.002)	15.878	-0.038	-0.070(0.004)	18.9
F9-47	00:42:36.8	-73:36:05.7	18.573(0.009)	18.2923(0.007)	18.140	-0.023	-0.280(0.011)	21.7
F9-48	00:42:36.9	-73:22:52.9	18.249(0.011)	18.1023(0.008)	17.925	0.031	-0.146(0.014)	10.1
F9-49	00:42:39.3	-73:30:06.2	16.93(0.003)	16.4403(0.002)	16.724	0.059	-0.489(0.004)	109.2
F9-50	00:42:40.6	-73:40:37.0	18.158(0.009)	17.9283(0.019)	17.762	0.089	-0.229(0.021)	9.8
F9-51	00:42:41.1	-73:22:13.5	17.186(0.004)	17.0583(0.003)	16.972	0.064	-0.127(0.005)	24.0
F9-52	00:42:41.2	-73:29:11.6	16.352(0.004)	15.9433(0.002)	16.171	0.039	-0.408(0.004)	76.1
F9-53	00:42:41.3	-73:41:30.4	16.853(0.014)	16.5423(0.002)	16.456	0.042	-0.310(0.014)	19.1
F9-54	00:42:41.7	-73:38:45.1	17.502(0.011)	17.1683(0.006)	16.885	0.299	-0.333(0.013)	22.9
F9-55	00:42:41.7	-73:31:24.7	17.539(0.005)	17.4073(0.004)	17.180	0.106	-0.131(0.006)	19.3
F9-56	00:42:41.9	-73:38:54.2	18.059(0.007)	17.9973(0.005)	17.649	0.092	-0.061(0.009)	6.9
F9-57	00:42:42.7	-73:38:52.5	18.294(0.007)	18.1113(0.004)	17.922	0.026	-0.182(0.008)	20.8
F9-58	00:42:43.1	-73:35:30.9	17.804(0.005)	17.5463(0.004)	17.502	-0.024	-0.257(0.006)	35.8
F9-59	00:42:44.1	-73:21:08.9	17.689(0.059)	16.7713(0.004)	16.377	0.044	-0.917(0.059)	10.5
F9-60	00:42:44.5	-73:29:57.1	16.686(0.004)	16.3733(0.003)	16.391	0.030	-0.312(0.005)	54.3
F9-61	00:42:45.1	-73:29:08.9	17.287(0.005)	17.2543(0.003)	16.962	-0.016	-0.032(0.006)	5.5
F9-62	00:42:45.6	-73:22:22.1	17.404(0.006)	17.1233(0.003)	17.270	0.111	-0.280(0.007)	36.8
F9-63	00:42:45.6	-73:27:33.8	17.293(0.01)	16.8893(0.003)	16.961	-0.034	-0.403(0.010)	32.3
F9-64	00:42:45.9	-73:46:26.9	18.131(0.006)	18.0283(0.005)	17.784	0.003	-0.102(0.008)	12.5
F9-65	00:42:46.8	-73:27:21.1	17.49(0.005)	17.2993(0.004)	17.187	0.025	-0.190(0.006)	27.3
F9-66	00:42:48.6	-73:30:30.8	17.266(0.005)	17.0893(0.004)	16.992	-0.055	-0.176(0.006)	25.4

Continued on next page

Table B.5 – *Continued from previous page*

Field-ID	RA	Dec	*Rc*	Hα	*V*	$B-V$	Hα − *Rc*	SNR
F9-67	00:42:50.4	-73:28:36.6	18.073(0.007)	17.7753(0.007)	17.798	-0.045	-0.297(0.010)	26.3
F9-68	00:42:50.6	-73:21:08.3	18.326(0.008)	18.2113(0.006)	17.924	0.109	-0.114(0.010)	10.8
F9-69	00:42:53.0	-73:43:11.5	18.153(0.006)	17.9913(0.004)	17.755	0.074	-0.161(0.007)	20.8
F9-70	00:42:53.1	-73:29:45.7	16.907(0.015)	16.7293(0.005)	16.526	0.082	-0.177(0.016)	10.3
F9-71	00:42:53.4	-73:20:12.6	17.495(0.005)	17.1793(0.004)	17.126	0.168	-0.315(0.006)	42.7
F9-72	00:42:53.9	-73:26:15.1	17.57(0.005)	17.4863(0.005)	17.364	0.184	-0.083(0.007)	11.3
F9-73	00:42:54.6	-73:28:30.4	17.876(0.008)	17.7403(0.008)	17.467	0.023	-0.135(0.011)	11.2
F9-74	00:42:55.5	-73:45:11.4	17.821(0.005)	17.5073(0.003)	17.551	-0.049	-0.313(0.006)	46.7
F9-75	00:42:55.6	-73:17:36.9	18.041(0.102)	17.2113(0.014)	16.908	0.074	-0.829(0.103)	5.6
F9-76	00:42:56.3	-73:32:33.5	18.043(0.014)	17.9313(0.005)	17.790	-0.151	-0.111(0.015)	7.1
F9-77	00:42:56.6	-73:25:14.9	18.541(0.016)	18.3963(0.011)	18.067	0.106	-0.144(0.019)	7.0
F9-78	00:42:59.5	-73:17:44.7	18.53(0.121)	17.6163(0.013)	17.338	0.053	-0.913(0.122)	5.1
F9-79	00:43:00.2	-73:32:25.1	17.707(0.009)	17.6263(0.009)	17.457	-0.037	-0.080(0.013)	6.1
F9-80	00:43:00.2	-73:20:38.5	18.082(0.024)	17.4903(0.017)	18.158	0.213	-0.591(0.029)	15.5
F9-81	00:43:02.2	-73:27:33.7	16.666(0.003)	16.2943(0.002)	16.479	-0.019	-0.371(0.004)	87.2
F9-82	00:43:02.6	-73:23:55.1	18.117(0.007)	17.9053(0.006)	17.796	0.041	-0.211(0.009)	20.8
F9-83	00:43:04.6	-73:34:50.9	18.5(0.053)	15.3793(0.002)	15.100	0.246	-3.120(0.053)	19.3
F9-84	00:43:05.2	-73:23:25.2	17.812(0.013)	17.7093(0.005)	17.411	0.068	-0.102(0.014)	7.0
F9-85	00:43:05.2	-73:32:07.9	18.027(0.007)	17.9703(0.006)	17.629	0.034	-0.056(0.009)	6.0
F9-86	00:43:05.7	-73:43:25.2	18.276(0.007)	18.2183(0.005)	17.841	-0.039	-0.057(0.009)	6.5
F9-87	00:43:06.1	-73:17:31.6	18.579(0.044)	16.8363(0.009)	16.708	0.072	-1.742(0.045)	19.3
F9-88	00:43:06.2	-73:18:10.2	17.793(0.049)	16.6963(0.005)	16.460	-0.041	-1.096(0.049)	14.0

Continued on next page

Table B.5 – *Continued from previous page*

Field-ID	RA	Dec	Rc	Hα	V	$B-V$	H$\alpha - Rc$	SNR
F9-89	00:43:06.9	-73:28:57.1	17.357(0.004)	17.1953(0.004)	17.046	0.032	-0.161(0.006)	26.5
F9-90	00:43:07.0	-73:40:13.1	16.752(0.003)	16.3443(0.002)	16.511	-0.014	-0.407(0.004)	94.2
F9-91	00:43:07.8	-73:28:53.5	18.525(0.009)	18.3883(0.009)	18.133	0.012	-0.136(0.013)	10.1
F9-92	00:43:08.6	-73:26:29.3	17.612(0.008)	16.8533(0.003)	16.726	0.121	-0.758(0.009)	63.9
F9-93	00:43:09.7	-73:25:11.4	16.845(0.003)	16.4193(0.002)	16.690	0.031	-0.425(0.004)	97.6
F9-94	00:43:10.2	-73:34:31.3	16.073(0.003)	15.4473(0.002)	15.596	-0.005	-0.625(0.004)	131.8
F9-95	00:43:10.5	-73:21:29.8	17.85(0.01)	17.6983(0.006)	16.886	0.184	-0.151(0.012)	12.1
F9-96	00:43:10.9	-73:18:47.1	17.552(0.033)	17.2183(0.006)	17.025	0.275	-0.333(0.034)	8.6
F9-97	00:43:12.1	-73:37:01.8	16.878(0.003)	16.6303(0.002)	16.561	0.114	-0.247(0.004)	61.3
F9-98	00:43:13.3	-73:44:22.2	17.684(0.004)	17.2553(0.003)	17.475	0.014	-0.428(0.005)	70.8
F9-99	00:43:14.6	-73:44:50.5	18.308(0.007)	18.2343(0.005)	17.861	-0.009	-0.073(0.009)	8.2
F9-100	00:43:14.8	-73:23:47.2	18.496(0.011)	18.3603(0.008)	18.048	0.051	-0.135(0.014)	9.4
F9-101	00:43:15.3	-73:44:06.7	17.334(0.004)	17.2093(0.003)	16.728	0.228	-0.124(0.005)	23.5
F9-102	00:43:15.5	-73:46:47.6	17.768(0.005)	17.6663(0.004)	17.439	0.021	-0.101(0.006)	15.1
F9-103	00:43:15.8	-73:17:56.0	17.356(0.014)	16.7043(0.006)	16.384	0.163	-0.651(0.015)	32.2
F9-104	00:43:16.4	-73:26:46.7	16.856(0.003)	16.7653(0.004)	16.619	0.062	-0.090(0.005)	17.3
F9-105	00:43:17.5	-73:29:31.9	18.324(0.008)	18.1033(0.008)	17.930	-0.020	-0.220(0.011)	17.6
F9-106	00:43:19.1	-73:37:45.2	16.362(0.002)	16.2163(0.002)	16.147	0.016	-0.145(0.003)	48.1
F9-107	00:43:19.5	-73:42:35.0	16.218(0.002)	15.7223(0.002)	15.933	-0.074	-0.495(0.003)	140.6

Table B.6: Hα emission sources identified in Field-10.

Field-ID	RA	Dec	Rc	Hα	V	$B - V$	Hα − Rc	SNR
F10-1	01:12:25.2	-73:18:04.5	17.445(0.005)	17.293(0.005)	17.317	-0.039	-0.152(0.007)	20.0
F10-2	01:12:34.0	-73:27:24.7	18.218(0.009)	18.04(0.024)	17.879	-0.210	-0.178(0.026)	6.4
F10-3	01:12:36.1	-73:24:40.8	17.983(0.007)	17.776(0.006)	17.812	0.018	-0.207(0.009)	20.4
F10-4	01:12:37.7	-73:35:19.0	17.506(0.005)	17.311(0.004)	17.356	-0.078	-0.195(0.006)	27.9
F10-5	01:12:38.6	-73:12:45.1	18.186(0.009)	18.083(0.009)	17.995	-0.068	-0.102(0.013)	7.7
F10-6	01:12:38.6	-73:38:13.2	17.351(0.006)	17.199(0.004)	17.046	-0.080	-0.152(0.007)	19.6
F10-7	01:12:40.3	-73:38:44.6	18.017(0.006)	17.915(0.008)	17.859	-0.016	-0.102(0.010)	9.8
F10-8	01:12:44.1	-73:26:58.1	17.095(0.004)	16.818(0.003)	16.927	-0.072	-0.276(0.005)	48.8
F10-9	01:12:45.3	-73:37:30.3	18.053(0.006)	17.927(0.007)	17.908	-0.005	-0.126(0.009)	13.0
F10-10	01:12:46.2	-73:25:56.4	18.213(0.006)	17.928(0.007)	18.064	-0.050	-0.285(0.009)	27.2
F10-11	01:12:47.5	-73:14:43.4	17.797(0.007)	17.686(0.008)	17.517	-0.313	-0.111(0.011)	10.0
F10-12	01:12:47.9	-73:14:43.7	18.64(0.019)	18.431(0.018)	17.757	-0.092	-0.209(0.026)	7.3
F10-13	01:12:48.4	-73:30:26.9	15.594(0.004)	15.33(0.002)	15.501	-0.041	-0.264(0.004)	52.3
F10-14	01:12:52.8	-73:17:56.9	17.398(0.007)	17.176(0.005)	17.199	0.041	-0.222(0.009)	23.4
F10-15	01:12:53.8	-73:30:26.1	14.794(0.005)	14.24(0.002)	14.740	-0.017	-0.555(0.005)	80.6
F10-16	01:12:58.0	-73:35:04.6	18.602(0.009)	18.256(0.008)	18.471	-0.028	-0.345(0.012)	24.6
F10-17	01:12:58.2	-73:17:05.7	18.454(0.01)	18.262(0.009)	18.244	-0.062	-0.193(0.013)	13.1
F10-18	01:13:08.2	-73:15:20.7	17.134(0.005)	16.716(0.002)	17.156	0.052	-0.417(0.005)	64.4
F10-19	01:13:13.1	-73:08:33.0	16.846(0.005)	16.674(0.003)	16.731	-0.080	-0.172(0.006)	27.2
F10-20	01:13:14.8	-73:25:22.8	18.046(0.007)	17.947(0.007)	17.847	0.053	-0.098(0.010)	9.5
F10-21	01:13:16.2	-73:28:36.9	17.538(0.005)	17.25(0.004)	17.319	-0.087	-0.288(0.006)	39.6
F10-22	01:13:16.6	-73:12:06.6	17.506(0.006)	17.262(0.004)	17.391	0.009	-0.245(0.007)	30.4

Continued on next page

Table B.6 – *Continued from previous page*

Field-ID	RA	Dec	*Rc*	Hα	*V*	$B-V$	H$\alpha - Rc$	SNR
F10-23	01:13:20.3	-73:33:06.7	17.544(0.005)	17.39(0.004)	17.406	-0.051	-0.155(0.006)	22.5
F10-24	01:13:20.6	-73:22:33.7	18.09(0.007)	18.025(0.007)	18.395	0.016	-0.065(0.010)	6.3
F10-25	01:13:26.3	-73:21:34.1	16.601(0.003)	16.179(0.002)	16.412	-0.063	-0.421(0.004)	96.9
F10-26	01:13:27.3	-73:16:21.0	17.95(0.007)	17.873(0.008)	17.830	0.156	-0.076(0.011)	6.9
F10-27	01:13:28.5	-73:31:54.9	18.43(0.009)	18.309(0.008)	18.283	-0.062	-0.122(0.012)	9.5
F10-28	01:13:28.9	-73:25:22.4	16.192(0.006)	15.822(0.002)	16.087	0.013	-0.370(0.006)	49.5
F10-29	01:13:29.3	-73:11:20.1	17.823(0.008)	17.663(0.011)	17.739	-0.027	-0.160(0.014)	11.0
F10-30	01:13:32.0	-73:12:26.0	16.841(0.004)	16.507(0.002)	16.692	-0.055	-0.334(0.004)	64.4
F10-31	01:13:32.8	-73:16:25.2	16.933(0.003)	16.855(0.008)	16.740	0.008	-0.079(0.009)	8.9
F10-32	01:13:33.0	-73:17:31.4	18.567(0.101)	17.705(0.02)	17.704	0.108	-0.861(0.103)	5.8
F10-33	01:13:33.9	-73:18:13.3	16.341(0.004)	16.228(0.009)	16.006	-0.087	-0.113(0.010)	10.9
F10-34	01:13:35.6	-73:18:09.7	17.872(0.011)	17.389(0.022)	17.246	0.118	-0.483(0.025)	15.8
F10-35	01:13:35.6	-73:17:04.3	16.951(0.004)	16.755(0.011)	16.520	0.009	-0.196(0.012)	15.3
F10-36	01:13:35.8	-73:16:22.4	17.636(0.006)	17.351(0.013)	17.398	0.202	-0.285(0.014)	17.5
F10-37	01:13:35.8	-73:17:40.5	17.223(0.027)	17.031(0.01)	16.806	0.075	-0.191(0.029)	6.1
F10-38	01:13:38.6	-73:21:32.3	16.98(0.004)	16.584(0.003)	16.828	-0.076	-0.396(0.005)	66.3
F10-39	01:13:39.6	-73:27:20.7	18.474(0.01)	18.395(0.008)	18.305	-0.032	-0.080(0.013)	6.0
F10-40	01:13:43.3	-73:36:32.3	18.37(0.009)	18.13(0.006)	18.170	-0.039	-0.241(0.011)	19.9
F10-41	01:13:44.4	-73:33:38.4	17.648(0.037)	17.109(0.007)	17.264	0.022	-0.540(0.038)	11.3
F10-42	01:13:44.5	-73:30:14.2	17.688(0.031)	17.079(0.003)	17.380	0.036	-0.608(0.031)	15.0
F10-43	01:13:45.2	-73:18:07.6	17.07(0.004)	17.002(0.012)	16.742	-0.091	-0.067(0.013)	5.2
F10-44	01:13:45.9	-73:16:19.7	17.582(0.006)	17.24(0.018)	17.184	0.041	-0.343(0.019)	15.5

Continued on next page

Table B.6 – *Continued from previous page*

Field-ID	RA	Dec	Rc	Hα	V	$B-V$	Hα $-$ Rc	SNR
F10-45	01:13:47.1	-73:17:54.8	16.559(0.004)	16.485(0.009)	16.258	-0.115	-0.074(0.010)	7.3
F10-46	01:13:47.2	-73:16:20.3	17.674(0.006)	17.325(0.019)	17.365	-0.029	-0.348(0.020)	15.0
F10-47	01:13:49.0	-73:18:50.9	17.224(0.005)	17.022(0.013)	16.976	-0.096	-0.203(0.014)	13.3
F10-48	01:13:50.8	-73:16:13.3	18.282(0.008)	18.136(0.012)	18.011	-0.199	-0.146(0.014)	9.4
F10-49	01:13:51.0	-73:18:00.7	15.614(0.005)	14.83(0.014)	14.933	0.091	-0.783(0.015)	37.5
F10-50	01:13:51.3	-73:17:58.0	16.765(0.027)	15.578(0.026)	15.943	0.186	-1.187(0.037)	19.3
F10-51	01:13:51.6	-73:23:07.6	17.119(0.004)	16.913(0.005)	16.918	-0.110	-0.205(0.006)	29.2
F10-52	01:13:52.3	-73:12:24.4	16.006(0.003)	15.529(0.002)	15.853	-0.019	-0.477(0.004)	107.0
F10-53	01:13:54.4	-73:17:49.8	16.352(0.003)	16.139(0.015)	15.710	0.132	-0.214(0.015)	12.7
F10-54	01:13:55.9	-73:15:56.5	17.245(0.005)	16.796(0.026)	17.233	0.118	-0.450(0.026)	13.9
F10-55	01:13:56.0	-73:10:15.3	17.338(0.005)	17.029(0.004)	17.316	0.107	-0.309(0.006)	42.1
F10-56	01:13:59.2	-73:16:53.0	17.102(0.004)	16.466(0.032)	16.484	0.240	-0.637(0.032)	14.9
F10-57	01:13:59.3	-73:15:13.3	17.677(0.014)	17.106(0.034)	17.436	0.147	-0.570(0.037)	12.1
F10-58	01:14:00.0	-73:15:12.3	17.564(0.032)	16.736(0.033)	17.029	-0.009	-0.827(0.046)	12.6
F10-59	01:14:00.7	-73:16:45.5	18.105(0.013)	16.918(0.046)	18.126	-0.376	-1.188(0.048)	15.1
F10-60	01:14:02.5	-73:27:43.8	17.503(0.005)	17.333(0.004)	17.300	0.019	-0.170(0.006)	24.6
F10-61	01:14:03.3	-73:16:50.7	18.098(0.047)	17.249(0.029)	17.988	-0.020	-0.848(0.055)	10.7
F10-62	01:14:06.9	-73:20:35.7	18.034(0.008)	17.797(0.009)	17.763	-0.079	-0.236(0.012)	17.6
F10-63	01:14:07.2	-73:16:16.6	17.36(0.005)	16.884(0.005)	17.245	0.033	-0.476(0.007)	54.5
F10-64	01:14:07.8	-73:23:43.2	18.038(0.008)	17.768(0.008)	17.781	-0.037	-0.270(0.011)	21.1
F10-65	01:14:17.3	-73:15:49.4	15.759(0.014)	15.529(0.007)	15.049	-0.153	-0.230(0.016)	13.3
F10-66	01:14:19.8	-73:10:07.8	16.665(0.028)	16.399(0.003)	16.144	-0.001	-0.265(0.028)	8.4

Continued on next page

Table B.6 – *Continued from previous page*

Field-ID	RA	Dec	*Rc*	Hα	*V*	$B-V$	Hα – *Rc*	SNR
F10-67	01:14:21.2	-73:17:55.1	17.11(0.005)	16.917(0.004)	16.921	-0.038	-0.194(0.006)	27.7
F10-68	01:14:21.3	-73:17:18.6	16.814(0.004)	16.711(0.003)	17.199	0.010	-0.102(0.005)	19.6
F10-69	01:14:22.6	-73:13:23.2	15.127(0.012)	15.021(0.001)	14.635	-0.033	-0.106(0.012)	8.3
F10-70	01:14:24.0	-73:14:05.3	17.346(0.028)	16.676(0.024)	16.887	0.075	-0.670(0.037)	13.6
F10-71	01:14:24.2	-73:14:02.4	16.741(0.006)	16.247(0.015)	16.437	0.028	-0.493(0.016)	24.5
F10-72	01:14:24.8	-73:25:42.9	17.733(0.005)	17.649(0.004)	17.431	0.021	-0.084(0.006)	12.7
F10-73	01:14:33.5	-73:24:34.6	17.909(0.005)	17.826(0.008)	17.724	-0.058	-0.083(0.009)	8.4
F10-74	01:14:36.1	-73:25:07.0	18.159(0.019)	17.637(0.005)	17.973	0.060	-0.522(0.020)	21.1
F10-75	01:14:37.8	-73:24:11.8	18.491(0.009)	18.419(0.01)	18.269	-0.034	-0.073(0.013)	5.2
F10-76	01:14:38.0	-73:18:23.2	15.938(0.025)	15.239(0.019)	14.650	0.011	-0.700(0.031)	16.4
F10-77	01:14:38.1	-73:18:26.8	17.104(0.066)	15.139(0.032)	14.947	-0.166	-1.965(0.073)	12.4
F10-78	01:14:38.9	-73:15:55.3	17.66(0.005)	17.565(0.009)	17.449	-0.004	-0.095(0.010)	8.9
F10-79	01:14:38.9	-73:16:32.9	18.582(0.01)	18.433(0.014)	18.387	0.022	-0.149(0.017)	8.1
F10-80	01:14:39.2	-73:20:38.1	17.561(0.006)	17.132(0.004)	17.374	-0.023	-0.430(0.007)	49.2
F10-81	01:14:40.7	-73:18:30.8	15.838(0.038)	14.822(0.053)	14.672	0.012	-1.016(0.065)	10.1
F10-82	01:14:41.1	-73:18:32.8	17.215(0.045)	15.583(0.03)	16.156	0.247	-1.632(0.054)	15.6
F10-83	01:14:41.2	-73:39:30.9	17.122(0.025)	16.54(0.003)	16.790	-0.059	-0.582(0.025)	17.9
F10-84	01:14:42.3	-73:10:12.1	17.509(0.004)	17.419(0.008)	17.253	-0.161	-0.090(0.009)	9.7
F10-85	01:14:45.0	-73:18:17.5	15.569(0.002)	15.49(0.005)	15.033	-0.052	-0.078(0.005)	14.1
F10-86	01:14:46.2	-73:20:35.2	17.125(0.005)	16.786(0.02)	16.699	-0.204	-0.339(0.021)	14.1
F10-87	01:14:46.4	-73:08:59.1	17.527(0.005)	17.097(0.003)	17.594	0.091	-0.431(0.006)	61.0
F10-88	01:14:48.2	-73:22:57.1	15.1(0.002)	14.899(0.005)	14.811	-0.240	-0.200(0.005)	34.0

Continued on next page

Table B.6 – *Continued from previous page*

Field-ID	RA	Dec	Rc	Hα	V	$B-V$	Hα − Rc	SNR
F10-89	01:14:49.1	-73:24:57.6	16.994(0.018)	16.444(0.009)	16.771	0.078	-0.549(0.020)	21.4
F10-90	01:14:49.5	-73:14:20.0	16.166(0.002)	15.903(0.002)	16.087	-0.091	-0.263(0.003)	82.4
F10-91	01:14:50.6	-73:28:36.5	17.739(0.005)	16.966(0.003)	17.514	-0.012	-0.774(0.006)	94.9
F10-92	01:14:51.0	-73:19:59.6	18.235(0.007)	18.093(0.012)	18.065	0.147	-0.142(0.014)	9.5
F10-93	01:14:52.3	-73:32:47.2	17.951(0.005)	17.644(0.005)	17.781	-0.069	-0.308(0.007)	37.9
F10-94	01:14:52.5	-73:33:05.3	17.966(0.007)	17.567(0.005)	17.826	-0.050	-0.399(0.009)	38.9
F10-95	01:14:54.0	-73:20:25.1	18.023(0.006)	17.758(0.016)	17.568	-0.201	-0.264(0.017)	13.7
F10-96	01:14:54.5	-73:20:06.2	16.04(0.002)	15.797(0.015)	15.470	-0.048	-0.242(0.015)	14.4
F10-97	01:14:55.1	-73:28:24.9	15.796(0.003)	15.116(0.002)	15.685	0.065	-0.679(0.004)	140.1
F10-98	01:14:55.3	-73:19:58.4	17.383(0.004)	16.755(0.025)	16.924	-0.103	-0.628(0.025)	18.8
F10-99	01:14:55.4	-73:20:31.9	15.258(0.002)	14.933(0.001)	15.096	-0.057	-0.325(0.002)	125.4
F10-100	01:14:56.0	-73:25:34.7	16.206(0.006)	15.918(0.002)	15.995	0.070	-0.288(0.006)	40.1
F10-101	01:14:56.1	-73:19:58.6	17.828(0.011)	17.205(0.025)	17.310	0.038	-0.624(0.027)	17.4
F10-102	01:14:56.3	-73:17:58.3	17.466(0.004)	17.386(0.005)	17.233	0.164	-0.080(0.006)	12.1
F10-103	01:14:56.4	-73:19:14.9	18.517(0.009)	17.688(0.035)	17.658	0.179	-0.829(0.036)	16.0
F10-104	01:14:56.8	-73:19:08.1	16.125(0.003)	16.011(0.006)	15.621	-0.043	-0.114(0.007)	16.1
F10-105	01:14:57.5	-73:19:47.9	17.695(0.006)	17.322(0.016)	17.155	0.175	-0.373(0.017)	18.5
F10-106	01:14:58.0	-73:19:56.8	18.108(0.007)	18.012(0.01)	17.638	-0.181	-0.096(0.012)	7.5
F10-107	01:14:58.3	-73:20:09.8	18.186(0.007)	17.959(0.016)	17.828	-0.122	-0.228(0.017)	11.8

C

Trawling for transits in a sea of noise: A Search for Exoplanets by Analysis of WASP Optical Lightcurves and Follow-up (SEAWOLF)

C.1 Introduction

Not all exoplanets are detected equally. A planet that transits its host star has greater scientific value because its radius can be determined and, because the orbital inclination is known, the geometric ambiguity in Doppler estimation of the planet mass is removed. Spectroscopy of the star during a transit can reveal absorption or scattering by the planet's atmosphere, if it has one. The planet can also be occulted by the star,

---

[0] Published work: Gaidos E., Anderson D. R., Lépine S., Colón K. D., Maravelias G., Narita N., Chang E., Beyer J., Fukui A., Armstrong J. D., Zezas A., Fulton B. J., Mann A. W., West R. G., Faedi F., *Trawling for transits in a sea of noise: A Search for Exoplanets by Analysis of WASP Optical Lightcurves and Follow-up (SEAWOLF)*, MNRAS, **437**, 3133, (2014).
Contribution to this project: (a) observations of 30 unique targets during 36 nights (2011-2013) using the Skinakas 1.3 m telescope, (b) data reduction and light-curve analysis to identify potential transits, (c) 24 reduced light-curves were used for the final analysis (performed by Eric Gaidos).

permitting differential measurement of the planet's reflected or emitted flux. These observations can determine the planet's albedo and/or constrain the efficiency with which heat is carried around the planet by rotation or atmospheric circulation.

The most productive tool for detecting transiting planets has been the *Kepler* space telescope (Borucki et al., 2010), data from which has yielded more than 2000 confirmed or candidate discoveries. However most of the systems discovered by *Kepler*, as well as those of the COnvection ROtation et Transits planétaires (CoRoT) satellite (Carone et al., 2012) are faint ($V \sim 15$), making follow-up observations difficult. Many of these host stars are at kpc distances and well above the Galactic plane, and may belong to an older, more metal-poor population distinct from the Solar neighborhood and perhaps hosting a different distribution of planets.

Ground-based surveys such as the Wide Angle Search for Planets (WASP, Pollacco et al., 2006) and the Hungarian Automated Telescope Network (HatNET Bakos et al., 2011) have discovered numerous giant planets transiting brighter, nearby stars.[1] Transiting geometries are uncommon and such surveys must monitor many stars over large portions of the sky. Because of the trade-off between field of view and telescope aperture, these surveys are limited to the brightest stars and, due to Malmquist bias, biased towards more luminous ones. The sensitivity of such surveys to smaller (non gas-giant) planets is limited by correlated photometric error or "red" noise which does not decrease with the square root of the number of observations (Pont et al., 2006; Smith et al., 2007). Earth's rotation means that surveys performed from a single site have restricted observing windows and are only efficient at detecting planets on short-period orbits (≤ 10 d). For these reasons, ground-based surveys have been most successful at detecting giant planets on close orbits around F and G stars.[2]

M dwarf stars have less than half the radius of their solar-type cousins, permitting the detection of concomittantly smaller planets for a given photometric sensitivity. Although such stars tend to be fainter and observed with poorer photometric precision, the net balance of these two effects can still favor cooler stars: this calculus motivates the MEarth transit survey for planets as small as Earth around late M-type dwarfs (Berta et al., 2012; Charbonneau et al., 2009).

K- and early M-type dwarfs represent an intermediate region of discovery space for

---

[1] Transiting planets have also been identified by screening planetary systems detected by the Doppler method. The first example (HD 209458) was found this way (Charbonneau et al., 2000; Henry et al., 2000), but this approach is limited by the pace of Doppler surveys and the small geometric probability that a planet will transit.

[2] Wide-field surveys must also contend with a high false positive rate by blends of bright stars with fainter eclipsing binaries.

transiting planet surveys. While ground-based detection of Earth-size planets around such stars is not feasible, it is possible to detect Neptune- or even super-Earth-size companions, at least on close-in orbits. Indeed, HAT-P-11b ($4.3R_\oplus$, $P = 4.89$ d) transits a K4 dwarf, and HAT-P-26b ($6.3R_\oplus$, $P = 4.23$ d) orbits a K1 dwarf (Hartman et al., 2011).[1]

The occurrence and properties of short-period or "hot" Neptunes are of considerable theoretical interest. Attempts to explain an apparent correlation between the occurrence of giant planets and stellar mass also predict an inverse relation with elevated numbers of Neptunes (i.e., "failed Jupiters") around low-mass stars (Laughlin et al., 2004). Hot Neptunes could form by accretion of rocky/icy planetesimals beyond the snowline and subsequent migration to the inner edge of the protoplanetary disk (Mordasini et al., 2009). However, McNeil & Nelson (2010) find that this scenario cannot explain the observed size distribution of close-in planets. Alternatively, planetesimals or protoplanets could migrate first, followed by accretion in place (Brunini & Cionco, 2005; Hansen & Murray, 2012). Finally, evaporation of mass from close-in giant planets has been proposed as an alternative formation mechanism for hot Neptunes (Baraffe et al., 2005; Boué et al., 2012). These three different pathways predict objects that are enriched in ice, rock, and gas, respectively. Hot Neptunes may be especially useful to test models of planet formation because both mass and radius can be accurately measured (by Doppler and transit, respectively) and these parameters are informative about the relative amounts of rock, ice and gas in the planet (Rogers et al., 2011). In contrast, the masses of Earth-size planets are too small to accurately measure and the radii of Jupiter-size planets are insensitive to mass due to support by electron degeneracy pressure.

We used data from the WASP survey to search for short-period Neptunes around a sample of low-mass stars (the SEAWOLF survey). Because this search pushes the envelope of WASP performance, we adopted a multistage search strategy:

- We selected late K- and early M-type dwarf stars observed by the WASP survey; in principle, smaller planets should be detectable around these smaller stars.
- We identified candidate transit signals, relaxing the signal-to-noise criterion for initial selection. This potentially includes smaller transit signals, but also large numbers of false positives.
- We predicted candidate transits using the WASP-generated ephemerides and

---

[1] Two other Neptune-size planets, both around early-type M dwarfs, were detected first by Doppler, then later found to transit: GJ 436b (Gillon et al., 2007), and GJ 3740b (Bonfils et al., 2012).

screened these with precision photometry obtained at 1–2 m telescopes.

We describe the WASP data and our follow-up observations and reduction in Section C.2, and our catalog of candidate transiting systems and the results of the follow-up program in Section C.3. We place limits on the occurrence of hot Neptunes around stars in our sample in Section C.4, and discuss the implications for theory as well as prospects for future transiting planet surveys in Section C.5.

C.2 Observations and Methods

C.2.1 Sample construction and stellar parameters

For our search sample we identified late-type (K4 to M4) dwarf stars in the inaugural (2004) fields of the WASP-North survey (Christian et al., 2006). We chose stars from the SUPERBLINK proper motion catalog (Lépine & Shara, 2005) with optical-to-infrared colors $V - J > 2$ consistent with late K- and M-type stars, and reduced proper motions $H_J \equiv J + 5 \log \mu + 5$ (a proxy for absolute magnitude) that place them on the dwarf color-magnitude locus, thus excluding K and M giants (Lépine & Gaidos, 2011). We restricted the sample to $V < 14$ because at fainter magnitudes the number of background stars with $\Delta m < 5$ falling within the same WASP photometric aperture significantly exceeds one. Such stars could produce false positives if they are eclipsing binaries. We also imposed a $J < 10$ cut to retain those stars for which high-precision, high cadence (few minute) photometry in the near-infrared (z or JHK passbands) could be performed on 1–2 m telescopes. Based on parallaxes (astrometric wherever available, photometric otherwise), the most distant stars in our survey are at ≈100 pc. The closest star is Laland 21185, only 2.5 pc away.

To estimate the properties of these stars, we adopted the empirical relations between $V - J$ color, effective temperature T_{eff}, stellar radius R_*, and stellar mass M_* for solar-metallicity K and M stars in Boyajian et al. (2012)[1]. According to these relations, $V - J = 2$ corresponds to $R_* \approx 0.71 R_\odot$, $T_{\text{eff}} \approx 4550$ K, and a spectral subtype of K4 (Cox, 2000). The coolest stars in our sample have $V - J \geq 4.5$ and should have M4 spectral types, with $R_* \approx 0.25 R_\odot$ and $T_{\text{eff}} \approx 3300$ K. The reddest star ($V - J = 5.39$) is the M4.5 dwarf GJ 3839.

---

[1] We used 2MASS J magnitudes while Boyajian et al. (2012) used Johnson J magnitudes. However, the CIT photometric system is closely related to the Johnson system and $J_{\text{CIT}} \approx J_{\text{2MASS}} - 0.065\,(J - K)_{\text{2MASS}} + 0.038$ (Skrutskie et al., 2006). Since late K-early M dwarfs have $J - K \approx 0.8$, the difference in $V - J$ color is only 0.014 magnitudes and was ignored.

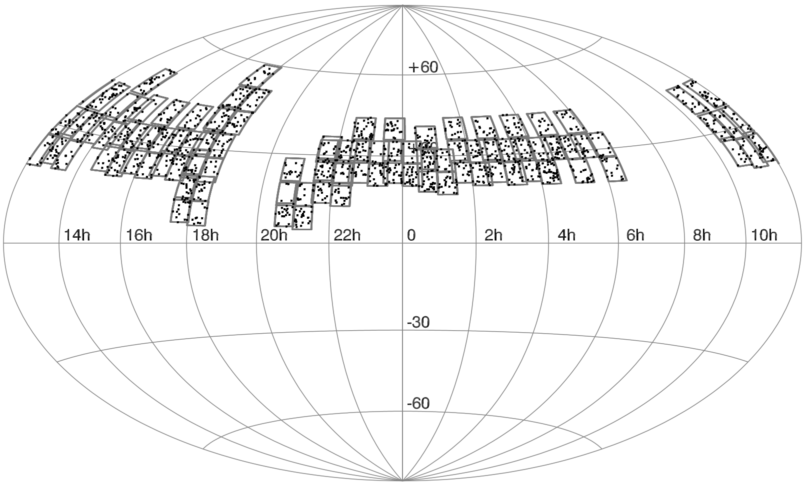

Figure C.1: Locations of the 2004 inaugural fields of the WASP-North survey and our selected SUPERBLINK K and M dwarf stars.

C.2.2 WASP Observations and Sources

We identified 1849 SUPERBLINK stars satisfying our criteria in the inaugural (2004) fields of the WASP-North survey. These 102 fields cover 4750 sq. deg. at declinations between +4.9 and +59.3 deg. (Fig. C.1). Stars were matched with sources generated by photometering WASP images with a circular aperture of radius 3.5 pixels (48 arc sec). 1763 WASP sources were matched to our selected SUPERBLINK stars; the median angular separation is 0.22 arc sec and the 95th percentile separation is 3.4 arc sec. Forty-six WASP sources were each matched to two SUPERBLINK stars. Of the 1763 matched sources, 1743 have more than 500 data points (the minimum required for lightcurve analysis) and the median number of observations is 8160 (Fig. C.2).

C.2.3 Light Curve Analysis

WASP lightcurves were processed to correct for systematic errors (Tamuz et al., 2005) and remove trends (Kovács et al., 2005). The latter step eliminates many artifacts with periods equal to rational multiples of 1 d. The light curves were then analyzed with the HUNTER hybrid search algorithm that incorporates the box-least squared algorithm (Kovács et al., 2002) and which is described in Collier Cameron et al. (2006). HUNTER searched for transit-like signals with periods of 0.3–30 d. Four criteria were applied to these signals: (i) mean flux > 3 microVegas ($m > 13.8$); (ii) periods not within 5% of

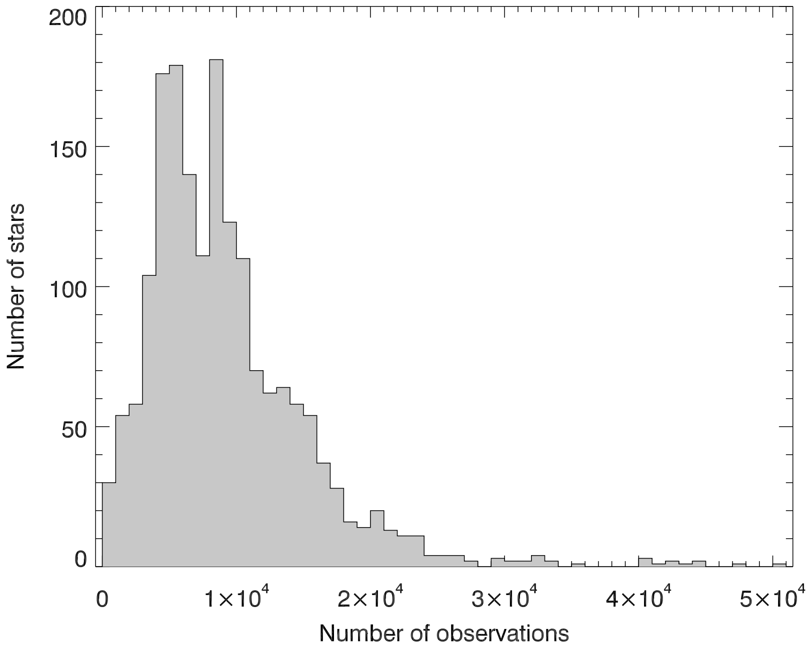

Figure C.2: Distributions of number of WASP observations per star in our sample. The median number of observations per star is 8160.

1 or 0.5 d (see Section C.2.4); (iii) signal detection efficiency > 6 (Kovács et al., 2002); (iv) at least three candidate transits.

Up to five periodic signals were identified for each source satisfying these criteria, and a total of 4364 signals were identified among 1130 stars. HUNTER calculated the signal-to-red noise (SRN) and $\Delta\chi^2$ parameter for each signal, where the latter is the decrease in χ^2 provided by the best-fit transit model relative to a constant light curve. In the case of pure white noise $\Delta\chi^2$ is the square of the signal-to-white noise ratio (Collier Cameron et al., 2006). Thus SRN and $\Delta\chi^2$ allow us to select based on the significance of a signal with respect to both the red noise and white noise properties of the data.

C.2.4 Selection of Candidate Transiting Systems

We next applied cuts with period, SRN, $\Delta\chi^2$ and ellipsoidal signal-to-noise ratio (a measure of the continuous variation of the signal over the period) to the 4364 HUNTER-identified signals to screen artifacts and astrophysical false positives (i.e., close binaries). Because of Earth's rotation, observations from a single longitude like those of

WASP-North can contain artifacts with periods near 1 d and integer ratios thereof. Furthermore, aliasing with the lunar cycle (29.5 d) produces a dispersion of a few percent around each rational period. Based on the distribution of signals (mostly artifacts) generated when no detrending is performed (see above), we removed signals with periods below 1.1 d and within 5% of 3/2, 2, 3, and 5 d (Fig. C.3). (A peak at 4 d is not statistically significant.) There is also a peak in the period distribution of signals at 8/3 d. This peak appears significant and is apparently one of a series of undertones (multiples) of the strong artifact at 1/3 d, the harmonic closest to the duration of a summer night at the WASP-North site (and which is removed along with all other signals below 1.1 d). However, we did not a priori remove the 1/3 d peak.

The distribution of signals with SRN and $\Delta\chi^2$ is strongly concentrated at SRN ~4.5 and $\Delta\chi^2$ ~30 (Fig. C.4). We assumed that these are nearly all artifacts or astrophysical false positives and that the clustering is a result of the selection criteria applied in Section C.2.3. We retained signals with $(SRN > 6) \cup (SRN > 3 \cap \Delta\chi^2 > 50)$ (outside the hatched zone of Fig. C.4). We also excluded signals with an ellipsoidal SNR > 8: these are possible close binaries (Collier Cameron et al., 2006). The remaining 901 signals were further screened with the following criteria: (i) observations had to completely span, ingress to egress, at least three putative transits; (ii) the putative transit duration τ had to be within a factor of two of the value for a planet on a circular orbit with zero impact parameter around a star with radius $0.6R_\odot$ (typical of a late K dwarf), i.e. $\tau = 1$ hr $(P/1\text{ d})^{1/3}$, where P is the Keplerian period; and (iii) the putative signal could not obviously be an artifact produced by periodic gaps or changes in noise level in the data. This left 92 candidate signals from 80 stars.

C.2.5 Follow-up Photometry

We used the ephemerides generated by the HUNTER pipeline to predict transits for our 92 candidates. The precision of the predicted transit center depended mostly on the precision of the period determination, and was generally ±1 hr. Follow-up photometry of some of these candidate transit events was obtained with 1–2 m ground-based telescopes. Details of the telescopes are reported in Table C.1 and of the observations in Table C.3. In general, we selected events to observe if the predicted transit center occurred when the star was at an airmass below 1.7, and at least 3 hr from sunset or sunrise. Ideally, we observed the entire transit window ($\pm 1\sigma$) as well as an hour before and after ingress/egress. However in many cases this was not possible. The minimum detectable transit depth δ_d and completeness C of these observations are calculated in Section C.4.

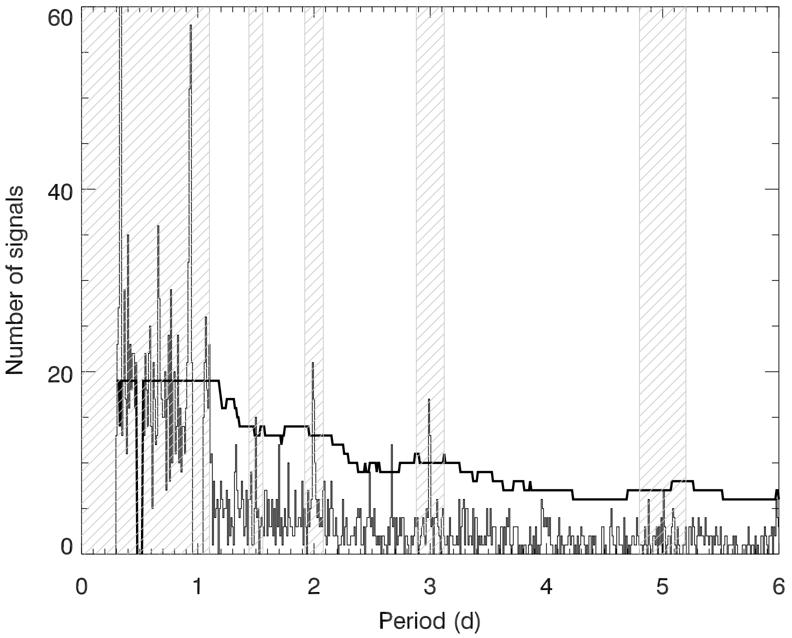

Figure C.3: Period distribution of signals from the WASP HUNTER pipeline. The upper solid curve is a significance threshold ($p = 10^{-4}$) based on the Poisson statistics of a running mean ($n = 50$). Clusters of artifacts are present at rational multiples of 1 d. The hatched regions indicate exclusion zones around these periods and at <1.1 d; signals within these zones were rejected.

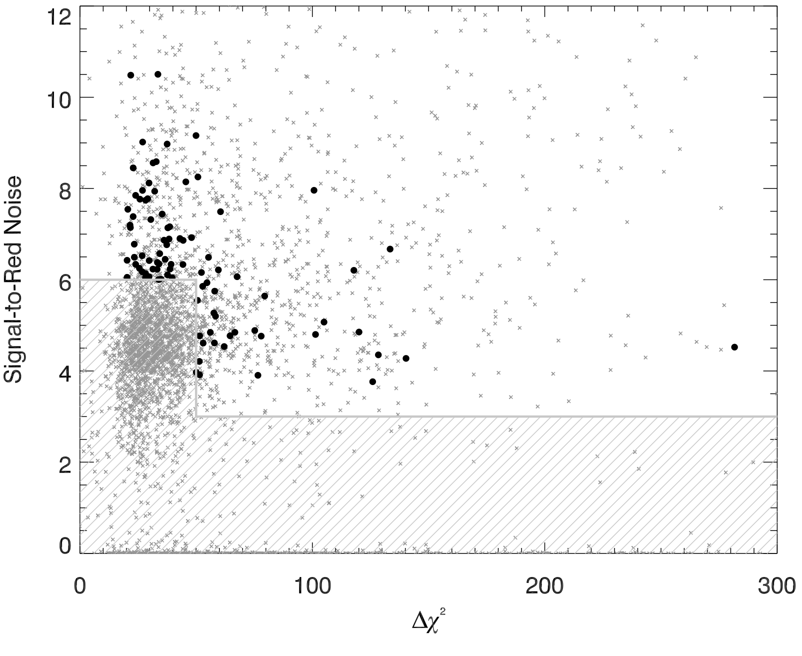

Figure C.4: Signals from the WASP HUNTER pipeline; signal-to-red noise ratio vs. $\Delta\chi^2$. Only signals outside the hatched zone were considered. The final candidate transiting systems are indicated by the large black points.

Although the details of the observing strategy and data reduction varied with telescope and instrument, there were several commonalities:

Defocused imaging photometry: A telescope was grossly defocused to produce a “doughnut”-shaped point spread function (PSF) several tens of pixels in diameter. Such “doughnuts” are out-of-focus images of the primary mirror. Defocusing permitted a signal $\gg 1 \times 10^6$ e^{-1} to be acquired in each integration, reducing Poisson error to $< 10^{-3}$. It also minimized error from image motion or changes in the distribution of the signal convolved with detector flat-fielding errors (e.g. Mann et al., 2011; Southworth et al., 2009). Circular aperture photometry was performed on the defocused images of the target and several comparison stars in multiple iterations. In each iteration the centroid of the stellar image within the aperture was computed and used as the aperture center.

Optimized pointings: The signal from a star of interest must be divided by that from one or more comparison stars to remove variations in atmospheric transmission. The number and relative brightness of comparison stars limits the precision of ground-based photometry. We chose pointings that maximized the number of comparison stars similar in brightness to the target star. We also avoided rings in the flat field due to dust particles near the focal plane. These can change between nights or even during observations, introducing flat-field error.

Comparison star selection: Each comparison star was compared with all the others to identify and exclude variables. A comparison signal was calculated from the weighted sum of the remaining reference stars, where the weights were chosen to minimize the RMS of the normalized target light curve outside the predicted transit window.

Lightcurve detrending: We performed linear regressions of each normalized light curve with airmass, position of the centroid, and variance in the distribution of the target star signal over the point-spread function. The first was to remove second-order extinction effects due to differences in the spectra of target and reference stars (Mann et al., 2011). The second partly removes flat-field errors introduced when the defocused images move due to imperfect guiding or absence of guiding. The third compensates for any non-linearity in the response of the detector which would scale with the variance in the light distribution.

C.3 Results

C.3.1 Candidate Signals

The final catalog of 92 candidate signals from 80 stars is presented in Table C.2. The "A", "B", or "C" designations indicate different signals from the same star. Based on the depths of the putative WASP transits and the estimated radii of these stars (see Section C.2.1) the median transiting planet radius would be $\sim 4\ R_{\oplus}$, i.e. Neptune-size. However, we expect that the large majority of these signals are artifacts or astrophysical false positives and not transiting planet. In Table C.2 we report the status of each candidate based on the follow-up photometry acquired to date: N = none, ? = ambiguous or requires further observations, X = eliminated, A = candidate transiting system. We have follow-up observations of 70 signals and we ruled out 39 signals and designated 28 as ambiguous or lacking sufficient data. In general, systems where the completeness C of our follow-up observations is >80% (as calculated in Section C.4.2), and no transit-like event was observed, were ruled out, and systems with one or more observations but where completeness was <80% were designated as "?". There are five exceptions to the rule: Two systems (03571+3023 and 14162+3234) have $C \approx 0.77$ but were ruled out. Six systems (15015+2400, 16389+3643B, 21302+2312A, 21409+1824, 22085+1425A and 22085+1425B) have $C > 0.8$ but the predicted event was close to the beginning or end of an observing window, a possible event was observed significantly before the predicted time or different observations had conflicting results: these are designated as "?".

C.3.2 Transit Candidates

Follow-up observations of four signals produced light curves that contain a transit-like signal: 03571+3023, 16442+3455, 17378+2257, and 18075+4402 (Fig. C.5). We have continued to observe predicted events for these stars to verify or rule out possible transits. 03571+3023 is variable lightcurves are not consistent between predicted events and one is flat, causing us to rule out this system. 16442+3455 (Ross 813) was mis-assigned to a white dwarf in the catalog of McCook & Sion (1987) but its colors and luminosity are clearly those of a late K or early M dwarf. 17378+2257 (GJ 686.1AB, HIP 86282) consists of a pair of dwarfs that have $V - J \approx 3$ and are designated as M0 stars in the Gliese catalog but listed as K5 in Reid et al. (1995). The molecular indices reported by Reid et al. (1995) and a spectrum obtained by us with the Mark

III spectrograph on the MDM 1.3 m McGraw-Hill telescope suggest a spectral type between K7 and M0. These stars are an X-ray source (Hünsch et al., 1999) and the S-index values of the Ca II HK lines in their spectra (Duncan et al., 1991) suggest the stars are comparatively active (Isaacson & Fischer, 2010), but Hα is not observed in emission (Young et al., 1989).

C.3.3 GJ 436b

GJ 436 aka SUPERBLINK star PM I11421+2642 or WASP source J114210.54+264230.4 is in our sample. The transit signal from its $4.3R_\oplus$ planet (Gillon et al., 2007) was not detected by the WASP pipeline and in fact no candidate signals were identified from this star. One possible explanation for the system's omission is that only one season of WASP data was obtained and the star fell 2.4 deg from the center of the field of view and thus was vignetted. Another contributing factor is the planet's high transit impact parameter ($b = 0.85$), which makes the transit unusually short. The data is also exceptionally noisy: the 5σ-filtered RMS is 1.2%, consistent with the nominal photometric error of 1.4% and about 2.5 times the typical value for a $V = 10.7$ star (see Eqn. C.1 below). The transit is only marginally apparent even after the data is correctly phase-folded (Fig. C.6). Although transits of GJ 436b were not detected by WASP, the inclusion of this system in our sample raises the question of whether we should expect additional hot Neptunes or whether this is the only such transiting system. For these reasons we carry out our statistical analysis for zero and one detections (Sec. C.4).

C.4 Analysis

C.4.1 Estimation of WASP detection limits

To place statistical constraints on the occurrence of hot Neptunes we calculated (i) the ability of HUNTER to detect planets in WASP lightcurves as a function of planet radius and orbital period, and (ii) the completeness with which our follow-up observations can rule out candidate transit signals (Section C.4.2). Our criteria for WASP/HUNTER detection is the same as that applied to the data: signal-to-red noise SRN > 6, or SRN > 3 and signal-to-*white* noise $> \sqrt{50}$.

The transit signal $\delta = (R_p/R_*)^2$, where R_p is the radius of the planet. The red-noise error in the mean of N observations in the transit interval is $\sigma_1 N^{-\gamma}$, where σ_1 is the error in a single WASP measurement of a given star and the index $\gamma \approx 0.5 - 0.05 \times (15 - V)$

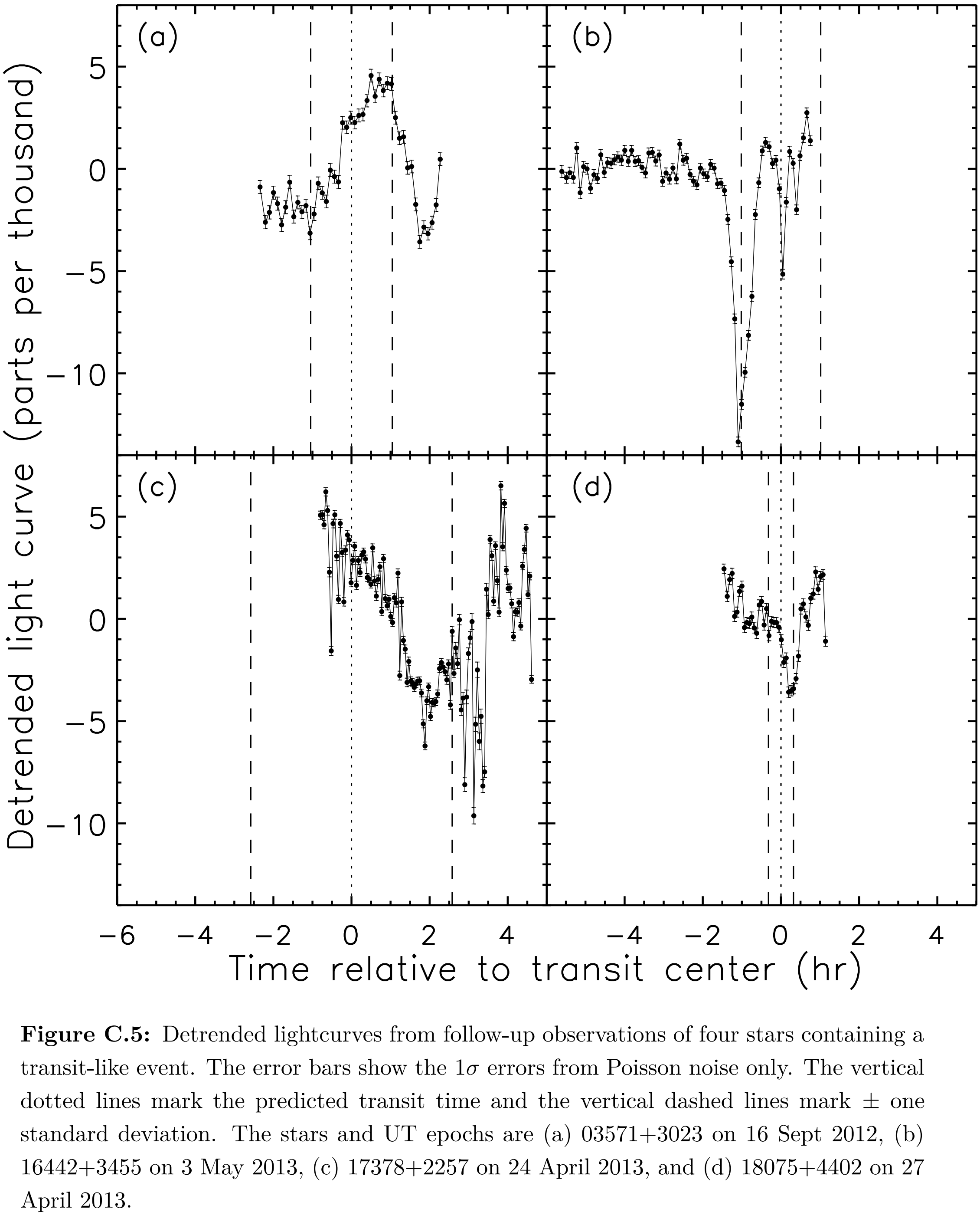

Figure C.5: Detrended lightcurves from follow-up observations of four stars containing a transit-like event. The error bars show the 1σ errors from Poisson noise only. The vertical dotted lines mark the predicted transit time and the vertical dashed lines mark ± one standard deviation. The stars and UT epochs are (a) 03571+3023 on 16 Sept 2012, (b) 16442+3455 on 3 May 2013, (c) 17378+2257 on 24 April 2013, and (d) 18075+4402 on 27 April 2013.

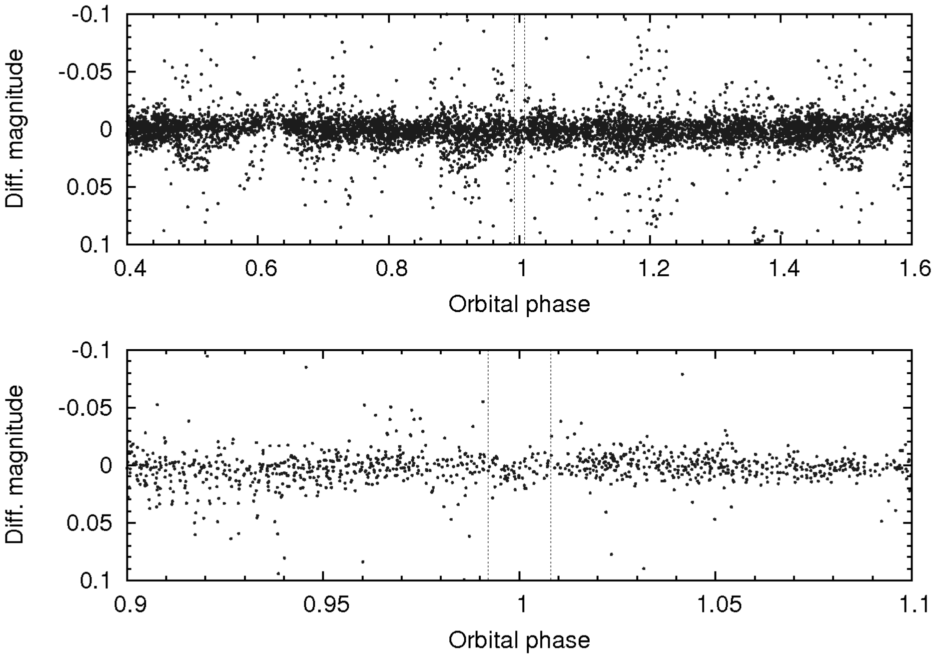

Figure C.6: WASP lightcurve of GJ 436, which hosts a hot Neptune on a 2.64 d orbit. The data has been phased according to the established ephemeris of the planet and the transit is marked by the vertical lines. The bottom panel plots on an expanded scale.

(based on Fig. 2 in Collier Cameron et al., 2006). The white-noise error is taken to be $\sigma_1 N^{-0.5}$. We constructed an empirical formula for σ_1 based on Fig. 2 in Collier Cameron et al. (2006):

$$\sigma_1 = 2.5 \times 10^{-3} \sqrt{1 + 8 \times 10^{(V-13)/5}}. \tag{C.1}$$

Assuming near-circular orbits for these close-in planets, the mean number of observations falling within a transit is taken to be $N = n\tau/P$, where τ is the duration of the transit and n is the total number of observations. The transit duration in hours is

$$\tau \approx 0.075 R_* P^{1/3} \sqrt{1 - b^2}, \tag{C.2}$$

where R_* is in solar units, P is in days, and b is the impact parameter (taken to be zero here).

Figure C.7 plots the limiting V magnitude for detecting a transiting Neptune-size (3, 4, or $5R_\oplus$) planet around a dwarf star in the WASP survey as a function of stellar $V - J$ color, our proxy for T_{eff} and stellar radius on the main sequence, for P =1.2 d or 10 d (see Section C.4.3 for a justification for this range). The $V - J$ and V of stars in our survey catalog are overplotted. Figure C.7 shows that WASP should be able to detect planets somewhat larger than Neptune (5–$6R_\oplus$) around nearly all of the stars in our sample, and planets slightly smaller than Neptune ($\sim 3R_\oplus$) around the coolest (M dwarf) stars, but only if they orbit quite close to their host. For orbital periods of 10 d only the largest Neptunes will be detectable around the M dwarfs.

The break in the slope of the detection contours at $V \approx$ 15–16 in Fig. C.7 is a result of a transition from a photon- or counting noise-limited regime to a red noise-dominated regime. Among stars with a fixed radius ($V - J$ color) and $V >$ 15–16, detection improves with brightness. However, for $V <$ 15–16 correlated noise becomes important (decreasing γ with brighter V). For a fixed N, this means that detection requires a lower σ_1 and hence an even brighter V. This positive feedback means that for a given stellar radius, planets below a certain size cannot be detected, regardless of apparent magnitude. This is a widely-appreciated limitation of ground-based surveys (Pont et al., 2006; Smith et al., 2007).

C.4.2 Estimation of follow-up completeness

To evaluate the significance of non-detection or detection of transits in our follow-up observations, we calculated the completeness, i.e. the probability that a transit with the characteristics of the WASP candidate would be detected, and the false-alarm

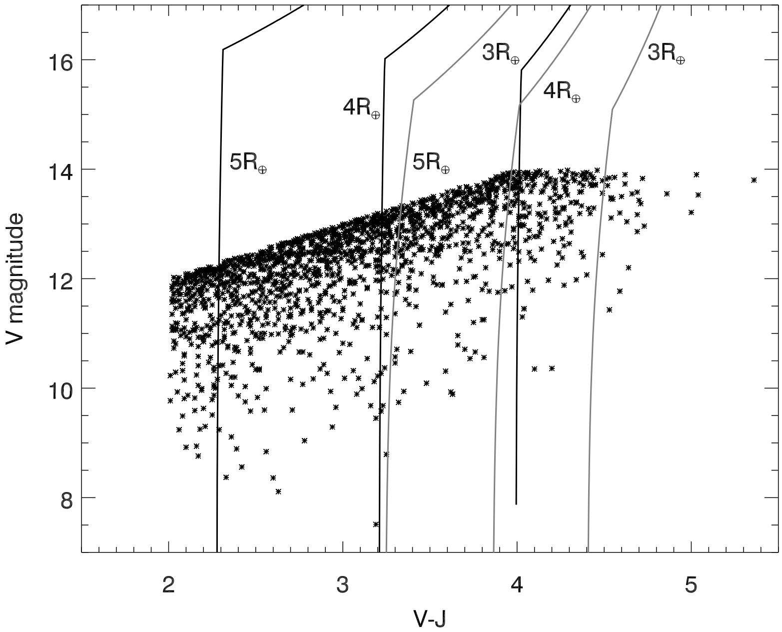

Figure C.7: Expected WASP detection limits for Neptune-size planets around late K and M dwarf stars, plotted vs. $V - J$ color (a proxy for $T_{\rm eff}$ and spectral type) and V magnitude. Transiting planets of specified radius (3, 4 or 5 $R_\oplus$), and orbital period (1.2 d, black curves, or 10 d, grey curves) should be detectable around stars to the right and below each curve. The stars of the SEAWOLF survey are plotted. Circular orbits, an impact parameter of zero and the median number of observations in our survey sample (8160) are assumed for these calculations.

probability, i.e. the probability that such an event would be erroneously identified in our data in the absence of an actual transit.

Each follow-up observation of a candidate transit event yielded a normalized, detrended lightcurve, plus errors based purely on counting statistics (Poisson or photon noise). False alarm probability and completeness were calculated by constructing two sets of Monte Carlo realizations of the data, the first set with no transit signal added, and the second containing a transit signal equal in depth to the WASP candidate. The first set was used to set the detection threshold, i.e. the transit depth corresponding to a false alarm probability (FAP) of 0.01. This means there is a 1% probability that a signal exceeding this threshold would be erroneously discovered in a lightcurve with these noise properties but containing no transit. We used the second set of Monte Carlo realizations plus the detection threshold determined from the first set to estimate the completeness or the recovery rate in follow-up photometry of transit signals with the properties of the WASP candidate.

To account for the effect of correlated or “red” noise on transit detection, we computed the discrete autocorrelation function A_k of the actual data and used this to construct artificial light curves s_i of pure noise:

$$s_i = s \sum_j A_{i-j} w_j, \tag{C.3}$$

where w_i is a white noise pattern and s is chosen so that s_i has the same total noise RMS as the actual signal.

Our simple transit model used a linear limb darkening law[1] and the “small planet” approximation ($R_p \ll R_*$) such that the transit signal is

$$f(t) = \delta \left[1 - u\,(1-\mu)\right], \tag{C.4}$$

for $r < 1$, where $\mu = \sqrt{1-r^2}$, u is the linear limb-darkening coefficient, the dimensionless radial coordinate is

$$r = \sqrt{\left(2(t-t_c)/\tau\right)^2 + b^2}, \tag{C.5}$$

and t_c is the transit center time. Based on the median estimated T_{eff} of our sample (4570 K) and assuming solar metallicity, we adopted values of u =0.80, 0.72, and 0.51 for Johnson V and R and Tiede J bandpasses, respectively (Claret, 2000), and u =0.75, 0.65, and 0.58 for Sloan *riz* bandpasses, respectively (Claret, 2004). To calculate the transit duration τ we assumed a circular orbit and a stellar radius based on $V-J$ and

---

[1] More complex limb-darkening laws are widely used but a linear law is completely adequate for creating and “detecting” fake transits at low signal-to-noise.

Boyajian et al. (2012) (see Section C.2.1). For each Monte Carlo realization, we drew a fixed value of impact parameter b from a uniform distribution limited to $\sqrt{3}/2$ (beyond which the transit duration is half the maximum value, resulting in exclusion from our sample).

To generate a distribution of false-positive transits, we fit the transit model to each transit-free light curve using the non-linear least-squares routine MPFIT (Markwardt, 2009), with t_c and δ as free parameters. For the fit, an initial value of δ was chosen from a uniform distribution between 0 and 0.002. An initial value of t_c was chosen from a normal distribution with a standard deviation equal to the transit prediction error, and limited to the observation window. Cases where the fitted depth was negative or the transit was more than two standard deviations from the predicted transit center were not counted, as these would have been excluded from the actual survey. We determined the 99 percentile value of the transit depth, corresponding to a false alarm probability of 0.01. This is our adopted detection limit δ_d. This value was converted to an equivalent planet radius using the stellar radius, and we also computed a corresponding SNR detection threshold based on the white-noise RMS of the light curve.

To calculate the completeness, we added artificial transits to the noise-only light curves and attempted to recover them. Each transit was modeled as described above, using the WASP candidate transit depth, a uniform distribution for b between 0 and $\sqrt{3}/2$ and a normal distribution for t_c. We then repeated the fitting process described above. To initially "detect" the transit, we smoothed each light curve with a boxcar filter having a width equal to the expected transit duration. The minimum of this lightcurve became the initial guess at t_c in a fit with MPFIT. We calculated the fraction of recovered transit depths that exceeded δ_d, rejecting fits with t_c deviating from the actual value by more than two standard deviations. This fraction is our estimated completeness C. Table C.3 reports values of δ_d and C for each follow-up observation.

C.4.3 Planet Occurrence

Our observations constrain the intrinsic occurrence f (planets per star, or in the limit of few planets, fraction of stars with planets) of close-in Neptune- to Saturn-size planets around late K and early M dwarf stars in the solar neighborhood. A standard procedure to estimate f is to maximize a likelihood function that is the product of the probabilities of detections and non-detections. Our multi-stage observational campaign required us to consider how we defined detections and non-detections. Specifically, our sample includes:

- Stars with no transit-like signal found in WASP data: These were counted as non-detections.
- Stars with a transit-like signal identified in WASP data but which were not screened with follow-up observations: These were considered as unconfirmed detections.
- Stars with transit-like signals in WASP data which our follow-up observations have ruled out as transit candidates with some completeness C: These are considered possible non-detections or unconfirmed detections.
- Stars with WASP signals that our follow-up photometry indicate are viable transit candidates: Given sufficient follow-up, these could become confirmed detections.

Following Gaidos et al. (2013) we generalized the likelihood formalism as an empirical Bayes/marginalized likelihood analysis in which the occurrence rate f is a "hyperparameter" of the prior probability that a star hosts a detectable transiting planet [1]. This prior is $\langle d_i \rangle f$, where $\langle d_i \rangle$ is the probability that a planet transits and is detected with the criteria in Section C.2.4, marginalized over the distributions of planet radius and orbital period. The log-likelihood is

$$\begin{aligned}\ln \mathcal{L} = & \sum_i^{ND} \ln\left(1 - f\langle d_i \rangle\right) + \sum_k^{CD} \ln\left[(1-F_k) f d_k\right] \\ & + \sum_j^{UD} \ln\left[(1-C_j) f d_j + C_j \left(1 - f\langle d_j \rangle\right)\right],\end{aligned} \tag{C.6}$$

where the summations are over non-detections (ND), confirmed detections (CD), and uncomfirmed detections (UD), C_j is the completeness of the follow-up observations that do not find a transit, and F_k is the false-alarm probability for detections confirmed by our follow-up observations. In the case of multiple observations of the same system we adopt the largest value of C_j.

If $fd \ll 1$ and $F \ll 1$, then

$$\begin{aligned}\ln \mathcal{L} \approx N_{CD} \ln f - f \sum_i^{ND} \langle d_i \rangle \\ + \sum_j^{UD} \ln\left[(1-C_j) f d_j + C_j \left(1 - f\langle d_j \rangle\right)\right],\end{aligned} \tag{C.7}$$

---

[1] Strictly speaking, the fraction of stars with such planets, which is equal to the number of such planets per star if the possibility of multiple planets in this restricted range of radii and orbital periods is neglected.

where N_{CD} is the number of confirmed detections. If C_i is not small for all stars (not the case here) then this can be further approximated as:

$$\begin{aligned}\ln \mathcal{L} \approx N_{CD} \ln f + \sum_j^{UD} \ln C_j \\ -f\left[\sum_i^{ND} \langle d_i \rangle + \sum_j^{UD} \left(C_j \langle d_j \rangle - \frac{1-C_j}{C_j} d_j \right)\right].\end{aligned} \tag{C.8}$$

Only the first two terms depend on f, and from these one readily derives the most likely value:

$$f_* = N_{CD} \left[\sum_i^{ND} \langle d_i \rangle + \sum_j^{UD} \left(C_j \langle d_j \rangle - \frac{1-C_j}{C_j} d_j \right)\right]^{-1} \tag{C.9}$$

If no transits are confirmed the most likely value of f is zero.

The detection probability d_i for a given candidate transit signal is the product of a geometric factor d_i^{geo} and a detection probability d_i^{det}. Assuming circular orbits,

$$d_i^{\mathrm{geo}} \approx 0.238 R_* M_*^{-1/3} P^{-2/3}, \tag{C.10}$$

where the stellar parameters are in solar units and P is the signal period in days. d_i^{det} is estimated by computing both the SRN and $\Delta\chi^2$ for the given δ, P, and a uniformly-distributed range of impact parameters, and determining the fraction of these which satisfy our selection criteria (Section C.2.4). The SRN is given by $\delta N^\gamma/\sigma_1$, $\Delta\chi^2 = \delta^2 N/\sigma_1^2$, and γ and N are estimated as before. All cases with $b > \sqrt{3}/2$ were excluded because of the restriction on candidate transit duration (Section C.2.4).

To calculate $\langle d \rangle$ we assumed a power-law distribution over radius $R_{\min} < R_p < R_{\max}$ with index α, and a flat log distribution with orbital period $P_{\min} < P < P_{\max}$ (Cumming et al., 2008; Howard et al., 2012), i.e.

$$dN = \frac{f\,(R_p/R_{\min})^{-\alpha}\, d\ln R_p\, d\ln P}{\alpha \ln (P_{\max}/P_{\min})} \tag{C.11}$$

where $R_p > R_{\min}$ and $P_{\min} < P < P_{\max}$. We calculated the minimum detectable planet radius R_{det} and the fraction of planets that would be detected, i.e.

$$d^{det} = \begin{cases} \frac{R_{\mathrm{det}}^{-\alpha} - R_{\max}^{-\alpha}}{R_{\min}^{-\alpha} - R_{\max}^{-\alpha}}, & \text{if } R_{\min} < R_{\mathrm{det}} < R_{\max} \\ 1, & \text{if } R_{\mathrm{det}} < R_{\min} \\ 0, & \text{if } R_{\mathrm{det}} > R_{\max} \end{cases} \tag{10b}$$

We marginalized over P and b assuming logarithmic and uniform distributions, respectively, and excluding values of either parameter that were also excluded during our selection of candidate transit signals, i.e. $b > \sqrt{3}/2$ and $P < 1.1$ d or periods within 5% of artifacts (Section C.2.4).

We adopted $R_{\rm min} = 3R_{\oplus}$ and $R_{\rm max} = 8R_{\oplus}$, i.e. slightly smaller than Neptune and Saturn, respectively. We adopted $P_{\rm min} = 1.2$ d and $P_{\rm max} = 10$ d following Howard et al. (2012) and Fressin et al. (2013). We determined that among 1728 stars with no detected signals within the range of $1.2 < P < 10$ and $3 < R_p < 8$, assuming $\alpha = 1.9$, then $\sum_i^{ND} \langle d_i \rangle = 16.8$. This is the expected number of detections around these stars if each had one such planet. It is not sensitive to the precise value of α.

We calculated the likelihood vs. occurrence rate using Eqns, C.7, C.10, and 10b. Excluding GJ 436b, and given that we have as yet no confirmed detections of new planets in our sample, we can only place an upper limit on the occurrence of hot Neptunes. In this case, we place a 95% confidence upper limit of 10.2% on f based on a log likelihood within 1.92 of the maximum value (Fig. C.8). We also estimate the most likely occurrence in the case of a single confirmed detection: $f = 5.3 \pm 4.4\%$ (Fig. C.8). The error is based on the assumption of asymptopic normality; a parabola was iteratively fitted to the log-likelihood curve and $\sigma_f = 1/\sqrt{2c}$, where c is the curvature of the parabola.

If there is more than one confirmed planet in our sample, the maximum likelihood estimate of f will be likewise higher. If we relaxed the assumption that all uncomfirmed detections are ruled out, then f could be significantly higher, and close to unity, because the number of WASP candidates that we have yet to screen is comparable to the expected number (~ 17) if every star had a hot Neptune. However, if our follow-up results are representative of the results as a whole, then it is more likely that all or nearly all of these unscreened systems will be ruled out as well.

C.4.4 Comparison with *Kepler*

We estimated the occurrence of 3–$8R_{\oplus}$ and $P < 10$ d planets around *Kepler* target stars using the January 2013 release of confirmed and candidate transiting planets (KOIs) from analysis of observation quarters Q1–Q8. The methods are described in Gaidos et al. (2013) and here we recapitulate only the most important details. To emulate the range of spectral types of the SEAWOLF survey, stars with $2 < V - J < 4.7$, with V magnitudes based on the relation $V = r + 0.44(g - r) - 0.02$ (Fukugita et al., 1996), were selected from the complete *Kepler* target catalog. We also required $K_p < 16$ and that each star was observed for at least seven of the first eight observing quarters. We estimated parameters for these 14,578 stars and 190 (candidate) planets by fitting

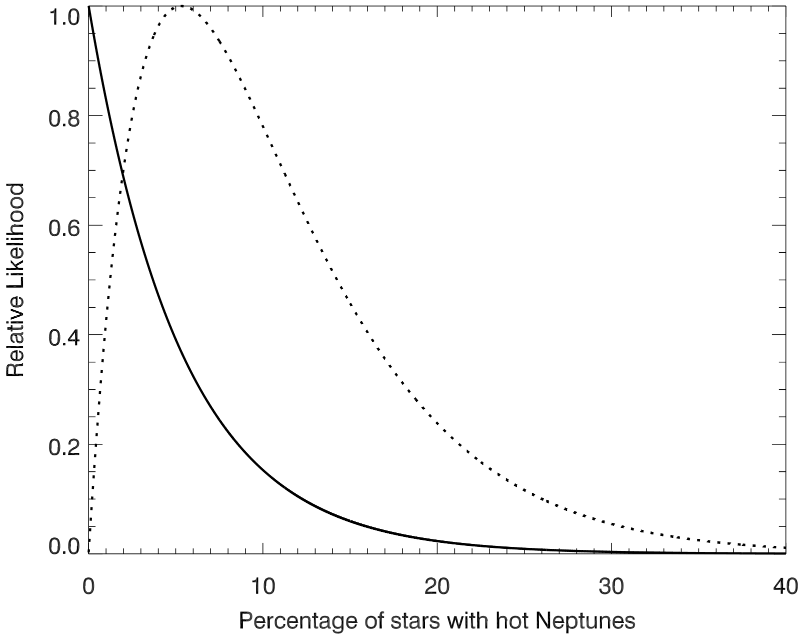

Figure C.8: Likelihood vs. occurrence of planets with 1.2 d $< P <$ 10 d and $3R_\oplus < R_p < 8R_\oplus$ around SEAWOLF stars. The dashed line is for the case of one confirmed detection and the solid line is for the case of no confirmed detections.

Dartmouth stellar evolution models (Dotter et al., 2008) using the Bayesian procedure described in Gaidos (2013). We then limited the analysis to 6422 stars with estimated $\log g > 4$ and g-D51 < 0.23. D51 is an AB magnitude based on a passband centered on 510 nm and the g-D51 color is an indicator of gravity among K dwarfs; the color-cut eliminates K giants (Brown et al., 2011). The median estimated $T_{\rm eff}$ of these stars is 4330 K. These stars host 136 candidate planets. Two of these have $3R_\oplus < R_p < 8R_\oplus$ and $P < 10$ d: KOIs 875.01 and 956.01 with R_p of 3.7 and $3.2R_\oplus$ on 4.22 and 8.36 d orbits, respectively.

We calculated the binomial log likelihood as a function of planet-hosting fraction f assuming a log distribution with orbital period and a power-law radius distribution in the limit that the transit probability is low (Gaidos et al., 2013; Mann et al., 2012):

$$f = \frac{N_p \left(R_1^{-\alpha} - R_2^{-\alpha} \right) \ln \left(P_2/P_1 \right)}{\alpha \sum_i^{ND} \langle f_i \rangle} \tag{C.12}$$

where N_p is the number of detected planets with $R_1 < R_p < R_2$ and $P_1 < P < P_2$, the summation in the denominator is over non-detections,

$$\langle f_i \rangle = \int_{R_1}^{R_2} \int_{P_1}^{P_2} R_p^{-\alpha} d_i(R_p, P)\, d\ln P d\ln R_p, \tag{C.13}$$

and $d_i(R_p, P)$ is the probability of detecting a planet around the ith star (Mann et al., 2012). For consistency with SEAWOLF we use $P_1 = 1.2$ d, $P_2 = 10$ d, and $\alpha = 1.9$.

The transit of a late K or early M dwarf by a Neptune-size planet produces a signal of magnitude 4×10^{-3}, far larger than the noise: The median 3 hr Combined Differential Photometry Precision (CDPP3) for the stars in our sample is 1.8×10^{-4} and the 99 percentile value is 6.6×10^{-4}. We estimated the cumulative SNR from a $3R_\oplus$ planet on a 10 d orbit monitored for 2 yr (8 quarters): this is the least detectable case. The stellar noise over the transit interval was taken to be the CDPP3 scaled by $\sqrt{3/\tau}$ where τ is the transit duration in hours. Fressin et al. (2013) found that the recovery rate of the *Kepler* detection pipeline is nearly 100% for SNR>16. Of the 9741 stars with CDPP3 values, for only 33 (0.3%) would the estimated SNR be < 16.

Thus the detection probability is essentially the geometric factor R_*/a, where a is the orbital semimajor axis, and independent of R_p. The R_p terms in Eqn. C.12 cancel and

$$f = N_p \ln(P_2/P_1) / \sum_i^{ND} F_i. \tag{C.14}$$

The detection probability becomes:

$$d_i(P) = \left(\frac{4\pi^2 R_*^3}{GM_*}\right)^{1/3} \frac{1 + e\cos\omega}{1 - e^2} P^{-2/3}, \tag{C.15}$$

where e is the orbital eccentricity and ω the longitude of periastron. Marginalizing over e and ω with an eccentricity distribution $n(e)$, and ignoring terms that do not depend on f,

$$\begin{aligned} \ln \mathcal{L} \approx N_D \ln f - 0.356 f \left[\int_0^1 \frac{n(e)de}{1-e^2}\right] \left(\frac{P_2}{1\ \mathrm{d}}\right)^{-2/3} \\ \times \frac{(P_2/P_1)^{2/3} - 1}{\ln(P_2/P_1)} \sum_j^{ND} \left(\frac{\rho_j}{\rho_\odot}\right)^{-1/3} + \cdots, \end{aligned} \tag{C.16}$$

where N_D is the number of detected planets and ρ is the mean stellar density. Adopting the function for $n(e)$ in Shen & Turner (2008), we found that the integral is only weakly dependent on the parameter a in their distribution, and is ≈ 1.20 for $a = 4$. Using a Rayleigh distribution like that in Gaidos et al. (2013) gives a similar value of 1.08 for the integral. Because each star can be explained by more than one stellar model with probability p, we used a weighted mean of $\rho^{-1/3}$ to calculate the likelihood:

$$\langle \rho^{-1/3} \rangle = \sum_i p_i \rho_i^{-1/3} / \sum_i p_i, \tag{C.17}$$

where the summation is restricted to main sequence models, i.e. $\log g > 4$.

Under these assumptions, we found that the occurrence of hot ($P < 10$ d) Neptunes is $0.33 \pm 0.21\%$ (Fig. C.9).

C.5 Discussion and Conclusions

We place a limit of 10% on the occurence of hot Neptunes ($P < 10$ d) around the late K and early M dwarfs in our SEAWOLF sample (95% confidence). In the event that a single planet candidate is confirmed, our maximum likelihood estimate of occurrence is $5.3 \pm 4.4\%$. From a Doppler survey of late F to early K stars, Howard et al. (2010) estimated an occurrence rate of about $8.1 \pm 4\%$ for planets with projected masses $M \sin i$ of 10-100$M_\oplus$, a mass range correspondingly approximately to our radius range, and $P < 50$ d. Assuming a logarithmic distribution with orbital period, and correcting by the factor $\ln(10/1.2)/\ln(50/1.2)$, the equivalent occurrence within 10 d is 4.6%, a value similar to our estimate for the case of a single detection. Based on the HARPS Doppler

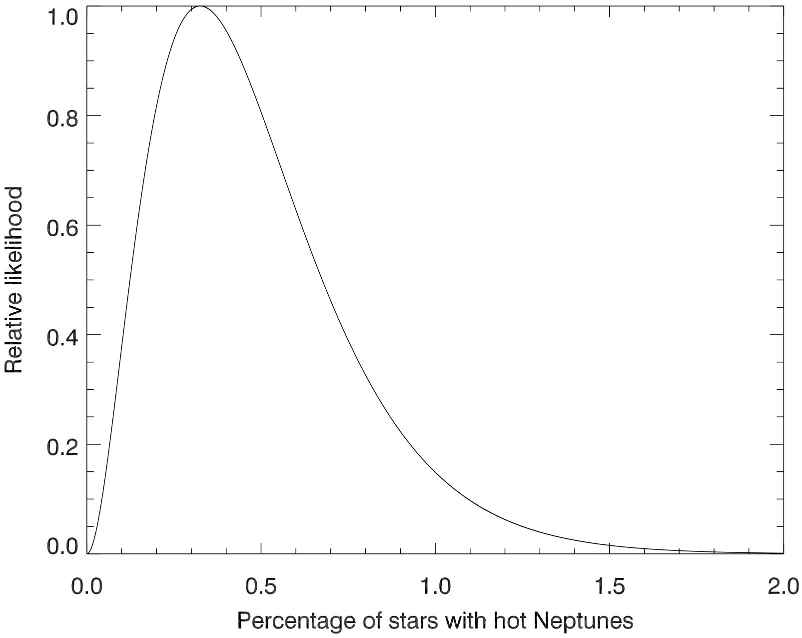

Figure C.9: Likelihood vs. occurrence of planets with $P < 10$ d and $3R_\oplus < R_p < 8R_\oplus$ around 6422 dwarf stars wtih $2 < V-J < 4.7$ observed by *Kepler* during at least 7 quarters of Q1-8.

survey, Mayor et al. (2011) estimated $11.1 \pm 2.4\%$ of solar-type stars have planets with 10-30$M_\oplus$ within $P < 50$ d, but only $1.17 \pm 0.52\%$ with masses of 30–100$M_\oplus$. Likewise, Bonfils et al. (2013) estimate that $3^{+4}_{-1}\%$ of M dwarfs have 10-100$M_\oplus$planets. That these Doppler-based values are consistent with the 5.3% occurrence we derive assuming a single SEAWOLF detection suggests that GJ 436b may be the only transiting hot Neptune in our sample.

We estimated the occurrence of hot Neptunes around the late K and early M dwarf stars observed by *Kepler* to be $0.32 \pm 0.21\%$, more than an order of magnitude lower than in the SEAWOLF catalog. Howard et al. (2012) report that the occurrence of 4–8$R_\oplus$ planets with $P < 10$ d around *Kepler* GK dwarfs is $0.23 \pm 0.03\%$, consistent with our estimate to within the errors (but for a different range of spectral types). One major caveat with interpreting the *Kepler* statistics is that late K spectral types also include red giant branch as well as dwarf stars; these luminosity classes can be difficult to distinguish by photometric colors alone and in the absence of spectroscopic screening, Malmquist bias will favor the inclusion of the large, more luminous stars (Gaidos & Mann, 2013). Planets will be more difficult to detect and will appear smaller around RGB stars, e.g. some "Earths" may actually be Neptunes. For this reason, it is possible that the statistical analysis of the *Kepler* results grossly underestimates the occurrence of hot Neptunes. However, our use of the g-D51 gravity-sensitive color in constructing our *Kepler* sample should limit this effect. More spectroscopy of *Kepler* targets in this range of $V - J$ colors is needed to quantify contamination by RGB stars.

Our determination of an order-of-magnitude lower relative occurrence of hot Neptunes around *Kepler* stars echoes the findings of Wright et al. (2012), who found a deficit of hot Jupiters around these stars. One intriguing possibility is that *Kepler* stars are older, more evolved, and have more massive convective envelopes than those in the Solar neighborhood, and that close-in giant planets have suffered tidally-driven decay of their orbits and been destroyed (Gaidos & Mann, 2013). However, in the regime where the orbital period P is much shorter than the eddy turnover timescale T, the rate of orbital decay is (Kunitomo et al., 2011):

$$\frac{\dot{a}}{a} = \frac{3}{4}\frac{M_p}{M_*}\frac{L_* P^2}{M_* \left(R_* - R_{\rm env}\right)^2}\left(\frac{R_*}{a}\right)^8, \tag{C.18}$$

where M_p is the mass of the planet, L_* is the stellar luminosity, $R_{\rm env}$ the inner radius of the convective envelope, and a the orbital semimajor axis of the planet. For a Neptune-mass planet on a 10 d orbit around an M0 dwarf star the theoretical orbital decay time is $> 10^{18}$ yr. The lower luminosity and smaller radius of K/M dwarfs relative to solar-type stars, and the lower mass of Neptunes relative to Jupiters means that this process is too slow to explain the deficit of Neptunes close to *Kepler* stars relative to the solar neighborhood. *Kepler* stars may also be more metal-poor than the solar enighborhood, but there is, as yet, no evidence that the occurrence of Neptunes depnds on the metallicity of the host star (Mann et al., 2013). Instead, the discrepancy must be explained by observational selection or differences in the efficiency in formation on or migration to close-in orbits.

The Next Generation Transit Survey (Wheatley et al., 2013) will monitor $\sim 1.6 \times 10^6$ K4-M4 dwarfs with $I < 17$ to search for hot Neptunes; about 2×10^5 of these stars will have $I < 15$ and are suitable for Doppler follow-up (P. Wheatley, personal communication). If our 0.32% occurrence rate from *Kepler* is correct the number of transiting hot (super)Neptunes in this survey will be ≤ 60, depending on actual detection efficiency. If the the occurrence rate is close to 5%, as suggested by Doppler surveys of nearby stars, the survey could find up to ~ 1000 such planets. These two values bracket an estimate by the NGTS team (Wheatley et al., 2013).

Acknowledgments

EG and KC acknowledge support from NASA grants NNX10AI90G (Astrobiology: Exobiology & Evolutionary Biology) and NNX11AC33G (Origins of Solar Sytems). GM acknowledges support from the State Scholarships Foundation of Greece in the form of a scholarship and fruitful discussions with E. Paleologou. AZ acknowledges the Foundation for Research and Technology-Hellas. Space astrophysics in Crete is supported in part by EU REGPOT project number 206469. NN acknowledges support by an NAOJ Fellowship, NINS Program for Cross-Disciplinary Study, and Grant-in-Aid for Scientific Research (A) (No. 25247026) from the Ministry of Education, Culture, Sports, Science and Technology of Japan. EC and JB were supported by NASA/University of Hawaii Space Grant fellowships. The SuperWASP-N Camera was constructed and operated with funds made available from WASP Consortium universities and the UK Science and Technology Facilities Council (STFC). We extend our thanks to the Director and staff of the Isaac Newton Group of Telescopes for their support of SuperWASP-N operations. We thank the staff of the MDM and Skinakas observatories for their invaluable and courteous assistance during many observing runs. The Las Cumbres Observatory Network operates Faulkes Telescope North, ELP at McDonald Observatory, and the Byrne Observatory; the last is located on the Sedgwick Reserve, a part of the University of California Natural Reserve System.

Table C.1: Telescopes used to obtain follow-up observations

Telescope/Observatory	D (m)	Latitude	Longitude	Instrument(s)	Passband(s)	Observations[1]
McGraw-Hill/MDM	1.3	31.95173 N	111.61664 W	B4K/R4K/Nellie	Sloan r, DES-Z	66
Faulkes North/Haleakala	2.0	20.70701 N	156.25748 W	SpectraCam 4K	Pan-STARRS Z	29
Skinakas	1.3	35.21173 N	024.89893 E	Andor DZ436	Bessel R	24
OAO 188 cm	1.88	34.57716 N	133.59387 E	ISLE[2]	J	19
LCOGT/BOS	0.8	34.68750 N	120.03889 W	SBIG	Sloan i’	5
LCOGT/ELP	1.0	30.67143 N	104.02195 W	kb73	Sloan i	4
UH88/Mauna Kea	2.2	19.82303 N	155.46937 W	OPTIC	Sloan z	1

Table C.2: Candidate Transit Systems Identified in WASP Data

Name[1]	RA			Dec			V	V-J	period	ephemeris	δ	status[2]
	hh	mm	ss.s	dd	mm	ss			(d)	(BJD)	(10^{-3})	
00177+2100	0	17	43.2	21	00	05	12.4	2.45	5.319	3878.1780	4.6	?
00492+2003	0	49	17.2	20	03	45	10.8	2.28	8.063	3502.8216	3.3	?
01086+1714A	1	08	40.4	17	14	33	10.7	2.66	5.530	4177.7331	4.3	X
01086+1714B	1	08	40.4	17	14	33	10.7	2.66	3.743	4169.6813	3.2	?
01550+4035	1	55	01.0	40	35	06	13.7	3.91	8.343	3387.8129	20.3	?
01578+3130	1	57	50.0	31	30	41	12.2	2.25	4.177	4225.8173	4.1	X
01587+3515	1	58	43.6	35	15	28	13.7	4.01	7.819	4191.1928	9.7	X
02083+2919	2	08	18.3	29	19	59	12.5	2.93	7.214	3786.2246	8.0	X
02111+2707	2	11	11.2	27	07	34	12.7	3.36	10.560	3894.2242	8.8	N
02192+2456A	2	19	17.5	24	56	38	13.8	4.09	6.985	4022.5748	11.9	N

Table C.2 is published in its entirety as a machine-readable table in the CDS. A portion is shown here for guidance regarding its form and content.

Table C.3: Observations of Candidate Transits

Star[1]	Observatory	t_c (MJD) (-2.45×10^6)	δ_d (10^{-3})	C
00177+2100	MDM	6191.85	16.6	0.032
00177+2100	MDM	6207.80	8.7	0.090
00492+2003	MDM	6195.75	2.3	0.644
01086+1714A	LCOGT/Faulkes	6212.81	1.4	0.940
01086+1714A	MDM	6284.71	6.4	0.206
01086+1714B	LCOGT/Faulkes	5898.79	7.5	0.047
01086+1714B	LCOGT/Faulkes	6157.03	3.9	0.360
01086+1714B	LCOGT/Faulkes	6564.98	7.2	0.061
01086+1714B	MDM	6583.69	5.1	0.165
01550+4035	LCOGT/BOS	6524.85	1.6	0.199

Table C.3 is published in its entirety as a machine-readable table in the CDS. A portion is shown here for guidance regarding its form and content.